A DESIGN STUDY OF RADIAL INFLOW TURBINES IN THREE-DIMENSIONAL FLOW

by

Yi-Lung Yang

B.S., National Taiwan University (1983)
M. S., Massachusetts Institute of Technology (1986)

SUBMITTED IN PARTIAL FULFILLMENT OF THE
REQUIREMENTS FOR THE DEGREE OF

DOCTOR OF PHILOSOPHY
in
Aeronautics and Astronautics
at the
Massachusetts Institute of Technology

June, 1991

©Massachusetts Institute of Technology 1991

Signature of Author _____
Department of Aeronautics and Astronautics
March 29,1991

Certified by _____
Dr. Choon S. Tan
Chairman of Thesis Committee

Certified by _____
Prof. James E. McCune
Thesis Committee Member

Certified by _____
Prof. Mark Drela
Thesis Committee Member

Accepted by _____
Professor Harold Y. Wachman
Chairman, Departmental Graduate Committee

ARCHIVES
MASSACHUSETTS INSTITUTE OF TECHNOLOGY
JUN 13 1991
LIBRARIES

A DESIGN STUDY OF RADIAL INFLOW TURBINES IN THREE-DIMENSIONAL FLOW

by

Yi-Lung Yang

submitted to the department of
Aeronautics and Astronautics
in partial fulfillment of the requirement
for the degree of Doctor of Philosophy

ABSTRACT

The development and the application of a computational tool based on an analytical theory for the design of turbomachinery blading in three-dimensional, inviscid flow are presented. In the design problem, the enthalpy or swirl distribution to be added/removed by a blade row is prescribed, and one then proceeds to determine the blade geometry; this is in contrast to the direct problem in which one proceeds to determine the performance of a blade row for a specified geometry. In the computational method, discretization of the governing equations in the theory is implemented via the use of finite-element method on the meridional plane and Fourier collocation technique in the circumferential direction. The three-dimensional design method is used to compute the blade shape in radial inflow turbine wheels in subsonic flow. This requires the following specifications: swirl distribution, number of blades, hub and shroud geometrical contour, location of blade leading and trailing edges, configuration of stacking axis, blockage distribution, wheel speed and mass flow rate. A technique of generating a smooth swirl distribution within the blade region from a specification of swirl and its derivative with respect to the meridional distance along the hub and shroud is proposed. Excellent agreements have been obtained between the computed results from the present design technique and those from direct inviscid computations based on Euler solver; this demonstrates the correspondence and consistency between the two techniques. The design method is then used to examine the influence of the following parameters on the design of a radial inflow turbine wheel proposed for helicopter powerplant application: (i) the swirl distribution within the blade region for a fixed power output; (ii) the stacking axis; (iii) the hub and shroud profiles; (iv) the number of blades; and (v) the thickness distribution. Two parameters are proposed as a measure of the goodness of a design; they are the pressure gradient on the bounding surfaces of the blade region and the wake number. The wake number has been developed to give a measure of the extent of secondary flow formation within the blade passage. Results from this design study suggest that the proposed technique of prescribing swirl distribution is a useful one and that a good design requires the specification of a swirl distribution that has its location of maximum loading near the leading edge. The computed results also demonstrate the sensitivity of the pressure distribution to a lean in the stacking axis and a minor alteration in the hub/shroud profiles. In most of these design calculations an inviscid region of reversed flow on the pressure surface of the blade has been observed. However, when a Navier-Stokes solver is used to analyze the flow through the designed wheel, no breakdown of flow within the blade passage has been observed. Furthermore, the computed values of swirl distribution and reduced static pressure distribution from the Navier-Stokes calculation agree fairly well with those from the present design calculation, implying that the flow in the designed turbine rotor closely approximates that of an inviscid flow. The present work illustrates the synergistic use of a design tool coupled to an analysis tool for implementing design; such an approach allows one to concentrate on the aerodynamic quantities of interest rather than on the choices of blade geometry.

Thesis Supervisor: Dr. Choon S. Tan
Title: Principal Research Engineer,
Department of Aeronautics and Astronautics.

Acknowledgements

I would first like to thank my supervisor, Dr. Choon S. Tan, for being a constant source of inspiration and encouragement during the course of this project. The advice and guidance he offered were greatly appreciated. Particular thanks are due to Professor Sir William Hawthorne for his invaluable insight and encouragement. The time and effort he spent throughout this research were deeply appreciated.

My thanks also go to Professor James E. McCune for his help and support. I am indebted to him for having given generously of his time. The contributions of Professor Mark Drela to the viscous flow aspects of the research were also invaluable.

I am also grateful to Dr. John J. Adamczyk of NASA-LEWIS Research Center who provided both the Euler and viscous codes. I am also indebted to James D. Heidmann of NASA-LEWIS Research Center for his assistance in the Euler and viscous calculations.

My friend and Post-doctoral Fellow at the Gas Turbine Laboratory, Dr. Andrew Wo, deserves special mention for the hours of discussions and for reviewing my results.

I would also like to acknowledge some of my GTL collegues: Earl Renaud, for his help with the computer facilities; Lou Catterfaster; Charlie Haldmann; Reza Shokrollah-Abhari; Gwo-Tung Chen; Quin Yuan; Dan Gysling; Pete Silkowski; Tonghuo Shang; Eric Strang; Seung Jin Song; who all made my stay at MIT a memorable one.

This project was sponored by the NASA Army Propulsion Directorate Grant NAG3-772, under the supervision of Mr. Pete Meitner. This support is gratefully acknowleged.

Finally, I would like to thank my family for their love and support which made this research possible.

Table of Contents

Abstract 2

Acknowledgements 3

Table of Contents 4

Nomenclature 8

List of Figures 10

Chapter 1 Introduction 17

1.1 Radial Inflow turbines 17

1.2 Design Specifications 18

1.3 Scope and Objectives of the Present Research 20

Chapter 2 Literature Survey of Inverse Design Methods 22

2.1 Blade to Blade Design Methods 22

2.1.1 Singularity Methods 23

2.1.2 Conformal Transformation Methods 24

2.1.3 Hodograph Methods 25

2.1.4 Stream Function/Potential Plane Methods 25

2.1.5 Taylor Series Expansion Methods 26

2.1.6 Potential/Stream Function Methods 26

2.1.7 Time-Marching Methods 27

2.1.8 Other Methods 28

2.2 Hub-to-Shroud Design Methods 28

2.3 Quasi-Three-Dimensional Design Methods 29

2.4 Three-Dimensional Design Methods 29

2.5 The Present Approach to Three-Dimensional Design 31

Chapter 3 Inverse Design Theory 33

3.1 Governing Equations 33
3.2 Theoretical Formulation 34
3.2.1 The Clebsch Approach 35
3.2.2 Mean Flow Equations 37
3.2.3 Periodic Flow Equation 38
3.2.4 Blade Boundary Condition 39
3.3 The Boundary Conditions 40
3.3.1 Stream Function 40
3.3.2 Velocity Potential 41
3.4 The Initial Conditions 41
3.4.1 Artificial Density 41
3.4.2 Blade Shape 42
3.5 The Kutta-Joukowski condition 42
3.6 Blockage Effects 43
3.7 Summary 45

Chapter 4 The Mean Swirl Schedule 46
4.1 Kinematic Constraints 46
4.2 Biharmonic Equation 48
4.3 Method of Specifying $r\overline{V}_\theta$ along the Hub & the Shroud 49
4.4 Summary 50

Chapter 5 The Numerical Technique 52
5.1 Grid Generation 52
5.1.1 Algebraic Method 52
5.1.2 Elliptic Method 53
5.2 The Elliptic Solver 54

5.3 The Convective Equation Solver 56
5.4 The Biharmomic Solver 57
5.5 The Computational Scheme 59

Chapter 6 Parametric Study of Inverse Designs 62
6.0 Two Parameters Used to Characterize a Design 63
6.1 Mean Swirl Schedule 68
6.1.1 Effect of the Maximum Loading Position 69
6.1.2 Effect of Regions of Vanishing $\frac{\partial r\overline{V}_\theta}{\partial n}$ 71
6.1.3 Effect of the Maximum Loading $(\frac{\partial r\overline{V}_\theta}{\partial s})_{max}$ 73
6.2 Stacking Position 76
6.3 Lean in Stacking Line 78
6.4 Slip Factor 79
6.5 Blockage Effects 80
6.6 Number of Blades 81
6.7 Exit Swirl 83
6.8 Modified Hub and Shroud Profiles 84
6.9 Summary 85

Chapter 7 Flow Analysis by Solving Euler and Navier-Stokes Equations 88
7.1 Euler and Navier-Stokes Codes Descripttion 88
7.2 Comparison between Design and Euler Results 90
7.3 Comparison between Design and Viscous Results 91
7.4 Effect of the Tip Clearance 95
7.5 Summary 98

Chapter 8 Conclusions and Suggestions for Future Work 100

8.1 Summary and Conclusions 100

8.2 Suggestions for Future Work 101

References 103

Table I : Turbine Design Conditions 107

Figures 108

Appendix A : An Expression for Velocity Jump Across the Blade 184

Appendix B : Mass-Average of the Continuity Equation with the Effect of Tangential Blockage, b 185

Appendix C : A Multigrid Method for the Poisson Equation 187

Appendix D : The Relationship between Number of Grid Points and Number of Harmonic Modes 191

Appendix E : Nondimensional Form of Variables 192

Appendix F : The Derivation of the Wake Number 192

Nomenclature

Roman Letters

B	number of blades
b	blockage, Eq.(3.33)
f	blade shape, Eq.(3.5)
H	enthalpy
$\underline{N}$	shape function, Eq.(5.5)
p	pressure
S	entropy
$S(\alpha)$	sawtooth function, Eq.(3.14)
T	temperature
t_n	blade normal thickness, Eq.(3.35)
t_θ	blade tangential thickness, Eq.(3.34)
V	absolute velocity
W	relative velocity

Greek Letters

α	blade surface, Eq.(3.5)
γ	ratio of specific heats
γ_s	shed vorticities, Eq.(4.1)
$\delta_p(\alpha)$	periodic delta function, Eq.(3.6)
ρ	density
ρ_a	artificial density, Eq.(3.20)
ψ	Stokes stream function, Eq.(3.22)

φ	lean angle of blade camber (see Fig. 6.16)
ω	impeller rotational speed
Γ	blade circulation
$\tilde{\Phi}$	periodic potential function, Eq. (3.17)
$\tilde{\phi}$	harmonic mode of periodic potential function, Eq. (3.25)
Ω	vorticity

Subscripts

bl	" at " the balde
r, θ, z	the $r-, \theta-, z-$ component
LE	blades leading edge
TE	blades trailing edge
t	total, stagnation

Superscripts

$+/-$	the blade pressure/suction surface
$\star$	rotary

Others

$\vec{()}$	vector quantity
$\overline{()}$	tangential mean, Eq.(3.8)
$\widetilde{()}$	periodic part
$\underline{()}$	column matrix
$[\,]$	matrix

List of Figures

Chapter 3

Fig. 3.1 Right-handed cylindrical coordinate system and nomenclature

Chapter 4

Fig. 4.1 An illustration of Prandtl wing theorem

Fig. 4.2 Schematic plot of $r\overline{V}_\theta$ distribution along the hub and shroud

Chapter 5

Fig. 5.1 The 4-node element

Chapter 6

Fig. 6.1 Velocity triangle at leading edge

Fig. 6.2 Grid used for calculation

Fig. 6.3a The blade camber at mid-span for two different grid sizes

Fig. 6.3b The distribution of $p_{red.}$ at mid-span for two different grid sizes

Fig. 6.4a The meridional velocity on the suction surface for Wake number = 1.86

Fig. 6.4b The meridional velocity on the suction surface for Wake number = 3.61

Fig. 6.5a The distribution of $r\bar{V}_\theta$, $\frac{\bar{W}_\theta}{r}$, and $\frac{\partial r\bar{V}_\theta}{\partial s}$ along the hub and shroud for case a

Fig. 6.5b The distribution of $r\bar{V}_\theta$, $\frac{\bar{W}_\theta}{r}$, and $\frac{\partial r\bar{V}_\theta}{\partial s}$ along the hub and shroud for case b

Fig. 6.5c The distribution of $r\bar{V}_\theta$, $\frac{\bar{W}_\theta}{r}$, and $\frac{\partial r\bar{V}_\theta}{\partial s}$ along the hub and shroud for case c

Fig. 6.5d The distribution of $r\bar{V}_\theta$, $\frac{\bar{W}_\theta}{r}$, and $\frac{\partial r\bar{V}_\theta}{\partial s}$ along the hub and shroud for case d

Fig. 6.5e The distribution of $r\bar{V}_\theta$, $\frac{\bar{W}_\theta}{r}$, and $\frac{\partial r\bar{V}_\theta}{\partial s}$ along the hub and shroud for case e

Fig. 6.5f The distribution of $r\bar{V}_\theta$, $\frac{\bar{W}_\theta}{r}$, and $\frac{\partial r\bar{V}_\theta}{\partial s}$ along the hub and shroud for case f

Fig. 6.5g The distribution of $r\bar{V}_\theta$, $\frac{\bar{W}_\theta}{r}$, and $\frac{\partial r\bar{V}_\theta}{\partial s}$ along the hub and shroud for case g

Fig. 6.5h The distribution of $r\bar{V}_\theta$, $\frac{\bar{W}_\theta}{r}$, and $\frac{\partial r\bar{V}_\theta}{\partial s}$ along the hub and shroud for case h

Fig. 6.5i The distribution of $r\bar{V}_\theta$, $\frac{\bar{W}_\theta}{r}$, and $\frac{\partial r\bar{V}_\theta}{\partial s}$ along the hub and shroud for case i

Fig. 6.6a The distribution of $r\bar{V}_\theta$ for case a

Fig. 6.6b The distribution of $r\bar{V}_\theta$ for case b

Fig. 6.6c The distribution of $r\bar{V}_\theta$ for case c

Fig. 6.6d The distribution of $r\bar{V}_\theta$ for case d

Fig. 6.6e The distribution of $r\bar{V}_\theta$ for case e

Fig. 6.6f The distribution of $r\bar{V}_\theta$ for case f

Fig. 6.6g The distribution of $r\bar{V}_\theta$ for case g

Fig. 6.6h The distribution of $r\bar{V}_\theta$ for case h

Fig. 6.6i The distribution of $r\bar{V}_\theta$ for case i

Fig. 6.7a The distribution of $p_{red.}$ for case a

Fig. 6.7b The $M_{rel.}$ on the suction side for case a

Fig. 6.7c The $M_{rel.}$ on the pressure side for case a

Fig. 6.8a The distribution of $p_{red.}$ for case f

Fig. 6.8b The $M_{rel.}$ on the suction side for case f

Fig. 6.8c The $M_{rel.}$ on the pressure side for case f

Fig. 6.9a The distribution of $p_{red.}$ for case g

Fig. 6.9b The $M_{rel.}$ on the suction side for case g

Fig. 6.9c The $M_{rel.}$ on the pressure side for case g

Fig. 6.10a The maximum adverse pressure gradient vs the region of $\frac{\partial r\bar{V}_\theta}{\partial n} = 0$

Fig. 6.10b The Wake number verse the region of $\frac{\partial r\bar{V}_\theta}{\partial n} = 0$

Fig. 6.11a The distribution of $p_{red.}$ for case h

Fig. 6.11b The $M_{rel.}$ on the suction side for case h

Fig. 6.11c The $M_{rel.}$ on the pressure side for case h

Fig. 6.12a The distribution of $p_{red.}$ for case i

Fig. 6.12b The $M_{rel.}$ on the suction side for case i

Fig. 6.12c The $M_{rel.}$ on the pressure side for case i

Fig. 6.13a The maximum adverse pressure gradient verse the maximum loading $-\frac{(\frac{\partial r\bar{V}_\theta}{\partial s})_{max}}{r_t\omega}$

Fig. 6.13b The Wake number verse the maximum loading $-\frac{(\frac{\partial r\bar{V}_\theta}{\partial s})_{max}}{r_t\omega}$

Fig. 6.14a The position of $(\frac{\partial r\bar{V}_\theta}{\partial s})_{max}$ vs stacking position for axisymmetric calculation

Fig. 6.14b The position of $(\frac{\partial r\bar{V}_\theta}{\partial s})_{max}$ vs stacking position for three-dimensional calculation

Fig. 6.15a The maximum adverse pressure gradient verse the stacking position

Fig. 6.15b The Wake number verse the stacking position

Fig. 6.16 The definition of the lean ange, φ

Fig. 6.17a The blade shape for lean angle, $\varphi = -6.65°$

Fig. 6.17b The blade shape for lean angle, $\varphi = 0.00°$

Fig. 6.17c The blade shape for lean angle, $\varphi = +6.65°$

Fig. 6.18a The distribution of $p_{red.}$ with lean angle $\varphi = -6.65°$

Fig. 6.18b The $M_{rel.}$ on the suction side with lean angle $\varphi = -6.65°$

Fig. 6.18c The $M_{rel.}$ on the pressure side with lean angle $\varphi = -6.65°$

FIG. 6.19a The distribution of $p_{red.}$ with lean angle $\varphi = 6.65°$

Fig. 6.19b The $M_{rel.}$ on the suction side with lean angle $\varphi = 6.65°$

Fig. 6.19c The $M_{rel.}$ on the pressure side with lean angle $\varphi = 6.65°$

Fig. 6.20a The maximum adverse pressure gradient verse the lean angle

Fig. 6.20b The Wake number verse the lean angle

Fig. 6.21a Velocity triangle at leading edge, slip factor = 0.95

Fig. 6.21b Velocity triangle at leading edge, slip factor = 0.86

Fig. 6.22a The distribution of $p_{red.}$ for slip factor = 0.95

Fig. 6.22b The $M_{rel.}$ on the suction side for slip factor = 0.95

Fig. 6.22c The $M_{rel.}$ on the pressure side for slip factor = 0.95

Fig. 6.23a The distribution of $p_{red.}$ for slip factor = 0.86

Fig. 6.23b The $M_{rel.}$ on the suction side for slip factor = 0.86

Fig. 6.23c The $M_{rel.}$ on the pressure side for slip factor = 0.86

Fig. 6.24a The maximum adverse pressure gradient verse the slip factor

Fig. 6.24b The Wake number verse the slip factor

Fig. 6.25a The normal thickness, t_n, for the input

Fig. 6.25b The tangential thickness, t_θ, from the output

Fig. 6.26a The distribution of $p_{red.}$ for case g, with blockage effects

Fig. 6.26b The $M_{rel.}$ on the suction side with blockage effects

Fig. 6.26c The $M_{rel.}$ on the pressure side with blockage effects

Fig. 6.27a The distribution of $p_{red.}$ for number of blades B=21

Fig. 6.27b The $M_{rel.}$ on the suction side for number of blades B=21

Fig. 6.27c The $M_{rel.}$ on the pressure side for number of blades B=21

Fig. 6.28a The maximum adverse pressure gradient verse the number of blades B

Fig. 6.28b The Wake number verse number of blades B

Fig. 6.29a The distribution of $r\bar{V}_\theta, \frac{W_\theta}{r}, and \frac{\partial r\bar{V}_\theta}{\partial s}$ along the hub and shroud with 30% of swirl left after trailing edge

Fig. 6.29b The distribution of $r\bar{V}_\theta$ with 30% of swirl left after the trailing edge

Fig. 6.30a The distribution of $p_{rel.}$ with 30% of swirl left

Fig. 6.30b The $M_{rel.}$ on the suction side with 30% of swirl left

Fig. 6.30c The $M_{rel.}$ on the pressure side with 30% of swirl left

Fig. 6.31a The distribution of $r\bar{V}_\theta, \frac{W_\theta}{r}, and \frac{\partial r\bar{V}_\theta}{\partial s}$ along the hub and shroud

Fig. 6.31b The distribution of $r\bar{V}_\theta$

Fig. 6.32a The distribution of $p_{red.}$, stacking at leading edge

Fig. 6.32b The $M_{rel.}$ on the suction side, stacking at leading edge

Fig. 6.32c The $M_{rel.}$ on the pressure side, stacking at leading edge

Fig. 6.33a The blade camber vs the meridional distance of the original and modified hub & shroud profiles

Fig. 6.33b Radial distribution of blade camber along constant z-section for the original and modified hub & shroud profiles

Chapter 7

Fig. 7.1 The mesh used for calculation

Fig. 7.2a The specified $r\overline{V}_\theta$ for design calculation

Fig. 7.2b The blade shape from the design calculation, number of blade $B = 14$

Fig. 7.3a The distribution of p_{red} on the suction surface from the design calculation

Fig. 7.3b The distribution of p_{red} on the pressure surface from the design calculation

Fig. 7.3c The distribution of p_{red} on the hub surface from the design calculation

Fig. 7.3d The distribution of p_{red} on the shroud surface from the design calculation

Fig. 7.4a The distribution of $r\overline{V}_\theta$ from the Euler calculation

Fig. 7.4b The difference in $r\overline{V}_\theta$ between design specification and Euler calculation

Fig. 7.5a The distribution of p_{red} on the suction surface from the Euler calculation

Fig. 7.5b The distribution of p_{red} on the pressure surface from the Euler calculation

Fig. 7.5c The distribution of p_{red} on the hub surface from the Euler calculation

Fig. 7.5d The distribution of p_{red} on the shroud surface from the Euler calculation

Fig. 7.6a The distribution of $r\overline{V}_\theta$ from the viscous calculation

Fig. 7.6b The difference in $r\overline{V}_\theta$ between design specification and viscous calculation

Fig. 7.7a The distribution of p_{red} on the suction surface from the viscous calculation

Fig. 7.7b The distribution of p_{red} on the pressure surface from the viscous calculation

Fig. 7.7c The distribution of p_{red} on the hub surface from the viscous calculation

Fig. 7.7d The distribution of p_{red} on the shroud surface from the viscous calculation

Fig. 7.8a The distribution of relative Mach number M_{rel} from the design calculation

Fig. 7.8b The distribution of relative Mach number M_{rel} from the viscous calculation

Fig. 7.9a The meridional velocity on the surface 1-point above the S.S

Fig. 7.9b The meridional velocity on the surface 1-point below the P.S.

Fig. 7.10a The distribution of entropy S at the leading edge

Fig. 7.10b The distribution of entropy S at the $\frac{1}{4}$ chord

Fig. 7.10c The distribution of entropy S at the $\frac{1}{2}$ chord

Fig. 7.10d The distribution of entropy S at the $\frac{3}{4}$ chord

Fig. 7.10e The distribution of entropy S at the trailing edge

Fig. 7.11a The distribution of streamwise vorticity Ω_r at the leading edge

Fig. 7.11b The distribution of streamwise vorticity Ω at the $\frac{1}{4}$ chord

Fig. 7.11c The distribution of streamwise vorticity Ω at the $\frac{1}{2}$ chord

Fig. 7.11d The distribution of streamwise vorticity Ω at the $\frac{3}{4}$ chord

Fig. 7.11e The distribution of streamwise vorticity Ω_z at the trailing edge

Fig. 7.12a The distribution of entropy S at the leading edge, number of blades $B = 21$

Fig. 7.12b The distribution of entropy S at the $\frac{1}{4}$ chord, number of blades $B = 21$

Fig. 7.12c The distribution of entropy S at the $\frac{1}{2}$ chord, number of blades $B = 21$

Fig. 7.12d The distribution of entropy S at the $\frac{3}{4}$ chord, number of blades $B = 21$

Fig. 7.12e The distribution of entropy S at the trailing edge, number of blades $B = 21$

Fig. 7.13a The distribution of streamwise vorticity Ω_r at the leading edge, number of blades $B = 21$

Fig. 7.13b The distribution of streamwise vorticity Ω at the $\frac{1}{4}$ chord, number of blades $B = 21$

Fig. 7.13c The distribution of streamwise vorticity Ω at the $\frac{1}{2}$ chord, number of blades $B = 21$

Fig. 7.13d The distribution of streamwise vorticity Ω at the $\frac{3}{4}$ chord, number of blades $B = 21$

Fig. 7.13e The distribution of streamwise vorticity Ω_z at the trailing edge, number of blades $B = 21$

Fig. 7.14a The distribution of $r\overline{V}_\theta$ from the viscous calculation with 3% of tip clearance

Fig. 7.14b The difference in $r\overline{V}_\theta$ between design specification and viscous calculation with 3% of tip clearance (only the blade region)

Fig. 7.15a The distribution of $p_{red.}$ on the suction surface from the viscous calculation with 3% of tip clearance

Fig. 7.15b The distribution of $p_{red.}$ on the pressure surface from the viscous calculation with 3% of tip clearance

Fig. 7.15c The distribution of $p_{red.}$ on the hub surface from the viscous calculation with 3% of tip clearance

Fig. 7.15d The distribution of $p_{red.}$ on the shroud surface from the viscous calculation with 3% of tip clearance

Fig. 7.16a The meridional velocity on the surface 1-point above the S.S. with 3% of tip clearance

Fig. 7.16b The meridional velocity on the surface 1-point below the P.S. with 3% of tip clearance

Fig. 7.17a The distribution of entropy S at the leading edge with 3% of tip clearance

Fig. 7.17b The distribution of entropy S at the $\frac{1}{4}$ chord with 3% of tip clearance

Fig. 7.17c The distribution of entropy S at the $\frac{1}{2}$ chord with 3% of tip clearance

Fig. 7.17d The distribution of entropy S at the $\frac{3}{4}$ chord with 3% of tip clearance

Fig. 7.17e The distribution of entropy S at the trailing edge with 3% of tip clearance

Fig. 7.18a The distribution of streamwise vorticity Ω_r at the leading edge with 3% of tip clearance

Fig. 7.18b The distribution of streamwise vorticity Ω at the $\frac{1}{4}$ chord with 3% of tip clearance

Fig. 7.18c The distribution of streamwise vorticity Ω at the $\frac{1}{2}$ chord with 3% of tip clearance

Fig. 7.18d The distribution of streamwise vorticity Ω at the $\frac{3}{4}$ chord with 3% of tip clearance

Fig. 7.18e The distribution of streamwise vorticity Ω_z at the trailing edge with 3% of tip clearance

Appendix B

Fig. B.1 Control volume for an axisymmetric flow

Appendix C

Fig. C.1a Test grid for multigrid study, uniform mesh

Fig. C.1b Log(residue) verse unit of work for mesh-a

Fig. C.2a Test grid for multigrid study, with distortion in Z direction

Fig. C.2b Log(residue) vs unit of work for mesh-b

Fig. C.3a Test grid for multigrid study, with distortion in both R and Z directions

Fig. C.3b Log(residue) vs unit of work for mesh-c

Chapter 1

Introduction

There are two problems of interest to designers of turbomachinery. One is the "inverse" problem in which the enthalpy or swirl distribution to be added/removed by a blade row is prescribed, and one then proceeds to determine the blade geometry. The other is the "direct" problem in which one proceeds to determine the performance of a blade row for a specified geometry. The direct problem has been solved in both two-dimensional and three-dimensional flows. The inverse problem has also been addressed and solved within the two-dimensional limit; not much work has been done, however, in developing a truly inverse design method in three-dimensional flow.

One can of course use the direct solution to solve the design problem of turbomachinery iteratively. One starts by guessing a blade shape, then calculates the flow field by using analysis programs, and compares the solution with the desired flow conditions. If these do not match, the blade geometry is altered. The whole process is repeated until the required conditions are achieved. In this case, the designer's experience and talents are vital in reducing the number of trials.

In the two papers on the "Theory of Blade Design for Large Deflections" published in 1984 (Ref. 1, 2), a new technique was presented for designing the shape of turbomachinery blades in three-dimensional flow. In this work, further development of the method and its application to a design study of radial inflow turbines are presented.

1.1 Radial Inflow Turbines

Small radial inflow turbines are suitable for a variety of applications; e.g. in turbochargers, space vehicles, and other systems where compact power sources are required.

Turbines of this type have a number of desirable characteristics, such as high efficiency, ease of manufacture, and sturdy construction. However, peak design-point efficiencies of the conventional radial inflow turbines seldom approach those of the most highly developed axial machines. The lower efficiencies of radial inflow turbines might have been a result of the economics of the historical market. Primarily the flow inside the rotors is very complex with strong three-dimensionality, hence an optimal design may be difficult to achieve.

A good example of the effect of the lack of knowledge of optimum blade shape is the use of radial filament blades for radial inflow turbines. This geometric restriction has no aerodynamic justification. These radial filament blades are used because they reduce the centrifugal bending forces and are easy to describe and manufacture. As a result, most of the radial inflow turbines used in industry have similar blade shapes and a similar overall performance. A rational design method is desirable for making a substantial improvement in the aerodynamic performance of radial inflow turbines.

1.2 Design Specifications

A number of inverse design methods are available for two-dimensional flow. It is convenient to prescribe a velocity or pressure distribution on the pressure and suction surfaces, so that the profile losses can be minimized. However, this type of design specification gives no independent control over the blade thickness and could result in problems associated with the closing of blade profiles. As an alternative, the velocity or pressure on the suction side and the thickness distribution are prescribed. In any case, none of the two-dimensional inverse design methods available seem to be applicable to the three-dimensional design of radial turbines.

In three dimensions the specification of the velocity (or pressure) distribution on the blade surfaces can not be easily implemented. This is not only due to the complication resulting from the necessity to prescribe the velocity (or pressure) as a function of two

independent variables, but also because additional constraints on the velocity distribution have to be satisfied in three-dimensional flow. For example, in the limit of the incompressible flow, the conservation of mass requires the velocities to be divergence free. As a result, it is not possible to specify the velocities on the blade surface arbitrarily.

A design specification that has been applied to the inverse design of blades in three dimensional flow is the distribution of the circumferentially averaged swirl velocity $r\overline{V}_\theta$ defined by:

$$r\overline{V}_\theta(r,z) = \frac{B}{2\pi}\int_0^{\frac{2\pi}{B}} rV_\theta(r,\theta,z)d\theta$$

where B is the number of blades. At first sight the specification of $r\overline{V}_\theta$ seems to be quite arbitrary and without any important influence on the behavior of the flow field. However, on closer inspection we can see that for an uniform upstream flow the bound circulation Γ on the blade is given by:

$$\Gamma B = 2\pi r\overline{V}_\theta$$

It will be shown later on that $r\overline{V}_\theta$ is directly related to the blade loading and therefore the pressure distribution (see Eq.(3.31)). At the same time, the specification of the $r\overline{V}_\theta$ distribution for three dimensinal problems has other advantages over the more conventional velocity or pressure distribution used in two-dimensional design methods. For example, it is fairly easy to obtain constant work along the span for a blade row which results in a zero spanwise variation of circulation and hence no shed vorticities. Thus, the exit kinetic energy loss can be reduced.

The important role played by $r\overline{V}_\theta$ has been recognized by several previous workers (see Chapter 2). For example, in the case of aircraft propellers, one can specify an optimum circulation distribution similar to that suggested by Theodorsen (Ref. 3) and hence reduce the induced losses (Smith Ref. 4). The distribution of circulation is also widely used in the design of marine propellers (Kerwin Ref. 5) in which the control of the loading can avoid cavitation and noise problems.

1.3 Scope and Objectives of the Present Research

In the present study, the three-dimensional design problem of a radial inflow turbine is addressed. The turbine is composed of a vaneless volute and one impeller rotating at a fixed speed. For simplicity, the flow is assumed to be steady and irrotational, and the fluid is inviscid and non-heat conducting. The blades are assumed to be thin and set at zero local angle of incidence. The impeller hub and shroud profiles are given and the mean swirl schedule is prescribed. The blade shape is determined iteratively from the requirement of no flow normal to the blades.

The objectives of the research are: (1) to develop a computational technique for implementing the inverse design of radial inflow turbines in three-dimensional flow; (2) to characterize $r\overline{V}_\theta$ distribution by parameters related to fluid mechanics; and (3) to develop guidelines for an $r\overline{V}_\theta$ distribution that would result in a good design. Two parameters are proposed as a measure of the goodness of a design; they are the pressure gradient on the bounding surfaces of the blade region and the wake number (see chapter 6). The resulting flow through the designed turbine wheel can be analyzed using a three-dimensional viscous code to assess the goodness of a particular design. If the viscous flow analysis indicates the presence of flow separation, strong secondary flow and high losses, then new parameters can be redefined and then use to generate a different $r\overline{V}_\theta$ distribution while maintaining the overall change in $r\overline{V}_\theta$ across the blade row constant. The whole process can be repeated until good flow conditions are achieved. It is hoped that the above process can help designers toward a more rational way of blading design in three-dimensional flow; it should be noted that in such a procedure, attention is focused on the flow quantities of interest rather than on the blade geometry.

The thesis will be organized as follows:

The literature relevant to the present work will be reviewed in chapter 2. We will see that very few three-dimensional design methods are reported in the published domain and

the convenience of using an $r\overline{V}_\theta$ specification will be pointed out.

In chapter 3, we will describe the theoretical background for the method and derive the relevant governing equations. It will be deduced from the theory that the mean swirl schedule $r\overline{V}_\theta$ is the natural flow quantity to specify in a design procedure for turbomachinery blading in three-dimensional flow.

In chapter 4, we will discuss the kinematic constraints on the mean swirl schedule $r\overline{V}_\theta$ and present an analytical method to control and interpolate the $r\overline{V}_\theta$ distribution within the blade region.

The numerical technique used to solve the relevant governing equations will be described in chapter 5.

A parametric study of radial inflow turbine design will be presented in chapter 6. The configuration is one that has been proposed for a helicopter power plant application. This design study consists of exploring the effect of the design parameters (namely the mean swirl schedule, stacking position, lean in stacking angle, slip factor, number of blades and modified hub & shroud profile) on boundary layer and secondary flow development within the blade passage. Some guidelines for an optimal $r\overline{V}_\theta$ distribution are then suggested.

In chapter 7, results from the present design code is compared to those from a direct Euler calculations. Three-dimensional viscous code has also been used to analyze the flow through the designed turbine wheel in terms of boundary layer and secondary flow development.

The conclusions from this study and some suggestions for further work are presented in chapter 8.

Chapter 2

Literature Survey of Inverse Design Methods

In this chapter, some of the previous inverse design methods used in turbomachinery are reviewed. Different approaches to the problem are discussed. Since the flow through a real turbomachine is three-dimensional, unsteady and viscous, an inverse design procedure under these conditions would be difficult to implement if not impossible. For this reason, approximations are made to simplify the governing equations into a form that would make the design problem solvable. Two approximations commonly used in all of the methods are that the flow is steady and inviscid.

Two-dimensional methods in the blade to blade plane will be reviewed first, followed by schemes in a plane normal to blade to blade plane, called the meridional plane. Then some quasi-three-dimensional methods are reviewed. Then fully three-dimensional design methods are introduced and described. Finally, the theory used in this thesis will be commented upon.

2.1 Blade to Blade Design Methods

The flow through an axial machine with a high hub-to-tip ratio can be considered as two-dimensional because the fluid is constrained to move on a nearly cylindrical surface of revolution. In these cases, we can take the flow at mid-span as being representative of the velocity field. When we unwrap the cylindrical surface of revolution, we have a row of airfoils which is called a cascade.

An inverse design method in a blade-to-blade plane is attractive because the velocity or pressure distribution can be prescribed along the airfoil, which allows a good control over the boundary layers. There are several schemes for solving the blade-to-blade problem. We will present only a few examples of each scheme.

2.1.1 Singularity methods

In this approach, the flow field and the blade shape are represented by a distribution of vortices and/or sources and sinks. The strength of these singularities determines the flow field. The blade shape can be determined from the boundary condition, i.e., the flow tangency to the airfoil surface.

One of the most popular and well known direct methods is Martensen's surface vorticity technique (Ref. 6). Wilkinson (Ref. 7) adopted this direct method to solve the inverse problem. In this method, the suction surface velocity and the blade thickness are prescribed. Then the Martensen's method is used to solve the actual velocity distribution on an initial blade shape. The difference between the desired and calculated velocity distribution is then assumed to be due to a vortex distribution on the mean camber line. The mean camber line is then adjusted to make it a streamline, and the thickness distribution is added symmetrically. The process is repeated until convergence is reached. A similar approach has been used by Murugesan & Railly (Ref. 8) who specified the velocity distribution on both suction and pressure sides. A distribution of vorticity around the blade surface is used to correct the difference between the calculated and the prescribed surface velocities. Schwering (Ref. 9) formulated the velocity in terms of the stream function. He prescribed the velocity on the airfoil surface which is the same as the strength of bound vorticity and obtained the airfoil geometry by locating the stagnation streamline. Recently, Lewis (Ref. 10) produced another inverse design procedure. In this method, the airfoil is discretized into panels and the direction of the panels is parallel to the local velocity. He allows for a variety of specifications, e.g., in the specification of the velocity on both sides of blade, or only of the velocity on suction surface together with a blade thickness.

Betz & Flügge-Lotz (Ref. 11) proposed a method for the design of thin radial cascade in the (r, θ) plane. They use vortices to account for the jump in the tangential velocity across the blade and source/sink distribution to account for the stream tube height vari-

ations. The vorticity is represented by a periodic delta function, i.e., all the vorticity is concentrated on the blades and the flow is irrotational everywhere else. In this method, the circulation is specified along the radius and the blade shape is calculated iteratively.

Another study was reported by Hawthorne et al. (Ref. 1) of the design of thin blades in cascades. The mean tangential velocity is specified as an input. Hawthorne et al. (Ref. 1) presented two different approaches to solve the problem, one using the Biot-Savart approach which is a classical aerodynamic representation of incompressible potential flow and the other using Clebsch's formulation. The Clebsch approach is used here because it can be readily extended to three-dimensional flow.

Dang & McCune (Ref. 12) extended the Clebsch approach for the design of cascades with appreciable thickness. The thickness is modelled by considering a distribution of sources and sinks on the mean camber line. Since the velocity is discontinuous across the mean camber line, the accuracy and efficiency will be low. A "smoothing" expansion technique described in McCune & Dang (Ref. 13) was used to determine the highly non-linear nature of the flow field.

2.1.2 Conformal Transformation Methods

By means of the conformal transformation of a cascade of airfoils into a circle, the shape of the airfoils can be determined from a prescribed distribution of velocity given on the circle. Lighthill (Ref. 14) uses the transformation $Z = e^{\frac{2\pi z}{t}}$ to transform a cascade of blades into a single blade, and this single blade is then transformed into a circle on which the desired velocity is specified as a function of circle angle. The argument of the blade surface velocity can be calculated from a Poisson integral. A simple integration of this argument gives the blade shape.

Gostelow (Ref. 15) has extended the conformal technique to compressible subsonic flow using the assumption that the pressure-volume relation is linear. In a later report,

Gostelow et al. (Ref. 16), gave a detailed computational procedure.

2.1.3 Hodograph Methods

Hodograph Methods change the independent variables from (x, y) to (u, v) where x, y are physical coordinates and u, v are two components of velocity. In the hodograph plane, the full potential flow equations are linear; nevertheless, the boundary conditions in the hodograph plane are complicated. For example, the far field flow maps into a logarithmic singularity. These complications require careful treatment.

An early application is given by Cantrell & Fowler (Ref. 17) for incompressible flow. In their work, the surface velocity can be controlled precisely. It has been extended to subsonic flow by Uenishi (Ref. 18) and has been applied to transonic flow by Hobson (Ref. 19). Another example of the use of the hodograph plane in design problem for a single airfoil is given by Bauer et al. (Ref. 20). It was later applied to a cascade by Garabedian & Korn (Ref. 21) and Lorn (Ref. 22). They show that the system of equations is always hyperbolic if the variables x, y, u and v are assumed to be complex. The flow field is calculated by the method of characteristics in finite difference form. Further improvements in the method were introduced by Sanz (Ref. 23) and Sanz et al. (Ref. 24).

2.1.4 Stream Function/Potential Plane Methods

This method was first proposed by Stanitz (Ref. 25) to solve the channel flows. The methods change the independent variables from (x, y) to (ψ, ϕ) where x, y are physical coordinates and ψ is the stream function and ϕ is the potential. The solid surfaces correspond to lines of constant ψ and hence it is easy to impose the boundary conditions there. The desired velocity is specified for the input as a function of arc-length in the physical plane. Stanitz & Sheldrake (Ref. 26) have extended the method from channel flows to cascade. However, the blades need to have cusped leading and trailing edges to

avoid stagnation points as they are singular points of the transformed equations. Later, Schmidt (Ref. 27) introduced an implicit upwind difference scheme to allow for transonic shockless flow design.

2.1.5 Taylor Series Expansion Methods

These methods solve the equations of motion by using a pitchwise expansion of the flow variables in a Taylor series around the mean streamline. This approach is suitable for high solidity cascade design in shockless flow.

Wu & Brown (Ref. 28) have applied this approach for cascade design in compressible flow. The inlet and exit flow angles, a desired mean streamline shape and thickness distribution are specified. First, the flow along the mean streamline is calculated and then it is extended in the pitch direction by the use of Taylor Series. The blade shape is determined by the given mass flow.

A similar approach has been used by Novak & Haymann-Haber (Ref. 29) for cascades with a large radius change. The pressure difference across the blade and circumferential thickness is specified. A fourth order Taylor Series is then used to approximate the tangential flow field.

2.1.6 Potential/Stream Function Methods

If the flow is irrotational, a velocity potential can be defined and the governing equations reduced to a single scalar equation. The velocity is obtained from the gradient of velocity potential. Similarly, one can use the stream function instead of the potential.

An early work was carried out by Sator (Ref. 30) who solved the linearized potential equation. He used a finite difference scheme suggested by Murman & Cole (Ref. 31). In the subsonic region, a central difference operator is used. In the supersonic region, a backward difference operator is used. The leading edge shape is given along with pressure distribution

on the remainder of the airfoil. After convergence, an integral boundary layer calculation is used to determine the displacement thickness and to correct the profile coordinates.

A full potential equation was solved with a finite difference technique by Beauchamp & Seebass (Ref. 32). The computational method was used for designing shock-free turbomachinery blades. Cedar & Stow (Ref. 33) used a finite element technique for the design of turbomachinery blades.

Wang (Ref. 34) reported an inverse design method based on stream function equation. This method used the non-orthogonal curvilinear coordinates and the technique of artificial compressibility. The surface velocity is used as an input.

2.1.7 Time-Marching Methods

A technique which is widely used for the computation of transonic flow is the so-called "time-marching" technique. In this technique, the unsteady Euler equations are integrated forward in time until a steady state solution is reached. If the numerical scheme takes the conservative form, it can be used in both subsonic and supersonic or mixed subsonic/supersonic regions. Since there is no assumption that the flow is irrotational, this technique can be used with strong shock waves.

One of the first applications of this method for inverse design was given by Thompkins & Tong (Ref. 35) and Tong & Thompkins (Ref. 36). They specify the blade surface pressure for the input plus geometric constraints, such as a closed trailing edge. At the same time, Meauze (Ref. 37) provided another inverse design method. He prescribed a desired velocity distribution and the closure condition of the profile which was ensured by an iterative process on the solidity of the cascade. His second version of the design method allowed the blade thickness to be prescribed and the velocity on the suction side to be assigned. Later Meauze & Lesain (Ref. 38) extended this method to the design of cascades with a large variation of radius.

Finally, Singh (Ref. 39) reported another inverse design method based on Denton's (Ref. 40) time-marching scheme. His approach is similar to Meauze's. In his calculation, the initial guess of blade shape is provided with zero thickness.

2.1.8 Other Methods

Recently Giles et al. (Ref. 41) used a finite volume approach to solve the steady Euler equations on an intrinsic mesh. In this method, the boundary layer is modelled by its displacement thickness and is solved in a global Newton iteration implicitly. The scheme allows for analysis or design mode with a thin finite wake. In the design mode, the surface pressure is used for the input. For the closure of the leading edge and trailing edge two shape functions are introduced for a closed profile.

2.2 Hub-to-Shroud Design Methods

In this section , we will describe a design method in the hub-to-shroud plane, or meridional plane. The streamline curvature method has been widely used to solve the through flow problem. In this technique, the problem is usually solved numerically and iteratively on the streamlines. An integration of velocity gradient along a quasi-orthogonal grid determines the flow properties from hub to shroud. The method can be run in both analysis and inverse modes.

One of the earlier examples is that of Smith & Hamrick (Ref. 42). They prescribed the hub geometry and the velocity along the hub. The shroud profile in the meridional plane can be determined from the given mass flow.

Different design specifications were used by Wright & Novak (Ref. 43). A mass average of swirl schedule was used for the input of the design. Given the hub and shroud profile, a linear variation of velocity in the circumferential direction was assumed, and this scheme then gave the blade velocity distribution. A similar approach has also been reported by

Novak (Ref. 44) and later by Katsanis (Ref. 45). Not much work has been done in the inverse design in the meridional plane. In most cases, this technique is coupled with blade-to-blade flow field to form a quasi-three-dimensional problem as will be seen later on.

2.3 Quasi-Three-Dimensional Design Methods

In this approach, a three-dimensional flow is split into two two-dimensional problems. One is the hub-to-shroud through flow problem and the other is the blade-to-blade cascade problem. Ideally, the iteration of the solutions between these two planes can account for some three-dimensional effects. Typically, this process has been used for axial turbomachines where the three-dimensional effect is not too significant, e.g., the use of the radial-equilibrium theory in connection with a blade-to-blade program.

Kashiwabara (Ref. 46) applied the technique to axial, mixed, and radial blading design. In the design he prescribed the velocity distribution along the blade surfaces. The singularity method is used in the blade-to-blade calculation. The blade forces in the spanwise direction are neglected in the radial equlibrium.

Jennions & Stow (Ref. 47, 48) reported a quasi-three-dimensional design procedure. The effect of blade forces and blade-to-blade variations have been taken into account in the radial equilibrium equation. The scheme allows several choices of blade-to-blade inverse design.

2.4 Three-Dimensional Design Methods

An early three-dimensional inverse design method has been presented by Okurounmu & McCune (Ref. 49, 50) for subsonic and transonic flow in an axial machine of constant hub and tip radius. They assumed the blade rows to introduce small disturbances so that linearized lifting surface theory could be applied. The blades were assumed to have zero

thickness and were modelled by a prescribed bound vorticity. If the circulation was not uniform in the spanwise direction, the wakes could also be modelled by sheets of vorticity.

Using the Clebsch formulation to prescribe the flow field, Tan et al. (Ref. 2) presented a new way to design highly loaded blades. The mean swirl schedule $r\overline{V}_\theta$ is specified for the design. For an annular duct of constant hub and tip radius, the flow equations are solved by spectral methods where the velocity is expanded in a Fourier Series in the tangential direction and in a Bessel Series radially. The wrap angle, f, is represented by an axial Chebyshev Series and a Cosine Series in the radial direction. Borges (Ref. 51) applied this technique for a radial inflow turbine using a finite difference multi-grid scheme. He constructed and investigated the performance of two different impellers. The blades for the first impeller were designed by a conventional method, those for the second impeller were designed using his program to a swirl schedule which he formulated. This work showed that the second impeller gave a definite improvement in efficiency over a wide range of operation. Using a numerical scheme based on finite element method, Ghaly (Ref. 52) applied this method to a radial inflow turbine blades for subsonic flow. The parametric study given by him (Ref. 53) showed the important role of $r\overline{V}_\theta$ in this inverse design method. Zangeneh (Ref. 54, 55) extended the finite difference multi-grid method developed by Borges to subsonic flow and designed a small high speed radial inflow turbine. He showed that the specified swirl schedule agreed very well with the results from Euler calculation. The measurement of secondary flow is confirmed by viscous solutions.

Dang & McCune (Ref. 56) extended the above technique to the case of rotational flow but only considered a three-dimensional linear cascade with zero thickness. Due to the rotationality of the flow, it was necessary to keep track of the Bernoulli and drift surfaces. This introduced a further complication in the process. A numerical example was given for a linear blade row design with an incoming shear flow.

A numerical method was presented by Soulis (Ref. 57) for the design of thin turbomachinery blades with specified swirl across the blade span as suggested by W. R. Hawthorne.

The numerical scheme involves iterations between the direct solution of a finite-volume method and a design solution. Due to an approximation inherent to his program, this method cannot be applied to the design of rotating cascades or blade rows with strong shock.

A completely different approach has been published by Zhao et al. (Ref. 58) who used a Taylor Series expansion in the circumferential direction. This was an extention of the theory by Wu & Brown (Ref. 28). In this method, the $r\overline{V}_\theta$ distribution on the mean hub-to-shroud stream surface and blade circumferential thickness were specified. Assuming the flow to be irrotational and isentropic, the blade shape was determined by the hub-to-shroud stream surfaces that passed the design mass flow. They found that in order to have no velocity normal to the hub and shroud surfaces, the $r\overline{V}_\theta$ needs to be modified near the end wall. This condition, they call the annular constraint.

Recently, Turner (Ref. 59) has applied the double stream function formulation for three-dimensional Euler equations. Correct shock capturing was permitted by using a conservative form of discrete equations along with a pressure upwind scheme. The discrete equation system was solved by Newton's method. The code can be used for analysis as well as design purpose. The pressure jump across the blade and its thickness are specified for the inverse design. However, this method can only handle a small amount of stream surface wrapping. Therefore, the method is restricted to flow with little or no streamwise vorticity.

From the above description, it can be seen that relatively little work is done in the inverse problem of the three-dimensional flow. Except for Turner's method, the assumption of irrotationality is used.

2.5 The Present Approach to Three-Dimensional Design

The most important stage in the design of radial inflow turbines is the design of the

meridional profile and the blade shape of the rotor. Conventionally, the hub and shroud profiles are prescribed by elliptical arcs and the blade shape is radial. Using some of the available analysis codes, the hub and shroud profiles and blade shape are modified iteratively. Because the flow inside a radial inflow rotor is highly three-dimensional, the above optimal process is expensive and time consuming, even with today's powerful computers. Only recently, have three-dimensional inverse design methods become available. It is then feasible to assess design in terms of fluid mechanics instead of iterating on changes in geometry. As a result, an improvement in the performance of radial turbines become possible.

The theory upon which the current approach depend has been published in Ref. 1 & 2. Several previous workers, (namely, W. Ghaly, J. Borges and M. Zangeneh) have applied this theory to the design study of radial inflow turbines. They have demonstrated that this inverse design theory can improve the performance of radial inflow turbines over a wide range of operation. In particular, W. Ghaly has noted the sensitivity of the blade shape and the pressure field to minor alteration in the specified mean swirl schedule. Thus, it is suggested that one might, through the specification of a suitable swirl distribution, be able to control the resulting reduced static pressure distribution and hence the development of boundary layer and secondary flow in the blade passage. The present work has been undertaken to examine this aspect of the design procedure.

Chapter 3

Inverse Design Theory

In this chapter, the basic theory of the inverse design method will be presented. This inverse theory, developed by Tan et al. (Ref. 2), is based on the Clebsch's transformation. Further development of the method to compressible flow is made by Ghaly (Ref. 52). The correct treatment of blockage will be given in the section 3.6.

The basic idea is to represent the blades by sheets of bound vorticity as in classical aerodynamics. It will be shown in the following that the strength of this bound vorticity is related to the mean swirl schedule $r\overline{V}_\theta$ and the blade shape (i.e. the location of the bound vortex sheet representing the blades). In the direct problem, one would specify the blade geometry (or shape) and proceed to compute the required distribution of bound vorticity on the blade surface so that the associated flow field is one that satisfies the condition of zero normal velocity on the blade surface. By contrast, in the design problem, we would specify the distribution of bound vorticity (i.e. the mean swirl $r\overline{V}_\theta$) and proceed to determine the blade surface geometry (i.e. location of bound vortex sheet on which the normal velocity vanishes).

3.1 Governing Equations

The problem under consideration is that of a steady irrotational flow of an inviscid non-heat conducting ideal gas or liquid in a radial impeller of arbitary hub and shroud profiles, rotating at a constant speed ω. With these assumptions, the only vorticity in the flow field is that bound to the solid surfaces. This also implies that any swirl induced by the presence of blades/impeller will be of the free vortex type. The impeller blades are assumed to have zero thickness so that each blade is represented by a vortex sheet. The

blades are set at zero angle of incidence to avoid the occurrence of infinite velocity at the leading edge. This is not a limitation of the technique for one can readily account for this leading edge singularity as is done so in classical thin airfoil theory.

With the above assumptions, the flow is both homenthalpic and homentropic, i.e., the rothalpy (H_T^*, see Eq.(3.3)) and the entropy (S), are constant everywhere in the flow field. The governing equations are reduced to the following form:

$$\nabla \bullet (\rho \vec{W}) = 0 \tag{3.1}$$

$$\vec{W} \times \vec{\Omega} = 0 \tag{3.2}$$

$$H_T^* = H + \frac{1}{2}W^2 - \frac{1}{2}\omega^2 r^2 = H^* + \frac{1}{2}W^2 = H + \frac{1}{2}V^2 - \omega r \overline{V}_\theta = constant \tag{3.3}$$

$$(\frac{p}{p_T^*}) = (\frac{\rho}{\rho_T^*})^\gamma = (\frac{T}{T_T^*})^{\frac{\gamma}{\gamma-1}} \tag{3.4}$$

where p, ρ, T are the fluid pressure, density and temperature. $\vec{V}$ is the absolute velocity, and $\vec{W}$ is the relative velocity, i.e., the velocity vector relative to the rotating frame ($\vec{W} = \vec{V} - r\omega\vec{e}_\theta$). H_T^*, H^*, H are the rothalpy (rotary total enthalpy), rotary static enthalpy and static enthalpy. γ is the ratio of specific heats. Note that away from the blade the momentum equation is identically satisfied by the irrotationality condition.

3.2 Theoretical Formulation

Without any loss of generality, blade surfaces in a cylindrical coordinate system (see Fig. 3.1) may be represented by

$$\alpha(r, \theta, z) = \theta - f(r, z) = \pm\frac{n2\pi}{B} \tag{3.5}$$

where (r, θ, z) is the right-handed coordinate system, f is the angular coordinate of a point on the blade surface (Some manufacturers of radial inflow turbines call f the wrap angle), B is the number of blades, and n is zero or an integer. Thus the blade surface are at $\theta = f(r, z) \pm \frac{n2\pi}{B}$ or $\alpha = \frac{n2\pi}{B}$ for $n = 0, 1, 2, 3, ...B$.

From the above assumptions, the only vorticity in the flow field is that confined to the blade surfaces. The absolute vorticity bound to the blade can be written as

$$\vec{\Omega} = \overline{\vec{\Omega}}\delta_p(\alpha) \tag{3.6}$$

where $\delta_p(\alpha)$ is the periodic delta function (Ref. 61) given as

$$\delta_p(\alpha) = \frac{2\pi}{B}\sum_{n=-\infty}^{\infty}\delta(\alpha - \frac{n2\pi}{B}) = \sum_{n=-\infty}^{\infty} e^{inB\alpha} \tag{3.7}$$

and the over bar "-" defines a tangential mean, viz.,

$$\overline{A}(r,z) = \frac{B}{2\pi}\int_0^{\frac{2\pi}{B}} A(r,\theta,z)d\theta \tag{3.8}$$

The expression in Eq.(3.6) gives the correct representation of a flow field in which $\vec{\Omega} = 0$ everywhere except at the blade with the correct strength of the vortcity. An analytical expression relating this bound vorticity to the blade surface α and the mean swirl distribution $r\overline{V}_\theta$ will be derived in the next section.

3.2.1 The Clebsch Approach

In the Clebsch formulation (Ref. 60), the velocity may be written as the sum of a potential and a rotational part:

$$\vec{V} = \nabla\Phi + \lambda\nabla\mu \tag{3.9}$$

where $\Phi(r,\theta,z), \lambda(r,\theta,z)$ and $\mu(r,\theta,z)$ are scalar potentials (also called Clebsch variables). The vorticity vector can be obtained by taking the curl of the Eq.(3.9) to yield

$$\vec{\Omega} = \nabla\lambda \times \nabla\mu \tag{3.10}$$

Note that the form of Eq.(3.10) ensures that $\vec{\Omega}$ is divergence free, i.e. $\nabla \bullet \vec{\Omega} = 0$. Clearly, the vortex filaments lie at the intersection of the surfaces of constant λ and μ. This gives us a mean to locate the blade bound vorticity and relate the strength of the

blade bound vorticity to the physical quantities. For other applications of this physical interpretation, readers may refer to the works of Dang & McCune (Ref. 56), Hawthorne et al. (Ref. 62), Tan (Ref. 63) and Hawthorne & Tan (Ref. 90).

In the present problem, the vorticity filaments lie in the blades surfaces. It must be perpendicular to the gradient of blade surface α. Therefore, the blade surface $\alpha(r,\theta,z) = constant$ is the first Clebsch variable, so that a possible expression for the absolute vorticity takes the form of $\vec{\Omega} = (\nabla G(r,z) \times \nabla\alpha)\delta_p(\alpha)$. To identify the second Clebsch variable $G(r,z)$, we begin by first expressing the mean vorticity in terms of its component, as follows:

$$\overline{\vec{\Omega}} = \nabla G(r,z) \times \nabla\alpha = (-\frac{1}{r}\frac{\partial G}{\partial z}, \frac{\partial G}{\partial r}\frac{\partial f}{\partial z} - \frac{\partial G}{\partial z}\frac{\partial f}{\partial r}, \frac{1}{r}\frac{\partial G}{\partial r}) \tag{3.11}$$

We next write a expression for the mean vorticity by taking the curl of the mean velocity i.e.,

$$\overline{\vec{\Omega}} = \nabla \times \overline{\vec{V}} = (-\frac{1}{r}\frac{\partial(r\overline{V}_\theta)}{\partial z}, \frac{\partial \overline{V}_r}{\partial z} - \frac{\partial \overline{V}_z}{\partial r}, \frac{1}{r}\frac{\partial(r\overline{V}_\theta)}{\partial r}) \tag{3.12}$$

By comparing $\overline{\Omega}_r$ and $\overline{\Omega}_z$ given by Eq.(3.11) and (3.12), the Clebsch variable $G(r,z)$ is readily identified with $r\overline{V}_\theta$, so that Eq.(3.6) may be written as

$$\vec{\Omega} = (\nabla r\overline{V}_\theta \times \nabla\alpha)\delta_p(\alpha) \tag{3.13}$$

Upon integrating $\vec{\Omega}$ in Eq.(3.13), we arrive at

$$\vec{V} = \nabla\Phi + r\overline{V}_\theta \nabla\alpha - S(\alpha) \nabla r\overline{V}_\theta \tag{3.14}$$

where $S(\alpha)$ is the periodic sawtooth function (Ref. 61), given as

$$S(\alpha) = \sum_{n=-\infty}^{\infty} \frac{e^{inB\alpha}}{inB} \tag{3.15}$$

From the above velocity decomposition, we observe that the mean swirl schedule $r\overline{V}_\theta$ is one of the independent physical variables that one can prescribe, and that the blade surface $\alpha = constant$ is the sought parameter. This constitutes the inverse design problem.

Alternatively, one can also specify α from which the swirl schedule $r\overline{V}_\theta$ can be determined. This constitutes the direct problem.

It is convient to express the velocity in terms of a sum of a mean part $\overline{V}$ and a periodic part $\tilde{V}$, as

$$\overline{\vec{V}} = \nabla\overline{\Phi} + r\overline{V}_\theta \nabla \alpha \tag{3.16}$$

$$\tilde{\vec{V}} = \nabla\tilde{\Phi} - S(\alpha) \nabla r\overline{V}_\theta \tag{3.17}$$

Since in the upstream and downstream regions the flow field are irrotational, the last term on the right hand side (RHS) of Eq.(3.16) and Eq.(3.17) vanishes in those regions of the flow field. The theoretical formulation has made use of a Fourier series to represent the θ-dependence of the flow variables. As such, the mean flow can be regarded as the zeroth mode of this Fourier series representation.

3.2.2 Mean Flow Equations

The continuity equation, Eq.(3.1), may be also written as

$$\nabla \cdot \vec{W} = -\vec{W} \cdot \nabla \ln \rho \tag{3.18}$$

By taking the pitch average of equation (3.18), we have the mean flow as

$$\nabla \cdot \overline{\vec{W}} = -\overline{\vec{W} \cdot \nabla \ln \rho} \tag{3.19}$$

The non-linear term on the RHS of Eq.(3.19) couples the periodic flow to the mean flow; this is to be expected as the equation of continuity for a compressible fluid is nonlinear.

To solve the mean flow numerically, it is convenient to introduce an artificial density $\rho_a(r,z)$ to account for compressiblity effects (Ghaly, see Ref. 52). The artificial density $\rho_a(r,z)$ is defined as

$$\nabla \cdot \rho_a \overline{\vec{W}} = 0 \tag{3.20}$$

Comparing Eq.(3.19) with Eq.(3.20) we obtain the governing equation for ρ_a as

$$\overline{\vec{W}} \bullet \nabla \ln \rho_a = \overline{\vec{W} \bullet \nabla \ln \rho} \tag{3.21}$$

with an appropriate initial condition. We see that the artificial density has a physical meaning in the limit of $B \rightarrow \infty$ (This is referred to the Bladed Actuator Duct, Tan et al., Ref. 2). In the Bladed Actuator Duct limit, the effect of individual blades on the flow field is smeared out in the tangential direction so that the periodic part of the flow vanishes, hence $\widetilde{\vec{W}} = 0, \overline{\rho} = \rho_a$.

The mean velocity may either be formulated using the Clebsch expression in Eq.(3.16) or in terms of the more familiar Stokes stream function which has often found application in throughflow and actuator disc calculations. Here, for historical reasons, we will adopt the use of Stokes stream function, ψ, for the description of the mean flow. Thus, an alternative expression for the mean velocity which satisfies the definition of artificial density ρ_a in Eq.(3.20) is

$$\begin{aligned} \rho_a \overline{W}_r &= -\frac{1}{r}\frac{\partial \psi}{\partial z} \\ \overline{W}_\theta &= \frac{r\overline{V}_\theta}{r} - r\omega \\ \rho_a \overline{W}_z &= \frac{1}{r}\frac{\partial \psi}{\partial r} \end{aligned} \tag{3.22}$$

The governing equation for ψ is obtained by equating the definition of $\overline{\Omega}_\theta = \frac{\partial \overline{V}_r}{\partial z} - \frac{\partial \overline{V}_z}{\partial r}$ (see Eq.(3.12)) in terms of ψ from the above definition, and therefore we have

$$[\frac{\partial^2}{\partial r^2} - \frac{1}{r}\frac{\partial}{\partial r} + \frac{\partial^2}{\partial z^2} - \frac{\partial(\ln \rho_a)}{\partial r}\frac{\partial}{\partial r} - \frac{\partial(\ln \rho_a)}{\partial z}\frac{\partial}{\partial z}]\psi = r\rho_a[\frac{\partial r\overline{V}_\theta}{\partial z}\frac{\partial f}{\partial r} - \frac{\partial r\overline{V}_\theta}{\partial r}\frac{\partial f}{\partial z}] \tag{3.23}$$

Eq.(3.23) is elliptic when the flow is subsonic and hyperbolic when the flow become supersonic. Note that the right hand side vanishes outside the blade region as the flow is irrotational there.

3.2.3 Periodic Flow Equation

The continuity equation for the periodic part of the flow is obtained by subtracting the pitch-averaged continuity equation in equation (3.19) from the continuity equation in equation (3.18), yielding

$$\nabla \bullet \tilde{\vec{V}} = -\vec{W} \bullet \nabla \ln \rho + \overline{\vec{W} \bullet \nabla \ln \rho} \tag{3.24}$$

As the flow is spatially periodic from blade passage to blade passage, it is convenient to express the periodic velocity potential $\tilde{\Phi}$ in the form of the Fourier Series in the circumferential direction, and we have

$$\tilde{\Phi} = \sum_{n=-\infty,\neq 0}^{+\infty} \widetilde{\phi_n}(r,z) e^{inB\theta} \tag{3.25}$$

Substituting Eq.(3.17) and Eq.(3.25) into Eq.(3.24), we get

$$\nabla^2_{2D} \tilde{\phi}_n = \frac{e^{-inBf}}{inB} \nabla^2 r\overline{V}_\theta - e^{-inBf}\left(\frac{\partial f}{\partial r}\frac{\partial r\overline{V}_\theta}{\partial r} + \frac{\partial f}{\partial z}\frac{\partial r\overline{V}_\theta}{\partial z}\right) + [-\vec{W} \bullet \nabla \ln \rho + \overline{\vec{W} \bullet \nabla \ln \rho}]_{FT(n)} \tag{3.26}$$

where $\nabla^2_{2D} = \frac{1}{r}\frac{\partial}{\partial r}(r\frac{\partial}{\partial r}) + \frac{\partial^2}{\partial z^2} - \frac{n^2B^2}{r^2}$ and $FT(n)$ denotes the Fourier coefficients of the nth mode. Note that the RHS of Eq.(3.26) vanishes when $n = 0$ so that $\tilde{\phi}_0 \equiv 0$, as it should, since $\overline{\tilde{\vec{W}}} \equiv 0$ by definition. Since it is assumed that the specified $r\overline{V}_\theta$ distribution is such that no trailing vorticity appears downstream of the blade row, and that the upstream flow is irrotational, the first two terms on the RHS of Eq.(3.26) vanish identically upstream and downstream of the blade row.

3.2.4 Blade Boundary Condition

The procedure for determining the blade shape is an iterative one. A first guess for the blade shape is used to compute the velocities from ρ_a, ψ and $\widetilde{\phi_n}$. Then, the blade shape is updated by using the blade boundary condition which means that there is no velocity normal to the blade surface. This can be written in the form :

$$\vec{W}_{bl} \bullet \nabla \alpha = 0 \tag{3.27}$$

where $\vec{W}_{bl} = \frac{1}{2}(\vec{W}^+ + \vec{W}^-)$ is the velocity at the blade ($+/-$ represents the blade pressure/suction surface). We may expand the above equation in the following:

$$\overline{W}_r \frac{\partial f}{\partial r} + \overline{W}_z \frac{\partial f}{\partial z} = \frac{r\overline{V}_\theta}{r^2} - \omega + (\tilde{\vec{V}})_{bl} \bullet \nabla\alpha \tag{3.28}$$

Eq.(3.28) may appropriately be integrated to obtain the blade shape $f(r,z)$ with an initial condition. This specification of an integration constant for f is called the "stacking condition" (Tan et al., Ref. 2), as will be discussed later.

3.3 The Boundary Conditions

Poisson's equation requires a specification of either the Dirichlet or the Neumann boundary conditions in order to have an unique solution mathematically. This corresponds to the specification of the inflow/outflow boundary conditions and the requirement of no flow through the solid wall. Here, the boundary conditions for Eq.(3.23) and Eq.(3.26) will be discussed separately.

3.3.1 Stream Function

First we will discuss the boundary conditions for the stream function, Eq.(3.23), which is obtained from the definition of the mean tangential vorticity. We have :

- along the inflow section, ψ is given (based on an uniform flow)
  The upstream flow may be considered to be uniform if the upstream boundary is far enough from the leading edge.

- along the outflow section, $\frac{\partial\psi}{\partial n} = 0$ (parallel flow)
  Because the influence of the blade row decreases exponetially and there is no pressure jump at the trailing edge, the downstream flow may be considered to be parallel at a distance far enough from the trailing edge.

- along the hub and shroud, ψ is constant (no flow normal to the wall)

3.3.2 Velocity Potential

The requirement of the conservation of mass for periodic flow is contained in Eq.(3.26). The corresponding boundary conditions for Eq.(3.26) are:

- along the inflow section, $\frac{\partial \tilde{\phi}_n}{\partial n} = 0$

  The upstream flow may be considered to be parallel if the upstream boundary is far enough from the leading edge.

- along the outflow section, except $\tilde{\phi}_n = 0$ at hub (to have an unique solution), $\frac{\partial \tilde{\phi}_n}{\partial n} = 0$

  Because the influence of the blade row decreases exponetially, the downstream flow may be considered to be parallel at a distance far enough from the trailing edge.

- along the hub and shroud, $\frac{\partial \tilde{\phi}_n}{\partial n} = \frac{\partial r\overline{V}_\theta}{\partial n} \frac{e^{-inBf}}{inB}$ (no flow normal to the wall)

3.4 The Initial Conditions

The mean continuity equation in Eq.(3.21) and the blade boundary condition in Eq.(3.28) are two first order convective equations. Each of these equations requires the specification of an initial condition on a line extending from the hub to the shroud (not coinciding with any streamlines). The specification of the initial condition for these two equations will be discussed next.

3.4.1 Artificial Density

We assume that the flow is steady and that far upstream the approaching flow is axisymmetric, irrotational and reversible. The initial condition for the artificial density Eq.(3.21), can be given from the mean flow far upstream (referred to as the Bladed Actuator Duct), i.e.,

- along the inflow section, $\rho_a = \overline{\rho}$ is specified.

3.4.2 Blade Shape

The initial condition for the blade shape is referred to as the blade stacking condition. This specification of the stacking condition is similar to the design of a three-dimensional blade shape using the strip theory. In the strip theory, two-dimensional blades are designed by blade-to-blade method and we need to specify an axis from the hub to shroud along which all the designed two-dimensional blade sections are to be stacked. Here, the initial condtion for the Eq.(3.28) is

- $f = f_{st}(r_{st}, z_{st})$; f_{st} must be a line from hub to shroud (not coinciding with any of the streamlines)

3.5 The Kutta-Joukowski Condition

The Kutta condition ensures smooth flow at a sharp trailing edge. This translates to the fact that, in subsonic flow, the pressure must be continuous at the trailing edge. Accordingly, the swirl schedule should be such as to satisfy this condition. The homentropic assumption implies that all the thermodynamic properties will be continuous if either p or ρ or T is. Here, the way to impose the Kutta-Joukowski condition is by specifying $H^+ = H^-$ explicitly in our inverse design method (where $+/-$ represents the blade pressure/suction side respectively). As the rothalpy is uniform (see Eq.(3.3)), we have

$$H^+ - H^- = \frac{1}{2}(W^-)^2 - \frac{1}{2}(W^+)^2 = \frac{1}{2}(\vec{W}^- + \vec{W}^+) \times (\vec{W}^- - \vec{W}^+) = -\vec{W}_{bl} \bullet \triangle\vec{W} \qquad (3.29)$$

However, the velocity jump $\triangle\vec{W}$ across the blade (from the definition of the bound vorticity) can be written in the form (Ref. 2, see Appendix A) of

$$\triangle\vec{W} = \frac{2\pi}{B}\frac{\overline{\vec{\Omega}} \times \nabla\alpha}{|\nabla\alpha|^2} = \frac{2\pi}{B}\left(\frac{\nabla\alpha \bullet \nabla r\overline{V}_\theta}{|\nabla\alpha|^2}\nabla\alpha - \nabla r\overline{V}_\theta\right) \qquad (3.30)$$

Substituting the above expression into Eq.(3.29), and using the fact that $\vec{W}_{bl}$ lies on the blade surface, i.e., $\vec{W}_{bl} \bullet \nabla\alpha = 0$, we obtain

$$H^+ - H^- = \frac{2\pi}{B}[\vec{W}_{bl} \bullet \nabla r\overline{V}_\theta] \tag{3.31}$$

so that the Kutta-Joukowski condition can be satisfied by setting the right hand side of the above equation to zero, i.e.,

$$\vec{W}_{bl} \bullet \nabla r\overline{V}_\theta = 0 \tag{3.32}$$

It is worthy to note that as the incidence angle at the blade leading edge is assumed to be zero, the pressure there should be continuous in a way similar to that at the trailing edge. Therefore the condition of zero incidence at the blade leading edge implies that $r\overline{V}_\theta$ should satisfy Eq.(3.32) at the leading edge as well.

For a free vortex design, $r\overline{V}_\theta$ is constant along the leading edge and the trailing edge (no shed vorticity), so that there is no trailing vorticity downstream of the blade row. If we impose $\frac{\partial r\overline{V}_\theta}{\partial s} = 0$ at the leading edge and the trailing edge where s is the meridional distance along the quasi-streamline coordinate, then Eq.(3.32) is identically satisfied.

3.6 Blockage Effects

In general, the thickness along the shroud is very small, so the assumption of zero thickness would be a good approximation. However, in the hub region, due to the stress considerations, the blades are designed with a relatively thick section compared to the shroud region. To partially account for this effect, we introduce the blockage, $b(r,z)$, on the mean flow, and neglect the periodic variation of flow quantities caused by the thickness (see Ref. 64, 65). For the mean flow, we have

$$\nabla \bullet b\rho\overline{\vec{W}} = 0 \tag{3.33}$$

where

$$b = 1 - \frac{t_\theta}{(\frac{2\pi r}{B})} \tag{3.34}$$

and t_θ is the tangential thickness, r is the radius and B is the number of blades.

For stress considerations, the normal thickness t_n is usually specified, which can be related to the tangential thickness due to the blade wrap by (see Ref. 54)

$$t_\theta = t_n\sqrt{1 + r^2(\frac{\partial f}{\partial r})^2 + r^2(\frac{\partial f}{\partial z})^2} \tag{3.35}$$

The artificial density to account for the effect of blockage will be defined as

$$\nabla \bullet \rho_a b\overline{\vec{W}} = 0 \tag{3.36}$$

Comparing Eq.(3.19) with Eq.(3.36) we obtain a governing equation for artificial density ρ_a as (see Appendix B)

$$\overline{\vec{W}} \bullet \nabla \ln \rho_a = \overline{\vec{W}} \bullet \nabla \ln \overline{\rho} + \frac{\nabla \bullet \overline{(b\tilde{\rho}\tilde{\vec{W}})}}{b\overline{\rho}} \tag{3.37}$$

The stream function which satisfies Eq.(3.36) is

$$\begin{aligned} b\rho_a \overline{W}_r &= -\frac{1}{r}\frac{\partial \psi}{\partial z} \\ \overline{W}_\theta &= \frac{r\overline{V}_\theta}{r} - r\omega \\ b\rho_a \overline{W}_z &= \frac{1}{r}\frac{\partial \psi}{\partial r} \end{aligned} \tag{3.38}$$

Once again, the governing equation for ψ is obtained by equating the definition of $\overline{\Omega}_\theta$, this gives

$$[\frac{\partial^2}{\partial r^2} - \frac{1}{r}\frac{\partial}{\partial r} + \frac{\partial^2}{\partial z^2} - \frac{\partial(\ln b\rho_a)}{\partial r}\frac{\partial}{\partial r} - \frac{\partial(\ln b\rho_a)}{\partial z}\frac{\partial}{\partial z}]\psi = r\rho_a b[\frac{\partial(r\overline{V}_\theta)}{\partial z}\frac{\partial f}{\partial r} - \frac{\partial(r\overline{V}_\theta)}{\partial r}\frac{\partial f}{\partial z}] \tag{3.39}$$

Applying the same procedure to the section 3.2.3, the governing equation for the periodic velocity potential $\tilde{\phi}_n$, will be modified accordingly as

$$\nabla^2_{2D}\tilde{\phi}_n = \frac{e^{inBf}}{inB}\nabla^2 r\overline{V}_\theta - e^{-inBf}(\frac{\partial f}{\partial r}\frac{\partial r\overline{V}_\theta}{\partial r} + \frac{\partial f}{\partial z}\frac{\partial r\overline{V}_\theta}{\partial z}) - [\vec{W}\bullet\nabla \ln \rho - \overline{\vec{W}}\bullet\nabla \ln \overline{\rho} - \frac{\nabla \bullet \overline{(b\tilde{\rho}\tilde{\vec{W}})}}{b\overline{\rho}}]_{FT(n)} \tag{3.40}$$

We see that the blockage b has no influence on the periodic flow $\tilde{\phi}_n$ from the last term on the RHS. When there is no blockage, i.e., $b = 1$, Eq.(3.37), Eq.(3.39) and Eq.(3.40) become identical to their original forms in Eq.(3.21), Eq.(3.23) and Eq.(3.26) respectively. The corresponding boundary conditions for Eq.(3.37), Eq.(3.39) and Eq.(3.40) are the same as before.

3.7 Summary

Given the mean swirl schedule, the hub and shroud profile, number of blades and stacking condition, the current method can give us the detailed three-dimensional blade shape and the entire flow field. The governing equations in terms of the stream function ψ (Eq.(3.23), artificial density ρ_a (Eq.(3.21)), velocity potential $\widetilde{\phi_n}$ (Eq.(3.26)) and blade shape f (Eq.(3.28)), need to be solved simultaneously. As they are nonlinear, the solution scheme is an iterative one.

The analysis shows that the mean swirl schedule is the only velocity component that may be specified as an input. Moreover, this schedule is proportional to the circulation around the blades from Kelvin theorem, i.e.,

$$\Gamma = \frac{2\pi}{B}[(r\overline{V}_\theta)_{L.E.} - r\overline{V}_\theta(r,z)] \tag{3.41}$$

It is also related to the work done across the blade row from the Euler's turbine equation.

$$H_{T_2} - H_{T_1} = \omega[(rV_\theta)_2 - (rV_\theta)_1] \tag{3.42}$$

The enthalpy jump across the blade (or pressure jump when the fluid is incompressible) is related to the rate of change of the mean swirl schedule (see Eq.(3.31)). However, there could be many $r\overline{V}_\theta$ distributions within the blade region to give a same overall change in $r\overline{V}_\theta$ across the blade row. It is conjectured that there could be an optimum $r\overline{V}_\theta$ distribution that results in a flow field with minimum loss, be it of viscous origin or due to the resulting secondary flow and boundary layer development.

Chapter 4

The Mean Swirl Schedule

From the previous chapter, we have seen the important role played by the mean swirl schedule in this three-dimensional design method. In this chapter, we will first discuss the kinematic constraints on the mean swirl schedule. Then, we will describe a method to generate the mean swirl schedule within the blade region. The specification of the mean swirl schedule can be shown to reduce to a boundary value problem. Finally, we propose a procedure for controlling the distribution of the mean swirl schedule along the hub and the shroud.

4.1 Kinematic Constraints

The previous analytical studies assume the flow to be irrotational and inviscid; therefore, if we take a closed circuit C and allow it to wrap around a blade, we arrive at

$$\Gamma_c = 0 = \oint_c \vec{u} \bullet d\vec{l} = \oint_{ABCD} \vec{u} \bullet d\vec{l} = \oint_{AB} \vec{u} \bullet d\vec{l} - \oint_{DC} \vec{u} \bullet d\vec{l} + \Gamma_W - \Gamma_1 = \gamma_s \Delta n + \Gamma_W - \Gamma_1$$

where Γ_c, Γ_w and Γ_1 are the circulation at upstream, blade circulation at the wall and blade circulation near the wall (see Fig. 4.1). The γ_s and Δn are the shed vorticity from the blade and the distance from station 1 to the wall. In the limit of $\Delta n \rightarrow 0$, we get

$$\frac{\partial \Gamma_B}{\partial n} = \gamma_s \tag{4.1}$$

where n is the distance normal to the hub and shroud surfaces. This is the so-called "Prandtl Wing Theorem". The strength of the vortex sheet shed by a wing is equal to the spanwise gradient in the circulation along the wing. Now the circulation on the blade can be related to the mean swirl schedule by Kelvin Theorem (see Eq.(3.41)), i.e.

$$\Gamma_B = \frac{2\pi}{B}[(r\overline{V}_\theta)_{L.E.} - (r\overline{V}_\theta)] \tag{4.2}$$

By combining Eq.(4.2) with Eq.(4.1) and noting that $(r\overline{V}_\theta)_{L.E.}$ is a constant, we arrive at

$$\frac{\partial(r\overline{V}_\theta)}{\partial n} = \gamma_s \tag{4.3}$$

We see that there are shed vorticities from the blade due to a non-vanishing normal gradient of the mean swirl at the wall. The vanishing of the normal gradient of the mean swirl schedule along the hub and the shroud is dictated by the need to satisfy the boundary condition of no normal flow along the hub and the shroud. This point has been noted by Smith (Ref. 66), Tan (Ref. 64, 67), Falcao (Ref. 68) and Tan et al. (Ref. 2), thus

$$\frac{\partial(r\overline{V}_\theta)}{\partial n} = 0 \tag{4.4}$$

at the hub and shroud.

This implication results in an additional constraint on the blade shape f at the hub and shroud. As the velocity is tangent to the walls, i.e.

$$\vec{W}^+ \bullet \vec{n} = 0 \ \ and \ \ \vec{W}^- \bullet \vec{n} = 0 \tag{4.5}$$

By taking the difference between these two, we have

$$\triangle \vec{W} \bullet \vec{n} = 0 \tag{4.6}$$

Substituting for $\triangle\vec{W}$ from Eq.(3.30) and simplifying, we obtain

$$\frac{\nabla\alpha \bullet \nabla r\overline{V}_\theta}{|\nabla\alpha|^2}\frac{\partial f}{\partial n} + \frac{\partial r\overline{V}_\theta}{\partial n} = 0 \tag{4.7}$$

We have noted from Eq.(4.4) that $\frac{\partial r\overline{V}_\theta}{\partial n} = 0$ along the hub and the shroud; furthermore the dot product $\nabla\alpha \bullet \nabla r\overline{V}_\theta$ is in general not equal to zero, therefore

$$\frac{\partial f}{\partial n} = 0 \tag{4.8}$$

at the intersection of the blade with the walls, i.e., the dihedral angle needs to be zero, which has been shown by Smith (Ref. 69) and Brebner & Wyatt (Ref. 70).

It is also interesting to note that when $\frac{\partial r\overline{V}_\theta}{\partial n}$ is zero at the endwalls, the boundary condition for the periodic velocity potential (see section 3.3.2) is reduced to

$$\frac{\partial \tilde{\phi}_n}{\partial n} = 0 \tag{4.9}$$

along the hub and shroud.

4.2 Biharmonic Equation

The boundary conditions that need to be imposed on the mean swirl schedule can be summarized as follows:

- at the leading edge : $r\overline{V}_\theta$ is a constant which is given; the condition of zero incidence requires that $\frac{\partial r\overline{V}_\theta}{\partial s} = 0$.
- along the hub and shround : $r\overline{V}_\theta$ is prescribed as a mean to control the loading distribution; the $r\overline{V}_\theta$ distribution must also satisfy the kinematic constraint that $\frac{\partial r\overline{V}_\theta}{\partial n} = 0$.
- at the trailing edge : $r\overline{V}_\theta$ is a constant which is specified; the Kutta-Joukowski condition requires that $\frac{\partial r\overline{V}_\theta}{\partial s} = 0$.

Obviously, along each boundary defining the blade region, two boundary conditions are specified. This means we need at least a fourth order partial differential equation to generate the $r\overline{V}_\theta$ distribution for the specification. Here, the biharmonic equation is adopted to generate the distribution of $r\overline{V}_\theta$, i.e., we solve

$$\nabla^4 (r\overline{V}_\theta) = R(r,z) \tag{4.10}$$

where

$$\nabla^4 = (\frac{\partial^2}{\partial r^2} + \frac{1}{r}\frac{\partial}{\partial r} + \frac{\partial^2}{\partial z^2})^2$$

to obtain a smooth continuous distribution of $r\overline{V}_\theta$ within the blade region. The source term $R(r,z)$ can be used as a mean to control/tailor the $r\overline{V}_\theta$ distribution in a desirable way. Here, $R(r,z)$ is set to zero for simplicity in the present study. The present study concentrates on the effect of prescribing $r\overline{V}_\theta$ distribution along the hub and the shroud only.

4.3 Method of Specifying $r\overline{V}_\theta$ along the Hub and the Shroud

As we alluded to in the previous section, the proposed method for controlling/tailoring the distribution of $r\overline{V}_\theta$ is to prescribe the $r\overline{V}_\theta$ distribution along the hub and shroud. The specification of $r\overline{V}_\theta(r,z)$ is thus reduced from the need of specifying on a two-dimensional domain to one on a one-dimensional domain, i.e., along the boundaries of the blade region.

Since the design and the biharmonic codes require the evaluation of $\nabla^2 r\overline{V}_\theta$ (see Eq.(3.26) & Eq.(4.10)), a continuity of the second derivative of $r\overline{V}_\theta$ along the hub and shroud is suggested. This implies that the flow field and hence the pressure field will be smooth. As we have seen from Eq.(3.31), pressure jump is closely related to the first derivative of $r\overline{V}_\theta$. It suggests that a specification of $(\frac{\partial r\overline{V}_\theta}{\partial s})_{max}$ could be helpful. Moreover, the shape of the loading is mainly controlled by the second derivative of $r\overline{V}_\theta$, so it is useful to choose the magnitude of $\frac{\partial^2 r\overline{V}_\theta}{\partial s^2}$ along the hub and shroud. Because of the requirement of zero incidence at the leading edge and the need to satisfy Kutta-Joukowski condition at the trailing edge, two transition curves are needed at both ends to have $\frac{\partial r\overline{V}_\theta}{\partial s} = 0$. This gives us the current choice. Namely, we separate the meridional distance along the hub and shroud into three sections. This corresponds to Section 1 : from the leading edge to position A, Section 2 : from position A to position B, and Section 3 : from position B to the trailing edge. (see Fig. 4.2). The boundary conditions for each section are listed below:

- Section 1 : $r\overline{V}_\theta(s)$ is quartic in s

specify $r\overline{V}_\theta = (r\overline{V}_\theta)_{L.E.}$, $(r\overline{V}_\theta)' = 0$, $(r\overline{V}_\theta)'' = 0$ *at* *L.E.*

specify $(r\overline{V}_\theta)' = (r\overline{V}_\theta)'_{max}$, $(r\overline{V}_\theta)'' = (r\overline{V}_\theta)''_{A-B}$ *at* *A*

- Section 2 : $r\overline{V}_\theta(s)$ is quadratic in s

  obtain from section 1, $r\overline{V}_\theta = (r\overline{V}_\theta)_A$, $(r\overline{V}_\theta)' = (r\overline{V}_\theta)'_A$, $(r\overline{V}_\theta)'' = (r\overline{V}_\theta)''_A$ *at* *A*

- Section 3 : $r\overline{V}_\theta(s)$ is quintic in s

  obtain from section 2, $r\overline{V}_\theta = (r\overline{V}_\theta)_B$, $(r\overline{V}_\theta)' = (r\overline{V}_\theta)'_B$, $(r\overline{V}_\theta)'' = (r\overline{V}_\theta)''_B$ *at* *B*

  specify $r\overline{V}_\theta = (r\overline{V}_\theta)_{T.E.}$, $(r\overline{V}_\theta)' = 0$, $(r\overline{V}_\theta)'' = 0$ *at* *T.E.*

These specifications are applied both at the hub and the shroud with the additional note that the condition of $(r\overline{V}_\theta)'' = 0$ at the leading edge and the trailing edge is not required by the constraints, but numerical continuity of $\nabla^2 r\overline{V}_\theta$ at the leading edge and the trailing edge is preferred. By altering the location of position A (the maximum loading position) and position B (the extent of the finite loading), the value of the maximum derivative of $r\overline{V}_\theta$ at position A, and the slope of the loading from postion A to position B, a variety of distributions of $r\overline{V}_\theta$ can be obtained.

4.4 Summary

The kinematic constraints on the mean swirl schedule require $\frac{\partial r\overline{V}_\theta}{\partial n} = 0$ along the hub and the shroud. This results in an additional constraint on f along the hub and shroud. Failure to satisfy Eq.(4.4) and Eq.(4.8) will not produce infinitely large induced velocities due to γ_s along the hub and shroud numerically. However, Eq.(4.5) will not be satisfied in general, i.e., the velocity jump across the blade will not be tangent to the wall.

The biharmonic equation gives us a possible way to interpolate the distribution of $r\overline{V}_\theta$. If one uses only Poisson's equation to generate the $r\overline{V}_\theta$ distribution, then the Dirichlet and Neumann boundary conditions cannot be satisfied simultaneously. One may use some

linear interpolation, but the results show that the derivative of the $r\overline{V}_\theta$ distribution will not be smooth along the hub and shroud. The choice of the biharmonic equation seems to be a useful one.

The right hand side of the biharmonic equation is set to be zero in the current study. Thus, the specification of $r\overline{V}_\theta(r,z)$ reduces to boundary conditions only. The requirement of the continuity of the second derivative of $r\overline{V}_\theta$ suggests that at least a quadratic function is needed to prescribe the $r\overline{V}_\theta$ for the loading. The control of $r\overline{V}_\theta$ distribution along the hub and shroud has been separated into three sections in the current study. Away from the leading edge and trailing edge, the derivative of $r\overline{V}_\theta$ was assumed to vary linearly with meridional distance. The first and the third sections are added in order to satisfy the zero incidence at the leading edge and Kutta-Joukowski condition at the trailing edge.

The characteristic of a $r\overline{V}_\theta$ distribution in the present study will depend on the choice of the distances from the leading edge to position A and to position B, the magnitude of $(\frac{\partial r\overline{V}_\theta}{\partial s})_{max}$, and the magnitude of $(\frac{\partial^2 r\overline{V}_\theta}{\partial s^2})_{A-B}$ along the hub and the shroud. In chapter 6, we will discuss the suitable values of these parameters for a design of radial inflow turbine rotors proposed for a helicopter power plant application.

Chapter 5

The Numerical Technique

In this chapter, the numerical technique based on the finite element method to solve the relevant equations will be presented. First the domain is discretized into a finite number of points by grid generation. A desired loading can then be chosen by prescribing $r\overline{V}_\theta$ along the hub and the shroud (see section 4.3). After that, Eq.(4.10) is solved to obtain a smooth $r\overline{V}_\theta$ distribution. Finally, the blade shape Eq.(3.28) is obtained by solving Eq.(3.21), Eq.(3.23) and Eq.(3.26) all together.

5.1 Grid Generation

As Fourier series is used for the spatial dependence in the tangential direction, the grid required by the current inverse design reduces to a two-dimensional mesh in the meridional plane. If the hub and shroud profile is given, generating a mesh on this plane can be achieved by either an Algebraic method or an Elliptic method (Ref. 71).

5.1.1 Algebraic Method

This is also known as Trans-finite interpolation which is the simplest and cheapest way to generate a mesh. It also permits easy control of the grid by users. The disadvantage is that if there is a discontinuity on the boundary, this information will propagate into the mesh. The basic approach is to cast the expression for (r, z) coordinates in terms of the mapping coordinates (ξ, η) as

$$\begin{aligned} r(\xi,\eta) &= \tfrac{1}{2}[r_{(IMAX,J)}\xi + r_{(1,J)}(1-\xi)] + \tfrac{1}{2}[r_{(I,JMAX)}\eta + r_{(I,1)}(1-\eta)] \\ z(\xi,\eta) &= \tfrac{1}{2}[z_{(IMAX,J)}\xi + z_{(1,J)}(1-\xi)] + \tfrac{1}{2}[z_{(I,JMAX)}\eta + z_{(I,1)}(1-\eta)] \end{aligned} \tag{5.1}$$

where the algebraic mapping is given by

$$\begin{aligned} \xi &= \frac{I-1}{IMAX-1} \\ \eta &= \frac{J-1}{JMAX-1} \end{aligned} \tag{5.2}$$

We see that the trans-finite interpolation uses a direct form, and no numerical iteration is needed. Other forms of transfomation are possible; however, a certain amount of ingenuity is required.

5.1.2 Elliptic Method

One of the most highly developed techniques for generating grids is the elliptic method. It is based on the fact that the stream function ψ and potential function ϕ for incompressible flow form an orthogonal body fitted computational mesh. Instead of solving ψ and ϕ, we solve two elliptic equations for mapping coordinates ξ and η. The advantage of this method is that it produces a smooth grid and can be controlled by a variety of modifications. However, the resulting equations are usually solved iteratively. Here, the two elliptic equations are

$$\begin{aligned} \xi_{rr} + \eta_{zz} &= P(\xi, \eta) \\ \eta_{rr} + \xi_{zz} &= Q(\xi, \eta) \end{aligned} \tag{5.3}$$

where P and Q are terms which control the point spacing on the interior of the domain. Equations (5.3) are then transformed into physical coordinates by interchanging the roles of the independent and dependent variables. This yields a system of two elliptic equations of the form

$$\begin{aligned} \alpha r_{\xi\xi} - 2\beta r_{\xi\eta} + \gamma r_{\eta\eta} &= -\mid \underline{J} \mid^2 (P r_\xi + Q r_\eta) \\ \alpha z_{\xi\xi} - 2\beta z_{\xi\eta} + \gamma z_{\eta\eta} &= -\mid \underline{J} \mid^2 (P z_\xi + Q z_\eta) \end{aligned} \tag{5.4}$$

where

$$\begin{aligned} \alpha &= r_\eta^2 + z_\eta^2 \\ \beta &= r_\xi r_\eta + z_\xi z_\eta \\ \gamma &= r_\xi^2 + z_\xi^2 \end{aligned}$$

$$| \underline{J} | = \frac{\partial(r,z)}{\partial(\xi,\eta)} = r_\xi z_\eta - r_\eta z_\xi$$

This system of equations is solved on an uniform-spaced grid in the computational plane (ξ, η). This provides the (r, z) coordinates of each point in the physical space.

5.2 The Elliptic Solver

Eq.(3.23) for the Stokes' stream function and Eq.(3.26) for the velocity potential are two second order Elliptic equations (for subsonic flow). The Finite Element Method is used to solve for these two equations. The nonlinear part of the differential operator in Eq.(3.23) and Eq.(3.26) is moved to the right hand side (RHS). As the solution procedure is iterative, the RHS is assumed to be given from the previous iteration or from an initial guess, so that the equations may be treated as linear equations.

Here, we use a 4-node isoparametric element to interpolate the variables (see Fig. 5.1). The coordinates r and z are expressed in terms of the coordinates of the four corner nodes by

$$\left\{ \begin{array}{c} r \\ z \end{array} \right\} = \sum_{i=1}^{4} (1 + \xi_i \xi)(1 + \eta_i \eta) \left\{ \begin{array}{c} r_i \\ z_i \end{array} \right\} = \underline{N}^T \left\{ \begin{array}{c} r_i \\ z_i \end{array} \right\} \tag{5.5}$$

where $\underline{N}^T$ is the transpose of the shape function vector. The Jacobian can be in terms of the coordinates of r_i and z_i by

$$[\underline{J}] = \left[\begin{array}{cc} \frac{\partial r}{\partial \xi} & \frac{\partial z}{\partial \xi} \\ \frac{\partial r}{\partial \eta} & \frac{\partial z}{\partial \eta} \end{array} \right] \tag{5.6}$$

Then the derivative of variables in the physical plane can be expressed in terms of those in the computational plane, by using

$$\left\{ \begin{array}{c} \frac{\partial}{\partial r} \\ \frac{\partial}{\partial z} \end{array} \right\} = [\underline{J}]^{-1} \left\{ \begin{array}{c} \frac{\partial}{\partial \xi} \\ \frac{\partial}{\partial \eta} \end{array} \right\} = \left[\begin{array}{cc} I_{11} & I_{12} \\ I_{21} & I_{22} \end{array} \right] \left\{ \begin{array}{c} \frac{\partial}{\partial \xi} \\ \frac{\partial}{\partial \eta} \end{array} \right\} \tag{5.7}$$

If we use the Galerkin method, the variational form of equation (3.23) becomes

$$\begin{aligned} I = & \frac{1}{2}\int\int \underline{\psi}^T[\frac{1}{r}(\frac{\partial \underline{N}^T}{\partial r})(\frac{\partial \underline{N}}{\partial r}) + \frac{1}{r}(\frac{\partial \underline{N}^T}{\partial z})(\frac{\partial \underline{N}}{\partial z})]\underline{\psi} dA + \int\int \underline{\psi}^T \underline{N}^T \underline{N}\underline{q} dA \\ = & \frac{1}{2}\underline{\psi}^T[k]\underline{\psi} + \underline{\psi}^T \underline{q} \end{aligned} \tag{5.8}$$

Where $\underline{q}$ is the nodal value of $[\frac{1}{r}\frac{\partial ln\rho_a}{\partial r}\frac{\partial \psi}{\partial r} + \frac{1}{r}\frac{\partial ln\rho_a}{\partial z}\frac{\partial \psi}{\partial z} + \rho_a\frac{\partial r\overline{V}_\theta}{\partial z}\frac{\partial f}{\partial r} - \rho_a\frac{\partial r\overline{V}_\theta}{\partial r}\frac{\partial f}{\partial z}]$. The evaluation of $[k]$ and $\underline{q}$ is done by Gaussian Quadrature. For stationary value of I, i.e., $\frac{\delta I}{\delta \underline{\psi}} = 0$, we obtain the Euler equation

$$[k]\underline{\psi} = -\underline{q} \tag{5.9}$$

with the corresponding boundary conditions. This is done locally from element to element. To assemble the contribution from each element, we apply the direct stiffness technique to obtain the global matrix over the whole domain as

$$[K]\underline{\psi} = -\underline{Q} \tag{5.10}$$

The same procedure applies to the periodic velocity potential in Eq.(3.26). The system of equations (5.10) can be solved directly by LU decomposition or iteratively, such as via the conjugate gradient method. Here we use the latter procedure. Because these equations are nonlinear and coupled, there is no need for an exact solution of ψ or $\widetilde{\phi_n}$ before the blade camber, f (Eq.(3.28)) or artificial density, ρ_a (Eq.(3.21)) have converged during the intermediate iterations.

The multigrid scheme (Ref. 72, 73, 74) is useful for saving computational time for Eq.(3.23) and Eq.(3.26). In Appendix C, we will demonstrate the performance of the multigrid coupled with the conjugate gradient method. For a test problem with a fixed RHS, the multigrid scheme can save about half of the computational time. However, when this scheme is coupled with our inverse design code, the benefit is not so obvious. This is because for each global iteration, after the new blade camber is obtained, it typically requires ten sweeps of the conjugate gradient method to update ψ and $\widetilde{\phi_n}$ on the finest level. Improved accuracy in ψ or $\widetilde{\phi_n}$ does not improve the overall convergence rate. Therefore,

the design code combined with the multigrid scheme is not as efficient as one would have expected.

5.3 The Convective Equation Solver

Eq.(3.21) for the artificial density and Eq.(3.28) for the blade camber are two first order hyperbolic equations. One way to solve these equations is by the method of characteristics. Here, one tries to locate the streamlines from the blade velocity and integrate the information along each streamline. An alternative way to do this is to use a direct numerical differentiation and integration, based on the Finite Element Method that evaluates its derivative. The RHS of Eq.(3.21) and Eq.(3.28) may be considered given from an initial guess or the previous iteration. The operator $\overline{W}_r\frac{\partial}{\partial r}+\overline{W}_z\frac{\partial}{\partial z}$ can be separated into two parts; one part that consists of the unknown nodal points will be kept on the LHS and the other part that consists of the given initial nodal points will be moved to the RHS together with the original RHS values. For example, Eq.(3.28) can be written as

$$\overline{W}_r\frac{\partial f}{\partial r}+\overline{W}_z\frac{\partial f}{\partial z}=q \tag{5.11}$$

where q equals $[\frac{r\overline{V}_\theta}{r^2}-\omega+\tilde{\vec{V}}_{bl}\bullet\nabla\alpha]$.

Now consider one element where f_1 and f_4 are given (see Fig. 5.1). The unknowns f_2 and f_3 will be determined by satisfying Eq.(5.11) at nodes 1 and 4 (alternatively, two Gaussian points could give a better weighted accuracy), so from Eq.(5.7) we have

$$\begin{Bmatrix} \left[\overline{W}_{r_4}(I_{11}N_{i,\xi}f_i+I_{12}N_{i,\eta}f_i)+\overline{W}_{z_4}(I_{21}N_{i,\xi}f_i+I_{22}N_{i,\eta}f_i)\right]_{\xi=1,\eta=1} \\ \left[\overline{W}_{r_1}(I_{11}N_{i,\xi}f_i+I_{12}N_{i,\eta}f_i)+\overline{W}_{z_1}(I_{21}N_{i,\xi}f_i+I_{22}N_{i,\eta}f_i)\right]_{\xi=1,\eta=-1} \end{Bmatrix} = \begin{Bmatrix} q_4 \\ q_1 \end{Bmatrix} \tag{5.12}$$

where $N_{i,\xi}$ means $\frac{\partial N_i}{\partial\xi}$ and the free index i represents the sum from 1 to 4. Now the known values f_1 and f_4 can be moved to the RHS, and Eq.(5.12) can be rewritten as

$$[\underline{k}]\begin{Bmatrix} f_2 \\ f_3 \end{Bmatrix}=\underline{q} \tag{5.13}$$

Eq.(5.13) can be used to determine the unknowns f_2 and f_3 on each element. Between the two adjacent elements, the average value will be used for f. After all the unknowns f have been evaluated along the span, this procedure will march to the next streamwise location using the previous solutions as the new initial conditions. This procedure allows one to integrate forward or backward depending on the position of the stacking line. Likewise, the solution for ρ_a from Eq.(3.21) can be implemented through the same procedure.

As we mentioned in section 4.1, there is an additional constraint on the blade shape f at the hub and shroud, i.e., $\frac{\partial f}{\partial n} = 0$. Because the value of $\frac{\partial f}{\partial n}$ is influenced by every f along the boundary, the boundary condition $\frac{\partial f}{\partial n} = 0$ is imposed explicitly, i.e., the value of f along the hub and shroud is altered after the blade camber is determined. The same technique used in the above is adopted. Here, $\overline{W}_r$ and $\overline{W}_z$ are replaced by $-\cos\nu$ and $\sin\nu$, where ν is the angle normal to the boundary side 1-4, and q is set to be zero. Given the values of f_1 and f_4, f_2 and f_3 are obtained by satisfying $\frac{\partial f}{\partial n} = 0$.

5.4 The Biharmonic Solver

To obtain the mean swirl schedule, the biharmonic equation, Eq.(4.10), is used to interpolate the distribution. The biharmonic equation can be solved by the Finite Element Method as in structural mechanics. A simple triangular element developed by Bazeley et al. (Ref. 75) is used. The element (BCIZ) makes use of the area coordinate for the shape function with $r\overline{V}_\theta$, $(r\overline{V}_\theta)_{,r}$ and $(r\overline{V}_\theta)_{,z}$ as the nodal variables. The element is compatible in $r\overline{V}_\theta$, but the adjacent normal gradient $(r\overline{V}_\theta)_{,n}$ is not. Following the same procedure as in Sec.5.2, the resulting system equations for each element are:

$$[k]\underline{r\overline{V}_\theta} = +\underline{q} \tag{5.14}$$

where

$$[k] = \int\int [r(\frac{\partial \underline{N}^T}{\partial r^2} + \frac{\partial \underline{N}^T}{\partial z^2})(\frac{\partial \underline{N}}{\partial r^2} + \frac{\partial \underline{N}}{\partial z^2}) + \frac{1}{r}(\frac{\partial \underline{N}^T}{\partial r})(\frac{\partial \underline{N}}{\partial r})]dA$$

and

$$\underline{q} = \int\int r\underline{N}^T R(r,z)dA$$

Now if we assemble the local nodal variables, we get the global system matrix. To solve this system matrix requires double precision accuracy since $r\overline{V}_\theta$ and its gradients are used at the same time; thus the amount of memory size will be six times the total number of nodes. Furthermore, we have found this method to be rather inefficient in terms of practical implementation.

An alternate approach, which we eventually adopt, is based on the idea of reducing the biharmonic equation into two coupled Poisson equations (Ref. 76, 77, 78, 79). Since each of the Poisson equations is well-posed, the system equations may be solved through an iterative means as described in the following.

$$\begin{aligned}
&\nabla r\overline{V}_\theta^{(k)} = \omega^{(k-1)} \quad in\ G \\
&r\overline{V}_\theta^{(k)} = r\overline{V}_{specified} \quad on\ \partial G \\
&r\overline{V}_\theta^{(k)} = (1-\epsilon)r\overline{V}_\theta^{(k-1)} + \epsilon r\overline{V}_\theta^{(k)} \\
&\nabla\omega^{(k)} = R \quad in\ G \\
&\omega^{(k)} = \nabla r\overline{V}_\theta^{(k)} - c[\tfrac{\partial r\overline{V}_\theta^{(k)}}{\partial n} - g] \quad on\ \partial G \\
&\omega^{(k)} = (1-\delta)\omega^{(k-1)} + \delta\omega^{(k)}
\end{aligned} \tag{5.15}$$

where G is the domain of the blade region, ∂G is the boundary of the blade region, c is an arbitrary nonzero constant, ϵ and δ are two relaxation constants and g is set to be zero for vanishing normal gradient of $r\overline{V}_\theta$. These two Poisson equations can be solved by the same approach as that described in Sec.5.2. Solution procedure only requires single precision accuracy; thus the memory size will be two times the total number of nodes. Thus, this is a more suitable method than the previous one. Since under-relaxation is used, small numbers of conjugate gradient iterations (usually 10 - 15) are needed on each local iteration. The CPU time will be dependent on c, ϵ and δ. Typically, the solution requires $k = 250$ global iterations to achieve machine accuracy with $c = 1$, $\epsilon = \delta = 0.15$.

5.5 The Computational Scheme

Computer programs have been written to implement the numerical procedures described in this chapter. The whole procedure is summarized in the following:

Step 1. Grid Generation

Given the hub and shroud profiles, grid generation is used to generate an appropriate two-dimensional mesh. The required resolution of mesh depends on the number of the periodic harmonic modes used to represent the spatial dependence in the tangential direction. In order to resolve the information of the highest frequency, a minimum number of mesh points is needed (see Appendix D). From the Appendix D, the minimum number of mesh points required is also related to the change in the blade shape. Thus, a prior idea about the distribution of $\frac{\overline{W}_\theta}{r}$ (see Eq.(3.28)) helps in determining the clustering of mesh. For the far upstream and downstream boundaries, the flow can be approximated to be parallel at a distance far enough from the leading and the trailing edge. At present, the numerical upstream and downstream boundaries are set at a distance of quarter chord (averaged meridional distance between the hub and the shroud) from the leading and the trailing edge.

Step 2. Mean Swirl Schedule

The distances from the leading edge to position A and to position B, the magnitude of $(\frac{\partial r\overline{V}_\theta}{\partial s})_{max}$ and $(\frac{\partial^2 r\overline{V}_\theta}{\partial s^2})_{A-B}$, are the parameters used to control $r\overline{V}_\theta$ distribution along the hub and the shroud. The distance from the leading edge to position A will affect the blade shape significantly. The distance from the leading edge to position B sets the region of finite loading (see chapter 4). The magnitude of $(\frac{\partial r\overline{V}_\theta}{\partial s})_{max}$ is closely related to the pressure jump across the blades. The magnitude of $(\frac{\partial^2 r\overline{V}_\theta}{\partial s^2})_{A-B}$ controls the shape of the loading. More details on these parameters will be discussed further in the next chapter.

After the values of $r\overline{V}_\theta$ and its normal gradient (to be zero) along the hub and the shroud are specified, the biharmonic solver is used to interpolate the $r\overline{V}_\theta$ distribution within the blade region.

Step 3. Inverse Design

In the inverse design program, the flow variables are nondimensionalized by the radius of blade tip, meridional velocity and rotary stagnation quantities at the leading edge (see Appendix E). Here, the values used for the input are:

- Velocity triangle and Mach number at the leading edge
- Ratio of specific heats, γ
- Stacking condition
- Mean swirl schedule, $r\overline{V}_\theta(r,z)$
- Normal thickness distribution of blade, $t_n(r,z)$

The design scheme starts with an initial guess of the blade camber, then it solves for the stream function ψ Eq.(3.23) and ϕ_n for each n from Eq.(3.26). Then, the velocity field is calculated to update the blade camber f Eq.(3.28), artificial density ρ_a Eq.(3.21) and density field. If the difference in the blade camber between the current iteration and the previous one is large, then the stream fuction and potential harmonic modes will be calculated again. The whole scheme is considered to achieve convergence when the maximum change in blade camber is less than a small number (10^{-5} radian typically). The outputs from the design program are:

- Blade shape f
- Velocity field (except $\overline{V}_\theta$ which has been specified), pressure field and etc.

Since there is a jump across the blade in the density, its gradient will behave like a periodic delta function. The method to evaluate the gradients of the density (or $\ln \rho$) is to take a Fourier Transformation (FT) and then evaluate the gradients in the Fourier space. The inverse Fourier Transformation (IFT) is used to obtain the physical values from Fourier coefficients. A fast Fourier Transform (Ref. 80) has been used to evaluate the FT and IFT of $\vec{W}$ and $\ln \rho$. Lanczos smoothing (Ref. 81) has also been used to suppress the Gibbs phenomenon due to the sawtooth behavior.

Chapter 6

Parametric Study of Inverse Designs

In this chapter, the computational tool that has been developed based on the analytical theory in chapter 3 is applied to the design study of a radial inflow turbine proposed for a helicopter power plant application. For turbines, the pressure field would tend to have a favorable distribution throughout so that the real flow could be predicted based on an inviscid assumption. By examining the simplest case, the radial inflow turbine, some guidelines can be obtained for an optimal $r\overline{V}_\theta$ distribution in terms of "parameters" related to fluid mechanics.

Not much is known today about the optimization of the efficiency of radial turbines. Probably the most useful correlations and studies are those carried out by NASA and summarized in Reference 82, Chapter 10, by Rohlik, which gives a good guide to the state of the art of high-performance radial inflow turbines. However, the design of blade shapes in this three-dimensional flow field is still in an elementary stage. It has been shown by Borges (Ref. 51) and Zangeneh (Ref. 54) that the use of the present inverse design method for designing a radial turbine rotor can lead to an improvement in its overall efficiency by not only reducing the losses in the rotor, but also minimizing the exit kinetic energy by prescribing the mean swirl value to be zero at the trailing edge.

We will choose a turbine rotor (Ref. 83) proposed for application in a helicopter power plant for our case study. The design conditions are summarized in Table I. The velocity triangle at the leading edge of the rotor is shown in Fig. 6.1; the absolute flow angle at the leading edge is about 75° and the corresponding absolute Mach number was computed to be about 0.98. The impeller wheel will be designed to yield a blade camber distribution that will result in the complete removal of swirl at the trailing edge. Thus, the flow will leave the turbine wheel axially at the exit. The hub profile, the shroud profile and the

associated finite element mesh on the meridional plane are shown in Fig. 6.2. There are 97 uniformly-spaced grid points in the streamwise direction, and 33 grid points in the spanwise direction. The number of blades was taken to be 14. To save computational time, 4 complex harmonic modes are used for the periodic flow which corresponds to 9 Fourier collocation points between adjacent blade camber lines. When the solution of the current grid resolution is compared with a solution of grid resolution of $145 \times 49 \times 33$ (see chapter 7), the maximum difference in blade shape at the mid-span is no more than 0.01 radians (see Fig. 6.3.a). The maximum difference in reduced static pressure along the mid-span (which is at the maximum loading position on the suction surface) is no more than 7% of its maximum pressure jump (see Fig. 6.3b). Based on this results, a grid resolution of $97 \times 33 \times 9$ yields results of adequate accuracy that can be used for a design study.

The parameters that a designer can choose in this design method are the mean swirl schedule, stacking position, lean in stacking line, slip factor, number of blades and hub & shroud profile. We will present the influence of each parameter on the resulting design. Before we begin our study, we wish to propose two parameters that we can use to assess the goodness of a particular design. These two parameters will provide a quantitative measurement of the resulting design.

6.0 Two Parameters Used to Characterize a Design

The goodness of a design depends on the response of the boundary layer and secondary flow to the inviscid reduced static pressure field. In other words, a design based on the assumption of inviscid flow is "good" only if the viscous influence can be kept to be "minimal" e.g. a design with minimal aerodynamic loss. Therefore, the designer would like to pick a pressure field (if possible) that would minimize undesirable viscous effects such as flow separation from the walls with accompanying increased losses and blockage. When the wall boundary layers are thin and well behaved, the inviscid flow field would

be a fairly good approximation to that of the actual flow. Hence, a good control of the inviscid pressure gradients would help in developing an "optimal" design. Here, in a first attempt, two parameters are proposed to characterize a design.

The behavior of a viscous flow through the impeller (i.e. the development of secondary flow and boundary layer) is dictated by the reduced static pressure field. Therefore, the reduced static pressure gradient is the first quantity that we want to examine. Clearly, the larger the maximum adverse reduced static pressure gradient, the tendency of boundary layer to separate is higher; so $(\frac{\partial p_{rsd.}}{\partial s})_{max}$ is the first parameter that we would like to minimize in an inviscid design.

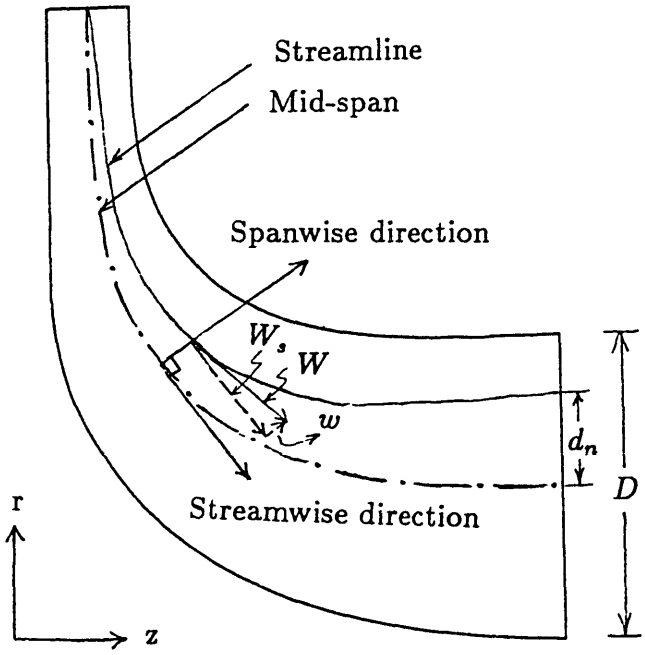
In general, the adverse reduced static pressure gradient on the suction surface is higher than the one on the pressure surface. As we will see later on that the reduced static pressure distribution on the pressure surface does not vary significantly in all cases; this is due to the fact that the velocities remain relatively close to zero on the pressure surface. Because the variation in the reduced static pressure from the pressure side to the suction side is close to a sawtooth function (see chapter 3), it may be sufficient to examine the maximum value of the adverse reduced static pressure gradient on the suction surface within the blade passage. In particular, only the maximum values of the adverse reduced static pressure gradients on the suction surface along the hub $(\frac{\partial p_{rsd.}}{\partial s})_h$, the mid-span $(\frac{\partial p_{rsd.}}{\partial s})_m$ and the shroud $(\frac{\partial p_{rsd.}}{\partial s})_s$ are pointed out to characterize a particular design.

The second parameter to be developed pertains to the development of secondary flow. The low momentum fluid within the blade passage will be driven by the secondary flow to the location of minimum reduced static pressure. Thus, the secondary flow would determine the position of the wake at outlet and can then have an influence on separation. It was suggested by W.R. Hawthorne that one can describe the movement of a fluid particle in the spanwise direction in terms of the Wake number (see Appendix F). However, an alternative derivation for the Wake number is given here. The distance (d_n) that a fluid particle travels in the spanwise direction from the leading edge to the trailing edge along

the middle of the passage is used as a measure of the spanwise motion, i.e.,

$$Wake\ No. = \frac{d_n}{D} \tag{6.1}$$

where D is a reference distance in the spanwise direction. For example, to prescribe the spanwise motion of a fluid particle on the suction surface, we may choose D as the blade height at the trailing edge. Thus, the Wake number on the suction surface gives the location of a fluid particle that deviates from the mid-span at the trailing edge (see the illustration below).



An illustration of the Wake number

Here, the mid-span location is constructed as followed: select a set of points along the hub and the shroud at equal fractional distance from the blade leading edge; then the mid-span location is at the mid-point along lines connecting these selected points along the hub to the corresponding points along the shroud. d_n may be calculated from $\int_0^{t_{T.E.}} w dt$,

where w is the velocity in the spanwise direction and $t_{T.E.}$ is the time that a fluid particle travels through the blade passage. The Wake number can thus be written as

$$Wake\ No. = \frac{1}{D}\int_0^{t_{T.E.}} w dt$$

or

$$Wake\ No. = \frac{1}{D}\int_{L.E.}^{T.E.} \frac{w}{W_s} ds$$

where W_s is the relative velocity along the mid-span on the suction surface and ds is the distance along the mid-span on the suction surface. If $W \gg w$ and $W \approx W_s$, then

$$Wake\ No. \approx \frac{1}{D}\int_{L.E.}^{T.E.} \frac{w}{W} ds \tag{6.2}$$

where W is the relative velocity along the streamline on the suction surface. For low speed flow, the rotary total pressure is constant everywhere in the flow field (see Eq.(3.3)), i.e.,

$$\frac{p}{\rho} + \frac{1}{2}W^2 - \frac{1}{2}\omega^2 r^2 = \frac{p_{rel}}{\rho} + \frac{1}{2}W^2 = constant \tag{6.3}$$

Upon differentiating Eq.(6.3) in the spanwise direction (or quasi-orthogonal), we have

$$\frac{\partial p_{rel}}{\partial n} + \rho W \frac{\partial W}{\partial n} = 0$$

or

$$\frac{\partial w}{\partial n} = -\frac{1}{\rho W}\frac{\partial p_{rel}}{\partial n} - \frac{\partial W_s}{\partial n} \tag{6.4}$$

In general, the first term in the RHS of Eq.(6.4) is positive and the second term is negative (i.e. the streamwise velocity on the hub is lower, $-\frac{\partial W_s}{\partial n}$ is negative). To obtain an upper bound of the spanwise motion of a fluid particle, we may neglect the second term in the RHS of Eq.(6.4), thus

$$w = \int \frac{\partial w}{\partial n} dn + constant \approx \int -\frac{1}{\rho W}\frac{\partial p_{rel}}{\partial n} dn + constant \tag{6.5}$$

To determine the integration constant in Eq.(6.5), we may apply the boundary condition at the hub or the shroud where w equals to zero. Thus, the spanwise velocity at mid-span

can be obtained by either setting

$$w \approx \int_{Hub}^{mid-span} -\frac{1}{\rho W}\frac{\partial p_{red}}{\partial n} dn$$

or

$$w \approx \int_{mid-span}^{Shroud} -\frac{1}{\rho W}\frac{\partial p_{red}}{\partial n} dn$$

Here, an average value of the above two expressions is used, i.e.,

$$w \approx \frac{1}{2}\int_{Hub}^{Shroud} -\frac{1}{\rho W}\frac{\partial p_{red}}{\partial n} dn = \frac{1}{2}\overline{\left(-\frac{1}{\rho W}\frac{\partial p_{red}}{\partial n}\right)}^{A} \times D_n \tag{6.6}$$

where $\overline{\left(-\frac{1}{\rho W}\frac{\partial p_{red}}{\partial n}\right)}^{A}$ is the spanwise average of $-\frac{1}{\rho W}\frac{\partial p_{red}}{\partial n}$ and D_n is a spanwise characteristic distance. The value $\overline{\left(-\frac{1}{\rho W}\frac{\partial p_{red}}{\partial n}\right)}^{A}$ can be approximated further by $-\frac{1}{\rho W}\overline{\left(\frac{\partial p_{red}}{\partial n}\right)}^{A}$ where ρW is taken to be the value at mid-span. Since $\frac{D_n}{D}$ is of the order of unity, the Wake number can finally be written as

$$Wake\ No. = \int_{L.E.}^{T.E.} \frac{\overline{-\left(\frac{\partial p_{red}}{\partial n}\right)}^{A}}{\frac{1}{2}\rho W^2} ds \tag{6.7}$$

We have now derived an approximate expression for the Wake number; it is an integral from the leading edge to the trailing edge of the spanwise gradient of pressure coefficient along the mid-span. For compressible flow, in particular when the Mach number is not close to unity, the variation in density is less than that in pressure (from isentropic relationship), and a mass average of the value of $\frac{\partial p_{red}}{\partial n}$ along the span is used in the calculation of the Wake number, so that the above expression of the Wake number can still be used to predict the appropriate trend of the spanwise motion of a fluid particle. The expression of the Wake number derived in Appendix F is different from the one derived here. However, both Wake numbers do give the same trend in the results to be presented here.

To illustrate the usefulness of the Wake number, an example of two different Wake numbers on the suction surface is shown in Fig. 6.4a and 6.4b, where the Wake numbers are 1.86 and 3.61 respectively. Here, Fig. 6.4a and 6.4b show the meridional velocity

on the suction surface with maximum loading near the leading edge (see section 6.1.1). Hence, there is not much difference between these two cases close to the trailing edge. We see that with a Wake number of 1.86, the velocity near the inlet is higher along the hub than along the shroud; the spanwise movement of a fluid particle is from the shroud toward the hub. For the case of a Wake number of 3.61, the fluid particle will be driven from the hub toward the shroud. Thus, in a real flow, we can expect that the location of the wake at the outlet will be lower for the Wake number 1.86 than the one with a Wake number 3.61. Similarly, the definition of the Wake number can be applied on the hub and the shroud surfaces to indicate the movement of low momentum fluid from the pressure side toward the suction side. In general, the spanwise gradient of reduced static pressure is significant on the suction , the hub and the shroud surfaces. Thus, we will examine the Wake numbers on these three surfaces only and try to minimize these Wake numbers in an inviscid design.

6.1 Mean Swirl Schedule

The mean swirl schedule is the only flow quantity that a designer can control in this theory. As the derivative of $r\overline{V}_\theta$ is related to the pressure jump across the blade (see Eq.(3.31)), and $\frac{r\overline{V}_\theta}{r^2} - \omega$ is related to the blade wrap (see Eq.(3.28)), we see the important role played by the distribution of $r\overline{V}_\theta$ in this inverse design method. Establishing the general effect of the mean swirl schedule on pressure distribution will be the first step of the present work.

There could be many choices of the $r\overline{V}_\theta$ distributions that will accomplish the same amount of work across the blade row. As we have discussed in Chapter 4, one way to generate the distribution of $r\overline{V}_\theta$ is by specifying the $r\overline{V}_\theta$ along the hub and the shroud and then interpolates by the biharmonic equation with its RHS equals zero. The way to control the distribution of $r\overline{V}_\theta$ along the hub and the shroud is by specifying the location

of the maximum loading (position A), region of finite loading (between position A and position B), the maximum loading (value of $(\frac{\partial r\overline{V}_\theta}{\partial s})_{max}$) and the slope of the loading (value of $(\frac{\partial^2 r\overline{V}_\theta}{\partial s^2})_{A-B}$). In the next three sections, the important characteristics of the $r\overline{V}_\theta$ distribution that will be examined are: (i) the maximum loading position A; (ii) the regions of vanishing spanwise gradient of $r\overline{V}_\theta$; and (iii) the maximum loading $(\frac{\partial r\overline{V}_\theta}{\partial s})_{max}$.

6.1.1 Effect of the Maximum Loading Position

The maximum loading position could be located at any point from the leading edge toward the trailing edge. In this section, we will attempt to assess the influence of the location of maximum loading on the reduced static pressure field. For consistent assessment, the values of $(\frac{\partial r\overline{V}_\theta}{\partial s})_{max}$ and $(\frac{\partial^2 r\overline{V}_\theta}{\partial s^2})_{A-B}$ for $r\overline{V}_\theta$ distribution along the hub and the shroud will be kept constant, and the influence of varying the maximum loading position A on the design will be investigated.

As the slip factor is 1 at the leading edge and the flow leaves the trailing edge axialy, the overall change in $r\overline{V}_\theta$ across the blade row is -1 (normalized by the $r_t\omega$). The distance along the hub is 0.5 and 0.338 along the shroud (normalized by the tip diameter). The minimal value of the maximum loading $\frac{(\frac{\partial r\overline{V}_\theta}{\partial s})_{max}}{r_t\omega}$ is constrained by the distance of the shroud and it is -1.5. There could be no upper limit of the maximum loading. However, if the maximum loading is too large (-2.5 in this case), there is reversed loading along the hub which is not desirable. Thus, an average value of the maximum loading $\frac{(\frac{\partial r\overline{V}_\theta}{\partial s})_{max}}{r_t\omega} = -2$ is used in this study. The value of $\frac{(\frac{\partial^2 r\overline{V}_\theta}{\partial s^2})_{A-B}}{\omega}$ is set to be 0 so that the maximum loading can be kept to be -2 along the shroud.

Here, we will vary the maximum loading position A from near the leading edge to near the trailing edge. The choice of the distance from the leading edge to position B_{Hub}, is the same as A_{Hub} along the hub, i.e., the second section of the loading is omitted. However, along the shroud this cannot be done easily because the meridional distance is shorter than that along the hub, hence the portion from position A_{Shroud} to position B_{Shroud} will

maintain the same maximum loading. Five different maximum loading positions have been examined. Fig. 6.5a, 6.5b, 6.5c, 6.5d, and 6.5e show the distributions of $r\overline{V}_\theta$, $\frac{\partial r\overline{V}_\theta}{\partial s}$ and $\frac{\overline{W}_\theta}{r}$ along the hub and shroud for each case. The contour plots of $r\overline{V}_\theta$ from the biharmonic interpolation are shown in Fig. 6.6a, 6.6b, 6.6c, 6.6d, and 6.6e. The control parameters are listed in Table 6.1.1.

Table 6.1.1 Control Parameters for Five Different Locations of Maximum Loading

Case	$A_{Hub} = B_{Hub}$	A_{Shroud}	B_{Shroud}
a	0.025	0.025	0.150
b	0.125	0.025	0.144
c	0.250	0.085	0.253
d	0.375	0.194	0.313
e	0.475	0.188	0.313

These five cases correspond to the maximum loading at location near the leading edge, at $\frac{1}{4}$ chord, at $\frac{1}{2}$ chord, at $\frac{3}{4}$ chord and at location near the trailing edge for the hub (the chord is mearsured by the meridional distance along the hub and the shroud). Also, there is a significant difference in the distribution of $\frac{\overline{W}_\theta}{r}$, especially along the hub where the radius is small. As the blade shape is directly related to the value of $\frac{\overline{W}_\theta}{r}$, case "a" will provide the smallest wrap angle. As the position of maximum loading is moved toward the trailing edge, the blade camber will need more and more wrap/turning in the exducer. Clearly, case "e" will give the largest blade wrap/turning f (see Fig. 6.5e).

From chapter 3, the strength of tangential component of the bound vorticity is related to the means swirl and blade wrap by $\overline{\Omega_\theta} = \frac{\partial r\overline{V}_\theta}{\partial r}\frac{\partial f}{\partial z} - \frac{\partial r\overline{V}_\theta}{\partial z}\frac{\partial f}{\partial r}$. Thus, the induced velocity in the meridional plane by the bound tangential vorticity is proportional to the derivative of f and $r\overline{V}_\theta$. In these five cases the gradient of the mean swirl schedule is about the same (no more than -2), so that the larger the blade turning the stronger will be the induced meridional velocity. The effect of the induced flow due to the bound tangential vorticity

$\overline{\Omega_\theta}$ (negative in these cases) will result in flow reversal (along the hub). Numerical results show that case "a" is the only one in which there is no reversed $\vec{W}_{bl}$ (see section 6.2). Hence, strong adverse streamwise pressure and spanwise pressure gradients are expected if the maximum loading position is at location near the trailing edge. It suggests that by locating the maximum loading position near the leading edge would tend to reduce the blade wrap and avoid flow reversal on the hub.

6.1.2 Effect of Regions of Vanishing $\frac{\partial r\overline{V}_\theta}{\partial n}$

In the previous section, we have set the maximum loading $(\frac{\partial r\overline{V}_\theta}{\partial s})_{max}$ and its location to be the same for both the hub and the shroud near the inlet (case "a"). This is becasue the inlet section is almost straight for this particular rotor (see Fig.6.2). By maintaining the same value of $r\overline{V}_\theta$ from the hub to the shroud (i.e., $\frac{\partial r\overline{V}_\theta}{\partial z} = 0$ near the inlet), the spanwise variation of pressure, velocities, etc. on both the pressure and suction surfaces near the inlet (i.e., $\frac{\partial p_{rel}}{\partial z} = 0$, $\frac{\partial V}{\partial z} = 0$, etc) may be kept to the minimum. Thus, it might be useful to examine the influence of the regions of relatively small spanwise gradient of $r\overline{V}_\theta$ on the design; this can be achieved by altering the distance from the leading edge to position B, i.e., the loading for the first and second sections along the hub is kept the same as the one along the shroud.

Without any loss of generality, we can again insist on the same value of $\frac{(\frac{\partial r\overline{V}_\theta}{\partial s})_{max}}{r_t\omega} = -2$ (the average) and $\frac{(\frac{\partial^2 r\overline{V}_\theta}{\partial s^2})_{A-B}}{\omega} = 0$ (i.e. the maximum loading along the shroud remains -2) for the hub and shroud. From the results in the previous section, the position of maximum loading should be chosen to be near the leading edge; thus it is appropriate to choose a distance of 0.025 from the leading edge to position A for both the hub and the shroud. Besides, the portion of constant loading (-2) will extend from $A_{Shroud} = 0.025$ to $B_{Shroud} = 0.15$ along the shroud (case "a"). By keeping the loading on the shroud the same, three cases of $r\overline{V}_\theta$ with different position of B_{Hub} along the hub will be examined.

Clearly, the longer the distance from the leading edge to position B_{Hub}, the regions of $\frac{\partial r\overline{V}_\theta}{\partial n} = 0$ are larger. The specified values of B_{Hub} are given in the Table 6.1.2a.

Table 6.1.2a Control Parameters for Three Different Lengths for Regions with Vanishing $\frac{\partial r\overline{V}_\theta}{\partial n}$

case	B_{Hub}
a	0.025
f	0.064
g	0.100

Further increase in the distance from the leading edge to position B_{Hub} beyond the value of 0.01 will result in a negative value of $r\overline{V}_\theta$ near the trailing edge. Hence, the location of B_{Hub} is set at 0.100 as its upper limit. With these inputs, the distributions of $r\overline{V}_\theta$, $\frac{\partial r\overline{V}_\theta}{\partial s}$ and $\frac{\overline{W}_\theta}{r}$ along the hub and shroud are plotted in Fig. 6.5a, 6.5f, and 6.5g. Fig. 6.6a, 6.6f, and 6.6g give the contour plot of the $r\overline{V}_\theta$ distribution from the biharmonic interpolation.

With these three different mean swirl distributions, the reduced static pressure distributions and relative Mach number contours from the design calculation are shown in Fig. 6.7, 6.8, 6.9 respectively. In these three cases the flow is reversed (i.e., negative meridional velocity) on the pressure surface from few percent of the chord to about middle of the chord (Fig. 6.7c, 6.8c, 6.9c). Hence, the velocities remain relatively close to zero on the pressure surface. The reduced static pressure distribution on the pressure surface is seen to be approximately the same among these three cases (see Fig. 6.7a, 6.8a, 6.9a). Under these circumstances, the pressure on the suction surface is essentially determined by the loading distribution, i.e., the specified $\frac{\partial r\overline{V}_\theta}{\partial s}$.

Fig. 6.10a and 6.10b show the effect of regions of vanishing spanwise gradient of the mean swirl on the maximum adverse pressure gradient and the Wake number. These results are summarized in the Table 6.1.2b.

Table 6.1.2b Effect of Different Lengths for Regions with Vanishing $\frac{\partial r\overline{V}_\theta}{\partial n}$ on the Maximum Adverse Pressure Gradient and Wake Number

case	$(\frac{\partial p_{red.}}{\partial s})_h$	$(\frac{\partial p_{red.}}{\partial s})_m$	$(\frac{\partial p_{red.}}{\partial s})_s$	$(Wake\ no)_h$	$(Wake\ no)_{s.s.}$	$(Wake\ no)_s$
a	0.816	0.800	1.209	6.309	3.261	4.652
f	0.917	0.937	1.226	5.726	2.965	4.813
g	1.065	1.133	1.267	5.269	2.677	4.887

where $(\frac{\partial p_{red.}}{\partial s})_h$, $(\frac{\partial p_{red.}}{\partial s})_m$, and $(\frac{\partial p_{red.}}{\partial s})_s$ are the maximum adverse reduced static pressure gradients along the hub, the mid-span and the shroud quasi-streamlines on the suction surface and $(Wake\ no)_h$, $(Wake\ no)_{s.s.}$, and $(Wake\ no)_s$ are the Wake numbers on the hub, the suction and the shroud surfaces.

Since the loading along the shroud is kept the same, the maximum adverse pressure gradient at the shroud is about the same. As case "a" has the smallest slope of $\frac{\partial r\overline{V}_\theta}{\partial s}$ from position B to the trailing edge, so will the $\frac{\partial p_{red.}}{\partial s}$ along the hub and mid-span (see Fig. 6.10a). Case "g" has the largest regions of vanishing spanwise gradient of the mean swirl hence the regions of the vanishing spanwise pressure gradient is increased (see Fig. 6.7a, 6.8a, 6.9a). Thus, the flow is more uniform in the spanwise direction in case "g" than the one in case "a", and the resulting velocities on the hub surface are increased and the velocities on the shroud surface are reduced relatively when we compare the results of case "g" with the results of case "a". Therefore, the Wake numbers are reduced on the suction and the hub surfaces and increased on the shroud surface when we increase the regions of vanishing $\frac{\partial r\overline{V}_\theta}{\partial n}$ (see Fig. 6.10b).

6.1.3 Effect of the Maximum Loading $(\frac{\partial r\overline{V}_\theta}{\partial s})_{max}$

In the previous two sections, we have obtained the following conclusions: (i) the maximum loading position should be located near the leading edge and (ii) the $r\overline{V}_\theta$ distribution along the hub and the shroud needs to be the same in order to reduce the spanwise variation of the flow field. Here, we will attemp to answer what value of the maximum loading

should be used in a design. In other words, whether a loading distribution with a smaller maximum loading over a region ($\frac{(\frac{\partial r\overline{V}_\theta}{\partial s})_{max}}{r_t\omega}$ less than -2) or a loading distribution with a larger concentrated maximum loading ($\frac{(\frac{\partial r\overline{V}_\theta}{\partial s})_{max}}{r_t\omega}$ greater than -2) is better.

From the theory we know the pressure jump across the blade is related to the streamwise derivative of $r\overline{V}_\theta$. Here, three different values of $(\frac{\partial r\overline{V}_\theta}{\partial s})_{max}$ are examined. For the first case, the maximum loading is the smallest one among these three cases, where $\frac{(\frac{\partial r\overline{V}_\theta}{\partial s})_{max}}{r_t\omega} = -1.75$ and the shape of the loading will have a larger region of plateau as shown in Fig. 6.5h. The second case is case "g" where the magnitude of the $\frac{(\frac{\partial r\overline{V}_\theta}{\partial s})_{max}}{r_t\omega}$ is -2 which is higher than case "h". For the last case, the magnitude of $\frac{(\frac{\partial r\overline{V}_\theta}{\partial s})_{max}}{r_t\omega}$ is set at -2.25 resulting in a loading distribution that is triangular in appearance (see Fig. 6.5i). The value of the $(\frac{\partial^2 r\overline{V}_\theta}{\partial s^2})_{A-B}$ is the same for these three cases which is chosen to be zero. The control points A_{Hub} and A_{Shroud} are set at 0.025 as before to reduce the blade wrap and to avoid flow reversal at the blade. Clearly, the distance from the leading edge to position B_{Shroud} is the largest for a loading with a large regions of plateau, and the smallest for a triangular shape of loading. The distance from the leading edge to position B_{Hub} is set by maximizing regions of $\frac{\partial r\overline{V}_\theta}{\partial n} = 0$ as long as there is no negative value of $r\overline{V}_\theta$ near the trailing edge along the hub. Fig. 6.6g, 6.6h, and 6.6i give the contour plots of the $r\overline{V}_\theta$ distributions from the biharmonic interpolation. The characteristic parameters for these $r\overline{V}_\theta$ distribution are indicated in the Table 6.1.3a.

Table 6.1.3a Control Parameters for Three Different Maximum Loading Distributions $(\frac{\partial r\overline{V}_\theta}{\partial s})_{max}$

case	$\frac{(\frac{\partial r\overline{V}_\theta}{\partial s})_{max}}{r_t\omega}$	B_{Hub}	B_{Shroud}
h	−1.75	0.150	0.250
g	−2.00	0.100	0.150
i	−2.25	0.050	0.075

The pressure distribution and Mach number contour from design code are plotted in Fig 6.9, 6.11 and Fig. 6.12 separately. Clearly, we see that regions of reversed flow on

the pressure surface are the smallest for case "i" (compare Fig. 6.9c, 6.11c, and 6.12c). However the magnitude of reversed flow is the largest for case "i". For case "h", a flat loading along the shroud extends toward the trailing edge and so the blade camber is highly wrap near the exducer. The resulting pressure field have the largest spanwise variation among these three cases (see Fig. 6.9, 6.11, 6.12).

Fig. 6.13a and 6.13b show the effect of the maximum loading $(\frac{\partial r\overline{V}_\theta}{\partial s})_{max}$ on the maximum adverse pressure gradient and Wake number respectively. The results are also summarized in the Table 6.1.3b.

Table 6.1.3b Effect of Different Maximum Loading Distributions $(\frac{\partial r\overline{V}_\theta}{\partial s})_{max}$ on the Maximum Adverse Pressure Gradient and Wake Number

case	$(\frac{\partial p_{rcd.}}{\partial s})_h$	$(\frac{\partial p_{rcd.}}{\partial s})_m$	$(\frac{\partial p_{rcd.}}{\partial s})_s$	$(Wake\ no)_h$	$(Wake\ no)_{s.s.}$	$(Wake\ no)_s$
h	0.806	1.436	1.629	6.001	2.869	4.322
g	1.065	1.133	1.267	5.269	2.677	4.887
i	1.236	0.974	1.163	4.874	3.046	4.210

Once again, we see that to reduce the maximum adverse pressure gradient on the suction surface, one should reduce the slope of $\frac{\partial r\overline{V}_\theta}{\partial s}$ from postion B to the trailing edge. As the slope of $\frac{\partial r\overline{V}_\theta}{\partial s}$ is the smallest for a triangular shape of loading (case "i") along the shroud, the maximum adverse pressure gradient is the smallest along the mid-span and the shroud (see Fig. 6.13a). However, along the hub, the meridional distance is the longest one and the increase of $(\frac{\partial r\overline{V}_\theta}{\partial s})_{max}$ will increase the slope of $\frac{\partial r\overline{V}_\theta}{\partial s}$ from B_{Hub} to the trailing edge. Thus, to reduce the maximum adverse pressure gradient along the hub, one should decrease the value of $(\frac{\partial r\overline{V}_\theta}{\partial s})_{max}$; to reduce the maximum adverse pressure gradient along the shroud, one should increase the distance from B_{Shroud} to the trailing edge.

The pressure jump at the blade near the inlet is the largest for a loading of triangular shape (case "i"). Because the area of passage reduces from the leading edge to mid-chord, the dynamic head is increased near the inlet. Therefore, the increase in Wake number due to a higher pressure jump at the blade near the inlet is compensated. As the pressure

jump reduces in magnitude from mid-chord to the trailing edge in case "i", it results in a decrease of the Wake number. Thus, the Wake numbers on the hub and the shroud surfaces is the smallest for case "i" (see Fig. 6.13b). In so far as the Wake number on the suction surface is concerned, there is not much difference among these three cases. The effect of the mean swirl schedule on the Wake number on the suction surface has been assessed in section 6.1.2. It suggests that a loading distribution with a triangular shape will result in design with a reduced blade wrap as well as a reduction in the streamwise and the spanwise pressure gradients.

6.2 Stacking Position

The blade boundary Equation Eq.(3.28), requires the specification of an initial condition (see section 3.4.2). This is referred to as the specification of a stacking position (r_{st}, z_{st}) as well as its stacking angle $f = f_{st}(r_{st}, z_{st})$. As the strength of the bound vorticity in the r and z directions is determined solely by the $r\overline{V}_\theta$ distribution, the change in the stacking condition will affect the bound tangential vorticity distribution only. Therefore, we can expect a change in the meridional velocity due to an alteration in stacking condition. In this section, we will simply choose the stacking angle $f_{st}(r_{st}, z_{st})$ to be zero along the stacking axis. The effects of different stacking positions will be studied first.

Five different $r\overline{V}_\theta$ distributions that we have referred to as case "a" to case "e" will be examined here. Several stacking positions will be chosen at (r_{st}, z_{st}) between the leading edge and the trailing edge. The calculations have first been done for the Bladed Actuator Duct flow model. Design calculation based on this model is computationally efficient when it is compared to that based on three-dimensional model. Fig 6.14a shows the stacking positions vs the position of maximum loading along the hub. We see that the loading of case "e" results in negative value of $\vec{W}_{bl}$ so that solution fails to obtain a converged blade shape. The loading in case "d" indicates that there are transonic regions due the higher loading

near the trailing edge and hence the higher turning of the blade shape over there. The loadings in case "a", "b", and "c" does not result in negative value of $\vec{W}_{bl}$ if stacking position is chosen to be at the maximum loading position or slightly downstream of it. The reason is that if the stacking position is near the maximum loading position, then the resulting tangential bound vorticity $\overline{\Omega}_\theta$ is small or even zero near the maximum loading position (if the stacking of the blade is straight, i.e., $\frac{\partial f}{\partial z} = 0$ and there is no spanwise variation of the mean swirl in the inducer, then $\overline{\Omega_\theta} = \frac{\partial r\overline{V}_\theta}{\partial r}\frac{\partial f}{\partial z} - \frac{\partial r\overline{V}_\theta}{\partial z}\frac{\partial f}{\partial r} \approx \frac{\partial r\overline{V}_\theta}{\partial r} \times 0 - 0 \times \frac{\partial f}{\partial r} \approx 0$). Hence, the induced meridional velocity is reduced and a negative value of $\vec{W}_{bl}$ can be avoided.

For three-dimensional flow (Number of blades is 14), the results for different stacking positions is shown in Fig 6.14b. It is seen that only with the loading distribution of case "a" that there exist no negative $\vec{W}_{bl}$ for stacking positions at the leading edge, the $\frac{1}{8}$ chord, and the $\frac{1}{4}$ chord. These results are consistent with results based on actuator duct model. Fig. 6.15a and 6.15b show the effect of different stacking postions on the maximum adverse pressure gradient and Wake number respectively. The results are also summarized in the Table 6.2.

Table 6.2 Effect of Different Stacking Positions on the Maximum Adverse Pressure Gradient and Wake Number

Stacking	$(\frac{\partial p_{rcd.}}{\partial s})_h$	$(\frac{\partial p_{rcd.}}{\partial s})_m$	$(\frac{\partial p_{rcd.}}{\partial s})_s$	$(Wake\ no)_h$	$(Wake\ no)_{s.s.}$	$(Wake\ no)_s$
Leading edge	0.816	0.800	1.209	6.309	3.261	4.652
$\frac{1}{8}$ *chord*	0.789	0.826	1.088	6.319	3.040	4.962
$\frac{1}{4}$ *chord*	0.717	0.843	1.060	6.692	3.386	4.750

For the loading distribution of case "a", there is no significant spanwise variation of the mean swirl near the inlet. If we stack the blade straight (i.e., $f_{st} = 0$) at the leading edge or $\frac{1}{4}$ chord, the strength of the bound tangential vorticity $\overline{\Omega}_\theta$ is small or zero within the region from the leading edge to $\frac{1}{4}$ chord. As a result, the flow field will be very similar for these three stacking positions (see Fig. 6.15).

6.3 Lean in Stacking Line

As we have mentioned in the previous section, the initial condition along the stacking line doest not need to be straight, i.e., $f_{st} \neq 0$. The value could be arbitrary. For simplicity, we shall choose the stacking value to be a straight line, but allowed it to lean in two different directions while maintaining the same amount of work done. (see the definition in Fig. 6.16). The results from these design calculations would allow us to assess the influence of the lean on the flow behavior.

We shall use the $r\overline{V}_\theta$ distribution of case "g" for the study here, and choose the stacking position at the leading edge. Three different lean angles are examined, i.e., $\varphi = -6.65°, 0.°$, and 6.65°. The maximum allowable lean angle φ is obtained whenever there is a negative value of $\vec{W}_{bl}$. This is not known apriori.

Fig. 6.17a, 6.17b, and 6.17c give the blade shapes for these three different lean angles. We see that these blade shapes have significant difference only near the leading edge. Near the leading edge, the non-vanished value of $\frac{\partial f}{\partial z}$ (i.e., the lean angle) can alter the sign and strength of $\overline{\Omega}_\theta$ (i.e., $\frac{\partial r\overline{V}_\theta}{\partial r}\frac{\partial f}{\partial z} - \frac{\partial r\overline{V}_\theta}{\partial z}\frac{\partial f}{\partial r}$) on the blade surface. This will alter the value of $\vec{W}_{bl}$ and hence the reduced static pressure distribution. Computed solutions from design calculation are shown in Fig. 6.18 for the case with $\varphi = -6.65°$ and in Fig. 6.19 for the case with $\varphi = +6.65°$. Comparing Fig. 6.9a with Fig. 6.18a and 6.19a, we see a non-zero lean angle results in a large spanwise gradient in the pressure.

Fig. 6.20a and 6.20b show the effect of different lean angles on the maximum adverse pressure gradient and Wake number respectively (see Table 6.3).

Table 6.3 Effect of Different Lean Angles φ on the Maximum Adverse Pressure Gradient and Wake Number

Lean angle	$(\frac{\partial p_{red.}}{\partial s})_h$	$(\frac{\partial p_{red.}}{\partial s})_m$	$(\frac{\partial p_{red.}}{\partial s})_s$	$(Wake\ no)_h$	$(Wake\ no)_{s.s.}$	$(Wake\ no)_s$
−6.65°	0.976	1.163	1.674	5.833	3.612	4.050
0°	1.065	1.133	1.267	5.269	2.677	4.887
6.65°	1.101	1.179	1.110	4.815	1.855	5.814

Clearly, the adverse streamwise pressure gradient on the shroud can be reduced by using a positive lean angle. The streamwise pressure gradient $\frac{\partial p_{rel.}}{\partial s}$ along the mid-span is not affected by the lean angle φ. This is similar to what we have seen in the previous section where different positions with $f_{st} = 0$ do not alter the pressure field significantly. Nevertheless, $\frac{\partial p_{rel.}}{\partial n}$ as well as the Wake number changes dramatically. It suggests that a positive lean angle φ can reduce the loading along the shroud and increase the loading along the hub (see Fig. 6.20b). As a result, the velocity is increased along the hub and decreased along the shroud. Hence, the Wake number is reduced on the suction and the hub surfaces but increased on the shroud surface.

6.4 Slip Factor

The slip factor, ratio of the tangential velocity over the blade rotating speed, is fixed (1 in our case) at the design point. Here, we neglect the constraints on the mechanical strength such that the rotational speed can be altered for a study of slip factor. In each case, the mass flow and the work done are kept the same for different slip factors. Two additional velocity triangles from the design point will be examined, i.e., one with a slip factor 0.95 and the other 0.86 (see Fig. 6.21). The reaction of the turbine wheel is increased from 0.5 to 0.53 and 0.57 respectively. However, the circulation on the blade is decreased to 97% and 93% of its design point respectively. Thus, the loading on each blade is decreased. We can expect the blade profile loss to be decreased by using a smaller slip factor. On the other hand, the windage loss would be increased due to a higher blade speed. The same normalized $r\overline{V}_\theta$ distribution (case "g") and stacking at the leading edge with $f_{st} = 0$ are used for the present study. The data for the study and results are summarized in the Table 6.4.

Table 6.4 Effect of Different Slip Factors on the Maximum Adverse Pressure Gradient and Wake Number

$slip$	$\omega(rmp)$	$(\frac{\partial p_{red.}}{\partial s})_h$	$(\frac{\partial p_{red.}}{\partial s})_m$	$(\frac{\partial p_{red.}}{\partial s})_s$	$(Wake\ no)_h$	$(Wake\ no)_{s.s.}$	$(Wake\ no)_s$
1	64,000	1.065	1.133	1.267	5.269	2.677	4.887
0.95	65,700	0.988	0.979	0.946	4.784	2.700	4.239
0.86	69,000	0.882	0.742	0.731	3.730	2.758	3.122

The results from design calculations are plotted in Fig. 6.22 and 6.23 for slip factors 0.95 and 0.86 separately. Comparing the results with Fig. 6.9, 6.22, and 6.23, for different slip factors, we see that the loading on each blade has been decreased due to an increase in the reaction for a smaller slip factor, hence, the streamwise pressure gradient $\frac{\partial p_{red.}}{\partial s}$, the spanwise pressure gradient $\frac{\partial p_{red.}}{\partial n}$ and regions of reversed flow reduce significantly.

Fig. 6.24a and 6.24b show the effect of different slip factors on the maximum adverse pressure gradient and Wake number respectively. The case of slip factor 0.86 gives the smallest Wake number on the shroud and the hub surfaces among these three cases. However, the Wake number on the suction surface incresaes slightly due to the reduction of the dynamic head on the suction surface (smaller loading). It suggests that a reduction in the slip factor can help the aerodynamic performance.

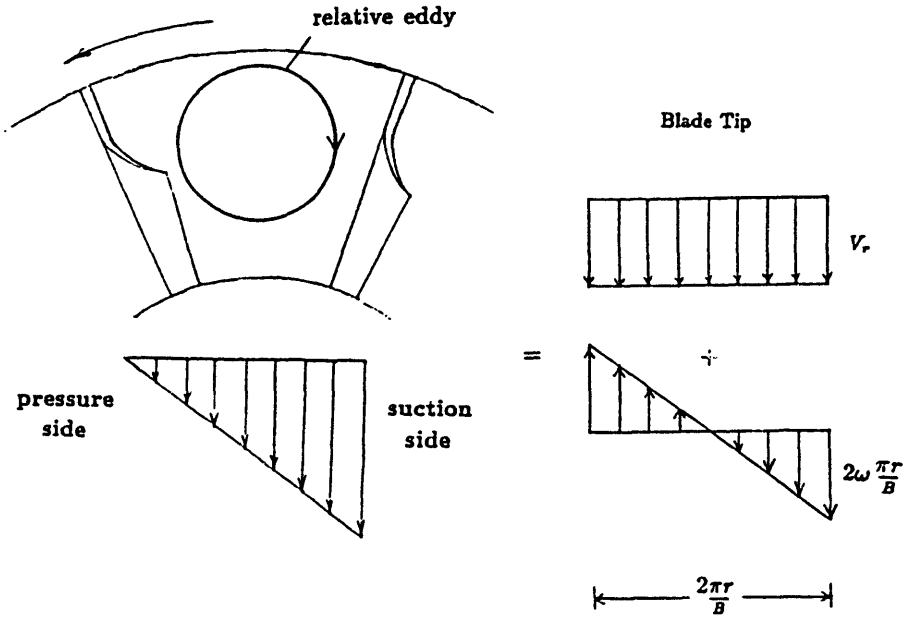
6.5 Blockage Effects

The thickness of blade is accounted for partially through the specification of blockage distribution (see section 3.6). Here, the normal thickness t_n of the blade is specified. Fig. 6.25a shows the distribution of the normal thickness t_n (normalized by the diameter) and the output of the tangential thickness t_θ from design calculation is shown in Fig. 6.25b. It is seen that the influence of the blade thickness appears to be more significant along the hub and the maximum effect is about a 40% decrease of the cross section area. Fig. 6.26 gives the reduced static pressure and Mach number contour from the design calculation

with blockage effects. In contrast to the situation with no bloackage (Fig 6.9), the Mach number on the suction side reaches a value as high as 0.9 (see Fig. 6.26b). In addition, regions of the reversed flow on the pressure side are reduced (see Fig. 6.26c). As one might have expected that the inclusion of blockage increases the mean level of velocity.

6.6 Number of Blades

The design technique allows one to specify the number of blades. From the original design conditions, we choose a number of blades to be 14. It is observed that there exists a large region of reverse flow on the pressure side. To reduce regions of the reversed flow, increasing the number of blades is one of the solutions. From the analysis of relative eddy on a radial filament blade, we can arrive at the number of blades needed to avoid reversed flow on the pressure surface. The flow field associated with a relative eddy at the mid-passage is $2\omega\frac{\pi r}{B}$ (see the illustration below).



An illustration of the relative eddy on the meridional velocity

The incoming flow is $\overline{V}_r$ so that the resulting velocity field can be approximated by the superposition of these two flow. For the velocity on the pressure surface to attain a value of near zero

$$2\omega\frac{\pi r}{B} = \overline{V}_r$$

i.e.

$$B = \frac{2\omega\pi r}{\overline{V}_r} \tag{6.8}$$

By using the above analysis, the number of blades needed to avoid the reversed flow on the pressure side is $B = \frac{2\omega\pi r}{\overline{V}_r} = 2\pi \tan\alpha \approx 23$.

Computed results for a design calculation using the loading distribution of case "g" with a blade number of 21 is shown in Fig. 6.27. One can see that there is no region of reversed flow on the pressure side (see Fig. 6.27c). The loading on each blade is reduced by virtue of an increase in blade number.

Fig. 6.28a and 6.28b show the effect of number of blades on the maximum adverse pressure gradient and Wake number respectively (see Table 6.6).

Table 6.6 Effect of Different Numbers of Blades B on the Maximum Adverse Pressure Gradient and Wake Number

No. of blades	$(\frac{\partial p_{red.}}{\partial s})_h$	$(\frac{\partial p_{red.}}{\partial s})_m$	$(\frac{\partial p_{red.}}{\partial s})_s$	$(Wake\ no)_h$	$(Wake\ no)_{s.s.}$	$(Wake\ no)_s$
14	1.065	1.133	1.267	5.269	2.677	4.887
21	0.693	0.581	0.495	5.207	3.026	4.128

Clearly, the streamwise and spanwise pressure gradient drop significantly by using more blades. As the distance along the shroud is shorter than the one along the hub, hence, the decrease of the maximum adverse pressure gradient is more significant at the shroud than at the hub (see Fig. 6.28a) The Wake numbers on the hub and the shroud surfaces are reduced for the 21-blade design as well. Nevertheless, the Wake number on the suction side increases (see Fig. 6.28b). This is due to the fact that the dynamic head reduces from a 14-blade design to a 21-blade design. Comparing the sum of the Wake numbers on the

hub, the suction and the shroud surfaces between a 14-blade design and a 21-blade design, we can expect that the low momentum fluid driven by the secondary flow will be higher for the 14-blade design.

6.7 Exit Swirl

The influence of exit swirl on the design is examined. As we have seen previously reversed flow appears on the pressure side for a 14-blade design. Here, we allow some residual swirl to remain at the trailing edge so as to alleviate the loading on each blade. The penalty is that the total work done by the rotor is reduced. From previous study, the number of blades has to increase to 21 to avoid reversed flow. Hence, if one uses 14-blade design, the loading should decrease by about 33% of its value at the leading edge in order to avoid reversed flow on the pressure surface. Based on this estimation, we specify a swirl deduction that has a residual swirl at the trailing edge plane equal to 30% of that at the leading edge. Fig. 29 shows the specified $r\overline{V}_\theta$ distribution with a residual swirl equal to 30% of that at the leading edge which is similar to case "g" loading except that the maximum gradient of the mean swirl schedule $\frac{(\frac{\partial r\overline{V}_\theta}{\partial s})_{max}}{r_t\omega}$ is reduced from -2 to -1.4 (30% off). We see that the $\frac{\overline{W}_\theta}{r}$ changes dramatically at the hub (see Fig. 6.29a). The corresponding mean swirl schedule from the biharmonic interpolation is shown in Fig. 6.29b. To prevent $\vec{W}_{bl}$ from becoming negative, the stacking position is set at $\frac{5}{8}$ chord to reduce the blade wrap near the trailing edge. The design calculation is shown in Fig. 6.30 and summaried in the Table 6.7 for the 30% of residual swirl at the exit.

Table 6.7 Effect of Different Exit Swirl on the Maximum Adverse Pressure Gradient and Wake Number

$r\overline{V}_\theta$ left	$(\frac{\partial p_{rel.}}{\partial s})_h$	$(\frac{\partial p_{rel.}}{\partial s})_m$	$(\frac{\partial p_{rel.}}{\partial s})_s$	$(Wake\ no)_h$	$(Wake\ no)_{s.s.}$	$(Wake\ no)_s$
0%	1.065	1.133	1.267	5.269	2.677	4.887
30%	0.395	0.340	0.632	2.901	1.061	4.332

The results show that the streamwise and spanwise gradients of pressure are reduced significantly by allowing some portion of the swirl left the trailing edge as expected. Also, there is no region of reversed flow on the pressure side (see Fig. 6.30c).

6.8 Modified Hub & Shroud Profile

The flow through turbine wheel with the original hub & shroud profile have been studied by Civinskas et al. (Ref. 83) and the resulting losses have been evaluated by a quasi-three-dimensional viscous analysis program. In their work, a region of reversed flow on the hub surface has been predicted. Also, the flow on the suction surface near the inlet region becomes transonic. Therefore, a modified hub & shroud profile has been suggested by them. In this section, we will examine the effect of altering the hub & shroud profiles on the pressure distribution within the blade passage.

The modified hub & shroud profile (see Fig. 6.31b) has a larger cross section for the inducer and a smaller cross section after mid-chord to the trailing edge. In order to obtain a meaningful comparison with the results obtained with the original hub & shroud profile (see Fig. 6.2). We assume the same stacking position and, as nearly as possible, the same $r\overline{V}_\theta$ distribution (case "g"). Fig. 6.31a shows the distribution of $r\overline{V}_\theta$ along the hub and shroud, and Fig. 6.31b shows the corresponding $r\overline{V}_\theta$ distribution from the biharmonic interpolation. The number of blade was also 14 and stacking specification is $f_{st} = 0$ at the leading edge. Fig. 6.32 gives the results from the design calculations. The results are summarized in the Table 6.8.

Table 6.8 Effect of Different Hub and Shroud Profiles on the Maximum Adverse Pressure Gradient and Wake Number

Profile	$(\frac{\partial p_{rel.}}{\partial s})_h$	$(\frac{\partial p_{rel.}}{\partial s})_m$	$(\frac{\partial p_{rel.}}{\partial s})_s$	$(Wake\ no)_h$	$(Wake\ no)_{s.s.}$	$(Wake\ no)_s$
Original	1.065	1.133	1.267	5.269	2.677	4.887
Modified	1.178	0.976	1.096	5.167	2.868	3.886

As the specified $r\overline{V}_\theta$ is similar along the hub and shroud, one might expect that the pressure distribution along the hub and the shroud is also similar between the original

and the modified profile (see Fig. 6.9a and Fig. 6.32a). However, near the inlet, the area of cross section increases, hence the velocities decrease (i.e. $\vec{W}_{bl}$ decreases). Because the pressure difference across the blade is directly related to the product of the rate of change of $r\overline{V}_\theta$ along the mean streamline at the blade and mean velocity at the blade ($\vec{W}_{bl}$), this results in a different loading along mid-span. We see that the maximum adverse pressure gradient along the mid-span is decreased along the mid-span, and also the Wake number is increased on the suction surface for the modified hub & shroud profile.

We have seen that the pressure gradient from pressure side to suction side on the hub and shroud surfaces is about the same for both the original and the modified profiles. Due to the fact that the area of passage decreases in the exducer, the flow is more uniform for the modified profile design than that for the original profile design. Hence, the Wake numbers on the hub and the shroud surfaces decrease for the modified profile. From these results, the sensitivity of the blade geometry and the pressure distribution to a variation in hub & shroud profiles is apparent.

The change in the blade camber distribution according to the modification in the hub and shroud profile is shown in Fig. 6.33. We see there is a significant reduction in the blade turning by using a smaller cross section area of the exducer.

Figure 6.33b shows a very large lean in the blade near the trailing edge which would yield prohibitive centrifugal bending stresses in practice. Modification of the $r\overline{V}_\theta$ distribution to materially reduce the lean would probably envolve the relaxation of the requirement that the maximum derivative of $r\overline{V}_\theta$ with respect to meridional distance must be the same on the hub and the shroud. It remains clear, however, that the aerodynamic features of the conventional radial filament designs are unlikely to be optimum.

6.9 Summary

A parametric study of the inverse design method is presented. The efforts concentrates on exploring the range of parameters which will affect the pressure field. Two parameters,

the maximum adverse reduced static pressure gradient and the Wake number, have been used to characterize a design. Some design guidelines have been proposed for radial inflow turbines. These design guidelines are summarized in the following.

The location of the maximum loading should be chosen to be as near to the leading edge as possible. The smaller the distance from the leading edge to position A, the smaller the blade wrap and the strength of $\overline{\Omega}_\theta$; this can prevent the formation of region of reversed flow in the hub.

Increased regions of vanishing spanwise gradient in $r\overline{V}_\theta$ (i.e., $\frac{\partial r\overline{V}_\theta}{\partial z} = 0$ near the inlet) can reduce the spanwise gradient of flow and pressure fields, and hence reduce the Wake number on the suction surface. However, the slope of $\frac{\partial r\overline{V}_\theta}{\partial s}$ from position B to the trailing edge will increase which will result in a higher adverse pressure gradient in the streamwise direction.

The choice of a triangular loading with its maximum gradient near the leading edge will result in a larger pressure jump at the leading edge compared to a flat loading so that the magnitude of reversed flow on the pressure side will be expected to increase. However, the resulting strength of bound tangential vorticity $\overline{\Omega}_\theta$ is smaller due to a smaller blade wrap, hence regions of reversed flow on the pressure surface is reduced. The secondary flow measured by the Wake number is reduced on the hub and the shroud surfaces for a $r\overline{V}_\theta$ distribution with a triangular shape. Also, the adverse streamwise pressure gradient is reduced because of a smaller slope in $\frac{\partial r\overline{V}_\theta}{\partial s}$ from B to the trailing edge. This suggest that a triangular type of loading is desirable (see Fig. 6.12).

The study shows that in order to avoid reversed flow on the blade, the stacking position should be set near the position of the maximum loading or slightly downstream of it such that the strength of the bound tangential vorticity $\overline{\Omega_\theta}$ is samll or zero. Hence, excessive induced meridional velocity (negative) due to $\overline{\Omega_\theta}$ can be avoided. The choice of stacking position (with $f_{st} = 0$) does not alter significantly the pressure distribution along the mid-span but the pressure distribution changes along the hub and the shroud (see Fig 6.15a).

This effect becomes even more significant when we lean the stacking line. The results show that the spanwise pressure gradient (or the Wake number) can be controlled through the choice of lean angle φ. A positive lean angle φ increases the loading along the hub and reduces the loading along the shroud (see Fig. 6.20a). This can reduce the maximum adverse pressure gradient along the shroud and the Wake number on the suction and the shroud surfaces significantly.

The study of slip factor shows that a smaller slip factor can reduce the aerodynamic loading on each blade, but the reaction of turbine wheel needs to be increased. There should be a trade off between $\overline{V}_\theta$ and $r\omega$ for an optimal slip factor.

The thickness of blades is partially accounted for in our blockage formulation. The results show considerably large effects on the hub because of a larger normal thickness and turning. We have found that the Mach number becomes as high as 0.9 on the suction surface. A correct treatment of blade thickness effect is important for a high Mach number flow.

To avoid the reversed flow on the pressure side of the blade, we increase the number of blades from 14 to 21 (instead of 23 from the analysis of relative eddy). The results show that the pressure gradient on each blade is reduced significantly.

An alternative way to reduce the loading on the blade is to allow some portion of the residual swirl after the trailing edge. But this would lead to a reduction in turbine work output. The study shows that the reversed flow on the pressure side disappears if we retain a residual swirl at the exit equal to 30% of that at the leading edge.

From the results of a modified hub & shroud profile, the sensitivity of the meridional profile on the pressure distribution is apparent. A larger region of reverse flow on the pressure side and the spanwise variation in the tip section of the impeller is due to the increase of cross section. However, reducing the cross section near the exducer reduces the spanwise gradient of pressure considerably.

Chapter 7

Flow Analysis by Solving Euler and Navier-Stokes Equations

In this chapter, we will demonstrate the consistency and correspondence of the inverse design procedure and the direct procedure. This is accomplished by comparing the results from the design calculation to the corresponding results from direct calculation based on an Euler solver. Then, solutions of the Navier-Stokes equations are obtained by using "average passage" code (see section 7.1). This permits an assessment of the performance of the designed rotor blades based on the losses generated in the passage, including the behavior of the boundary layers and their subsequent migration under the action of the reduced static pressure field. Finally, the interaction between the tip clearance flow and secondary flow is examined. The effect of tip clearance on the current design is also included.

7.1 Euler and Navier-Stokes Codes Description

The programs used to analyze the radial inflow turbine is a three-dimensional inviscid/viscous "average passage" codes developed by J. J. Adamczyk at NASA Lewis (Ref. 85, 86, 87). The codes use three averaging processes to obtain the average passage equations from the full Navier-Stokes equations. These are ensemble average, time averaging, and passage-to-passage average. Ensemble averaging yields the familiar Reynolds-averaged Navier-Stokes equations. This averaging process removes the random fluctuations from the flow field. Time averaging further simplifies the flow equations by removing the deterministic unsteady flow component which occurs because of the relative movement of different blade rows. Finally, the equations are passage-to-passage averaged, which

removes the effect of different blade count of stator and/or rotor blade rows. In this procedure, the flow is assumed to be spatially periodic from blade passage to blade passage. For multistage turbomachinery, with stator blade rows and/or rotor blade rows having different numbers of blades, this will not generally be true. The average passage equations obtained by the three averaging processes are discretized using a control volume approach in a cylindrical coordinate system. Using this control volume approach, all flow quantities are cell-centered. To obtain values of flow variables at cell surfaces, an averaging process is used which results in second-order accuracy. In the viscous solutions, a Baldwin-Lomax turbulence model is employed (Ref. 88).

The discretized average passage equations obtained by the control volume approach are solved using a four-stage Runge-Kutta time-stepping scheme. Second and fourth difference smoothing operators are used to avoid alternate point decoupling in the solution. The Riemann invariants C^+ and C^- are used to calculate the radial velocity component at the upstream boundary. Constant entropy is assumed from an upstream state to the inlet boundary, and this is used to determine the inflow temperature, pressure and density. At the downstream boundary, the static pressure at the hub is specified. All other downstream flow quantities are extrapolated from the interior of the flow domain. At the hub and shroud surfaces, an extrapolated normal pressure gradient boundary condition is employed in conjunction with an adiabatic wall. In the viscous solutions, the computational cells which lie in the stationary regions on the hub surface employ a zero velocity boundary condition. All other hub cells use the rotor speed as the velocity boundary condition. The shroud is stationary in the absolute frame of reference and is so modeled. For the inviscid solution, the flow is tangent to the hub, pressure and suction surfaces in the relative frame of reference and to the shroud surface in the absolute frame of reference. The mesh boundaries extending from the blade leading and trailing edges to the inflow and outflow boundaries, respectively, are periodic boundaries. At these boundaries, periodicity is enforced by setting the flow variables in the computational cell outside the computational

domain equal to those at the corresponding periodic location.

The codes contain a one-dimensional inviscid flow model for the clearance gap flow. This model conserves mass, momentum, and total enthalpy across the clearance gap. As a result, the pressure difference across the gap is zero. This is a rather simplied representation of the flow in the clearance region, but it does result in a flow across the clearance gap which serves to reduce the loading in the tip region. This model is simply implemented by enforcing the previously stated periodic boundary conditions. This model for the flow in the clearance gap was applied to the entire blade tip.

7.2 Comparison between Design and Euler Results

The design conditions are the same as in Chapter 6. In the computation, a finer mesh is used as shown in Fig. 7.1. The finer mesh consists of 145 grid points in the streamwise direction and 49 grid points in the spanwise direction. We also use 16 complex harmonic modes for the periodic flow calculation instead of the 4 used in chapter 6. This corresponds to 33 grid points in the tangential direction. For a direct calculation, the spacing of the grid is clustered closer to the blade surfaces in the blade to blade plane (see Fig. 7.1) which is different from the design calculation. Fig. 7.2a shows the specified $r\overline{V}_\theta$ distribution which is the loading distribution of case "g" in chapter 6 (see Fig. 6.5g). The resulting blade shape is shown in Fig. 7.2b with 14 blades and stacking $f_{st} = 0$ at $\frac{1}{4}$ chord of the impeller. The distributions of the reduced static pressure on the suction surface, the pressure surface, the hub surface and the shroud surface are plotted in Fig. 7.3a, 7.3b, 7.3c, and 7.3d respectively. These computed results will be referred to in the comparison with those from Euler calculation and Navier-Stokes calculation as well.

An Euler code based on Jameson's scheme developed by Adamczyk (see section 7.1) has been applied to compute the flow through the designed wheel at design conditions. From this computed flow field, the circumferential mean of the tangential velocity (and hence the

mean swirl schedule $r\overline{V}_\theta$) can be determined to compare with the specified $r\overline{V}_\theta$ distribution for the design calculation. (This provides a check of the inverse design procedure whereby one proceeds to determine the blade shape for a particular specification of the mean swirl schedule, $r\overline{V}_\theta$.) Fig. 7.4a. shows the $r\overline{V}_\theta$ distribution obtained from the Euler calculation. When this is compared to the specified $r\overline{V}_\theta$ distribution of Fig. 7.2a used for the inverse design calculation, the maximum difference between the two was found to amount to no more than two percent of the design value of $r\overline{V}_\theta$ at the blade leading edge (see Fig. 7.4b).

Results in Fig. 7.5a, 7.5b, 7.5c and 7.5d show the computed reduced static pressure distributions on the blade suction surface, the blade pressure surface, the hub surface, and the shroud surface. Comparing these results with those in Fig. 7.3 shows the excellent agreement between the computed results from the inverse design code and the direct inviscid code. In addition, similar results have been obtained for the use of 21 blades. The agreement in $r\overline{V}_\theta$ distribution is even better for it falls within one percent of the design value at the blade leading edge.

7.3 Comparison between Design and Viscous Results

A Navier-Stokes code developed by Adamczyk (see section 7.1) is used to analyze the flow through the designed radial inflow turbine rotor. In the viscous solutions, a Baldwin-Lomax turbulence model is employed. The transition from laminar flow to turbulent flow is achieved by specifying a point transition (2% of chord is used here). The Reynolds number based on radial velocity, density and radius at rotor tip is 8.51×10^5. The Prandtl number is assumed to be constant and is equal to 0.739, and the turbulent Prandtl number is assumed to be 0.9.

Using the same blade shape shown in Fig. 7.2b for the viscous code, the resulting $r\overline{V}_\theta$ distribution is shown in Fig. 7.6a. The maximum difference between the design specification and viscous prediction was found to be within five percent of the value of $r\overline{V}_\theta$ at the blade leading edge.

The prediction of reduced static pressure from the viscous calculation is plotted in Fig. 7.7. It is seen that there is a big difference in pressure distribution on the suction surface near the inlet section (compare Fig.7.3a and Fig. 7.7a). This is probably associated with the development of the incoming boundary layers on the hub and the shroud surfaces well before the leading edge. The reduced static pressure field could have resulted in the migration of viscous layers on the hub and the shroud surfaces onto the suction surface in the blade region (we will see next). This leads to the formation of two regions of low momentum fluid on the suction surface (one from the hub and the other from the shroud); the resulting flow field can be seen clearly in Fig. 7.9a. These two regions of low momentum fluid alter the flow field on the suction surface in the inducer (see Fig. 7.9a). We note that there is reversed flow on the pressure surface from inviscid calculation. Comparing Fig. 7.3b and 7.7b, the agreement of the pressure distribution on the pressure surface between the design and viscous solutions is good. No dramatic separation of the boundary layer has been observed on the pressure surface. Actually, when we compare the inviscid and viscous results at mid-span (see Fig. 7.8a and Fig. 7.8b), the major difference occurs only on the suction surface where viscous effect is expected to be significant. Here, the Mach number has been given a negative sign if the meridional velocity is reversed in Fig. 7.8. Comparing Fig. 7.3c & 7.3d with Fig. 7.7c & 7.7d, the agreement of the pressure distribution on the hub and the shroud surfaces is very good between the design and viscous solutions. From these results, there is no drastic breakdown of the boundary layers on the bounding walls for this designed impeller.

The evolution of entropy from the leading edge to the trailing edge is given in Fig. 7.10. From these plots, we see that the movements of low momentum fluid are from the pressure side toward the suction side on the hub and the shroud surfaces. The resulting secondary flow drives the low momentum fluid onto the suction surface. The absolute streamwise vorticity is shown in Fig. 7.11. The strength of the streamwise vorticity indicates the trend of the secondary flow. Toward the $\frac{3}{4}$ chord, the overall low momentum fluid on the

hub and the shroud surfaces have been moved to the suction surface together with the blade boundary layer fluid (see Fig. 7.10d). At the trailing edge, the low momentum fluid is pushed into the free stream (see Fig. 7.10e) by the two concentrated counter-rotating streamwise vortices on the suction surface (see Fig. 7.11e).

As we mentioned in chapter 6, in order to avoid reversed flow on the pressure surface, the number of blades should increase from 14 to 21. As noted previously, the same $r\overline{V}_\theta$ distribution shown in Fig. 7.2a is used for the 21-blade design. The reulting blade shape has been used for viscous analysis. In Fig. 7.12 and Fig. 7.13, we show the evolution of entropy and absolute streamwise vorticity from the leading edge to the trailing edge for the 21-blade design. The movements of low momentum fluid are from the pressure side toward the suction side on the hub and the shroud surfaces which is very similar to the results of 14-blade design. At the trailing edge, the resulting low momentum fluid is concentrated at about mid-span on the suction surface. The strength of the secondary movement is smaller than the one in 14-blade design as expected (see section 6.6).

The sources of the losses in the turbomachinery can consist of (1) bounding wall profile loss; (2) dissipation loss associated with the vorticity field; and (3) kinetic energy loss associated with the secondary motion. In the following analysis, a mass average of the total temperature and the total pressure is used to assess the performance of the turbine which includes only the first two sources of the losses. Here, Table 7.3a and Table 7.3b summarize the mass average of the total temperature and the total pressure for the 14-blade and 21-blade design respectively.

Table 7.3a Mass Average of the Total Temperature at Different Stations

No. of Blades	T_{t0}	T_{t1}	T_{t2}	T_{t3}
14	1.00000	1.00008	0.77644	0.77672
21	1.00000	1.00054	0.77714	0.77729

Table 7.3b Mass Average of the Total Pressure at Different Stations

No. of Blades	P_{t0}	P_{t1}	P_{t2}	P_{t3}
14	1.00000	0.98936	0.31122	0.31050
21	1.00000	0.98812	0.31001	0.30919

where stations 0, 1, 2, and 3 represent the far upstream, the blade leading edge, the blade trailing edge, and far downstream. The turbine efficiency can be defined as

$$\eta_t = \frac{actual\ work\ for\ a\ given\ pressure\ ratio}{ideal\ work\ for\ a\ given\ pressure\ ratio} \tag{7.1}$$

If the flow is adiabatic, then this definition is equivalent to

$$\eta_t = \frac{1 - \frac{T_{t2}}{T_{t1}}}{1 - (\frac{P_{t2}}{P_{t1}})^{\frac{\gamma-1}{\gamma}}} \tag{7.2}$$

Using Eq.(7.2), we see that the efficiency of 14-blade design is 0.968 where the efficiency for 21-blade design is 0.964. The performance is very similar for the same $r\overline{V}_\theta$ specification with a different number of blades, however, the performance of 14-blade design is slightly better. The mass average of entropy production can be computed in accordance with the following equation

$$\frac{\Delta S}{R} = \frac{\gamma}{\gamma - 1} ln(\frac{T_t}{T_{t0}}) - ln(\frac{P_t}{P_{t0}}) \tag{7.3}$$

Here, the computed mass average of entropy production is summarized in the Table 7.3c.

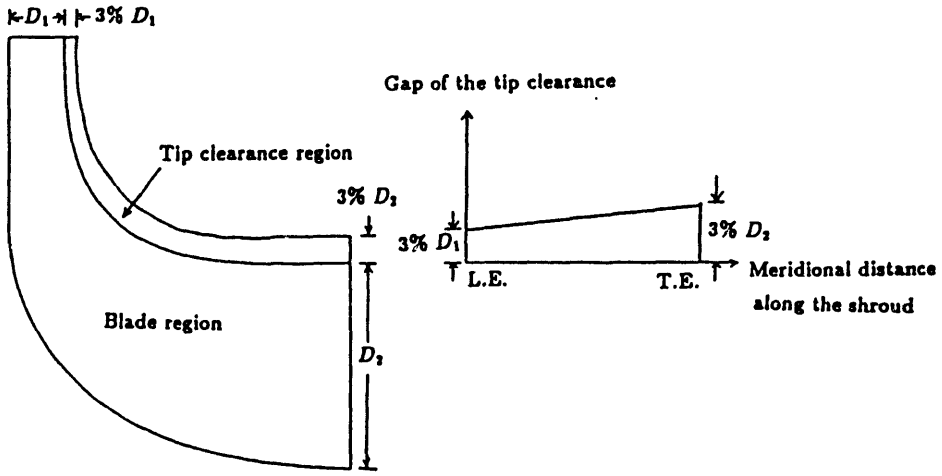
Table 7.3c Mass Average of the Entropy Production between Different Stations

No. of Blades	$(\frac{\Delta S}{R})_{0-1}$	$(\frac{\Delta S}{R})_{1-2}$	$(\frac{\Delta S}{R})_{2-3}$
14	0.01106	0.03967	0.00390
21	0.01432	0.04509	0.00344

From these calculation, the main losses (not including loss due to the kinetic energy associated with the secondary motion) occur within the blade passage, i.e., the losses in the upstream and downstream flows are relatively small. The viscous losses of the 14-blade design are smaller than those of the 21-blade design. It seems that reducing the adverse pressure gradient and the Wake number (see section 6.6) in 21-blade design does not improve the performance. The 50% increase of the blade surface and hence the skin friction losses evidently overwhelms any improvement due to these presumably favorable effects.

7.4 Effect of the Tip Clearance

The viscous average passage computer code described in the section 7.1 is used to study the effect of tip clearance on the current design. The same fine mesh is used (see Fig. 7.1) except that the shroud is moved axially as well as radially to account for the tip clearance. A typical three percent of the span is used for the tip clearance at the leading and the trailing edges. The actual tip clearance varies linearly between these two points (see the illustration below). In the computations, three additional grid points are added to account for the clearance flow.



An illustration of the tip clearance along the shroud

Using the designed blade shape shown in Fig. 7.2b, the resulting $r\overline{V}_\theta$ distribution with 3% of the tip clearance is shown in Fig. 7.14a. The maximum difference between the design specification and viscous prediction was found to be within seven percent of the design value of $r\overline{V}_\theta$ at the blade leading edge (see Fig. 7.14b). The effect of the tip clearance on the computed mean swirl is the greatest at the blade tip in the exducer.

The prediction of the reduced static pressure from the viscous calculation with 3% tip clearance is plotted in Fig. 7.15. As we have seen in the previous section, two regions of low momentum fluid are formed on the suction surface (see Fig.7.15a). Fig. 7.16 shows the meridional velocity near the suction and the pressure surfaces. Comparing Fig.7.9a and Fig.7.16a, we see that the incoming velocity is decreased at the mid-span for the case of 3% of the tip clearance. This is due to a 3% increase of area, some mass flow going through the tip clearance region (see Fig. 7.16a) and also the blockage caused by the boundary layers. The agreement of the pressure distribution between the design and viscous solutions is good for the pressure and the hub surfaces. However, on the shroud surface a tip leakage vortex occurs from the leading to the trailing edge (see Fig. 7.15d). This leakage vortex starts on the suction side of the blade and reaches the pressure side of the blade toward the trailing edge. This high loss region can be examined further in the sequence of entropy plots shown in Fig. 7.17.

The evolution of entropy from the leading edge to the trailing edge is given in Fig. 7.17 and the absolute streamwise vorticity is plotted in Fig. 7.18. Clearly, the incoming boundary layer on the shroud surface becomes thicker than the one without tip clearance (compare Fig. 7.10a and Fig. 7.17a). This is due to a 3% increase of area. At the mid-chord, two concentrated counter-rotating streamwise vorticities (one is due to the secondary flow on the shroud surface and the other is due to the tip leakage flow) are observed on the shroud surface near the suction side corner (see Fig.7.18c). Comparing Fig.7.10c and Fig. 7.17c, further low momentum fluid is driven into the free stream from the shroud surface possibly due to the interaction of the tip leakage flow and the secondary

flow. Toward the trailing edge, the movements of low momentum fluid are mainly driven by the tip leakage vortex (negative sign) and is from the suction side toward the pressure side on the shroud surface (see Fig. 7.17d). At the trailing edge, the tip leakage vortex has moved onto the pressure surface. The region of high losses is near the shroud surface and, in particular, concentrates at the core of the tip leakage vortex on the pressure surface (see Fig. 7.17e and 7.18e). Only one strong streamwise vorticity is observed after the trailing edge which is different from that without tip clearance. From the interaction of the tip clearance flow and the secondary flow on the shroud surface, this suggests that a reduction in the Wake number on the shroud surface from a design can reduce the tip clearance losses.

To assess the performance of the turbine, a mass average of the total temperature and the total pressure for the 0% and 3% of tip clearance is summarized in the Table 7.4a and Table 7.4b.

Table 7.4a Mass Average of the Total Temperature at Different Stations

Tip Clearance	T_{t0}	T_{t1}	T_{t2}	T_{t3}
0%	1.00000	1.00008	0.77644	0.77672
3%	1.00000	1.00097	0.78227	0.78222

Table 7.4b Mass Average of the Total Pressure at Different Stations

Tip Clearance	P_{t0}	P_{t1}	P_{t2}	P_{t3}
0%	1.00000	0.98936	0.31122	0.31050
3%	1.00000	0.97711	0.30671	0.30559

Using Eq.(7.2), we see that the efficiency of 0% of tip clearance is reduced from 0.968 to 0.944 for 3% of tip clearance. We see that there are 2.4% drop of efficiency due a 3% of tip clearance. The mass average of entropy production is summarized in the Table 7.4c.

Table 7.4c Mass Average of the Entropy Production between Different Stations

Tip Clearance	$(\frac{\Delta S}{R})_{0-1}$	$(\frac{\Delta S}{R})_{1-2}$	$(\frac{\Delta S}{R})_{2-3}$
0%	0.01106	0.03967	0.00390
3%	0.02742	0.07007	0.00341

The computed results seem to indicate that the presence of tip leakage flow introduces further losses in the upstream as well as in the blade passage. After the trailing edge, there is no significant difference in losses between the situation with and the situation without tip clearance. However, the loss due to kinetic energy associated with the secondary motion has not been included in the present analysis on loss. For a consistent comparison, we should also include this as well.

7.5 Summary

The numerical results show that there is consistency and direct correspondence between the current design method and the three-dimensional Euler code. The error between the prescribed $r\overline{V}_\theta$ and the calculated $r\overline{V}_\theta$ by Euler calculation is no more than two percent of the incoming swirl.

The agreement of the pressure distribution between the design and viscous calculations implies that there is no drastic flow breakdown. The reversed flow on the pressure side does not cause any flow breakdown as one might have thought.

Two counter-rotating streamwise vorticity regions are observed which are probably driven by the reduced static pressure field. This may have resulted in the migration of the low momentum fluid onto the suction surface. At the trailing edge, low momentum fluid was driven into the free stream region located on the suction side, at three quarters of the span (measured from the hub) where the two counter-rotating streamwise vorticities are observed. The usefulness of the Wake number on the secondary flow is confirmed

by comparing the location and the strength of the streamwise vorticity in the viscous solutions between the 14-blade and 21-blade designs. Similar conclusions on the generation of secondary flow and its movement are given by Zangeneh-Kazemi & Hawthorne in Ref. 89.

The mass average of the entropy production shows that the major losses occur in the blade passage (this does not include the loss due to kinetic energy associated with the secondary motion). The performance of 14-blade and 21-blade designs is similar by using the same specified mean swirl for the design.

Tip leakage flow introduces further losses in the blade passage. At the trailing edge, only one strong streamwise vorticity is observed, and the low momentum fluid become concentrated near the shroud surface which is different from the results without tip clearance. The mass average of entropy production shows that the losses in the blade passage are increased significantly. A decrease of 2.4% efficiency of the rotor is observed with the 3% of tip clearance used in the calculation. This value could have been higher if we include the loss due to the kinetic energy associated with the tip clearance vortex.

Chapter 8

Conclusions and Suggestions for Future Work

8.1 Summary and Conclusions

In the present investigation, we have shown how the new approach for inverse design can be used to design turbomachinery blading in three-dimensional flow. The computed results in chapter 6 illustrate the use of the technique to implement design studies in which one can isolate the influence of each design parameter, such as loading distribution, stacking position, lean in stacking angle, slip factor, number of the blades and hub & shroud profile geometry on the flow field while keeping the mass flow and the power the same. Some guidelines for choosing a good $r\overline{V}_\theta$ distribution based on reducing the adverse pressure gradient and the Wake number have been proposed. Furthermore, excellent agreement was obtained between the prescribed $r\overline{V}_\theta$ distribution and that obtained from a direct Euler calculation of the flow through the designed rotor. These results show the consistency and correspondence of the design code and a direct calculation. Finally, a three-dimensional viscous analysis program has been used to analyze the flow in the designed rotor from a given choice of $r\overline{V}_\theta$ distribution; this allows one to assess the extent of the viscous effects (such as the boundary layer behavior and formation of secondary flow). The agreement on the pressure distribution between the inviscid and viscous solutions suggests that the inviscid flow gives a good approximation of the real fow. Based on the current design procedure, it appears that it is possible to control the boundary layers based on the inviscid pressure field.

We shall attempt to summarize the important contributions of this study on the design of radial inflow turbines in the following:

(1) A way to specify the $r\overline{V}_\theta$ distribution has been proposed. This involves specification of $r\overline{V}_\theta$ along the hub and the shroud boundaries and interpolation of $r\overline{V}_\theta$ for the interior

domain in the blade region from a biharmonic equation. The distribution of $r\overline{V}_\theta$ along the hub and the shroud was separated into three sections which is generated through a polynomial fit.

(2) Some suggested design guidelines for radial inflow turbines are:

- The location of maximum loading should be near the leading edge in order to reduce the blade wrap and avoid reversed flow on the hub.
- A triangular shape of loading distribution reduces the maximum adverse pressure gradient on the suction surface and Wake numbers on the hub and the shroud surfaces.
- An increase in the regions of vanishing spanwise gradient of the mean swirl reduces Wake number on the suction surface.
- A positive lean angle reduces the loading along the shroud and increases the loading along the hub.
- The stacking position should be near the location of maximum loading or slightly downstream of it in order to reduce inviscid regions of flow reversal on the hub surface.

(3) The use of Wake number can give a measure of the formation of secondary flow.

(4) The consistency and the correspondence between the current inverse procedure and the direct problem have been established.

(5) The use of the design tool developed here and the viscous analysis tool allows one to concentrate on the aerodynamic quantities of interest rather than on the choices of blade geometry.

8.2 Suggestions for Future Work

As for future work, the following suggestions are made:

(1) During the course of this research, we have only considered a restricted class of $r\overline{V}_\theta$ distribution; in particular, the maximum streamwise gradients of $r\overline{V}_\theta$ along the hub and the shroud are chosen to be the same and the maximum loading position is set near the leading edge. These restrictions are based solely on aerodynamic considerations. However, the designed blade shapes have a highly lean angle at the trailing edge. From the structure point of view, such a blade shape may lead to very high centrifugal stresses. Consequently, investigations are needed to identify classes of $r\overline{V}_\theta$ distribution that would yield a compromise between aerodynamics and structure. Alternatively, the current procedure could be modified to allow for imposition of structural constraints. This might entail the specification of $r\overline{V}_\theta$ over part of the blade region and the blade camber distribution over remaining portion of the blade region.

(2) The design study should further be carried out to assess the fluid dynamic influence of the followings:

- A non-free vortex blading; this may require a proper treatment of the presence of trailing vorticity.
- Rotational incoming flow.
- Inclusion of splitter blades.
- Effects of blockage due to the presence of boundary layer and tip clearance flow.

(3) Development of an optimization scheme to couple the design and viscous calculations that allow the inclusion of aerodynamic as well as structural contraints.

(4) Experimental investigation should be undertaken to assess the adequacy of the ideas and concepts in these various studies. It is expected that the resulting experimental work will also lead to further improvements in the theory.

Reference

Ref. 1 Hawthorne, W.R.; Wang, C.; Tan, C.S. and McCune, J.E. : "Theory of Blade Design for Large Deflections : Part I – Two-Dimensional Cascades" Trans. ASME, J.Eng. for Gas Turbines and Power. Vol. 106 No 2, pp.346-353, 1984

Ref. 2 Tan, C.S.; Hawthorne, W.R.; McCune, J.E. and Wang, C. : "Theory of Blade Design for Large Deflections : Part II – Annular Cascades" Trans. ASME, J.Eng. for Gas Turbines and Power Vol. 106, pp.354-365, 1984

Ref. 3 Theodorsen, T. : "Theory of Propellers" McGraw Hill, New York, 1948

Ref. 4 Smith, L.H. : "Unducted Fan Aerodynamic Design" Trans. ASME, J. of Turbomachinery, Vol. 109, July 1987

Ref. 5 Kerwin, J.E. : "Marine Propellers" Annual Review of Fluid Mechanics, Vol. 18, pp.367-403, 1986

Ref. 6 Martensen, E. : "The Calculation of the Pressure Distribution on a Cascade of Thick Airfoils by Means of Fredholm Integral Equations of the Second Kind", NASA TT-F-702, 1959

Ref. 7 Wilkinson, D.H. : "A Numerical Solution of the Analysis and Design Problems for the Flow Past One or More Aerofoils in Cascades" ARC R & M 3545, 1967

Ref. 8 Murugesan, K. and Railly, J.M. : "Pure Design Method for Aerofoils in Cascade" J. Mech. Eng. Sci., Vol. 11 No 5, pp.454-467, 1969

Ref. 9 Schwering, W. : "Design of Cascades for Incompressible Plane Potential Flows with Prescribed Velocity Distribution" Trans. ASME, J. of Eng. Power, pp.321-332, 1971

Ref.10 Lewis, R.I. : "A Method for Inverse Aerofoil and Cascade Design by Surface Vorticity" ASME paper 82-GT-154, 1982

Ref.11 Betz, A. and Flügge - Lotz I. : "Design of Centrifugal Impeller Blades" NACA-TM-No.902, 1939

Ref.12 Dang, T.Q. and McCune, J.E. : "Design Method for Highly-Loaded Blades with Blockage in Cascade" Proceedings. ASME Conference 'Computation of Internal Flows : Methods and Applications', pp. 129-136, 1984

Ref.13 McCune, J.E. and Dang, T.Q. : "Periodic Internal Flows" Proceeding ASME Conference 'Computation of Internal Flows : Methods and Application', pp.123-128, 1984

Ref.14 Lighthill, M.J. : "A Mathematical Method of Cascade Design" ARC Rep. & Mem. 2104, 1945

Ref.15 Gostelow, G.R. : "Method of Designing Cascade Blades with Prescribed Velocity distribution in Compressible Potential Flows" NACA Rep. 978, 1950

Ref.16 Costello, G.R.; Cummings, R.L. and Sinnette J.T. : "Detailed Computational Procedure for Design of Cascade Blades with Prescribed Velocity Distributions in Compressible Potential Flows" NACA Rep. 1060, 1952

Ref.17 Cantrell, H.H. and Fowler, J.E. : "The Aerodynamic Design of Two-dimensional Turbine Cascades for Imcompressible Flow with a High-Speed Computer" Trans. ASME, J. of Basic Eng. Vol. 81 No 3, pp.349, 1959

Ref.18 Uenishi, A. : "A Design Method and the Performance of Two-Dimensional Turbine Cascades for High Subsonic Flows" ASME paper 71-GT-34, 1971

Ref.19 Hobson, D.E. : "Shock-free Transonic Flow in Turbomachinery Cascades" Ph.D. Thesis, Cambridge Univ., 1974

Ref.20 Bauer, F.; Garabedian, P. and Korn, D. : "Supercritical Wing Sections I", lecture notes in Economics and Mathematical systems, Vol. 66, Springer-Verlag, New York, 1972

Ref.21 Garabedian, P. and Korn, D. : "A Systematic Method for Computer Design of Supercritical Airfoils in Cascades" Comm. Appl. Math., Vol. 29, pp.369-382, 1976

Ref.22 Korn, D. : "Numerical Design of Transonic Cascades" J. of Computational Physics, Vol. 29, pp.20-34, 1978

Ref.23 Sanz, J.M. : "Design of Supercritical Cascades with High Solidity" AIAA J. Vol. 21 No.9, 1983

Ref.24 Sanz, J.M.; McFarland, E.R.; Sanger, N.L.; Gelder, T.F. and Cavicchi, R.H. : "Design and Performance of a Fixed, Non-accelerating Guide Vane Cascade that Operate Over an Inlet Flow Angle Range of 60 Degree" ASME paper 84-GT-75, 1984

Ref.25 Stanitz, J.D. : "Design of Two-Dimensional Channels with Prescribed Velocity Distributions Along the Channle Walls" NACA Rep. 1115, 1951

Ref.26 Stanitz, J.D. and Sheldrake, L.J. : "Application of a Channel Design Method to High-Solidity Cascades and Tests of an Impulse Cascade with 90° of Turning" NACA Rep. 1116, 1951

Ref.27 Schmidt, E. : "Computation of Supercritical Compressor and Turbine Cascade with a Design Method for Transonic Flows" Trans. ASME J. Eng. for Power, Vol. 102 No.1, pp.68-74, 1980

Ref.28 Wu, C. and Brown, C.A. : "A Theory of the Direct and Inverse Problems of a Compressible Flow Past Cascades of Arbitrary Airfoils" J. of the Aero. Science, No. 19, pp.183-196, 1952

Ref.29 Novak, A.R. and Haymann-Haber, G. : "A Mixed Flow Cascade Passage Design Based on a Power Series Expansion" ASME paper 82-GT-121, 1982

Ref.30 Sator, F.G. : "Inverse Computation of Profile Shapes for Given Transonic Flow-Configurations with and without Detached Bow-Shock in Two-Dimensional Turbomachinery Cascades" Trans. ASME J. Eng. for Power, Vol. 99 No.4, pp.601-607, 1977

Ref.31 Murman, E.M. and Cole, J.D. : "Calculation of Plane Steady Transonic Flows" AIAA J. Vol.23 No.2, pp.114-121, 1971

Ref.32 Beauchamp, P.P. and Seebass, A.R. : "Shock-free Turbomachinery Blade Design" AIAA Vol.23 No.2, pp.249-253, 1985

Ref.33 Cedar, R.D. and Stow, P. : "A Compatible Mixed Design and Analysis Finite Element Method for the Design of Turbomachinery Blades" Int. J. for Num. Methods in Fluids, Vol.5, pp. 331-345, 1985

Ref.34 Wang, Zhengming : "Inverse Design Calculations for Transonic Cascades" ASME paper 85-GT-6, 1985

Ref.35 Thompkins, W.T. and Tong, Siu shing : "Inverse or Design Calculations for Non-potential Flow in Turbomachinery Blade Passages" Trans. ASME. J. Eng. for Power, Vol. 104, pp.281-285, 1982

Ref.36 Tong, Siu shing and Thompkins, W.T. : "A Design Calculation Procedure for Shock-free or strong Passage Shock Turbomachinery Cascades" ASME paper 82-GT-220, 1982

Ref.37 Meauze', G. : "An Inverse Time Marching Method for the Definition of Cascade Geometry" Trans. ASMW. J. Eng. for Power, Vol.104, pp.650-656, 1984

Ref.38 Meauze', G. and Lesain, A. : "Use of an Inverse Method for the Design of High Efficiency Compressor and Turbine Blades with Large Change in Radius" ASME paper 84-GT-206, 1984

Ref.39 Singh, U.K. : "A Design Time Marching Method for the Generation of Blades in a Cascade" ASME paper 86-GT-167, 1986

Ref.40 Denton, J.D. : "An Improved Time Marching Method for Turbomachinery Flow Calculation" Trans. ASME. J. Eng. for Power, Vol.105, pp.514-524, 1982

Ref.41 Giles, M.; Drela, M. and Tompkins, W.T. : "Newton Solution of Direct and Inverse Transonic Euler Equations" AIAA paper 85-1530, 1985

Ref.42 Smith, K.J. and Hamrick, J.T. : "A Rapid Approximate Method for the Design of Hub Shroud Profile of Centrifugal Impellers of Given Blade Shape" NACA TN 3399, 1954

Ref.43 Wright, L.C. and Novak, R.A. : "Aerodynamic Design and Development of the General electric CF805-23 Aft Fan Component" ASME paper 60-WA-270, 1960

Ref.44 Novak, R.A. : "Streamline Curvature Computing Procedures for Fluid-Flow Problems" Trans. ASME. J. Eng. for Power, Vol.89, pp.478-490, 1967

Ref.45 Katsanis, T. : "Fortran Program for Calculating Transonic Velocities on a Blade-to-Blade Stream Surface of a Turbomachine" NASA TND-5427, 1969

Ref.46 Kashiwabara, Y. : "Theory on Blades of Axial, Mixed and Radial Turbomachines by Inverse Method" Bulletin of the JSME, Vol.16, No.92, pp.272-281, 1973

Ref.47 Jennions, I.K. and Stow, P. : "A Quasi-Three-Dimensional Turbomachinery Blade Design System : Part I – Through Flow Analysis" ASME paper 84-GT-26, 1984

Ref.48 Jennions, I.K. and Stow, P. : "A Quasi-Three-Dimensional Turbomachinery Blade Design System : Part II – Computerized System" ASME paper 84-GT-27, 1984

Ref.49 Okurounmu, O. and McCune, J.E. : "Lifting Surface Theory of Axial Compressor Blade Rows : Part I – Subsonic Comprssor" AIAA J. Vol.12, No.10, pp.1363-1372, 1974

Ref.50 Okurounmu, O. and McCune, J.E. : "Lifting Surface Theory of Axial compressor Blade Rows : Part II – Transonic Compressor" AIAA J. Vol.12, No.10, pp.1372-1380, 1974

Ref.51 Borges, J.E. : "Three-Dimensional Design of Turbomachinery" Ph.D. Dissertation, engineering Department, Cambuidge Univ., Sept. 1986

Ref.52 Ghaly, W.S. : "A Study and Design of Radial Turbomachinery Blading in Three-Dimensional Flow" Ph.D. Thesis, Department of Aeronautics and Astronautics, MIT, Sept. 1986

Ref.53 Ghaly, W.S. : "A Parametric Study of Radial Turbomachinery Blade Design in Three-Dimensional Subsonic Flow" Trans. of the ASME, Journal of Turbomachinery, Vol.112, pp.338-345, July 1990

Ref.54 Zangeneh-Kazemi, M. : "Three-Dimensional Design of Radial-Inflow Turbines" PhD Thesis, Cambridge University Engineering Department, 1988

Ref.55 Zangeneh, M. and Hawthrone, W.R. : "A Fully Compressible Three Dimensional Inverse Design Method Applicable to Radial and Mixed Flow Turbomachines" ASME paper 90-GT-198, 1990

Ref.56 Dang, T.Q. and McCune, J.E. : "A Three-Dimensional Blade Design Method in Rotational Flow" Proceedings International Conference on Inverse Design Concepts in Engineering Sciences (ICIDES) G.S. Dulikravich, ed. Univ. of Texas, Austin, 1984

Ref.57 Soulis, J.V. : "Thin Turbomachinery Blade Design Using Finite Volume Method" Inte. J. for Numerical Methods in Eng. Vol.21, pp.19-36, 1985

Ref.58 Zhao, Xiao-Lu; Sun, Chun-Lin and Wu, Chung-Hua : "A Simple Method for Solving Three-Dimensional Inverse Problem of Turbomachinery Flow and the Annular Constraint condition" Trans. ASME. J. of Eng. for Gas Turbines and Power, Vol.107, pp.293-300, 1985

Ref.59 Turner, M.G. : "Design and Analysis of Internal Flow Fields Usig a Two Stream function Formulation" MIT GTL Report NO.201, 1990

Ref.60 Lamb, Sir Horace : "Hydrodynamics" 6th ed. Dover Publications, New York, pp.248-249, 1932

Ref.61 Lighthill, M.J. : "Fourier Analysis and Generalized Functions" Cambridge, University Press, 1959

Ref.62 Hawthorne, W. R.; McCune, J. E.; Mitchell, N. A. and Tan, C.S. : "Non-Axi-Symmetric Flow Through an Annular Actuator Disc: Inlet Distortion Problem" Trans. ASME. J. of Eng. for Power, Vol.100, pp.604, 1978

Ref.63 Tan, C.S. : "Vorticity Modelling of Blade Wakes Behind Isolated Annular Blade-Rows : induced Disturbances in Swirling Flows" Trans. ASME. J. of Eng. for Power, Vol.103, pp.279-287, 1981

Ref.64 Hirsch, CH. and Warzee, G. : "A Finite-Element Method for Through Flow Calculations in Turbomachines" Trans. ASME. J. of Fluids Engineering, vol.98, pp.403-421, 1976

Ref.65 Hirsch, CH. and WArzee, G. : "An Integrated Quasi-Three-Dimensional Finite-Element Calculation Program for Turbomachinery Flows" ASME paper 78-GT-56, 1978

Ref.66 Smith, L.H. : "Secondary Flow in Axial-Flow Turbomachinery" Transactions ASME, pp.1065-1076, 1955

Ref.67 Tan, C.S. : "Three-Dimensional Incompressible and Compressible Beltrami Flow Through a Highly Loaded Isolated Rotor" MIT GT & PDL Report 147, 1980

Ref.68 Falcao, A. : "Three-Dimensional Flow Analysis in Axial Turbomachines" Ph.D. thesis, Cambridge University, 1970

Ref.69 Smith, L.H. and Yeh, Hsuan : "Sweep and Dihedral Effects in Axial-Flow Turbomachinery" Trans. ASME. J. of Basic Engineering, pp.401-416, Sep. 1963

Ref.70 Brebner, G.G. and Wyatt, L.A. : "The Velocities Induced by Distributions of Infinite Kinked Source and Vortex Lines Representing Wings with Sweep and Dihedral in Incompressible Flow" ARC Rep. & Mem. 3667, 1970

Ref.71 Anderson, D.A.; Tannehill, J.C. and Pletcher, R.H, : "Computational Fluid Mechanics and Heat Transfer" McGraw-Hill Book Company, pp.521-532, 1976

Ref.72 Gozani, J.; Nachshon, A. and Turkel, E. : "Conjugate Gradient Coupled with Multigrid for an Indefinite Problem" NASA Contractor Report 172379, June 1984

Ref.73 Deconinck, J. and Hirsch, C. : "A Multigrid Method for the Transonic Full Potential Equation Discretized with Finite Elements on an Arbitrary Body Fitted Mesh" Vrije Universiteit Brussel, Department of Fluid Mechanics

Ref.74 Pitkäranta J. and Sararinen, T. : "A Multigrid Version of a Simple Finite Element Method for the Stokes Problem" Math. of Computation, Vol.45, No.171, pp.1-14, 1985

Ref.75 Bazeley, G.P.; Cheung, Y.K.; Irons, B.M. and Zienkiewicz, O.C. : "Triangular Elements in Plate Bending - Conforming and Non-conforming Solutions" Proc. 1st Conf. Matrix Methods in Structural Mechanics, pp.547-576, AFFDL-TR-CC-80, Wright-Patterson A.F. Base, Ohio, 1966

Ref.76 Smith, J. : "The Coupled Equation Approach to the Numerical Solution of the Biharmonic Equation by Finite Differences I" SIAM, J. Numer. Anal. Vol.5, No.2, pp.323-339, June 1968

Ref.77 Smith, J. : "The Coupled Equation Approach to the Numerical Solution of the Biharmonic Equation by Finite Differences II" SIAM, J. Numer. Anal. Vol.7, No.1, pp.104-111, March 1970

Ref.78 Ehrlich, L.W. : "Solving the Biharmonic Equation as Coupled Finite Difference Equations" SIAM, J. Numer. Anal. Vol.8, No.2, pp.278-287, June 1971

Ref.79 Mclaurin, J.W. : "A General Coupled Equation Approach for Solving the Biharmonic Boundary Value Problem" SIAM, J. Numer. Anal. Vol.11, NO.1, pp.14-33, March 1974

Ref.80 Cooley, J.W. and Tukey, J.W. : "An Algorithm for the Machine Calculation of Complex Fourier Series" Math. Compt., 1965

Ref.81 Acton, F.S. : "Numerical Methods that usually work" Harper & Row Publishers, 1970

Ref.82 Rohlik, H.E. : "Radical Inflow Turbines" Ch.10 of "Turbine Design and Application" Vol.3, A. J. Glassman, ed., NASA SP-290, pp.31-58, 1975

Ref.83 Civinskas, K.C. and Povinelli, L.A. : "Application of a Quasi-Three-Dimensional Inviscid Flow and Boundary Layer Analysis to the Hub-Shroud Contouring of a Radial Turbine" NASA TM 83669, 1984

Ref.84 Adamczyk, J.J. : "Model Equation for Simulating Flows in Multistage Turbomachinery" ASME, paper 85-GT-226 and NASA TM-86869, 1985

Ref.85 Adamczyk, J.J.; Mulac, R.A. and Celestina, M.L. : "A Model for Closing the Inviscid Form of the Average-Passage Equation System" J. of Turbomachinery, Vo.108, No.4, pp.180-186, 1986

Ref.86 Celestina, M.L.; Mulac, R.A. and Adamczyk, J.J. : "A Numerical Simulation of the Inviscid Flow Through a Counter Rotating Propeller" J. of Turbomachinery, Vol.108, No.4, pp.187-193, 1986

Ref.87 Heidmann, J.D. and Beach, T.A. : "An Analysis of the Viscous Flow Through a Compact Radial Turbine by the Average Passage Approach" NASA TM 102471, 1990

Ref.88 Baldwin, B.S. and Lomax, H. : "Thin Layer Approximation and Algebraic Model for Seperated Turbulent Flows" AIAA paper 78-257, Huntsville, Alabama 1978

Ref.89 Zangench-Kazemi, M; Dawes, W. N. and Hawthorne, W. R. : "Three-Dimensional Flow in Radial Inflow Turbines" ASME paper No. 88-GT-103, 1988

Ref.90 Hawthorne, W. R. and Tan, C. S. : "Design of Turbomachinery Blading in Three-Dimensional Flow by the Circulation Method : A Progress Report" Proceedings International Conference on Inverse Design Concepts in Engineering Sciences (ICIDES) G.S. Dulikravich, ed. Penn State University, PA, 1987

Table I Turbine Design Conditions

Inlet Total Temperature, $°K$	1607
Inlet Total Pressure, N/m^2	1.637×10^6
Specific Work, J/g	466.2
Work Factor (Slip)	1
Rotor Tip Speed, m/s	682.8
Rotor Tip Diameter, m	0.2038
Rotative Speed, rpm	64,000
Mass Flow Rate, kg/sec	2.370
Power, Kw	1,105
Specific Ratio, γ	1.294
Number of Blades, B	14

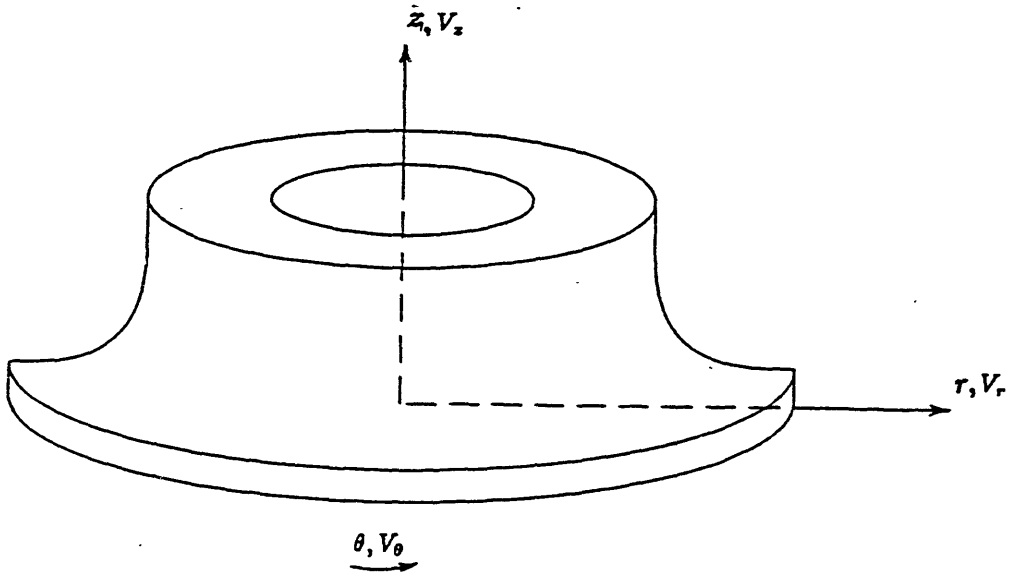


Fig. 3.1 Right-handed cylindrical coordinate system and nomenclature

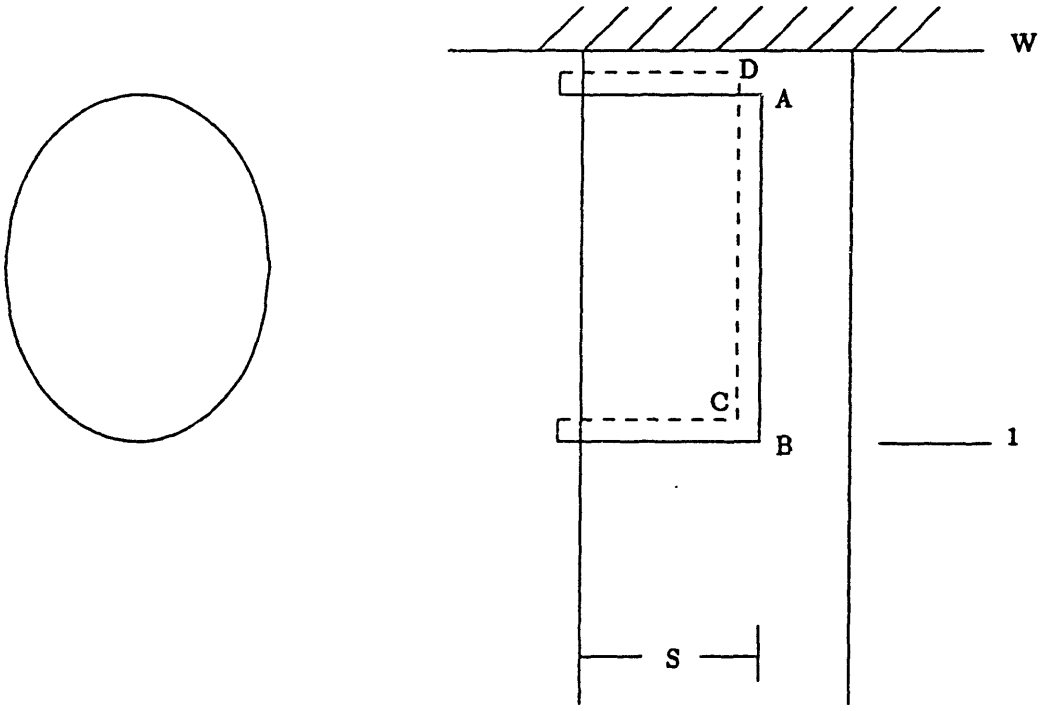


Fig. 4.1 An illustration of Prandtl wing theorem

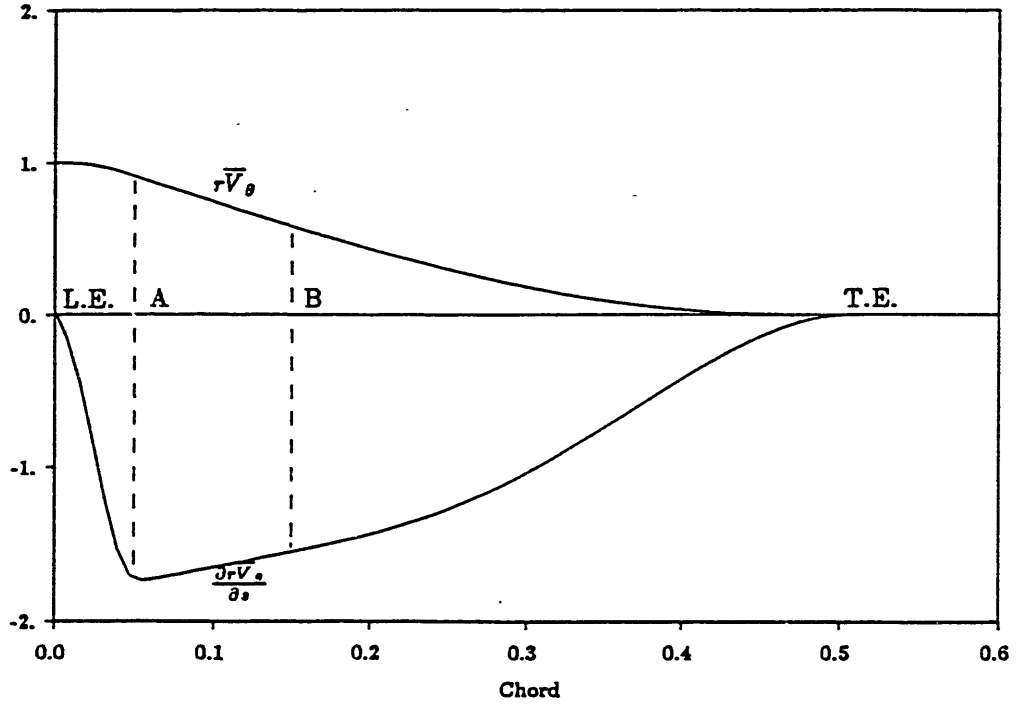


Fig. 4.2 Schematic plot of $r\overline{V}_\theta$ distribution along the hub and shroud

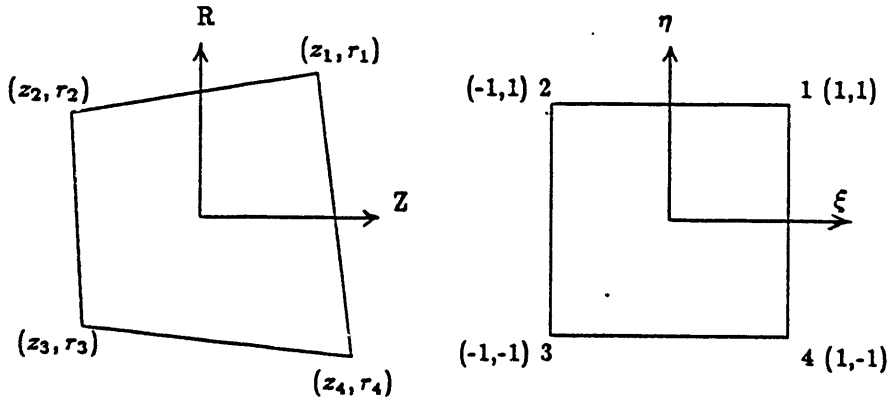


Fig. 5.1 The 4-node element

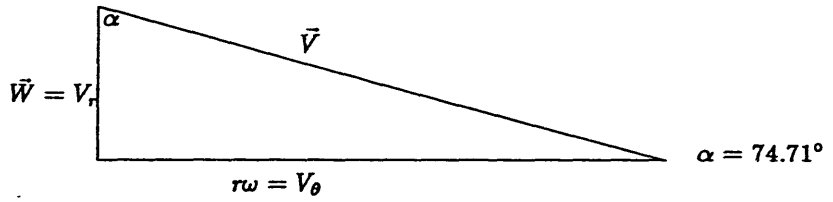


Fig. 6.1 Velocity triangle at leading edge

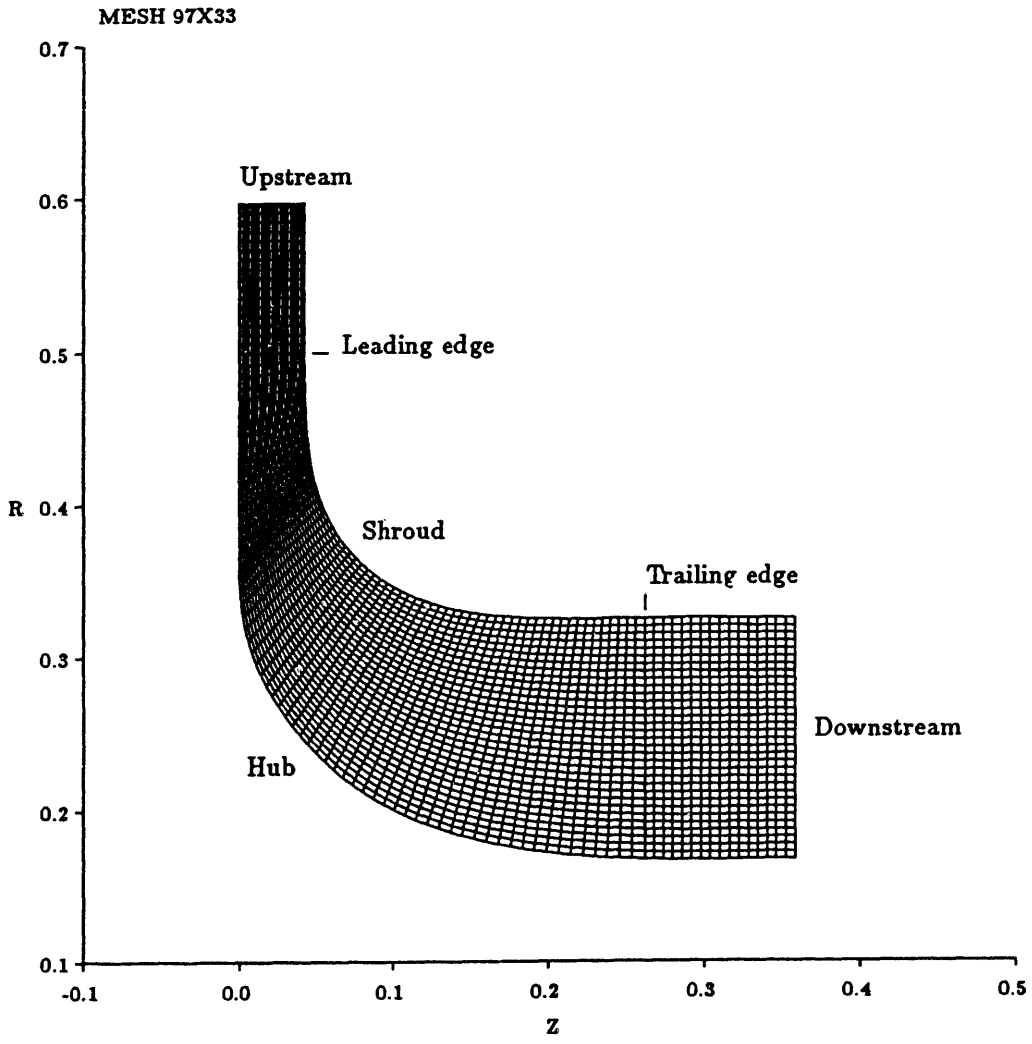


Fig. 6.2 Grid used for calculation

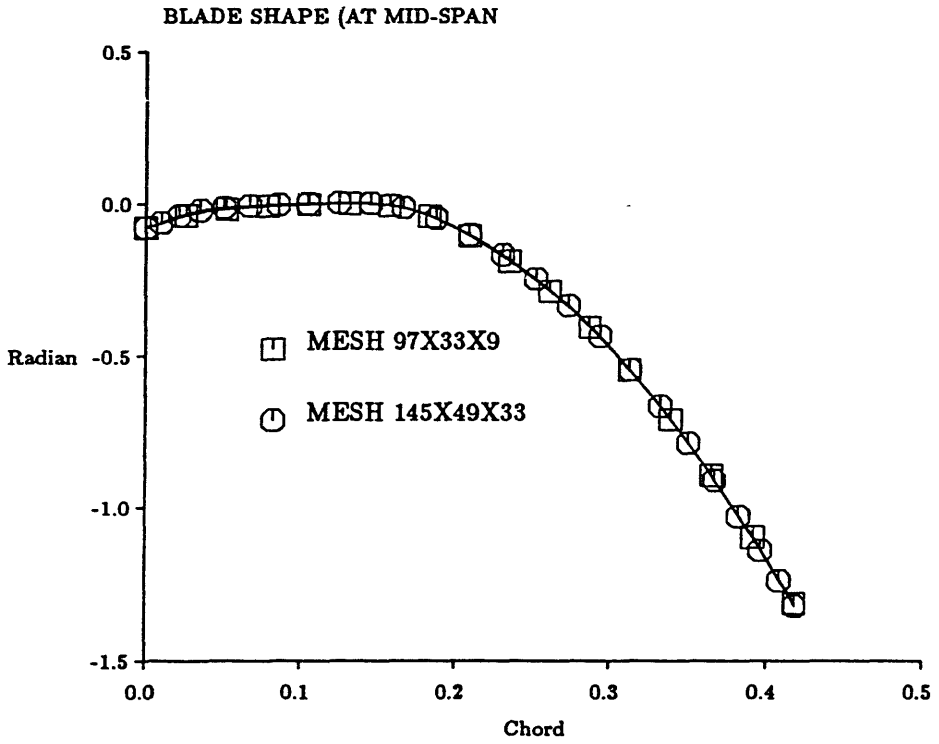


Fig. 6.3a The blade camber at mid-span for two different grid sizes

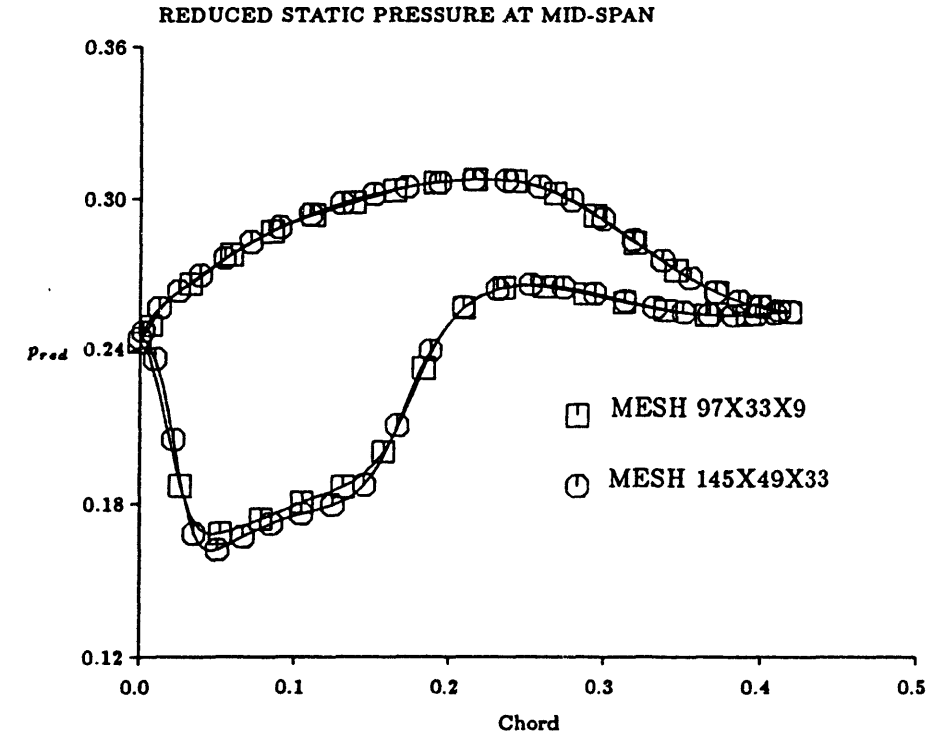


Fig. 6.3a The distribution of p_{red} at mid-span for two different grid sizes

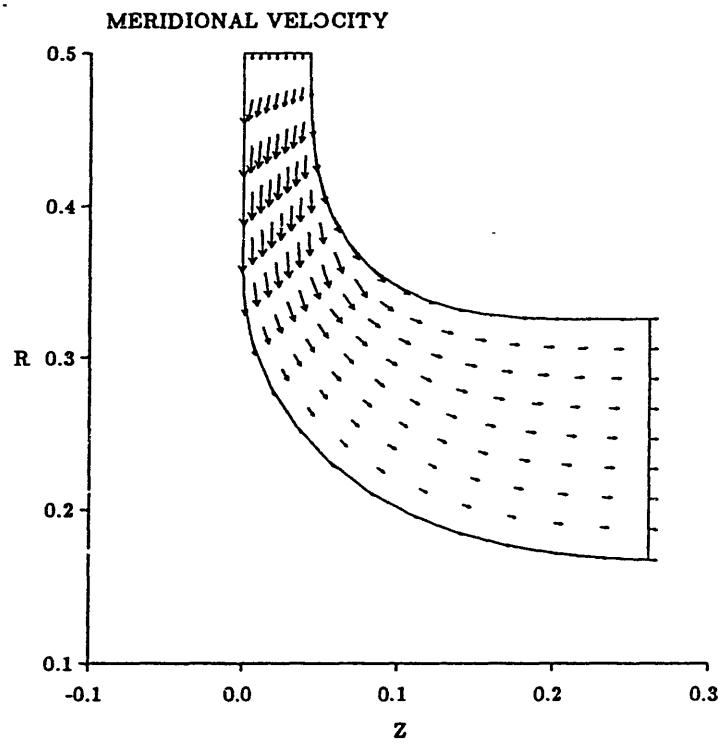


Fig. 6.4a The meridional velocity on the suction surface for Wake number = 1.86

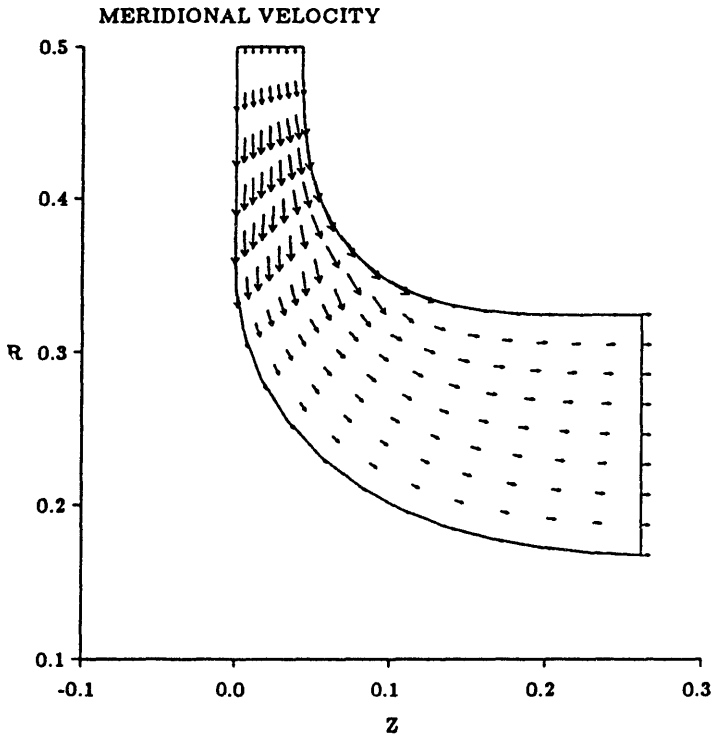


Fig. 6.4b The meridional velocity on the suction surface for Wake number = 3.61

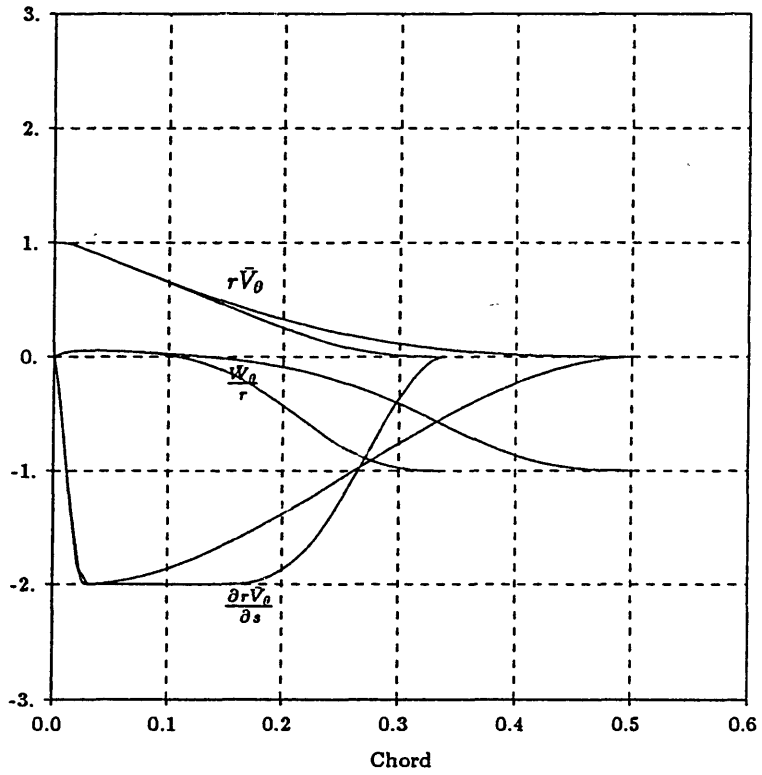


Fig. 6.5a The distribution of $r\bar{V}_\theta$, $\frac{\bar{W}_\theta}{r}$, $and \frac{\partial r\bar{V}_\theta}{\partial s}$ along the hub and shroud for case a

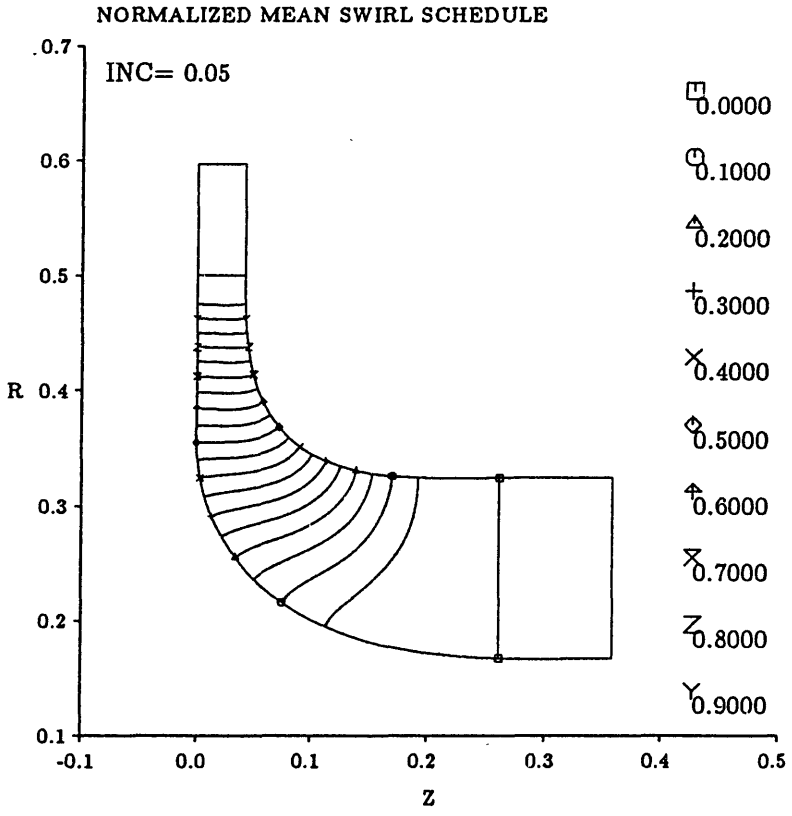


Fig. 6.6a The distribution of $r\bar{V}_\theta$ for case a

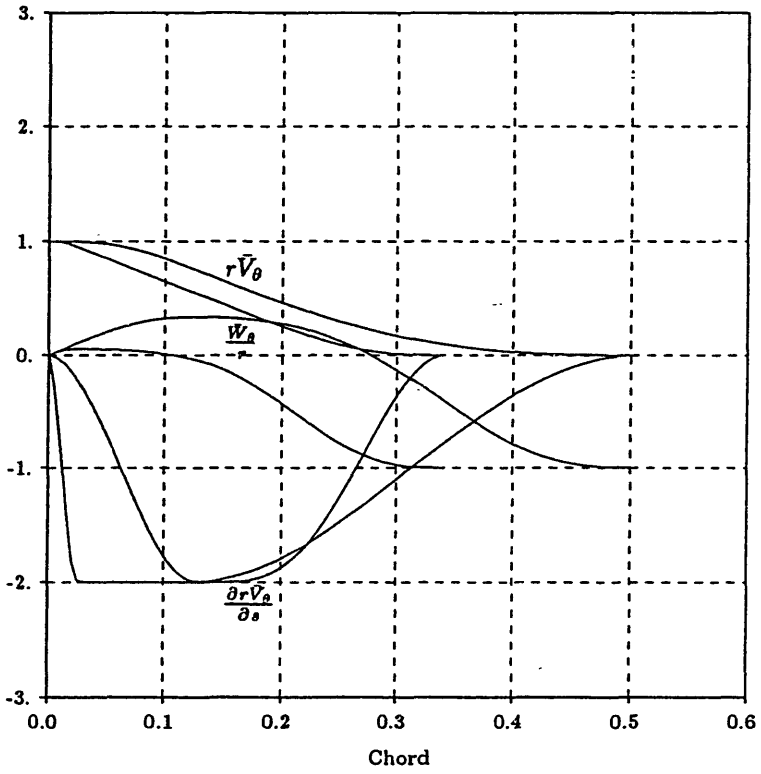


Fig. 6.5b The distribution of $r\bar{V}_\theta, \frac{\bar{W}_\theta}{r}, and \frac{\partial r\bar{V}_\theta}{\partial s}$ along the hub and shroud for case b

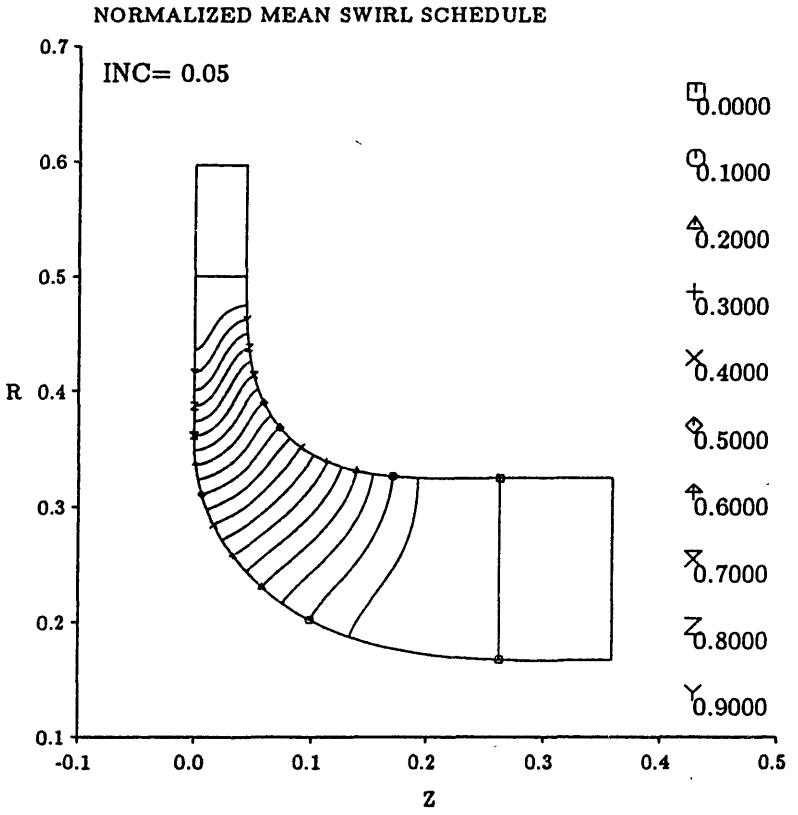


Fig. 6.6b The distribution of $r\bar{V}_\theta$ for case b

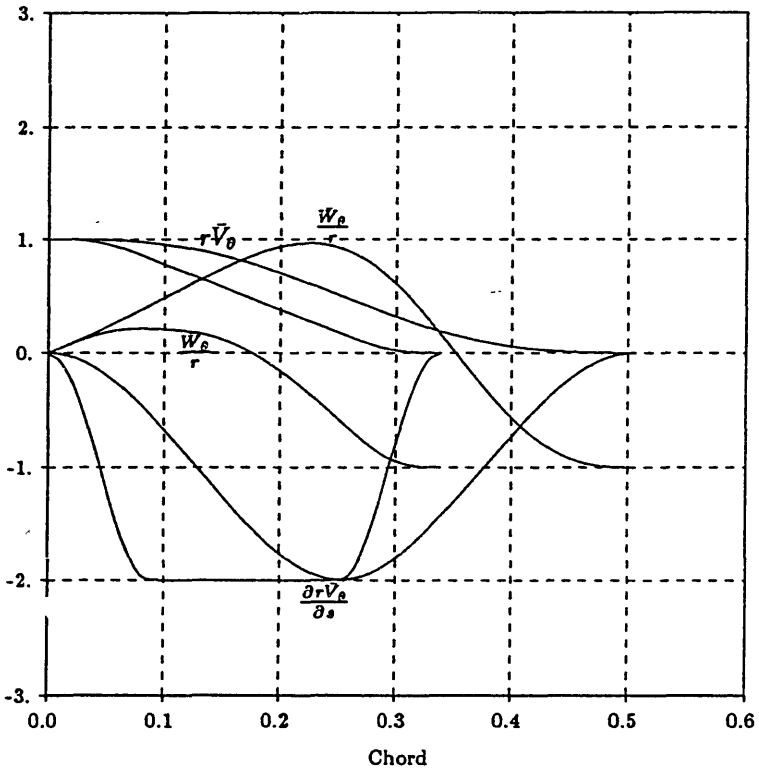


Fig. 6.5c The distribution of $r\bar{V}_\theta, \frac{\bar{W}_\theta}{r}, and \frac{\partial r\bar{V}_\theta}{\partial s}$ along the hub and shroud for case c

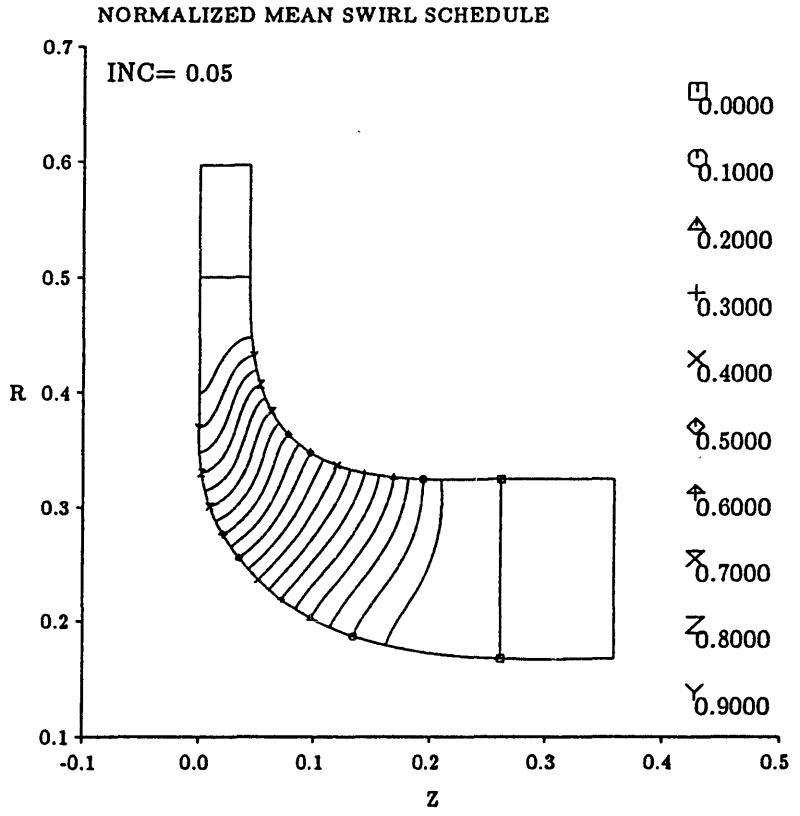


Fig. 6 6c The distribution of $r\bar{V}_\theta$ for case c

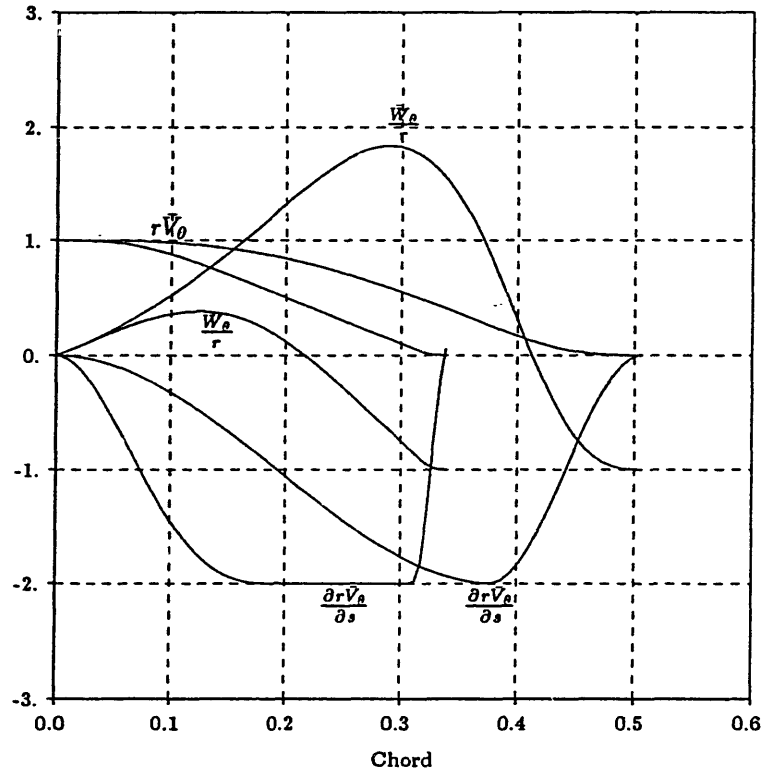


Fig. 6.5d The distribution of $r\bar{V}_\theta, \frac{\bar{W}_\theta}{r}, and \frac{\partial r\bar{V}_\theta}{\partial s}$ along the hub and shroud for case d

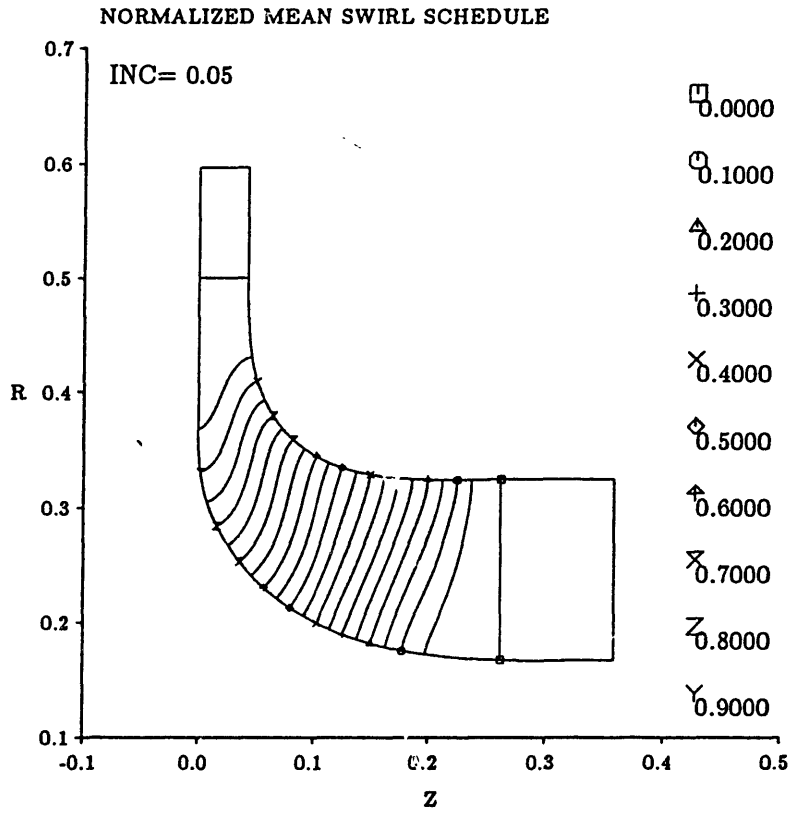


Fig. 6.6d The distribution of $r\bar{V}_\theta$ for case d

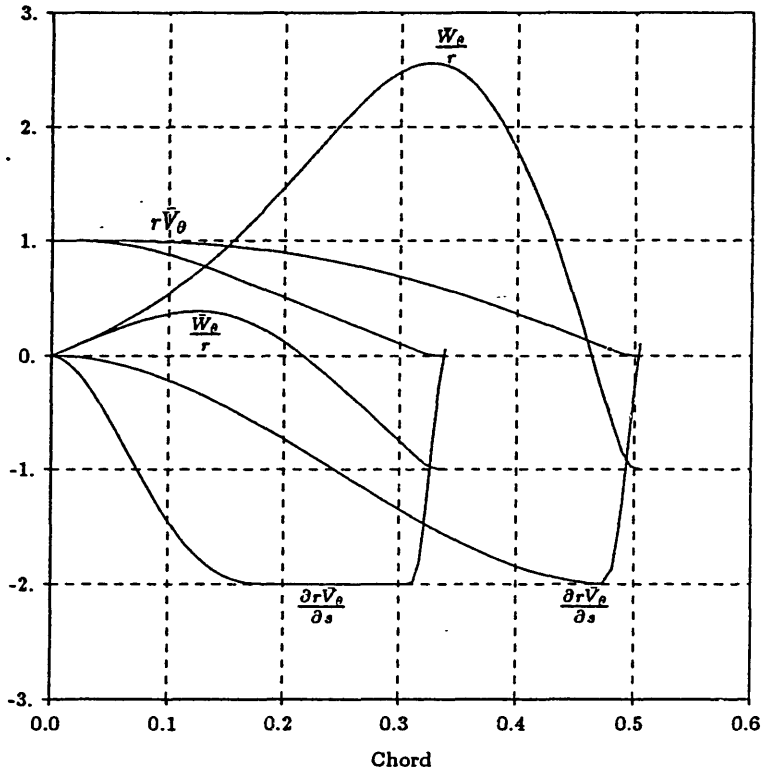


Fig. 6.5e The distribution of $r\bar{V}_\theta, \frac{W_\theta}{r}, and \frac{\partial r\bar{V}_\theta}{\partial s}$ along the hub and shroud for case e

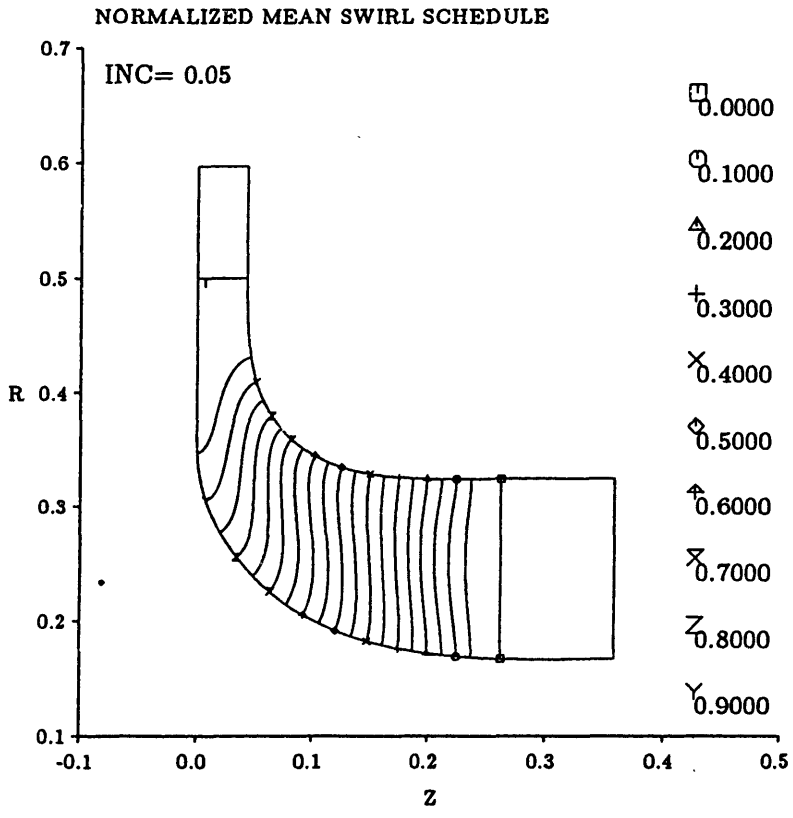


Fig. 6.6e The distribution of $r\bar{V}_\theta$ for case e

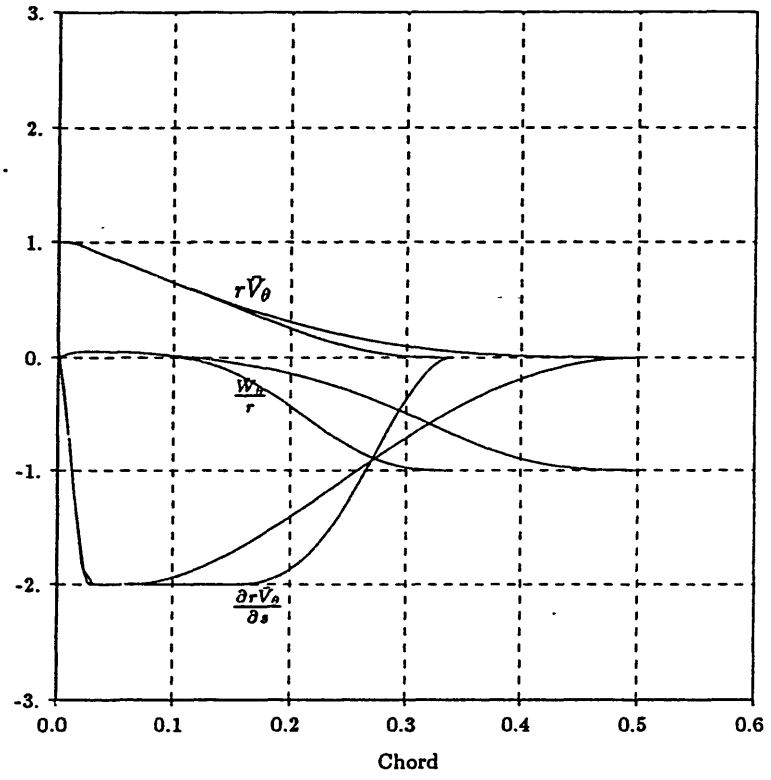


Fig. 6.5f The distribution of $r\bar{V}_\theta, \frac{\bar{W}_\theta}{r}, and \frac{\partial r\bar{V}_\theta}{\partial s}$ along the hub and shroud for case f

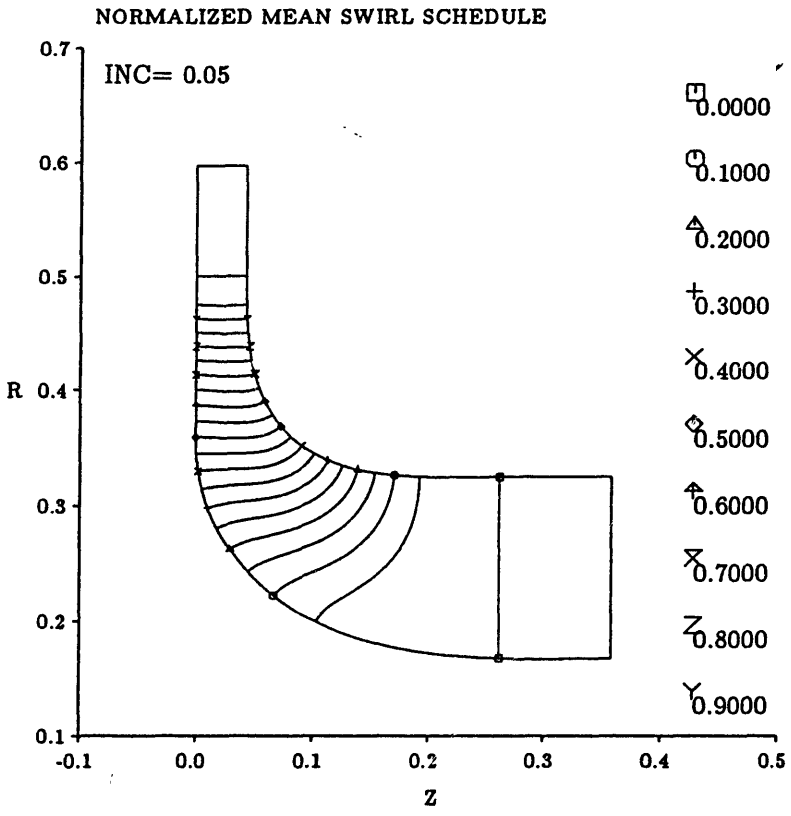


Fig. 6.6f The distribution of $r\bar{V}_\theta$ for case f

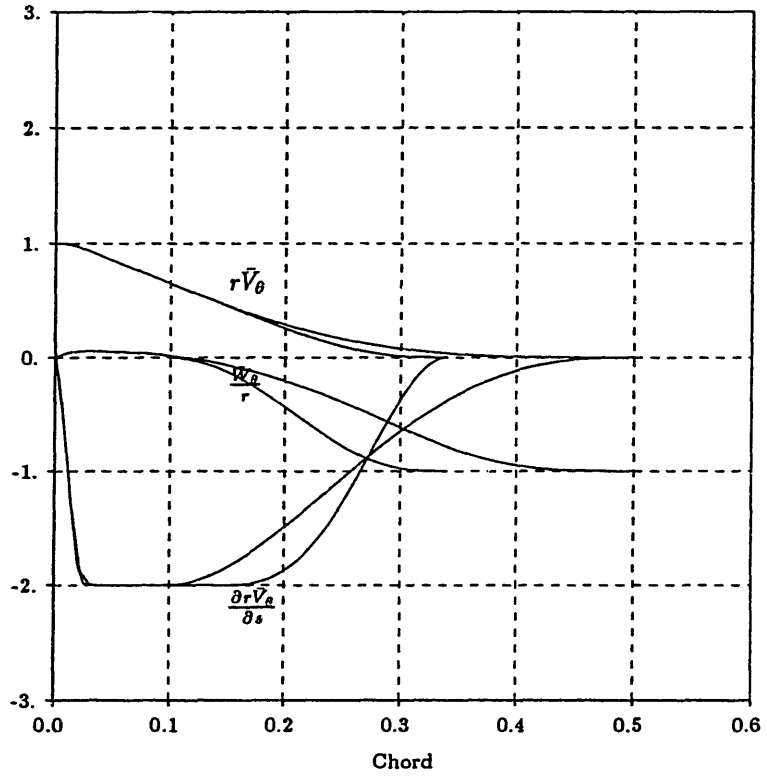


Fig. 6.5g The distribution of $r\bar{V}_\theta, \frac{\bar{W}_\theta}{r}, and \frac{\partial r\bar{V}_\theta}{\partial s}$ along the hub and shroud for case g

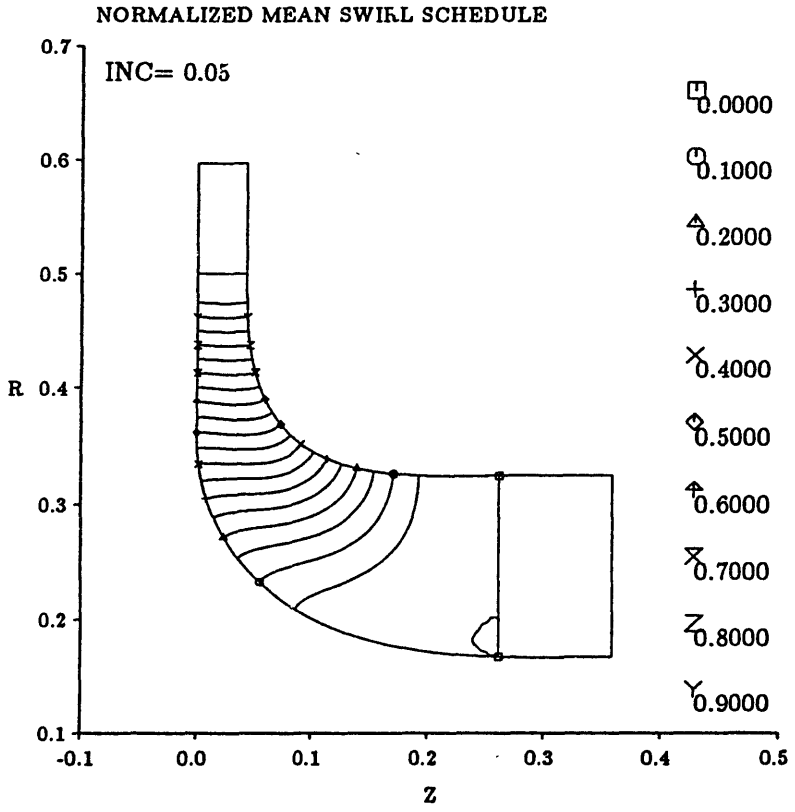


Fig. 6.6g The distribution of $r\bar{V}_\theta$ for case g

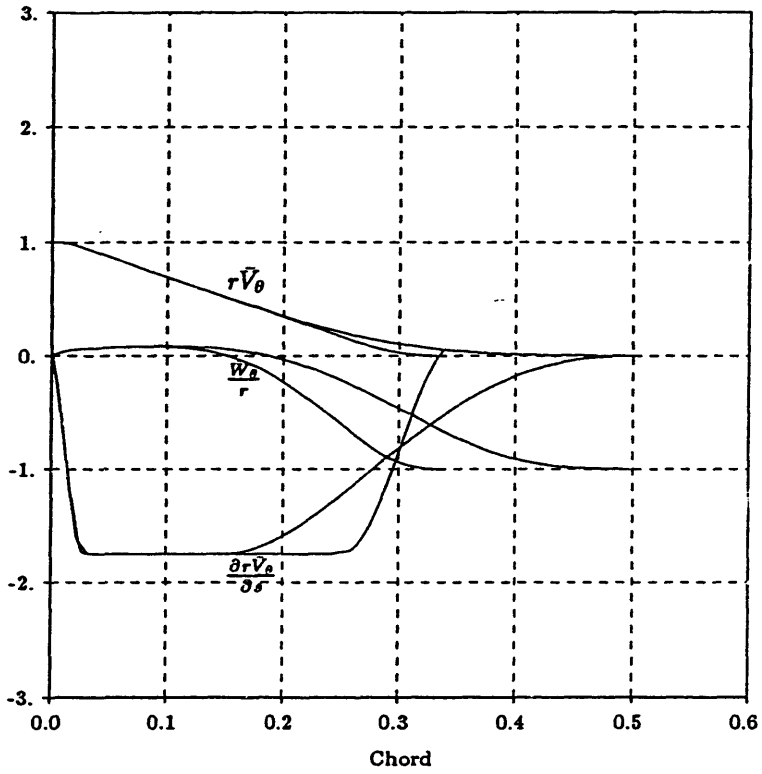


Fig. 6.5h The distribution of $r\bar{V}_\theta, \frac{\bar{W}_\theta}{r}, and \frac{\partial r\bar{V}_\theta}{\partial s}$ along the hub and shroud for case h

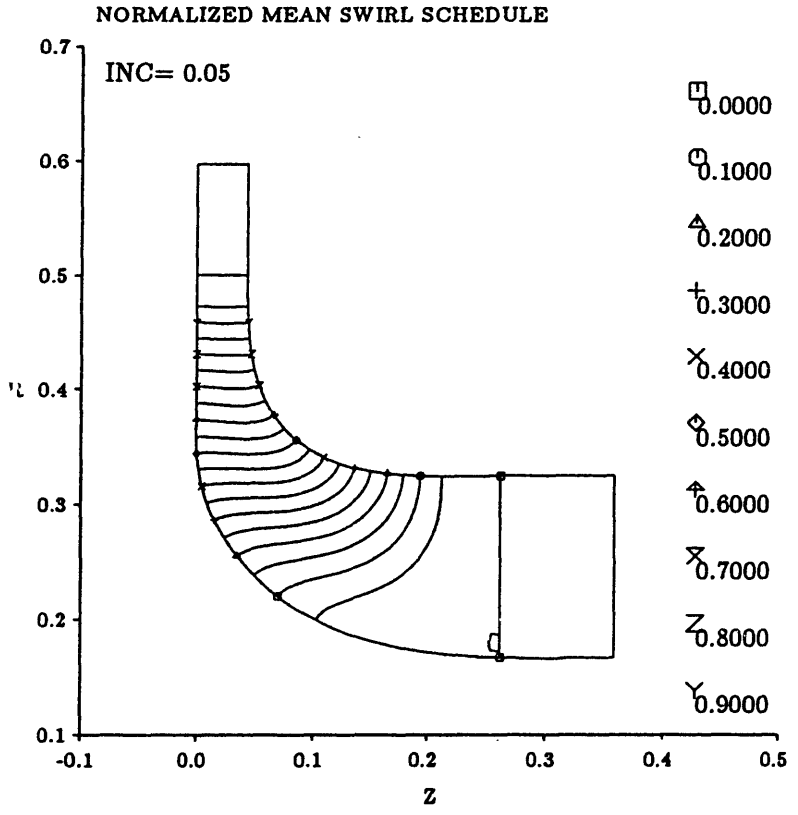


Fig. 6.6h The distribution of $r\bar{V}_\theta$ for case h

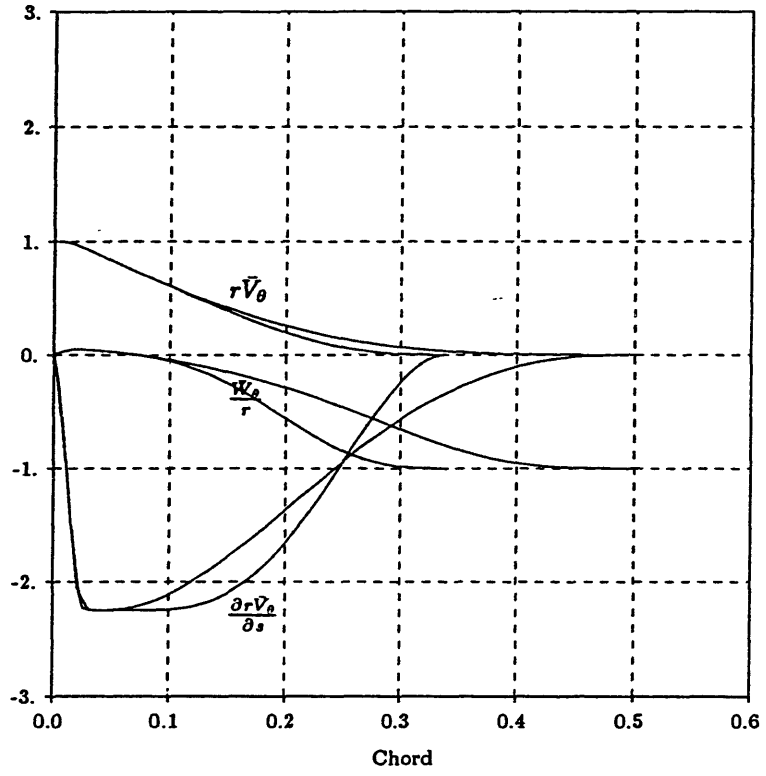


Fig. 6.5i The distribution of $r\bar{V}_\theta, \frac{\bar{W}_\theta}{r}, and \frac{\partial r\bar{V}_\theta}{\partial s}$ along the hub and shroud for case i

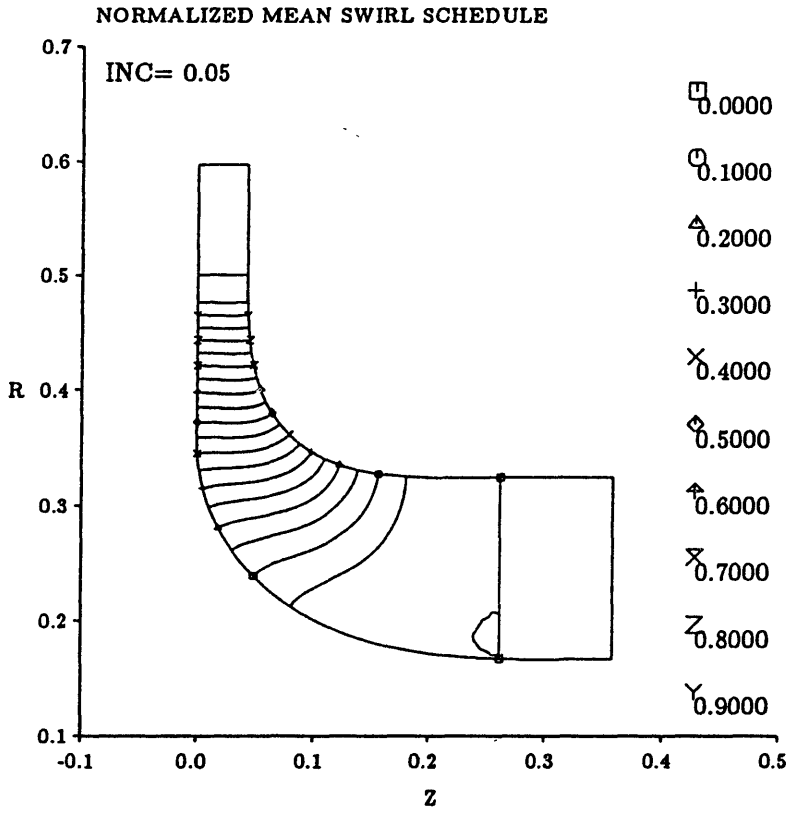


Fig. 6.6i The distribution of $r\bar{V}_\theta$ for case i

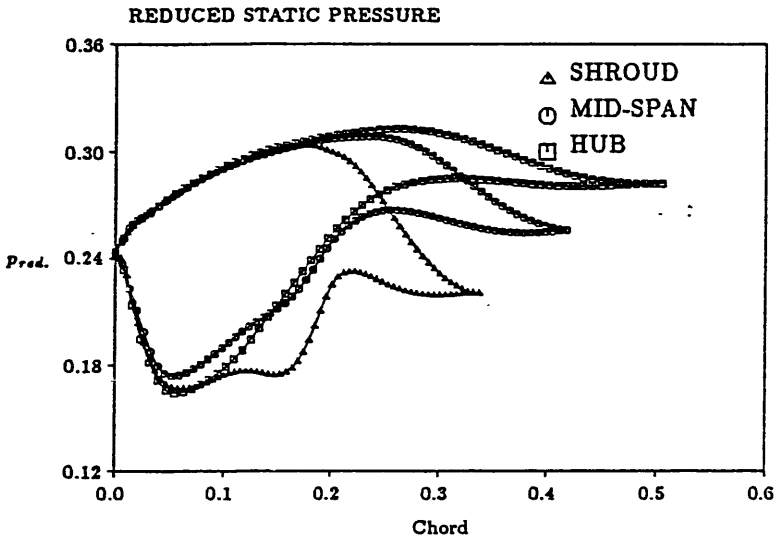


Fig. 6.7a The distribution of $p_{red.}$ for case a

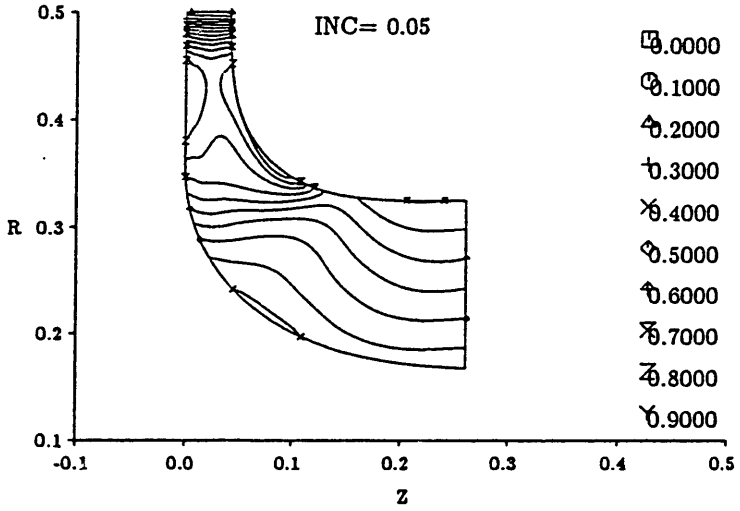


Fig. 6.7b The $M_{rel.}$ on the suction side for case a

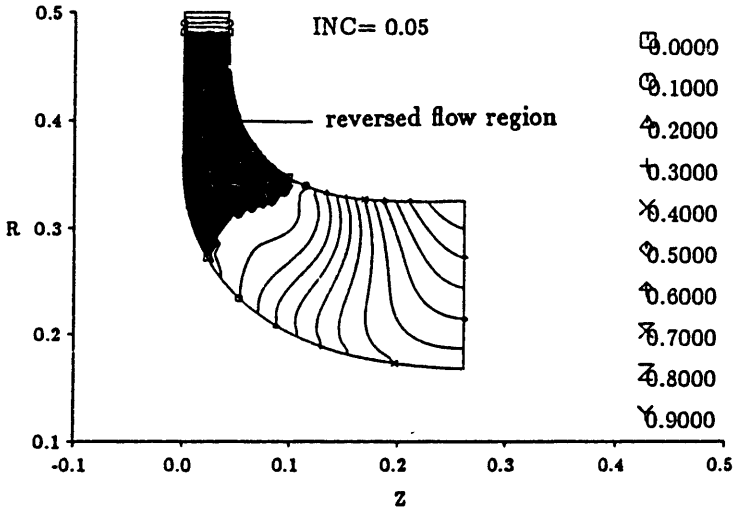


Fig. 6.7c The $M_{rel.}$ on the pressure side for case a

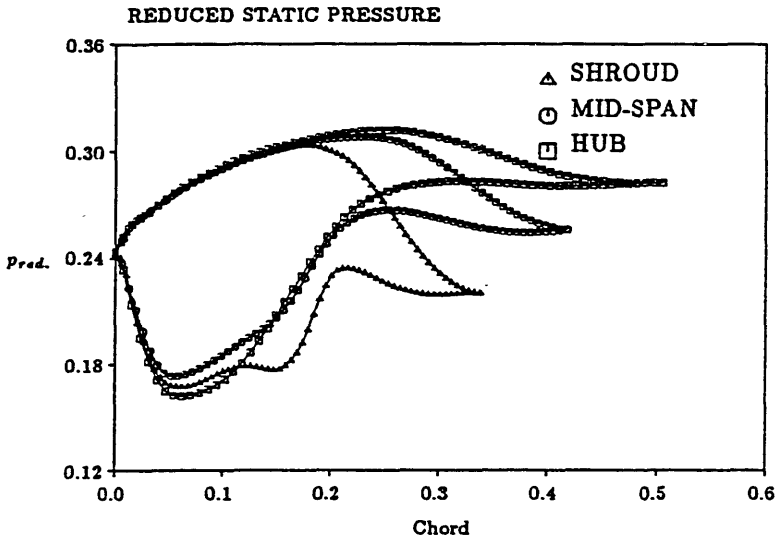


Fig. 6.8a The distribution of $p_{red.}$ for case f

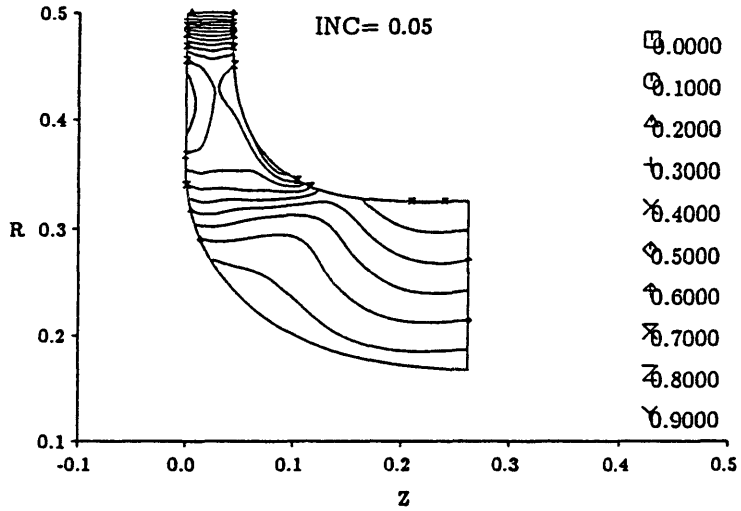


Fig. 6.8b The $M_{rel.}$ on the suction side for case f

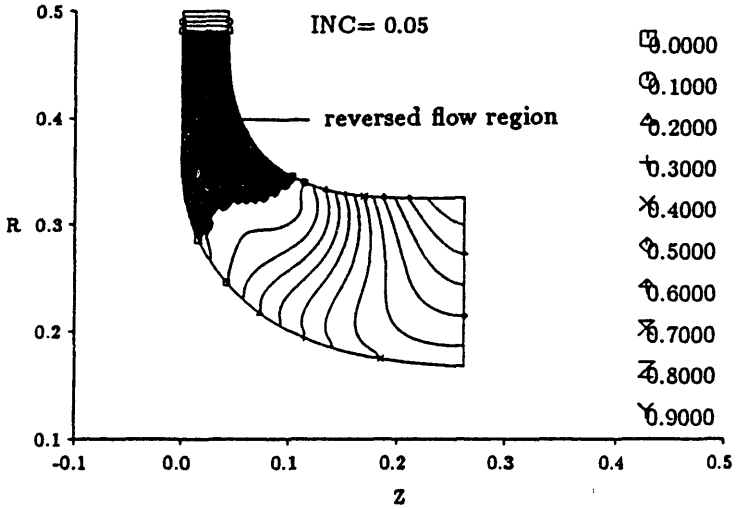


Fig. 6.8c The $M_{rel.}$ on the pressure side for case f

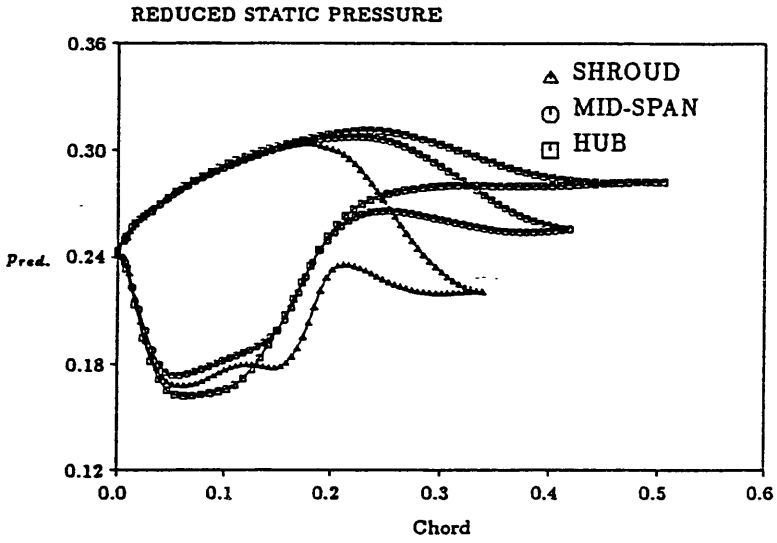


Fig. 6.9a The distribution of $p_{red.}$ for case g

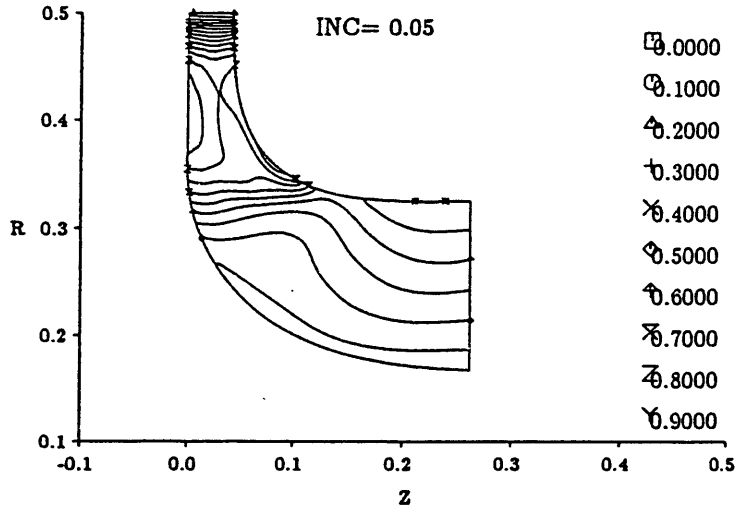


Fig. 6.9b The $M_{rel.}$ on the suction side for case g

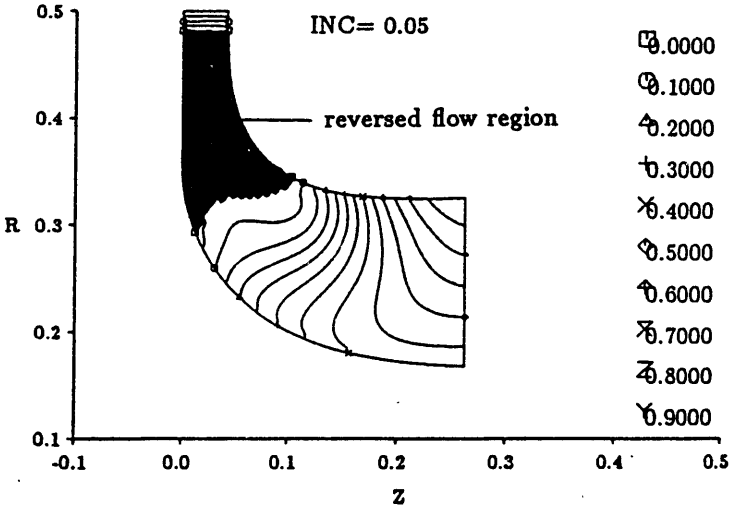


Fig. 6.9c The $M_{rel.}$ on the pressure side for case g

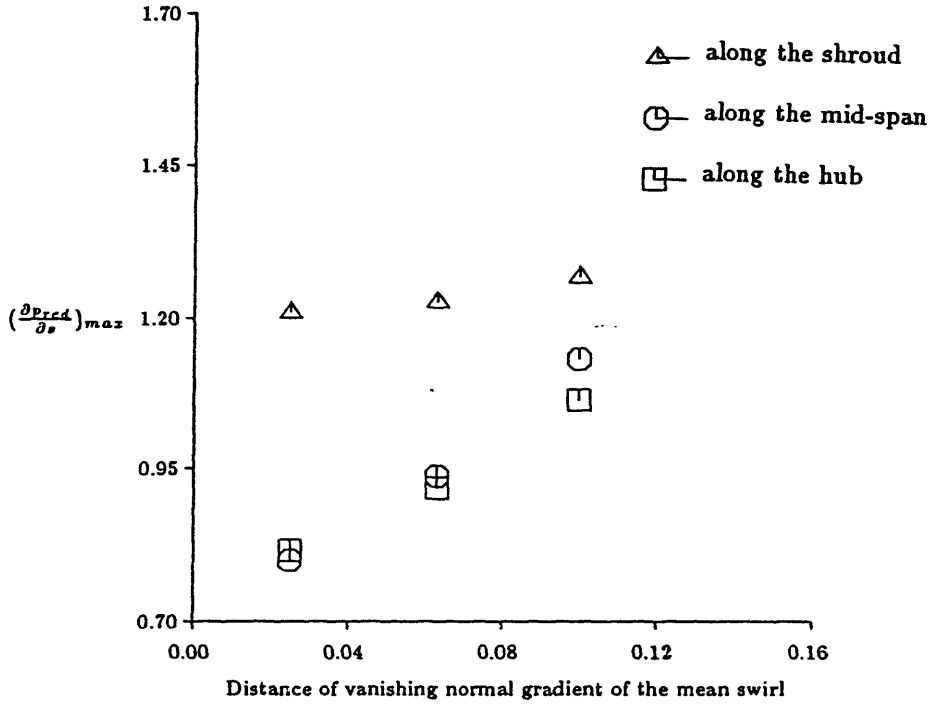


Fig. 6.10a The maximum adverse pressure gradient vs the region of $\frac{\partial r\overline{V}_\theta}{\partial n} = 0$

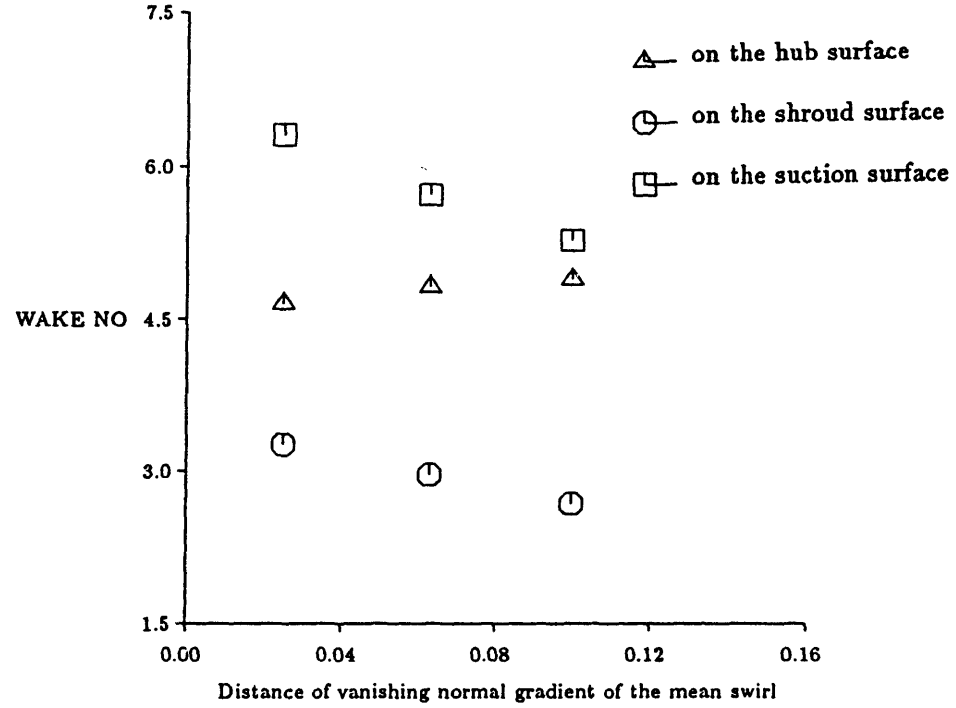


Fig. 6.10b The Wake number vs the region of $\frac{\partial r\overline{V}_\theta}{\partial n} = 0$

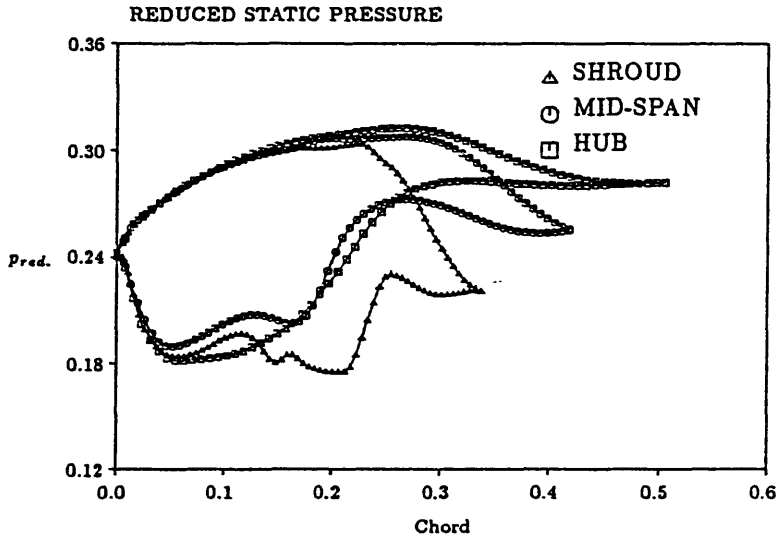


Fig. 6.11a The distribution of $p_{red.}$ for case h

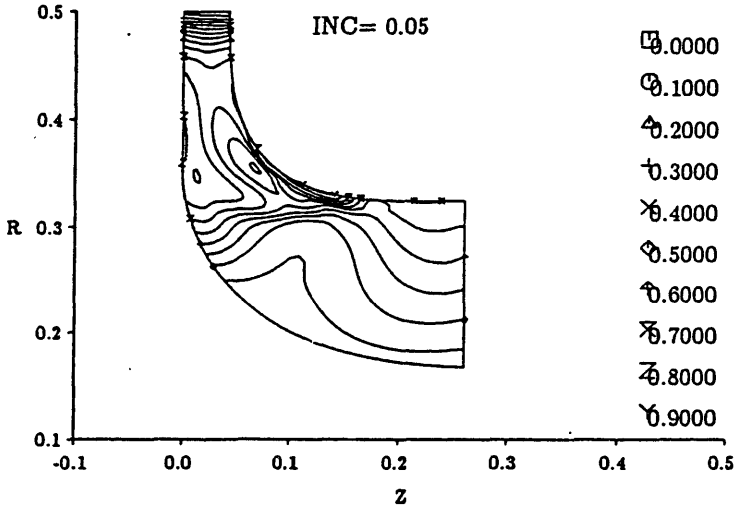


Fig. 6.11b The $M_{rel.}$ on the suction side for case h

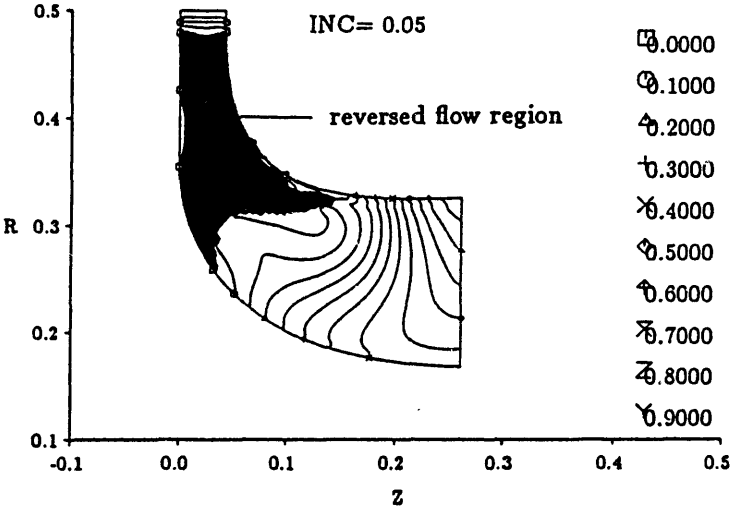


Fig. 6.11c The $M_{rel.}$ on the pressure side for case h

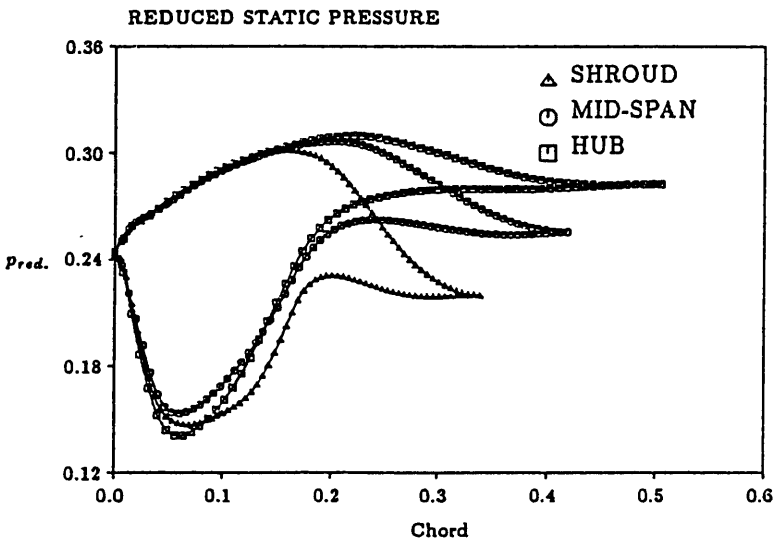


Fig. 6.12a The distribution of $p_{red.}$ for case i

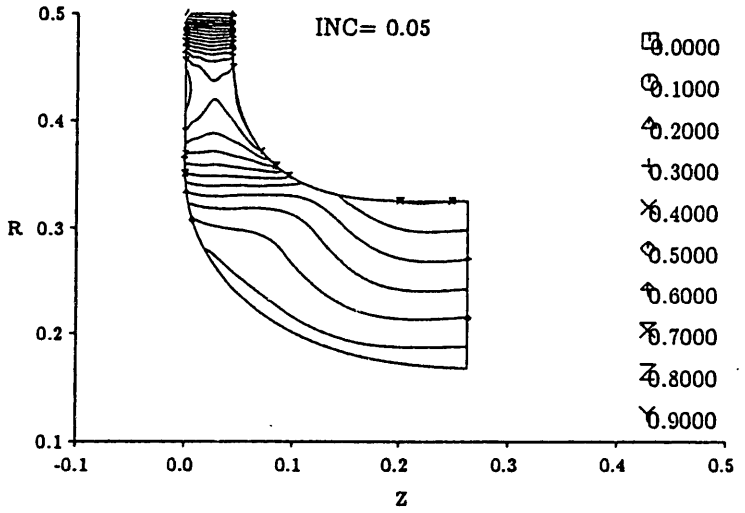


Fig. 6.12b The $M_{rel.}$ on the suction side for case i

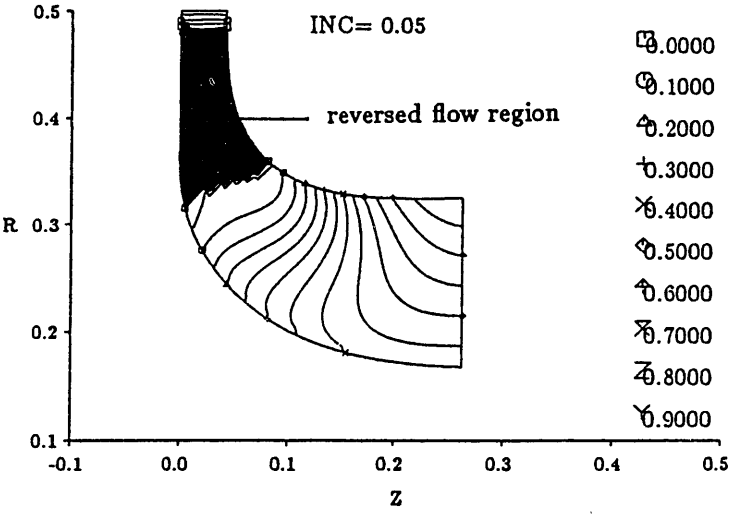


Fig. 6.12c The $M_{rel.}$ on the pressure side for case i

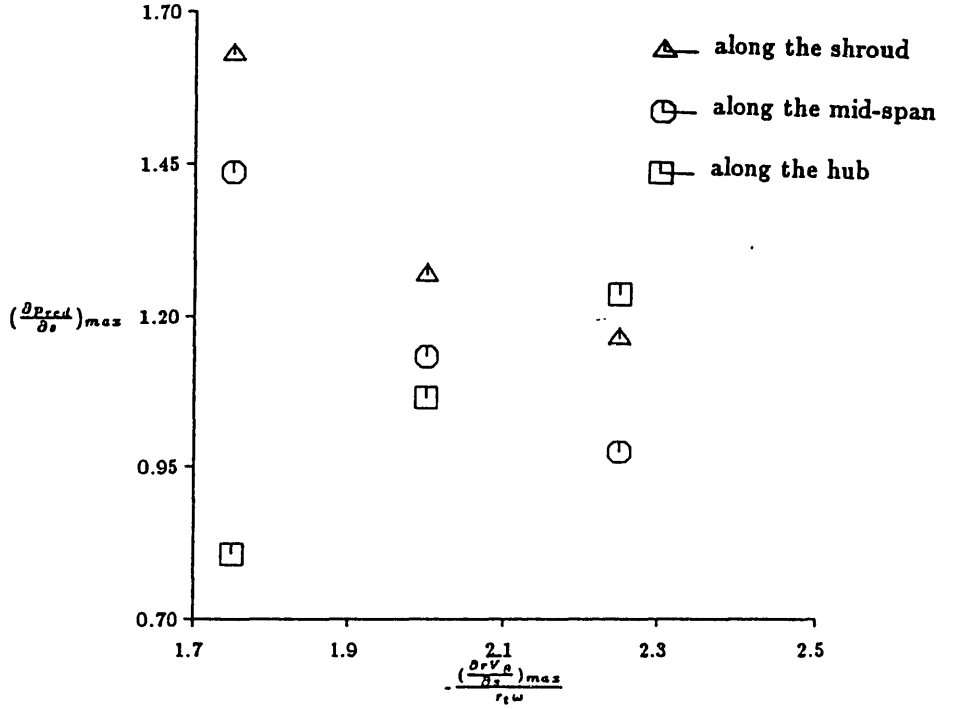


Fig. 6.13a The maximum adverse pressure gradient verse the maximum loading $\frac{(\frac{\partial r\overline{V}_\beta}{\partial n})_{max}}{r_t\omega}$

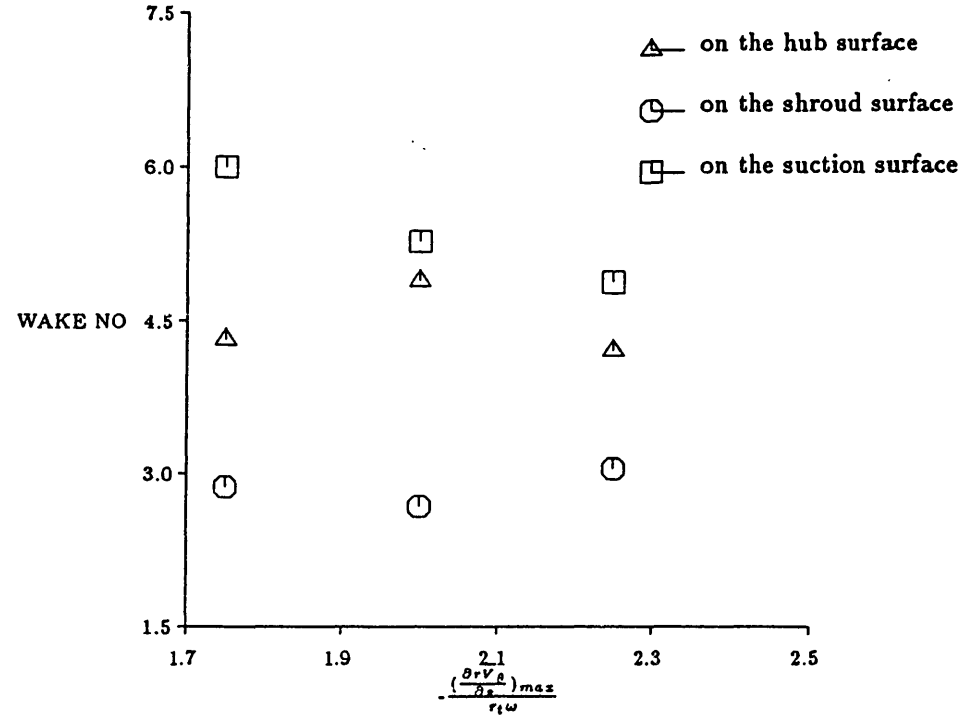


Fig. 6.13b The Wake number verse the maximum loading $\frac{(\frac{\partial r\overline{V}_\beta}{\partial n})_{max}}{r_t\omega}$

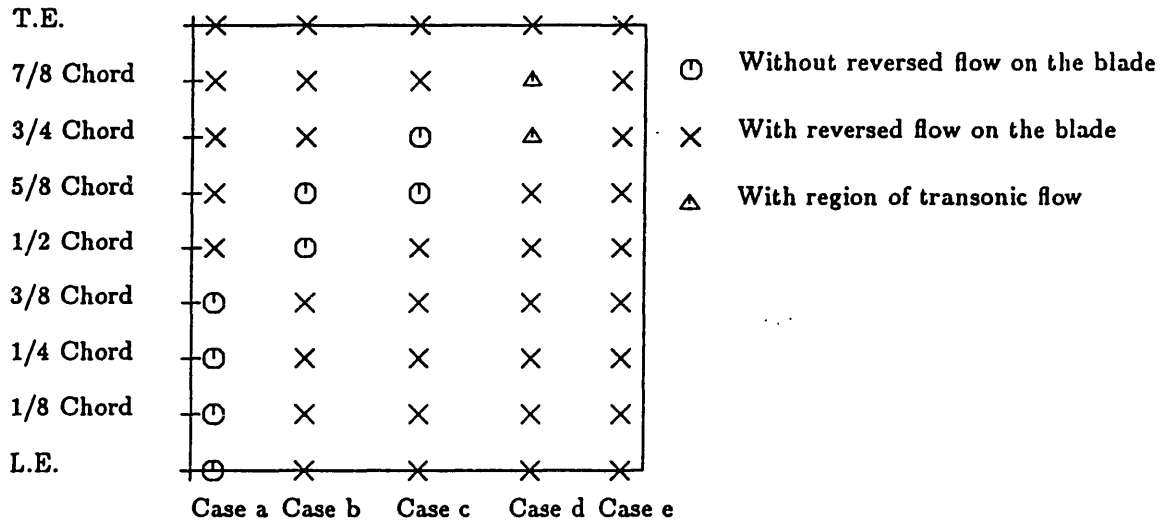


Fig. 6.14a The position of $(\frac{\partial r\bar{V}_\theta}{\partial s})_{max}$ vs stacking position for axisymmetric calculation

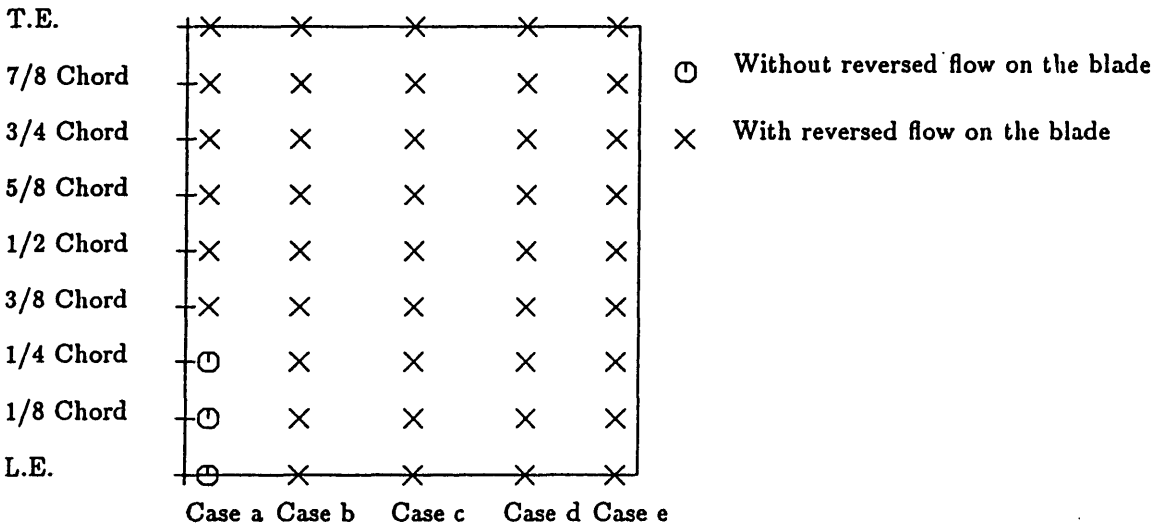


Fig. 6.14b The position of $(\frac{\partial r\bar{V}_\theta}{\partial s})_{max}$ vs stacking position for three-dimensional calculation

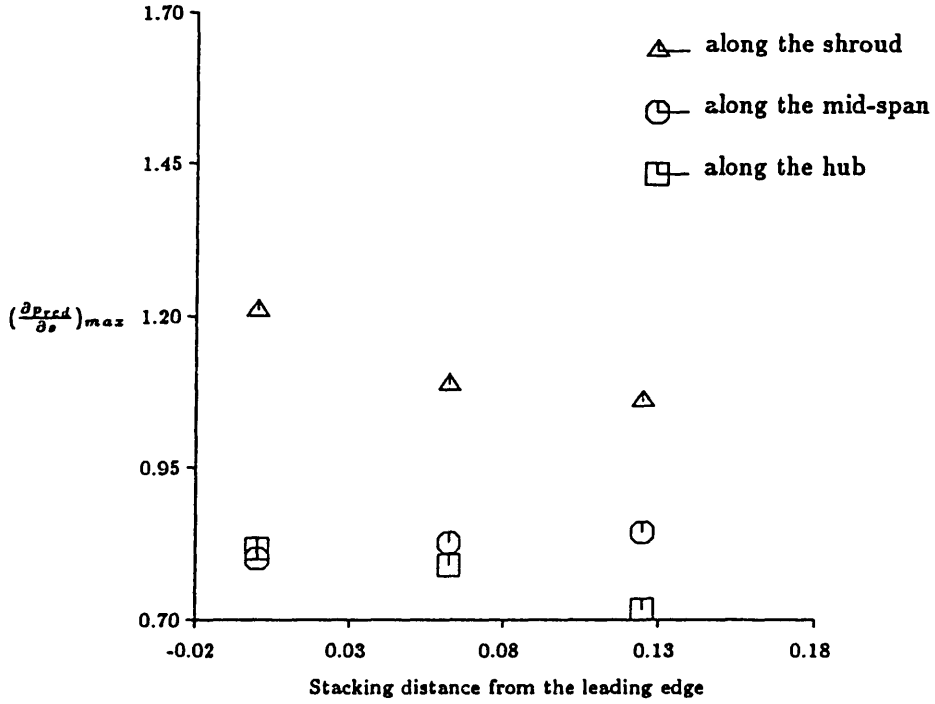


Fig. 6.15a The maximum adverse pressure gradient verse the stacking position

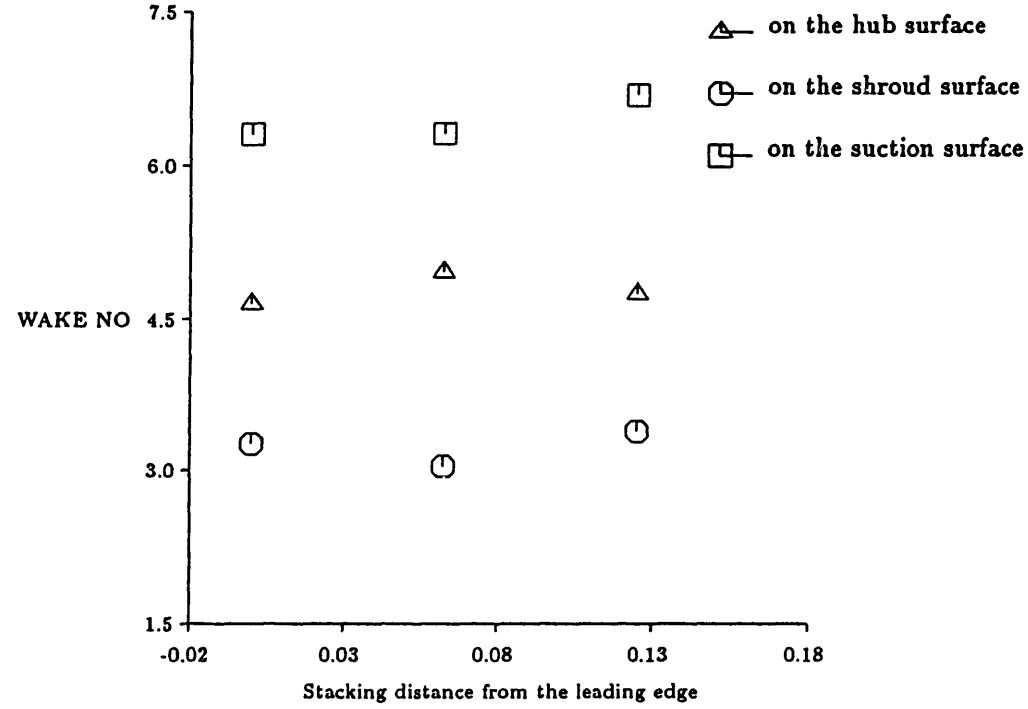


Fig. 6.15b The Wake number verse the stacking position

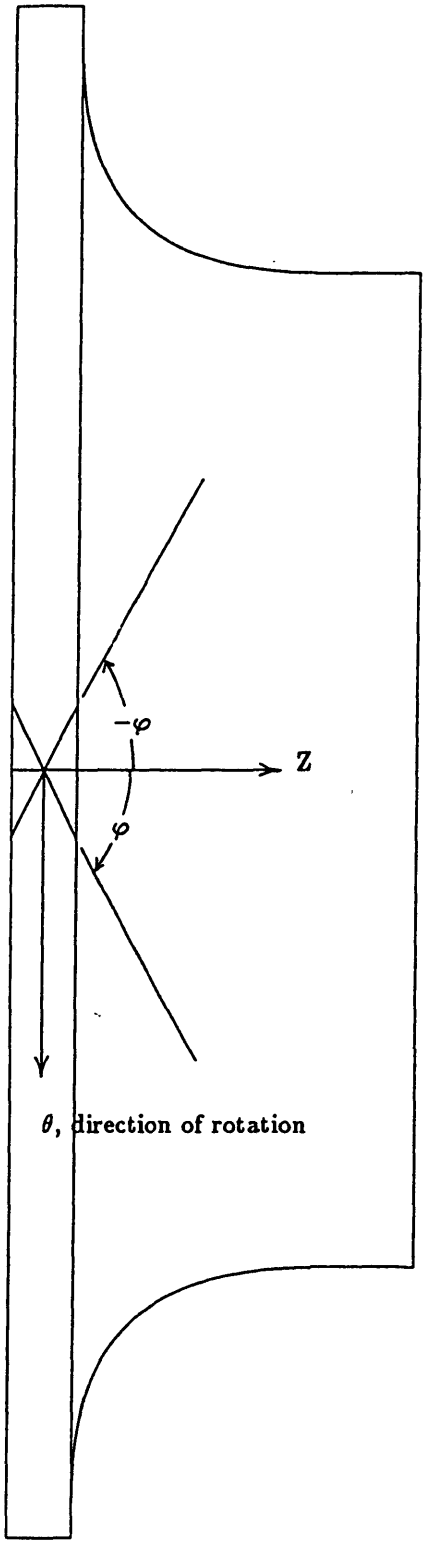


Fig. 6.16 The definition of the lean angle, φ

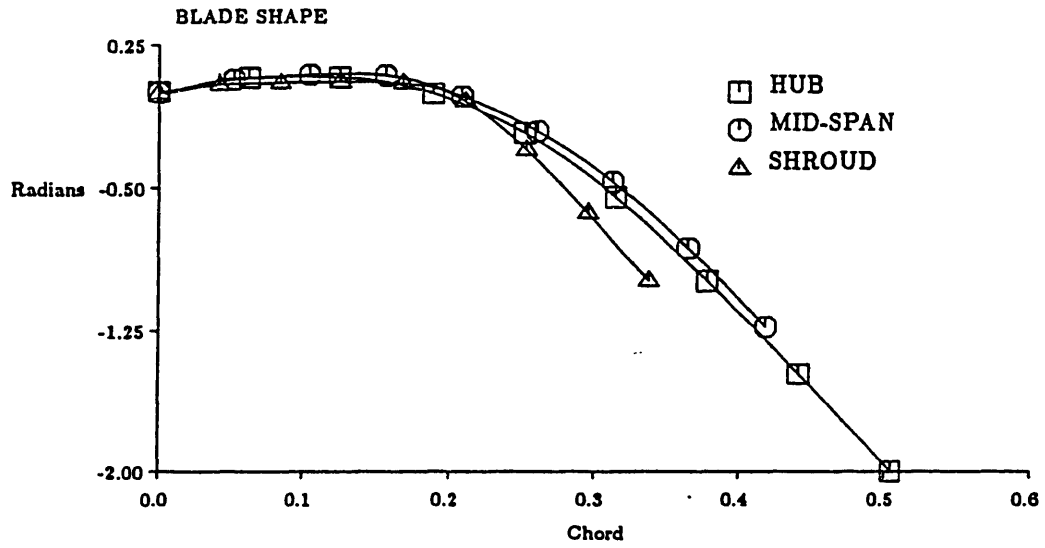


Fig. 6.17a The blade shape for lean angle, $\varphi = -6.65°$

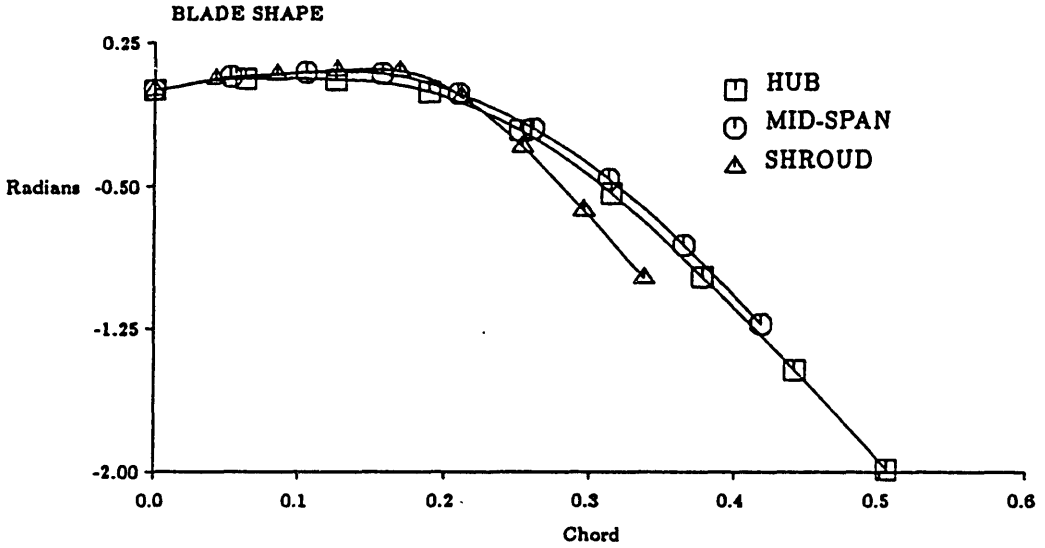


Fig. 6.17b The blade shape for lean angle, $\varphi = 0.00°$

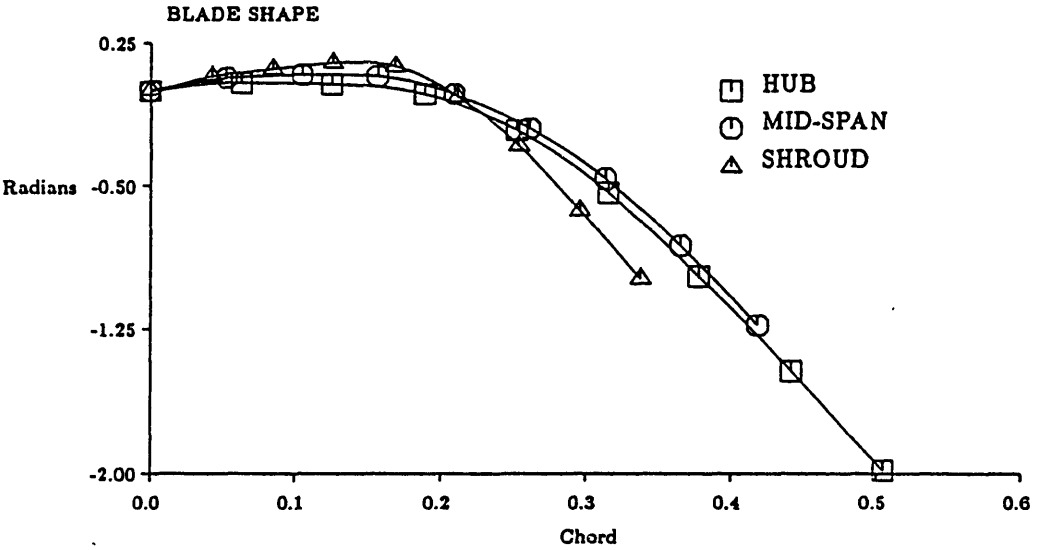


Fig. 6.17c The blade shape for lean angle, $\varphi = 6.65°$

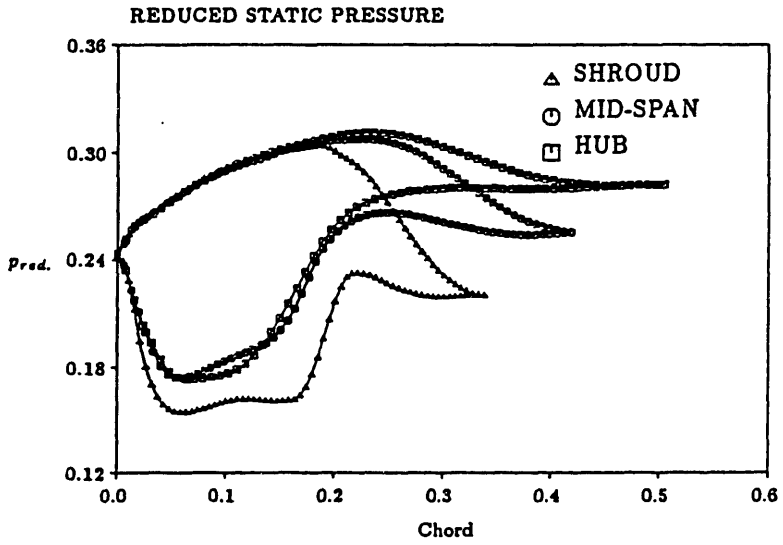


Fig. 6.18a The distribution of $p_{red.}$ with lean angle $\varphi = -6.65°$

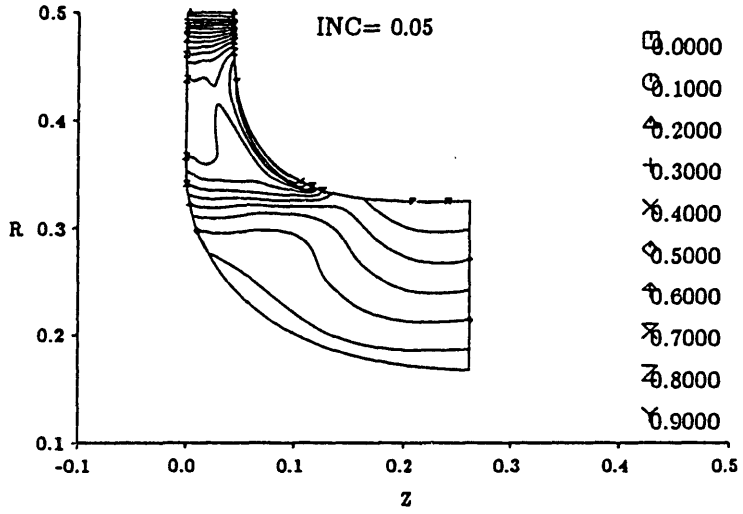


Fig. 6.18b The $M_{rel.}$ on the suction side with lean angle $\varphi = -6.65°$

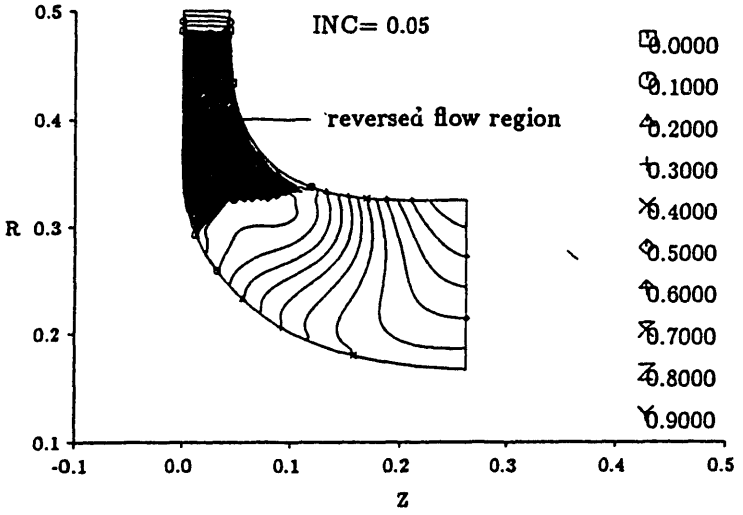


Fig. 6.18c The $M_{rel.}$ on the pressure side with lean angle $\varphi = -6.65°$

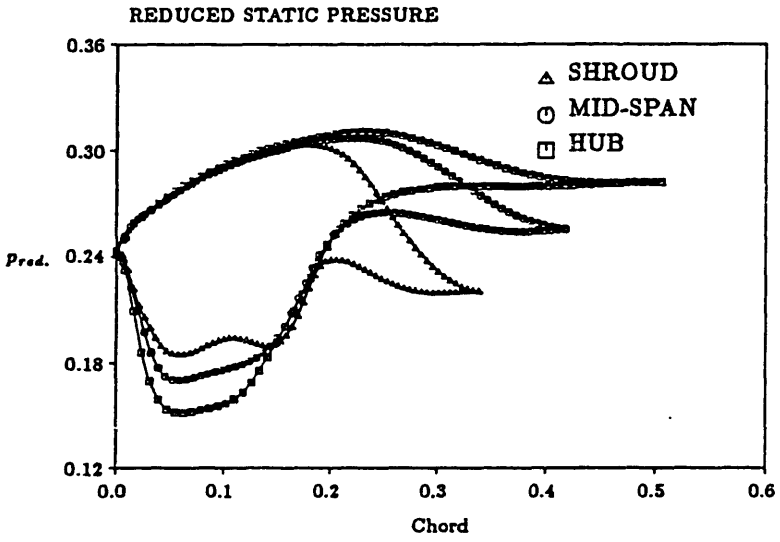


Fig. 6.19a The distribution of $p_{red.}$ with lean angle $\varphi = 6.65°$

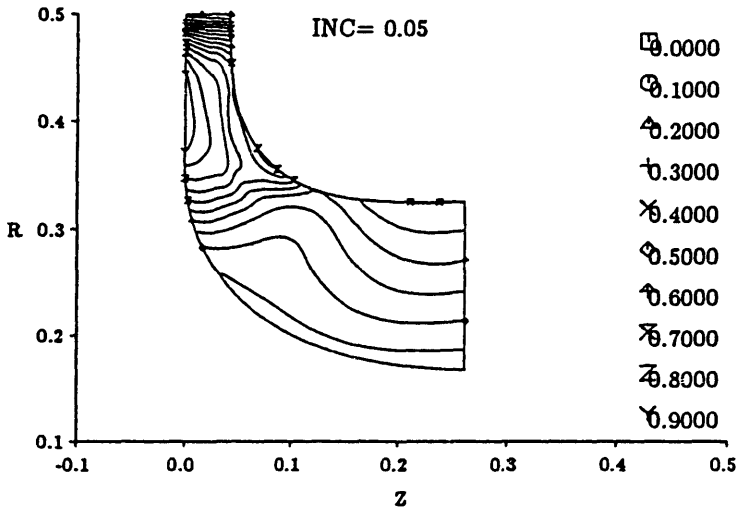


Fig. 6.19b The $M_{rel.}$ on the suction side with lean angle $\varphi = 6.65°$

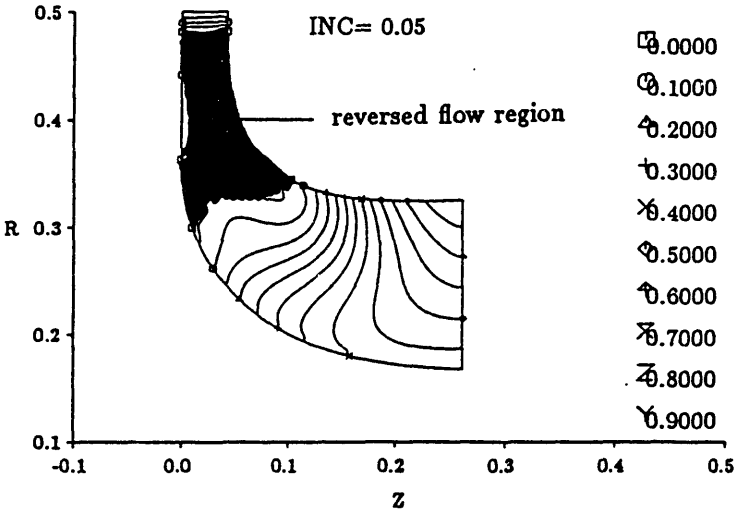


Fig. 6.19c The $M_{rel.}$ on the pressure side with lean angle $\varphi = 6.65°$

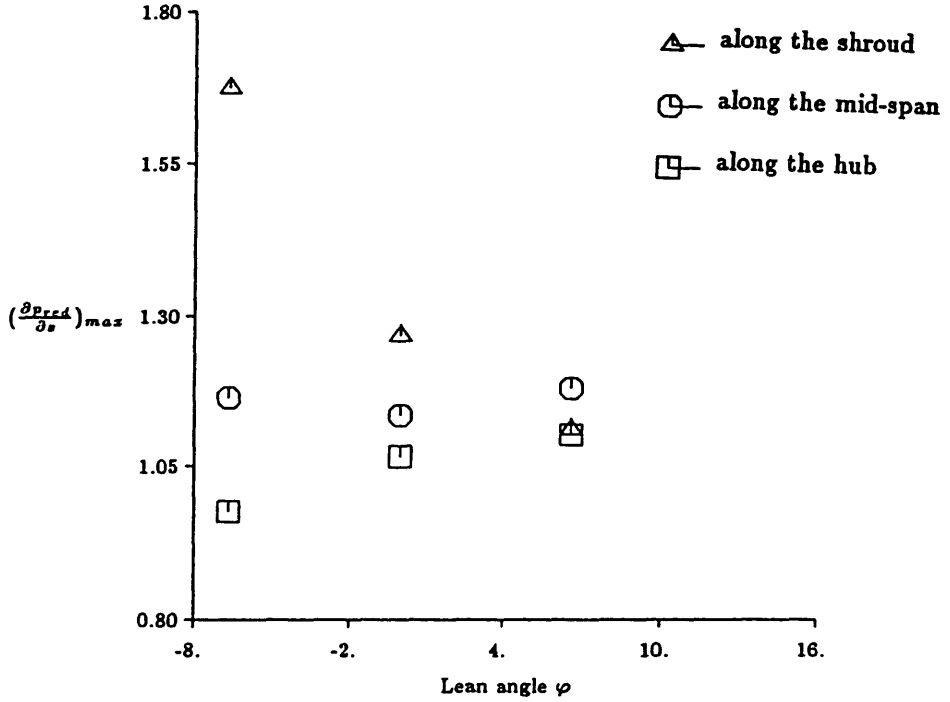


Fig. 6.20a The maximum adverse pressure gradient verse the lean angle

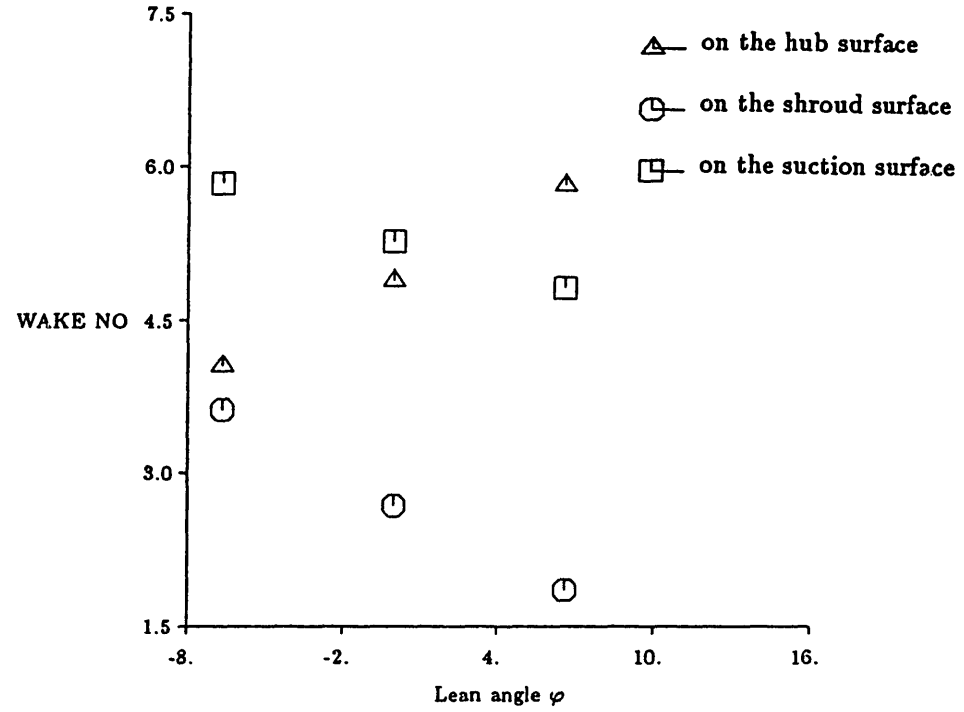


Fig. 6.20b The Wake number verse the lean angle

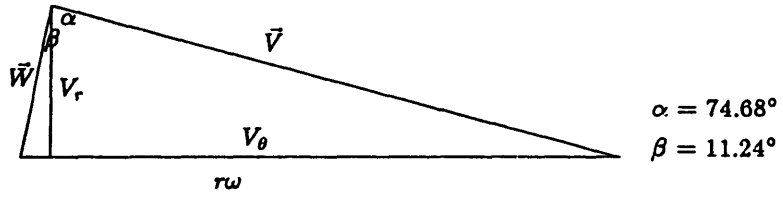


Fig. 6.21a Velocity triangle at leading edge, slip factor = 0.95

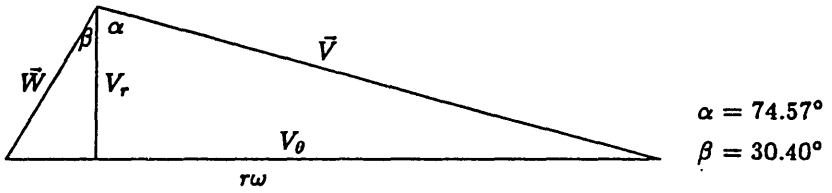


Fig. 6.21b Velocity triangle at leading edge, slip factor = 0.86

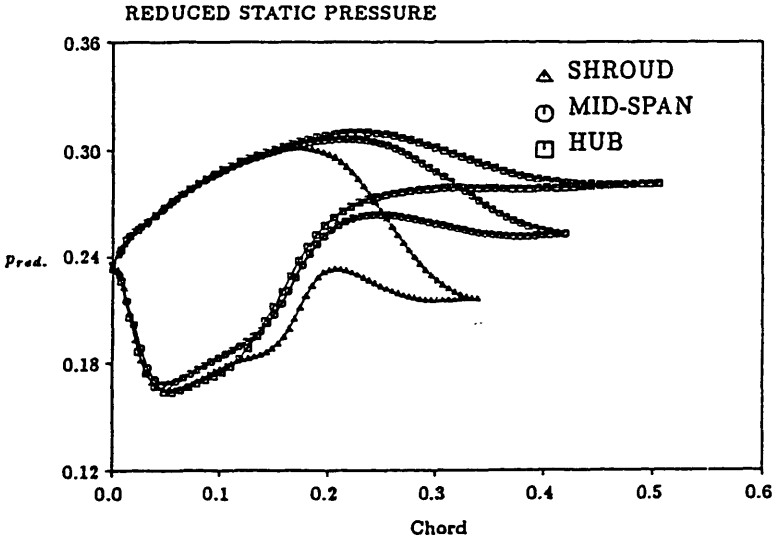


Fig. 6.22a The distribution of $p_{red.}$ for slip factor = 0.95

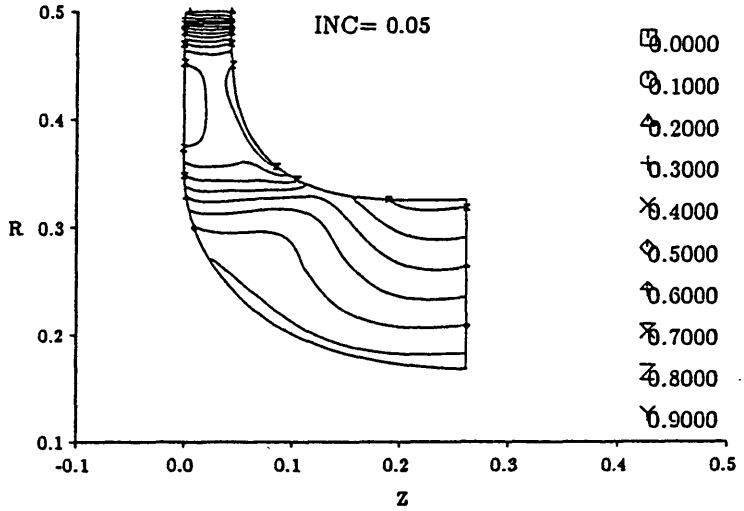


Fig. 6.22b The $M_{rel.}$ on the suction side for slip factor = 0.95

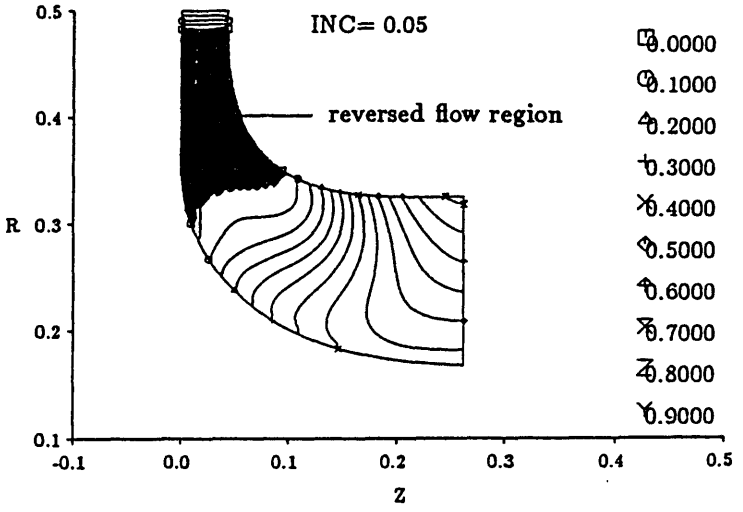


Fig. 6.22c The $M_{rel.}$ on the pressure side for slip factor = 0.95

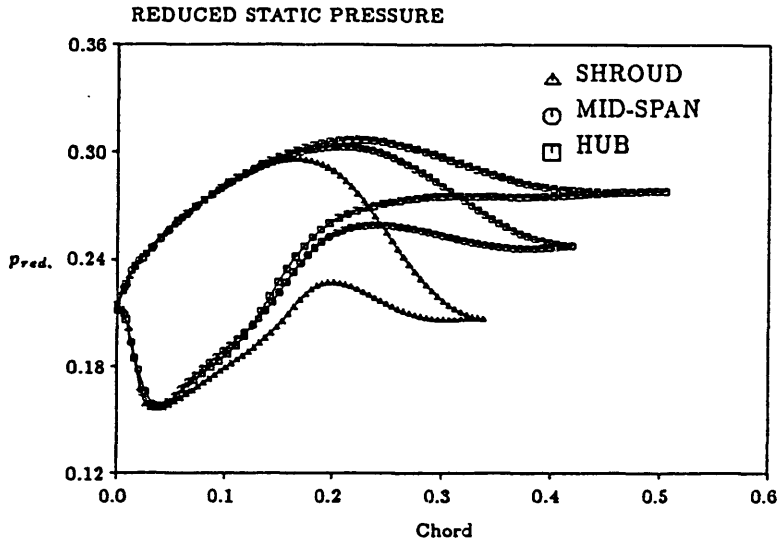


Fig. 6.23a The distribution of $p_{red.}$ for slipt factor = 0.86

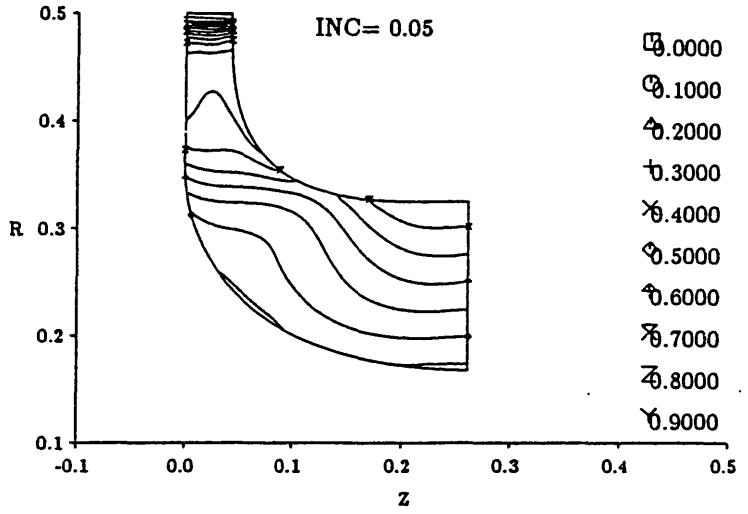


Fig. 6.23b The $M_{rel.}$ on the suction side for slipt factor = 0.86

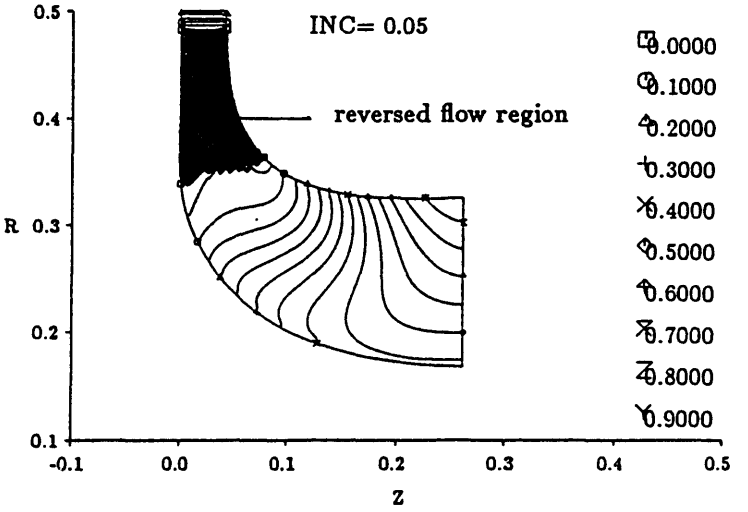


Fig. 6.23c The $M_{rel.}$ on the pressure side for slipt factor = 0.86

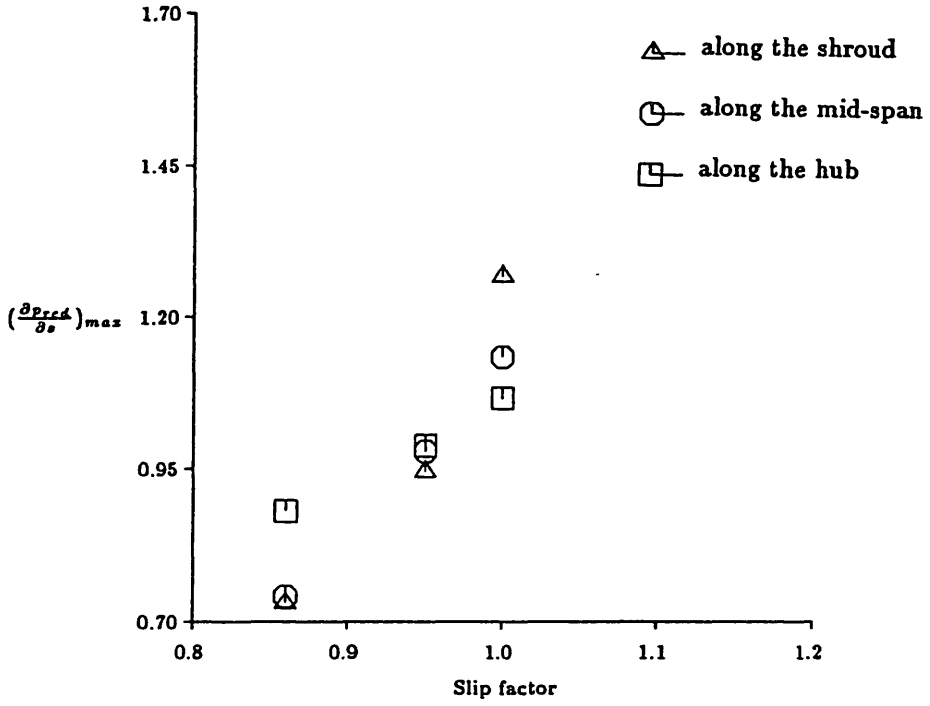


Fig. 6.24a The maximum adverse pressure gradient verse the slip factor

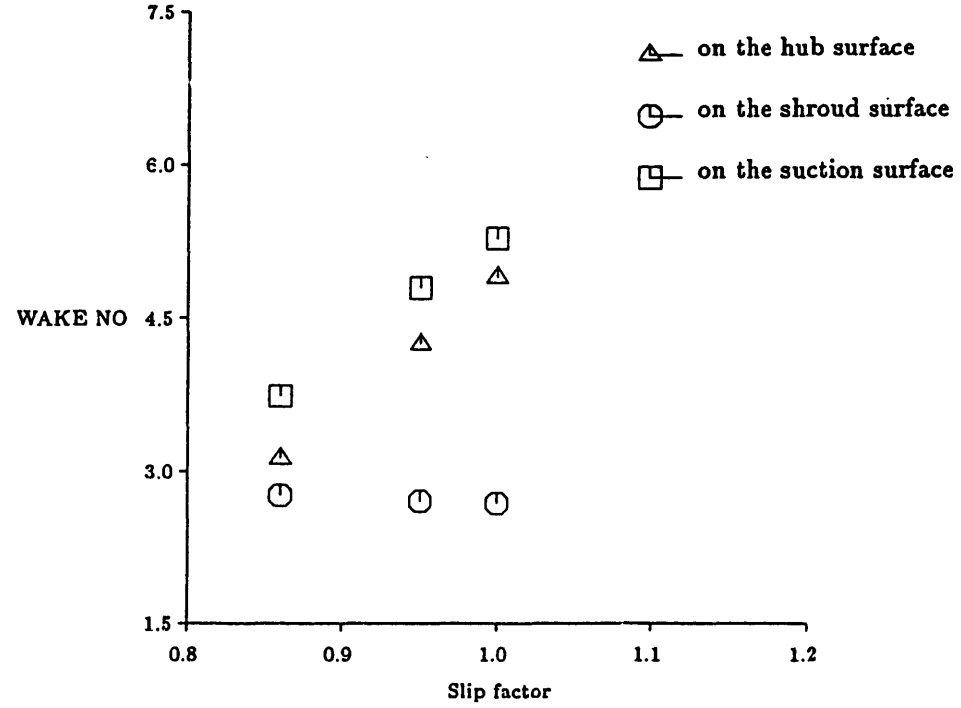


Fig. 6.24b The Wake number verse the slip factor

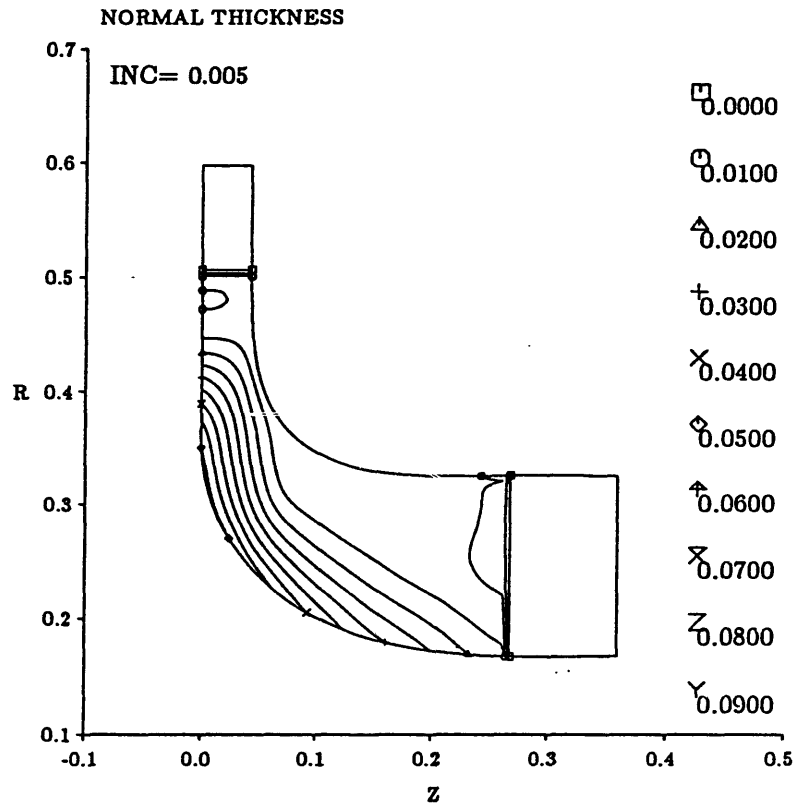


Fig. 6.25a The normal thickness, t_n, for the input

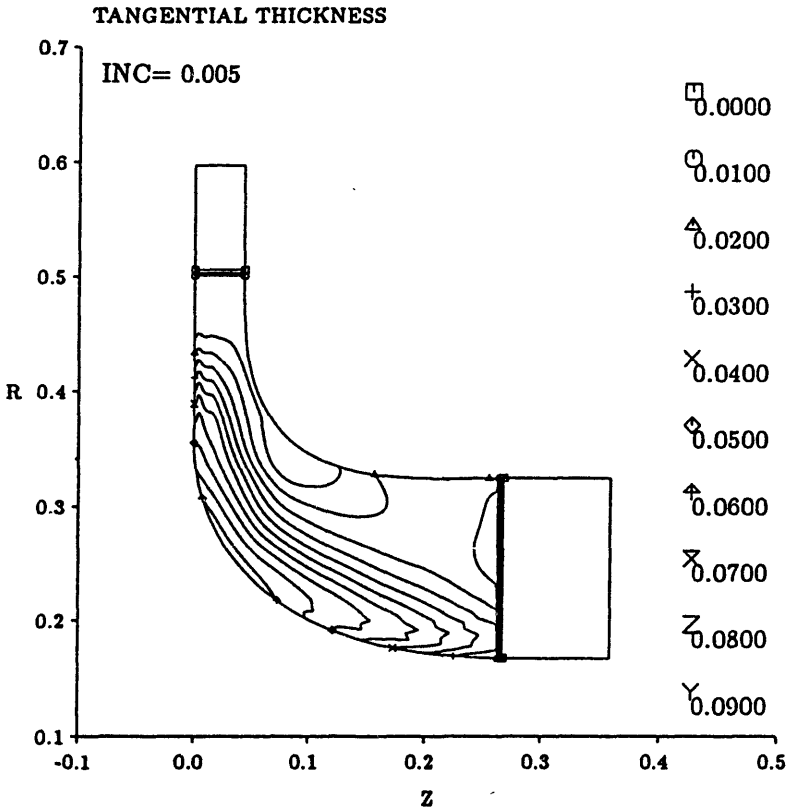


Fig. 6.25b The tangential thickness, t_θ, from the output

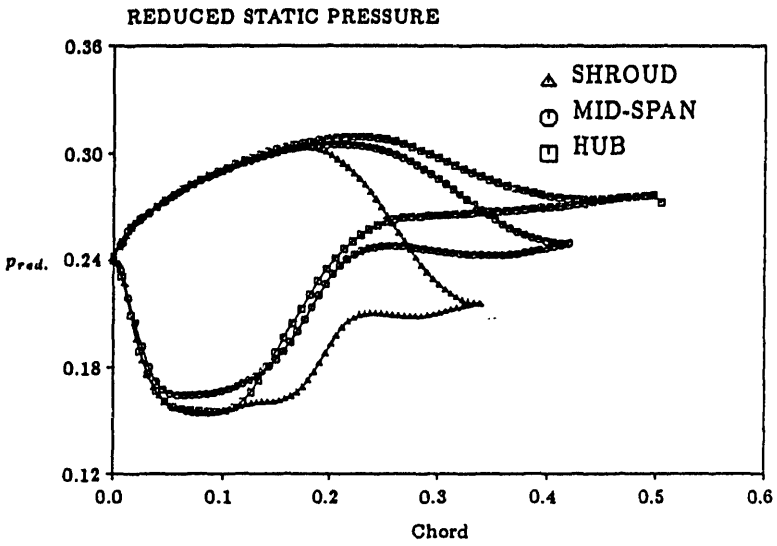


Fig. 6.26a The distribution of $p_{red.}$ for case g, with blockage effects

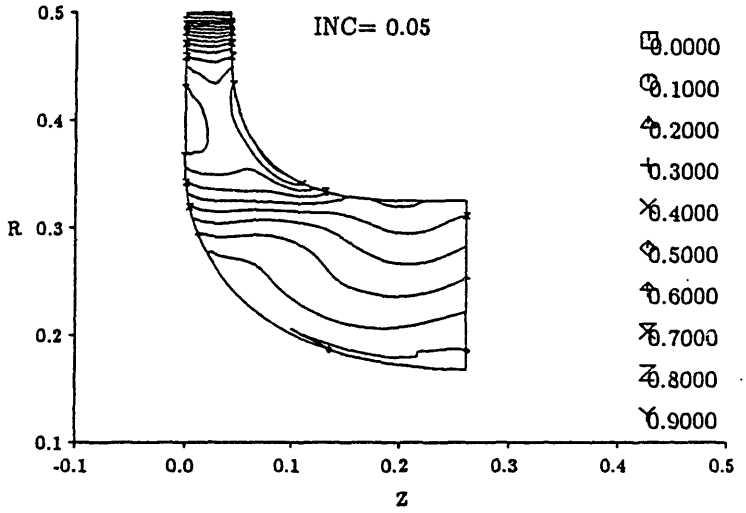


Fig. 6.26b The $M_{rel.}$ on the suction side with blockage effects

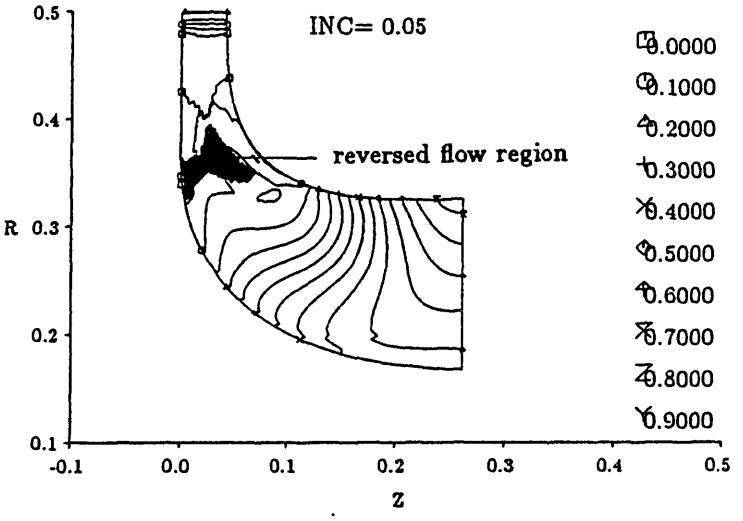


Fig. 6.26c The $M_{rel.}$ on the pressure side with blockage effects

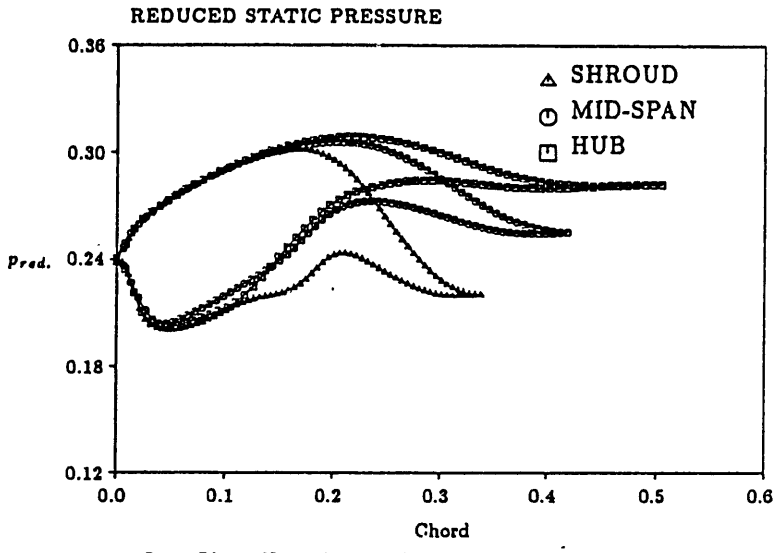


Fig. 6.27a The distribution of $p_{red.}$ for number of blades B = 21

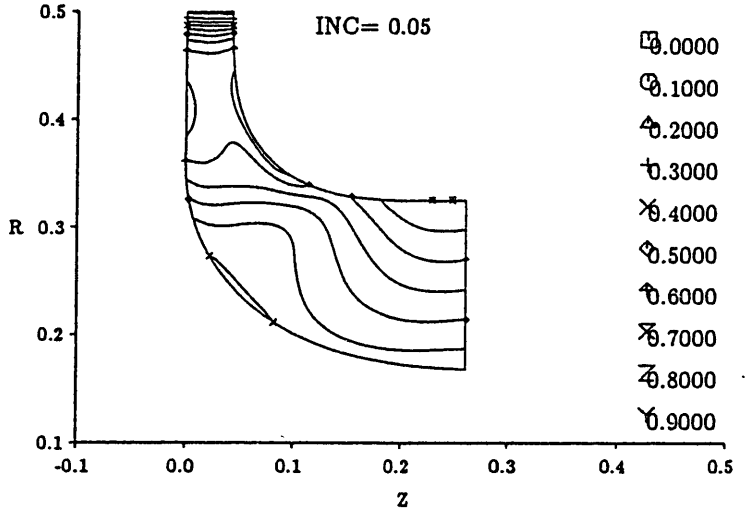


Fig. 6.27b The $M_{rel.}$ on the suction side for number of blades B = 21

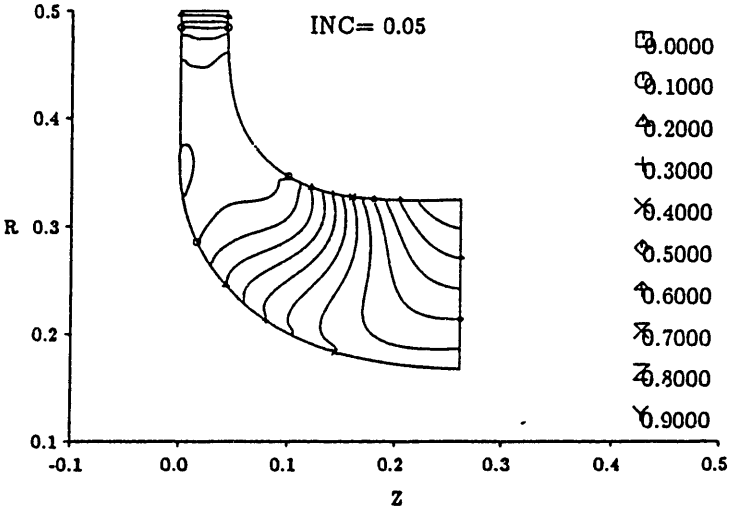


Fig. 6.27c The $M_{rel.}$ on the pressure side for number of blades B = 21

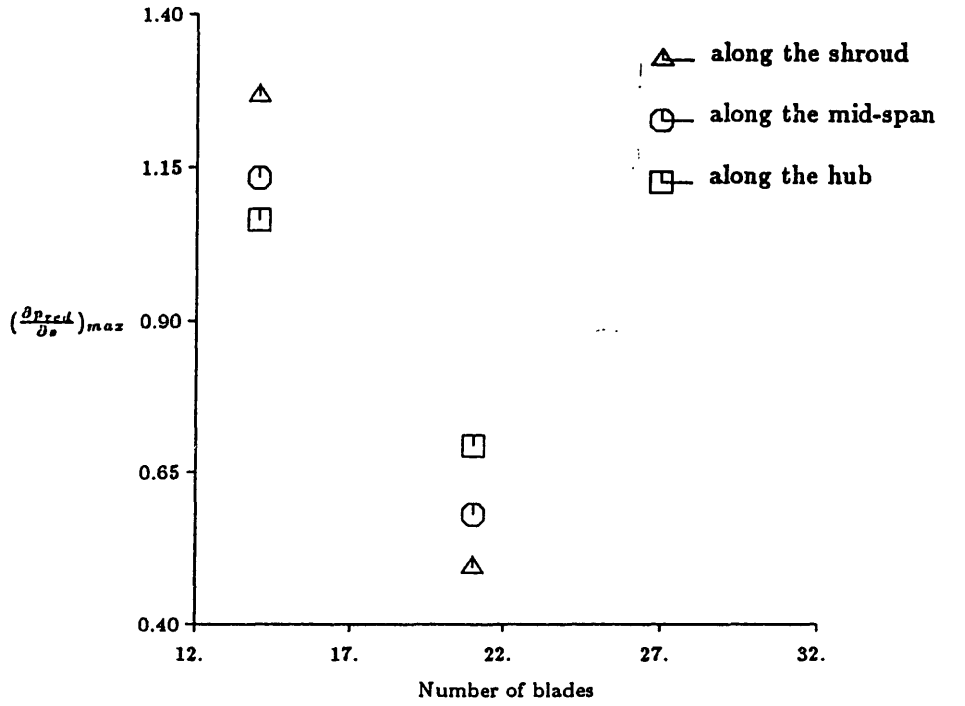


Fig. 6.28a The maximum adverse pressure gradient verse the number of blades

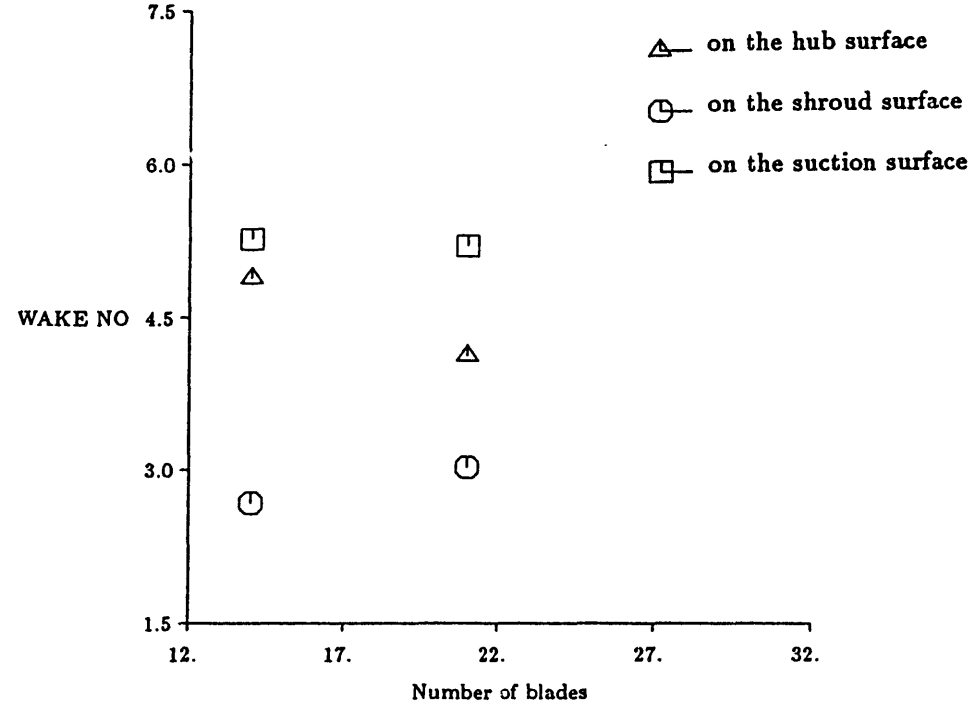


Fig. 6.28b The Wake number verse the number of blades

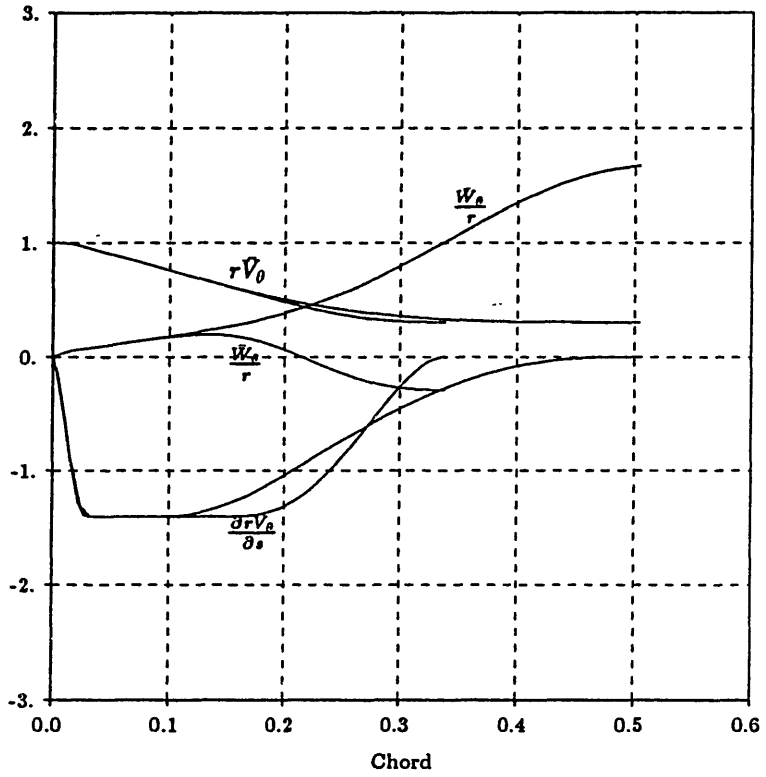


Fig. 6.29a The distribution of $r\bar{V}_\theta, \frac{W_\theta}{r}, and \frac{\partial r\bar{V}_\theta}{\partial s}$ along the hub and shroud with 30% of swirl left after trailing edge

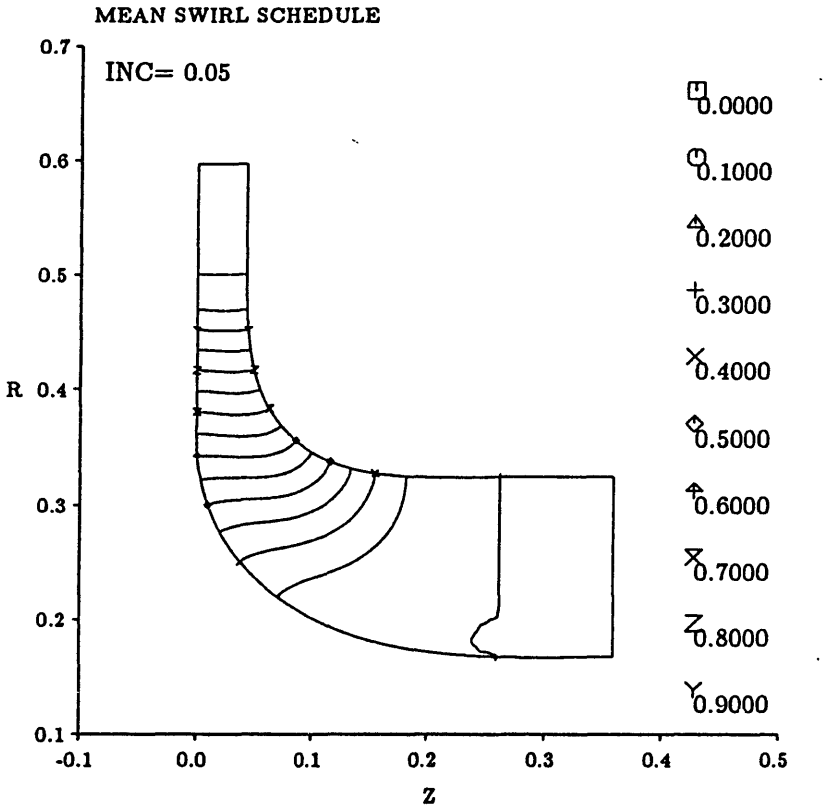


Fig. 6.29b The distribution of $r\bar{V}_\theta$ with 30% of swirl left after trailing edge

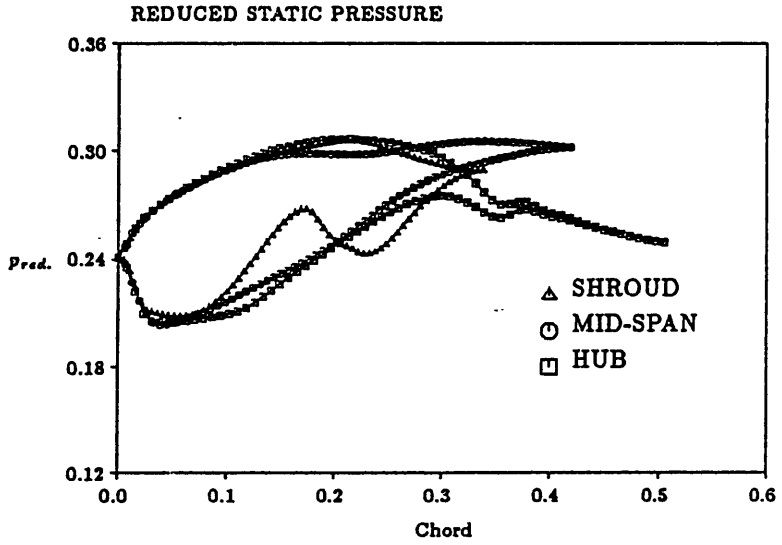


Fig. 6.30a The distribution of $p_{red.}$ with 30% of swirl left

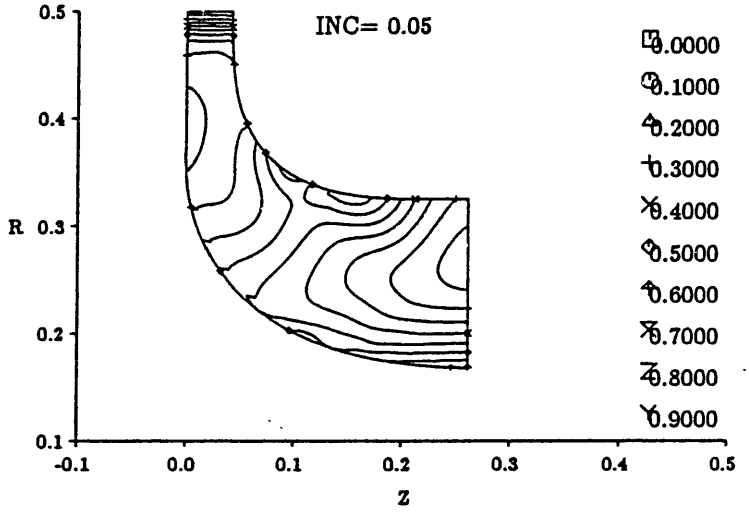


Fig. 6.30b The $M_{rel.}$ on the suction side with 30% of swirl left

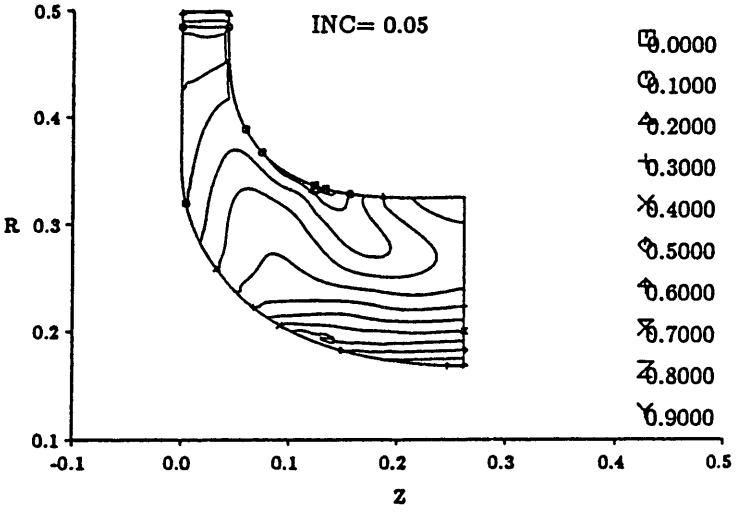


Fig. 6.30c The $M_{rel.}$ on the pressure side with 30% of swirl left

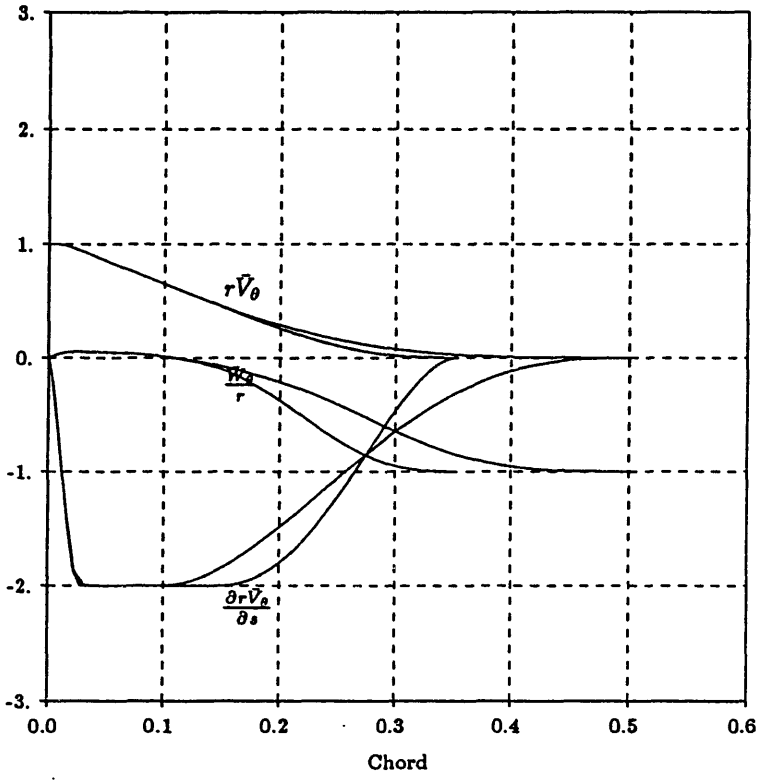


Fig. 6.31a The distribution of $r\bar{V}_\theta, \frac{W_\theta}{r}, and \frac{\partial r\bar{V}_\theta}{\partial s}$ along the hub and shroud

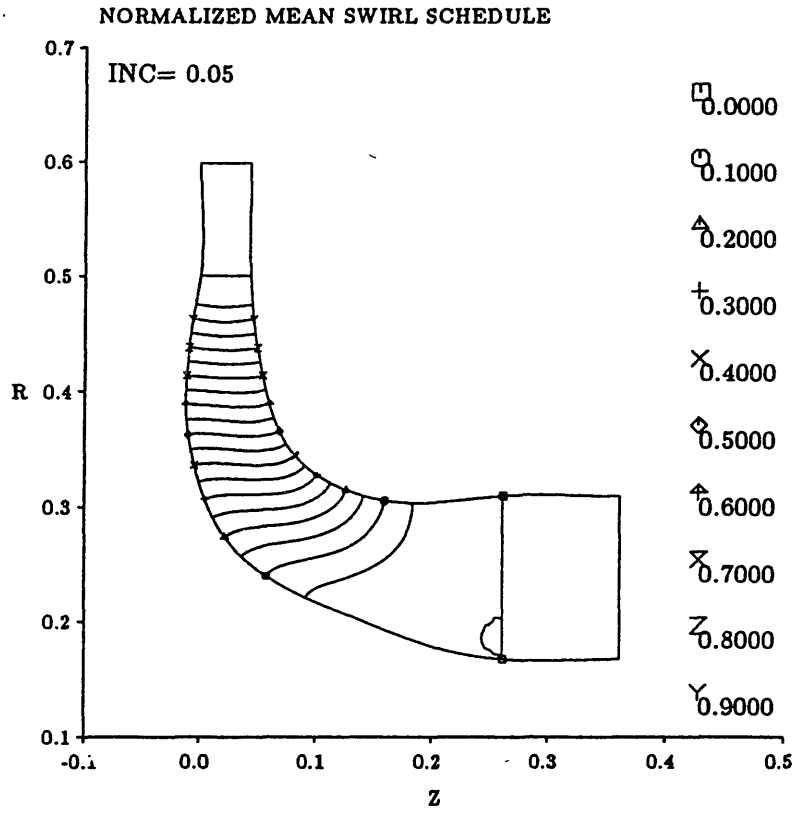


Fig. 6.31b The distribution of $r\bar{V}_\theta$

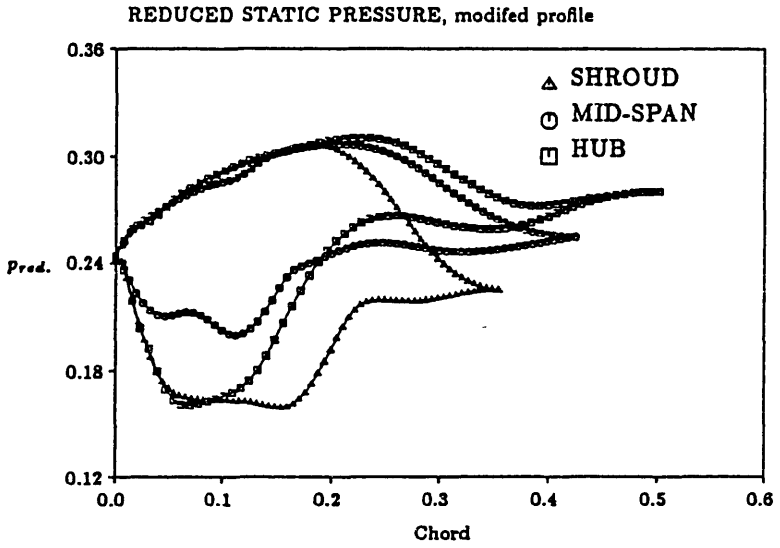


Fig. 6.32a The distribution of $p_{red.}$, stacking at leading edge

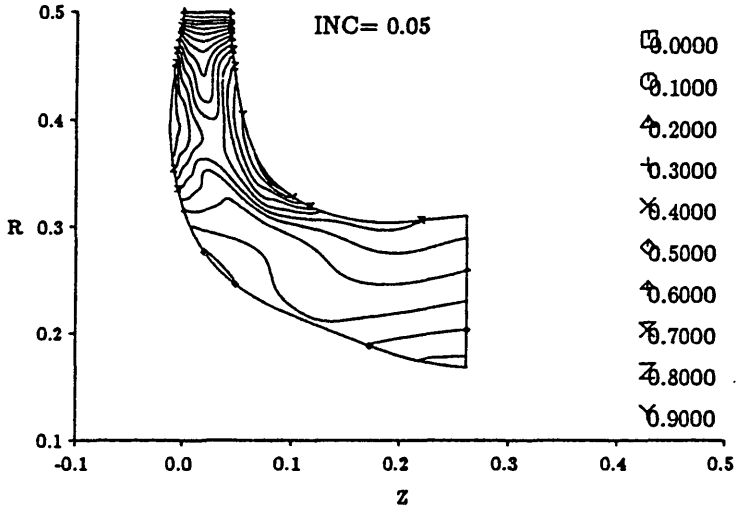


Fig. 6.32b The $M_{rel.}$ on the suction side, stacking at leading edge

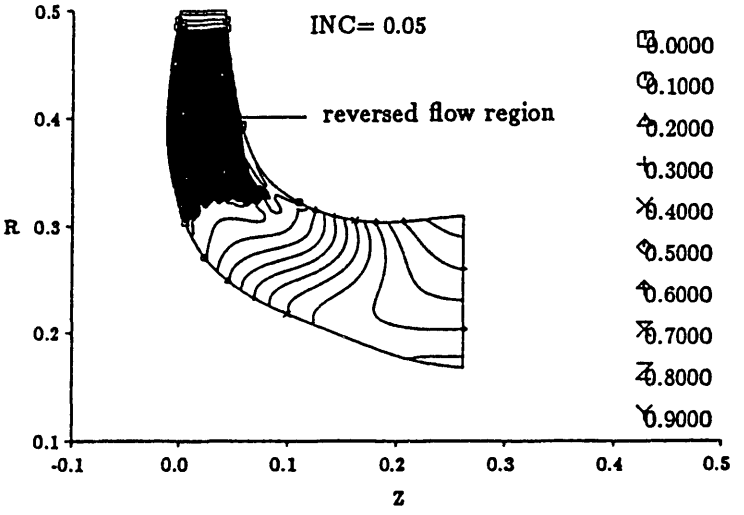


Fig. 6.32c The $M_{rel.}$ on the pressure side, stacking at leading edge

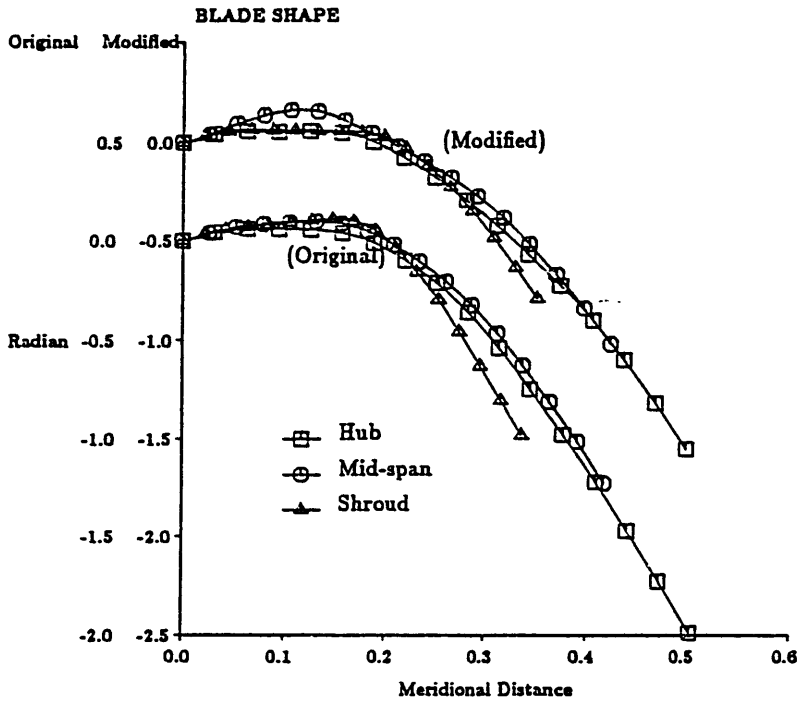


Fig. 6.33a The blade camber vs the meridional distance of the original and modified hub & shroud profiles

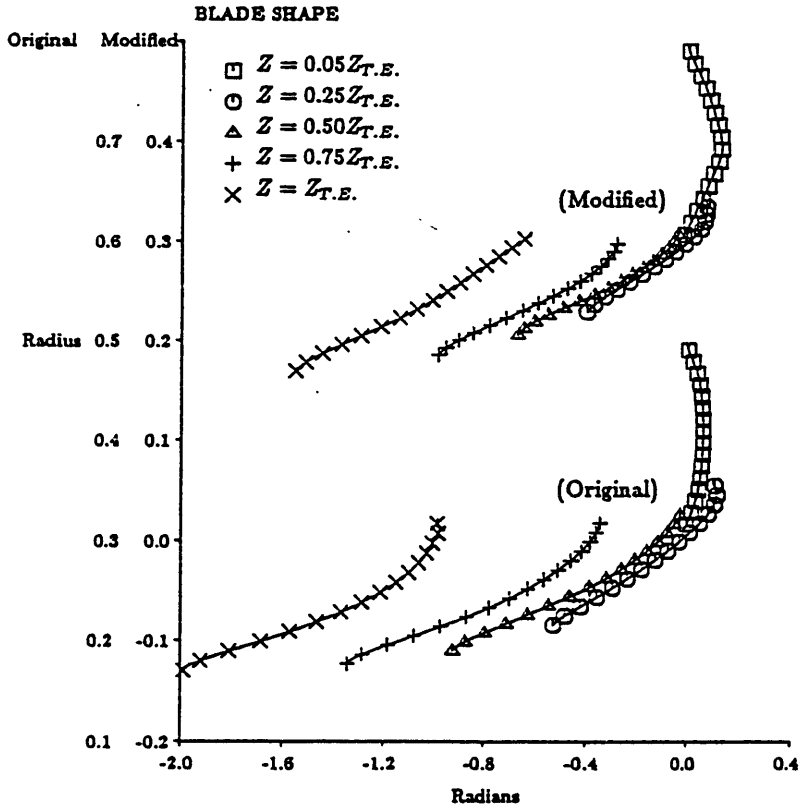


Fig. 6.33b Radial distribution of blade camber along constant z-section for the original and modified hub & shroud profiles

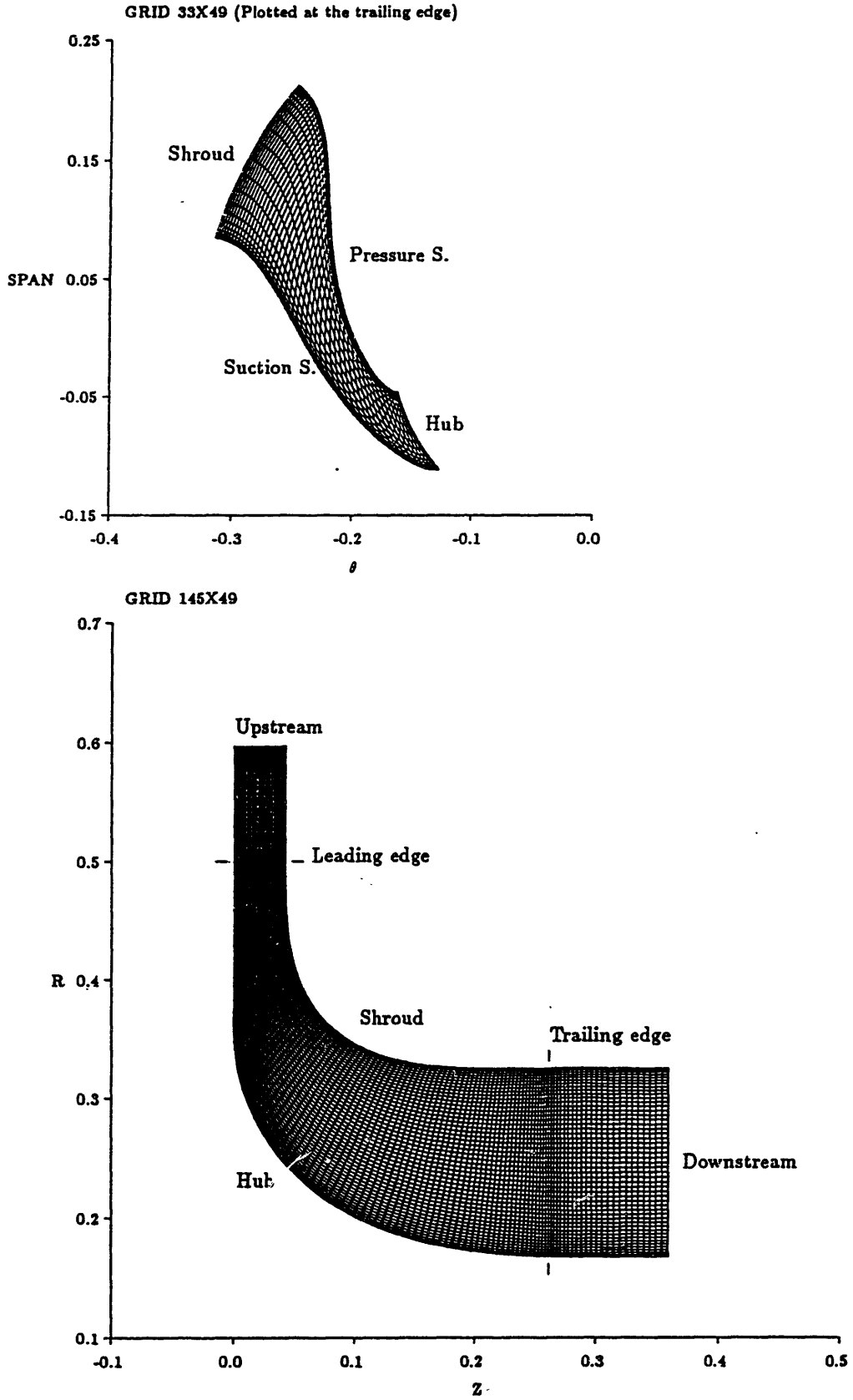


Fig. 7.1 The mesh used for calculation

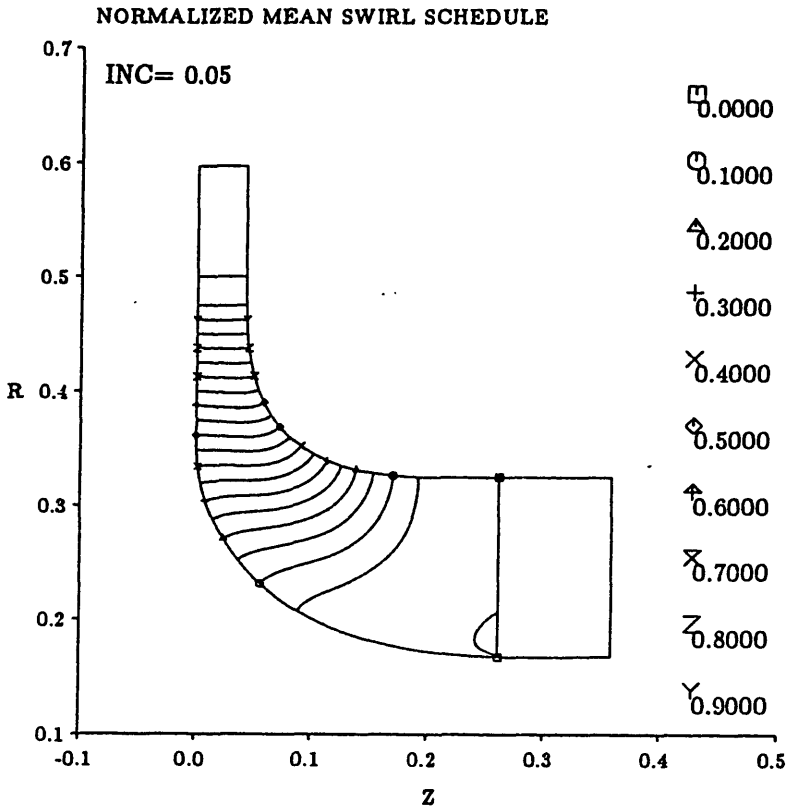


Fig. 7.2a The specified $r\bar{V}_\theta$ for design calculation

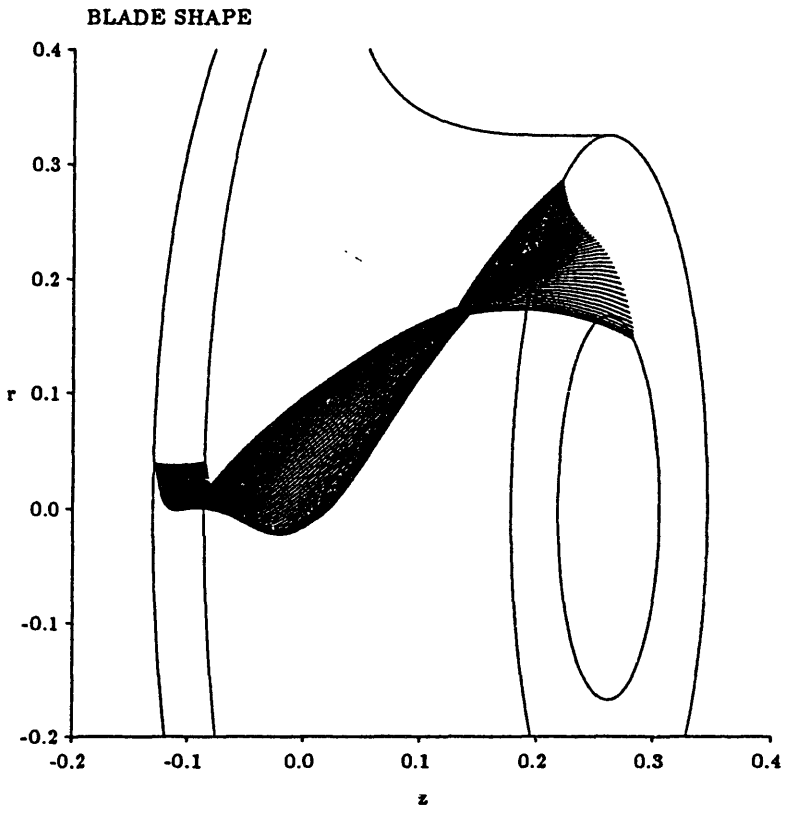


Fig. 7.2b The blade shape from design calculation, number of blades B = 14

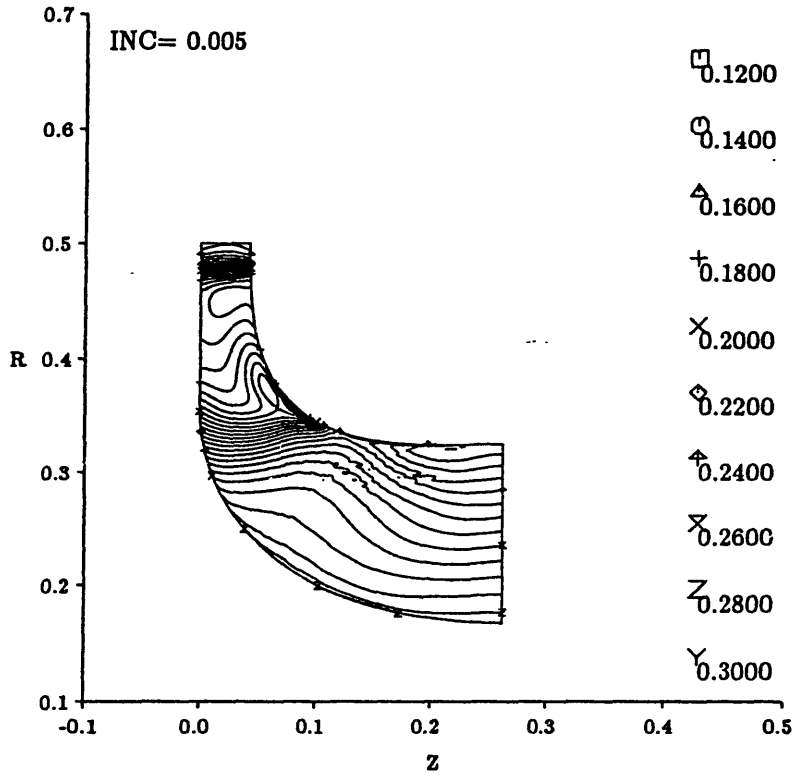


Fig. 7.3a The distribution of $p_{red.}$ on the suction side from the design calculation

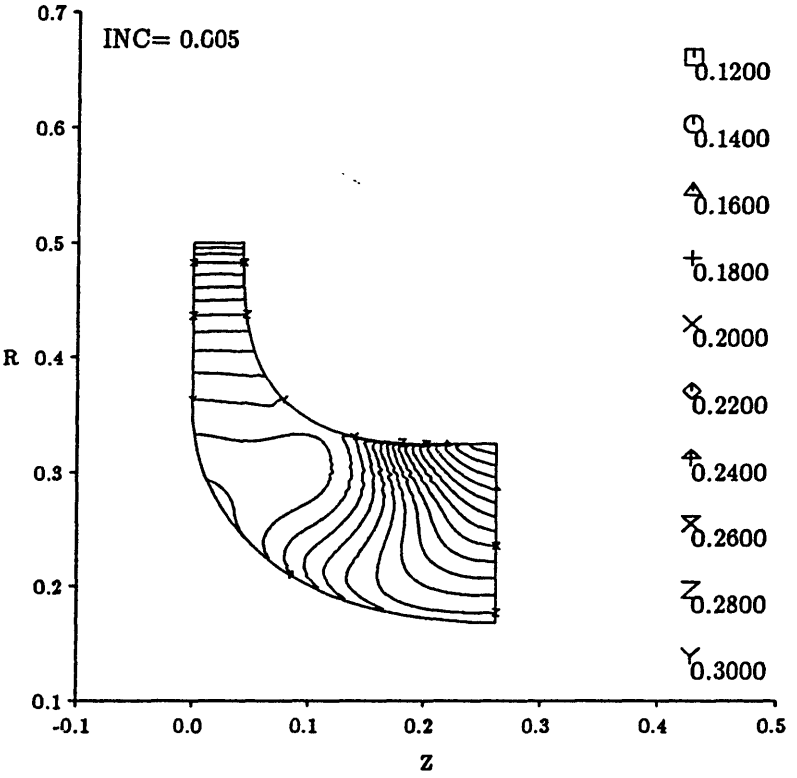


Fig. 7.3b The distribution of $p_{red.}$ on the pressure side from the design calculation

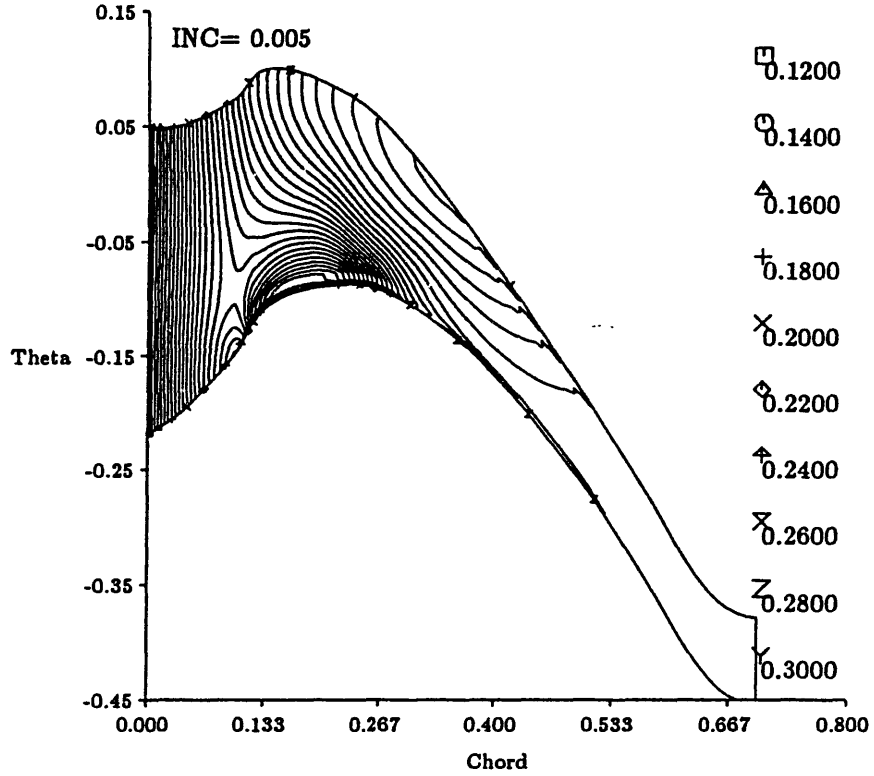


Fig. 7.3c The distribution of $p_{red.}$ on the hub surface from the design calculation

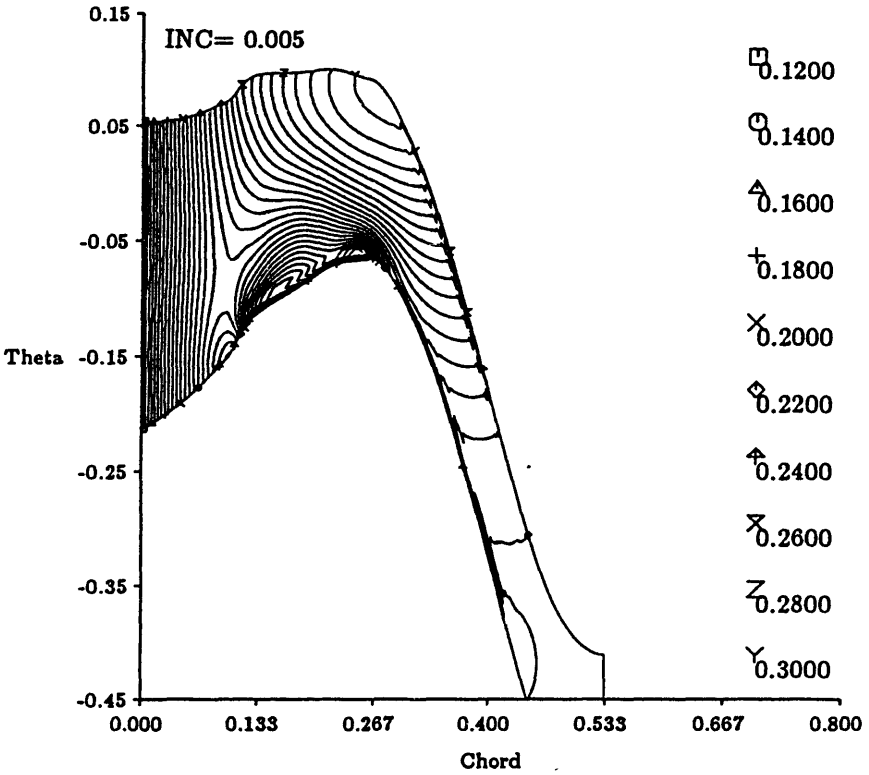


Fig. 7.3d The distribution of $p_{red.}$ on the shroud surface from the design calculation

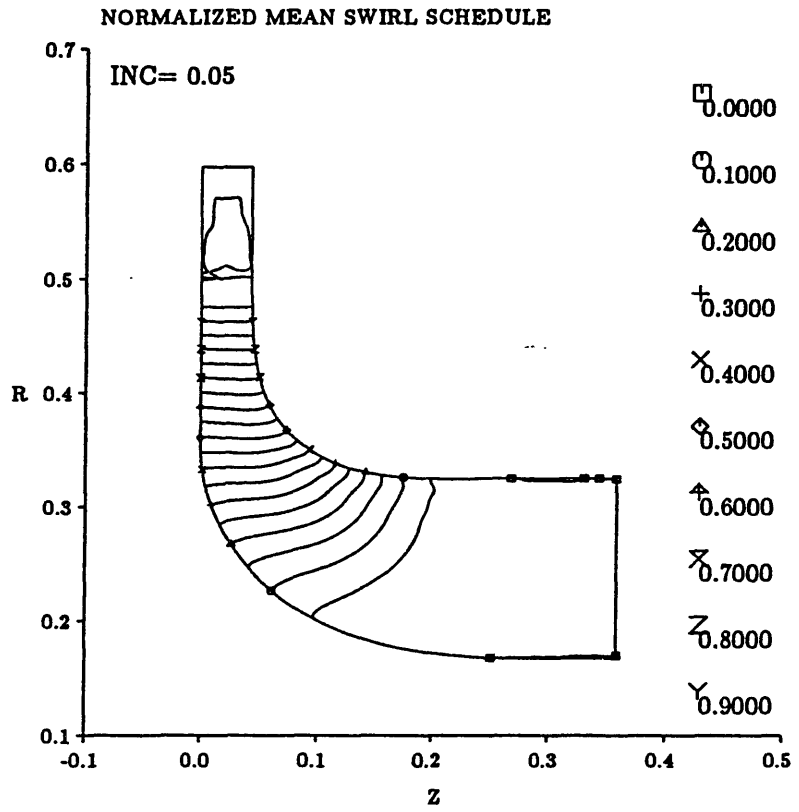


Fig. 7.4a The distribution of $r\bar{V}_\theta$ from the Euler calculation

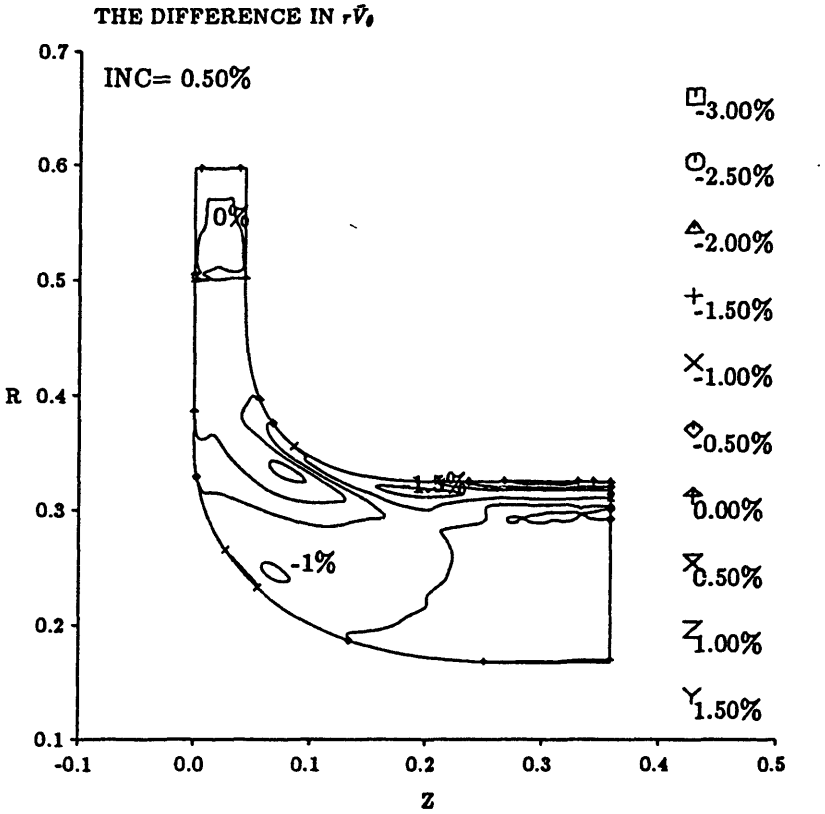


Fig. 7.4b The difference in $r\bar{V}_\theta$ between design specification and Euler calculation

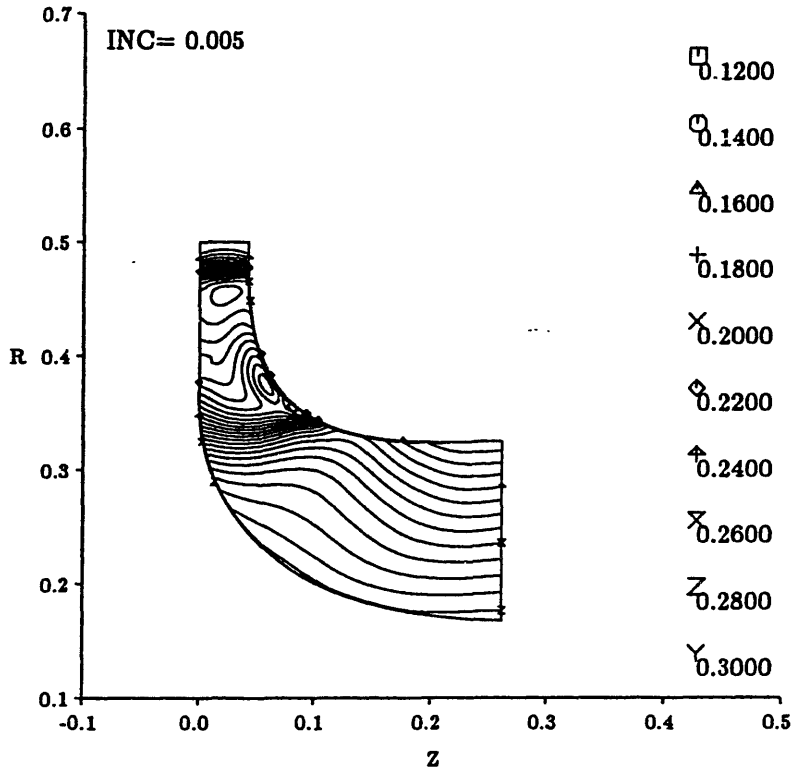


Fig. 7.5a The distribution of $p_{red.}$ on the suction side from the Euler calculation

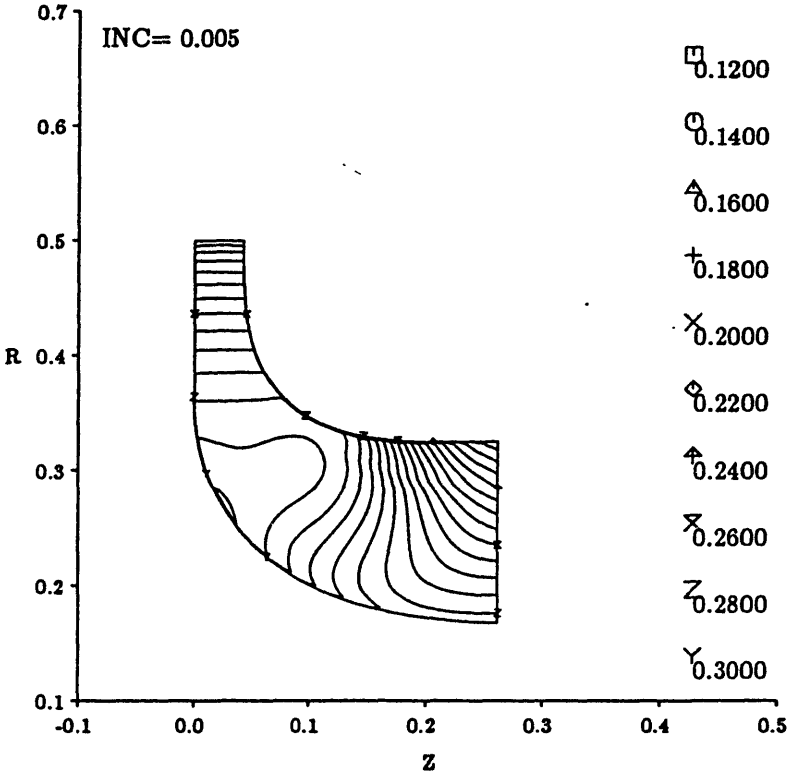


Fig. 7.5b The distribution of $p_{red.}$ on the pressure side from the Euler calculation

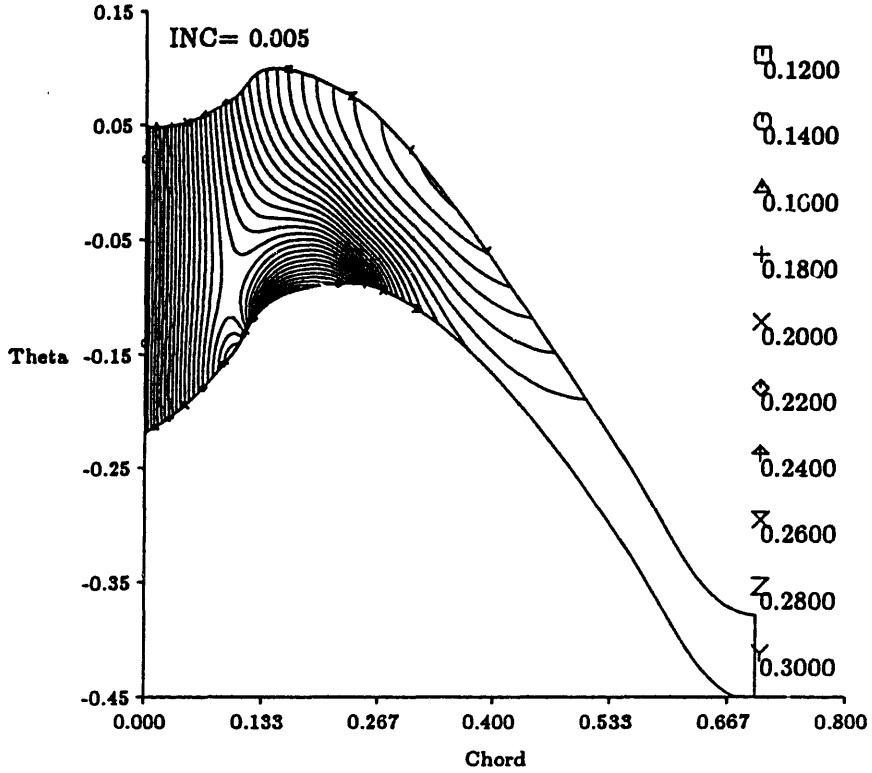


Fig. 7.5c The distribution of $p_{red.}$ on the hub surface from the Euler calculation

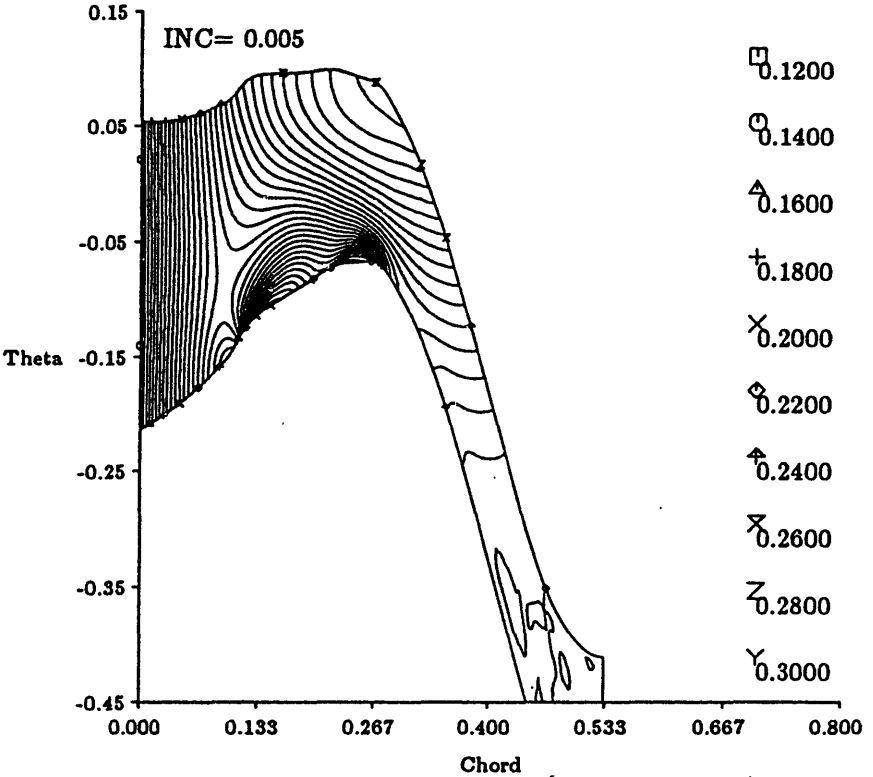


Fig. 7.5d The distribution of $p_{red.}$ on the shroud surface from the Euler calculation

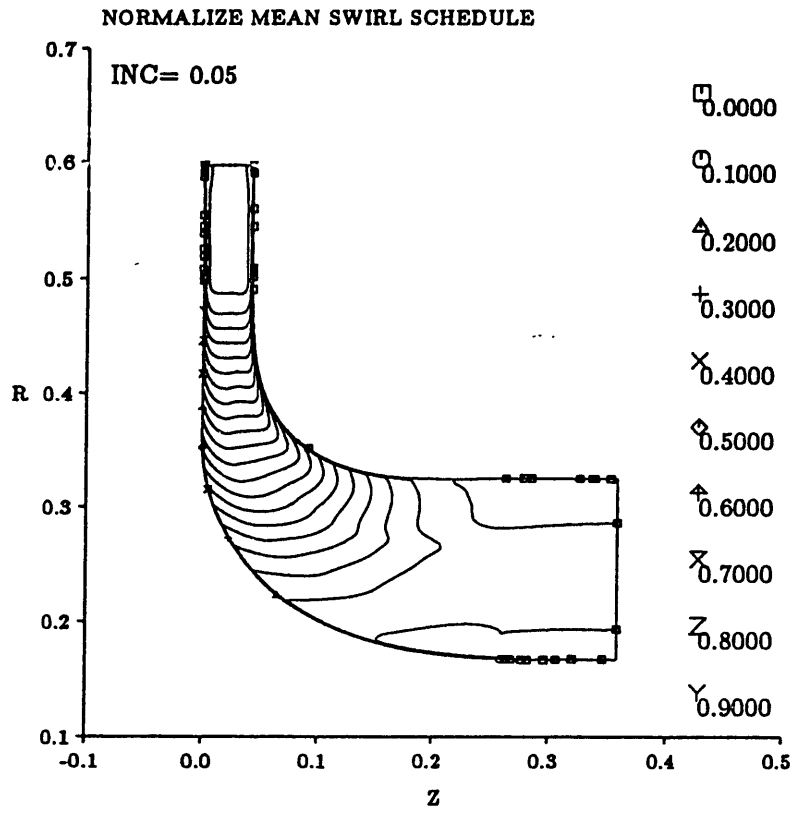


Fig. 7.6a The distribution of $r\bar{V}_\theta$ from the Viscous calculation

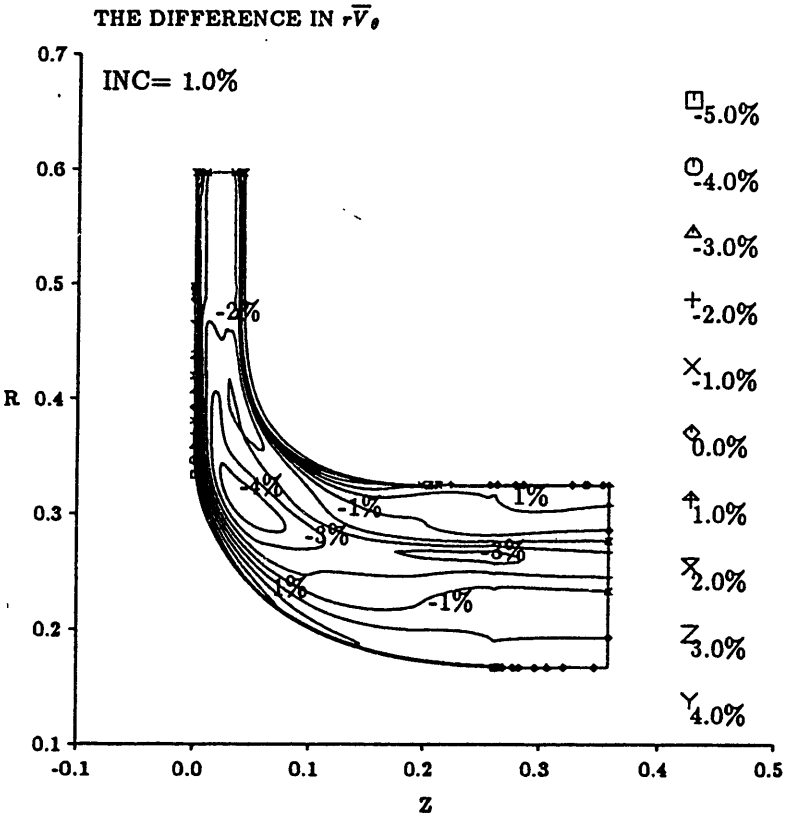


Fig. 7.6b The difference in $r\bar{V}_\theta$ between design specification and Viscous calculation

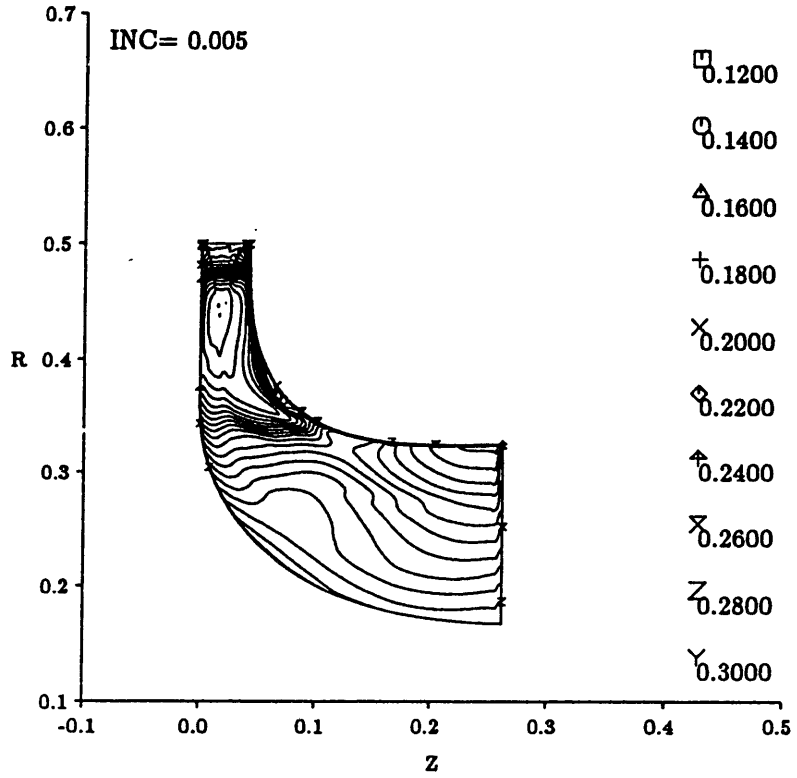


Fig. 7.7a The distribution of $p_{red.}$ on the suction side from the viscous calculation

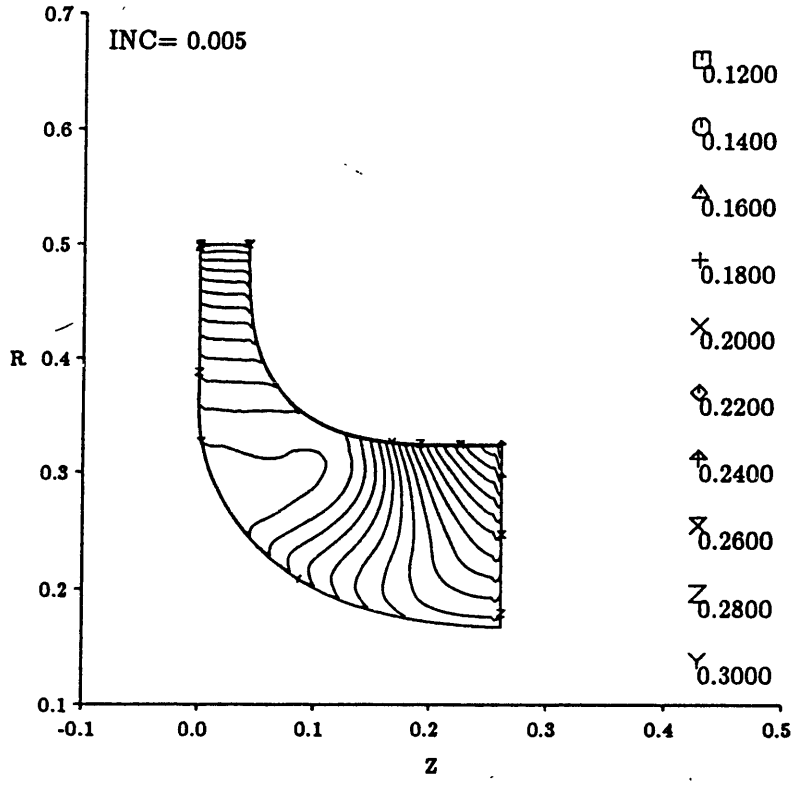


Fig. 7.7b The distribution of $p_{red.}$ on the pressure side from the viscous calculation

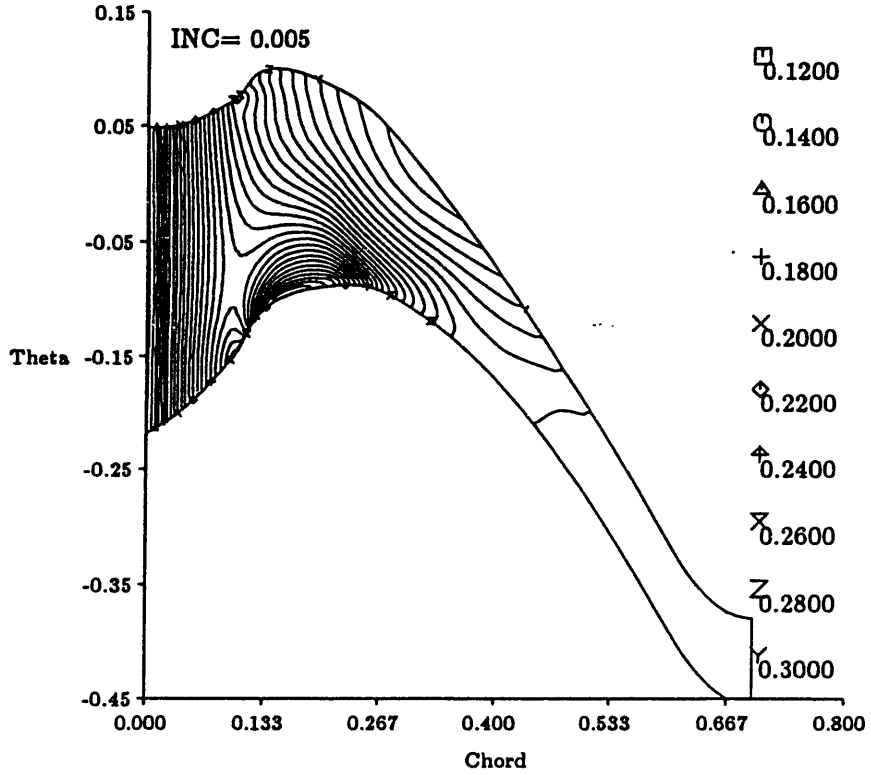


Fig. 7.7c The distribution of $p_{red.}$ on the hub surface from the viscous calculation

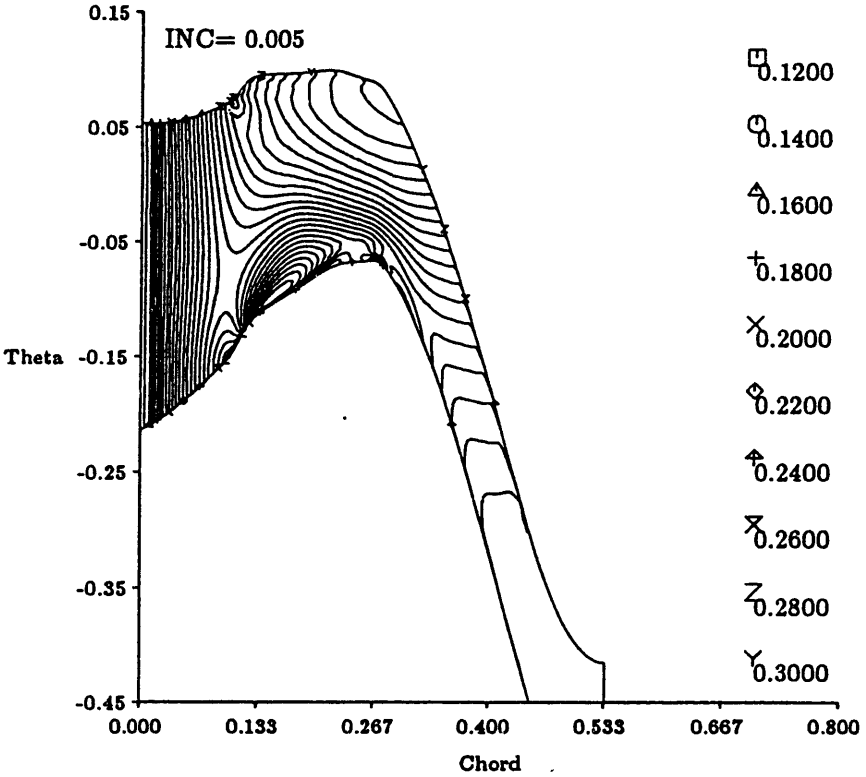


Fig. 7.7d The distribution of $p_{red.}$ on the shroud surface from the viscous calculation

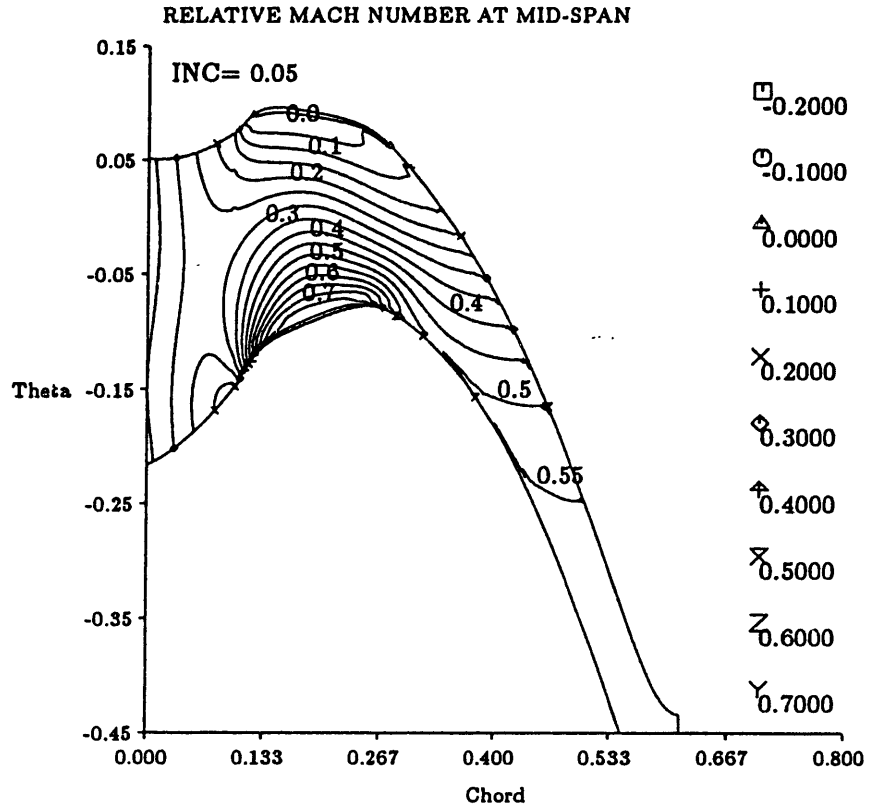


Fig. 7.8a The distribution of relative Mach number M_{rel} from the design calculation

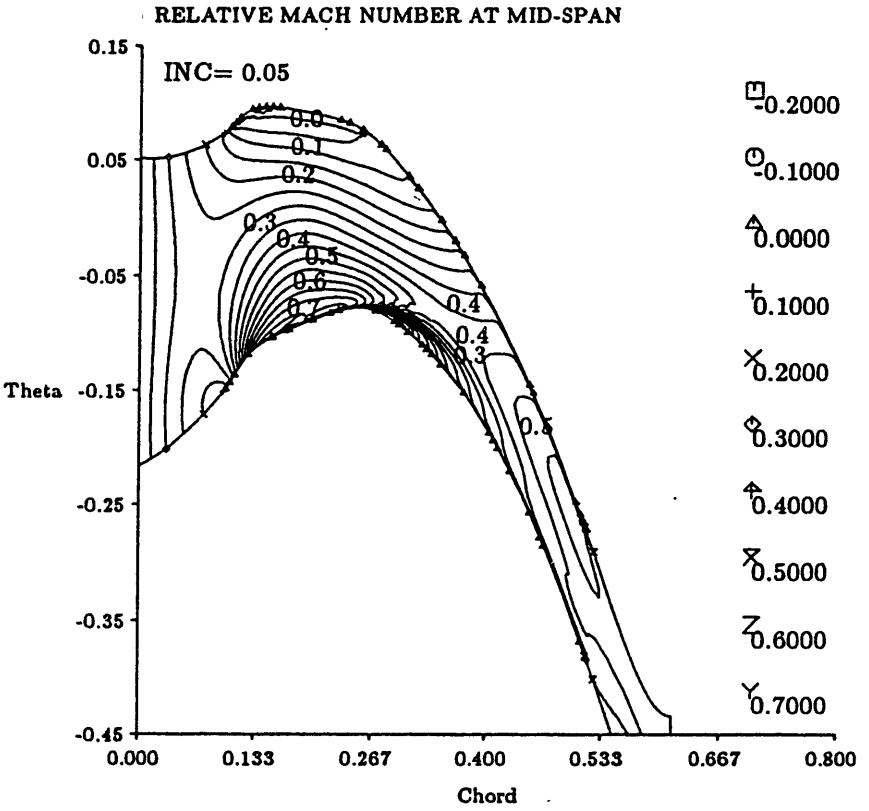


Fig. 7.8b The distribution of relative Mach number M_{rel} from the viscous calculation

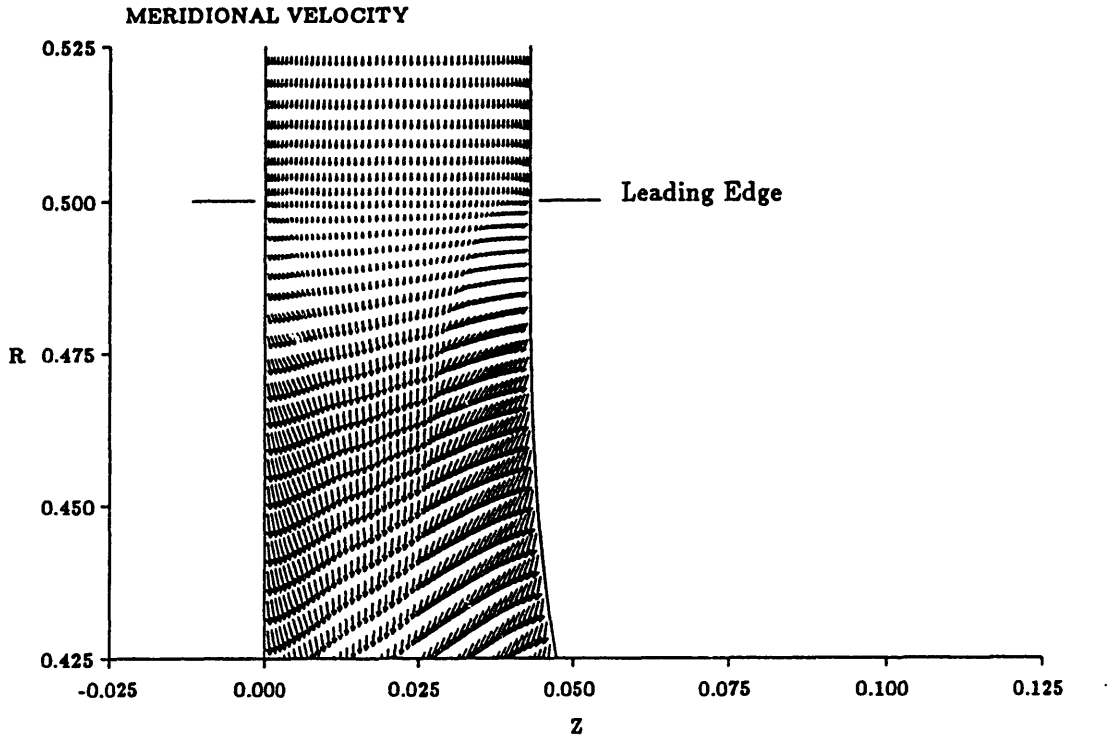


Fig. 7.9a The meridional velocity on the surface 1-point above the S.S.

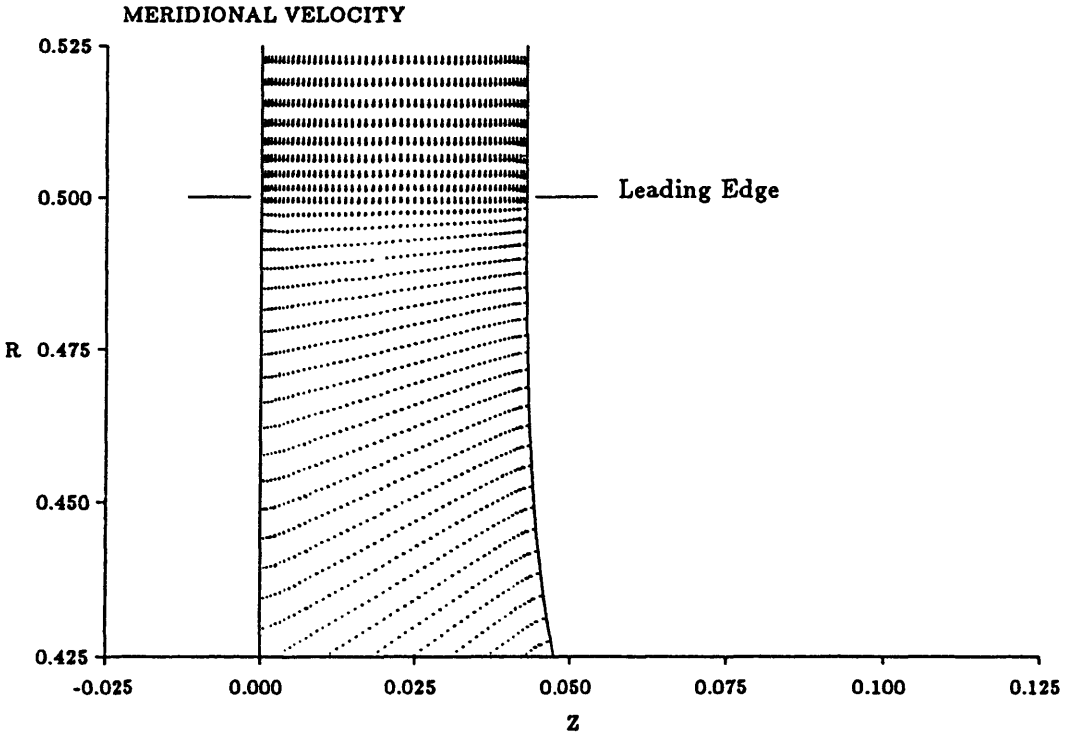


Fig. 7.9b The meridional velocity on the surface 1-point below the P.S.

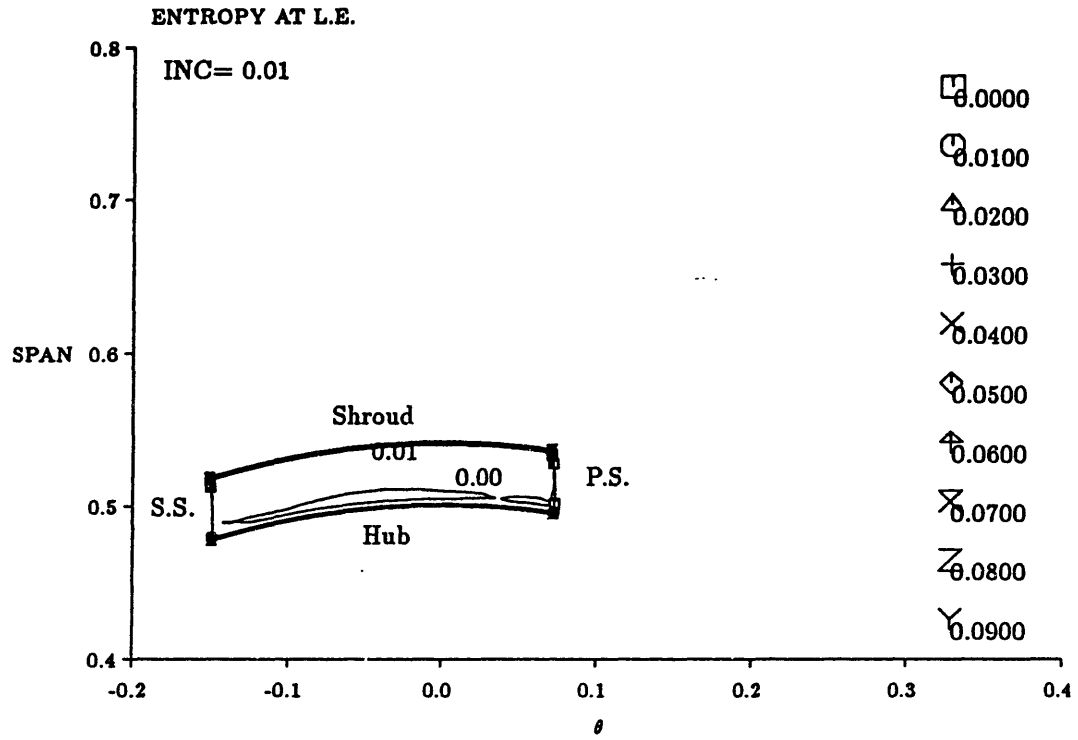


Fig. 7.10a The distribution of entropy S at the leading edge

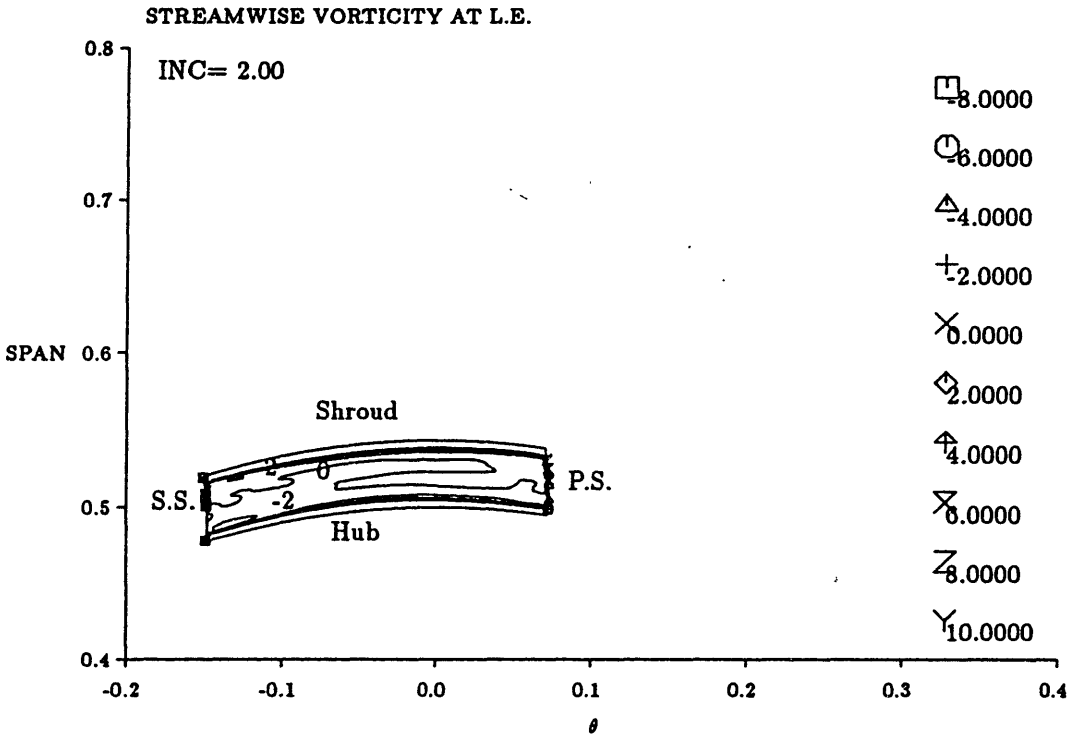


Fig. 7.11a The distribution of streamwise vorticity Ω_r at the leading edge

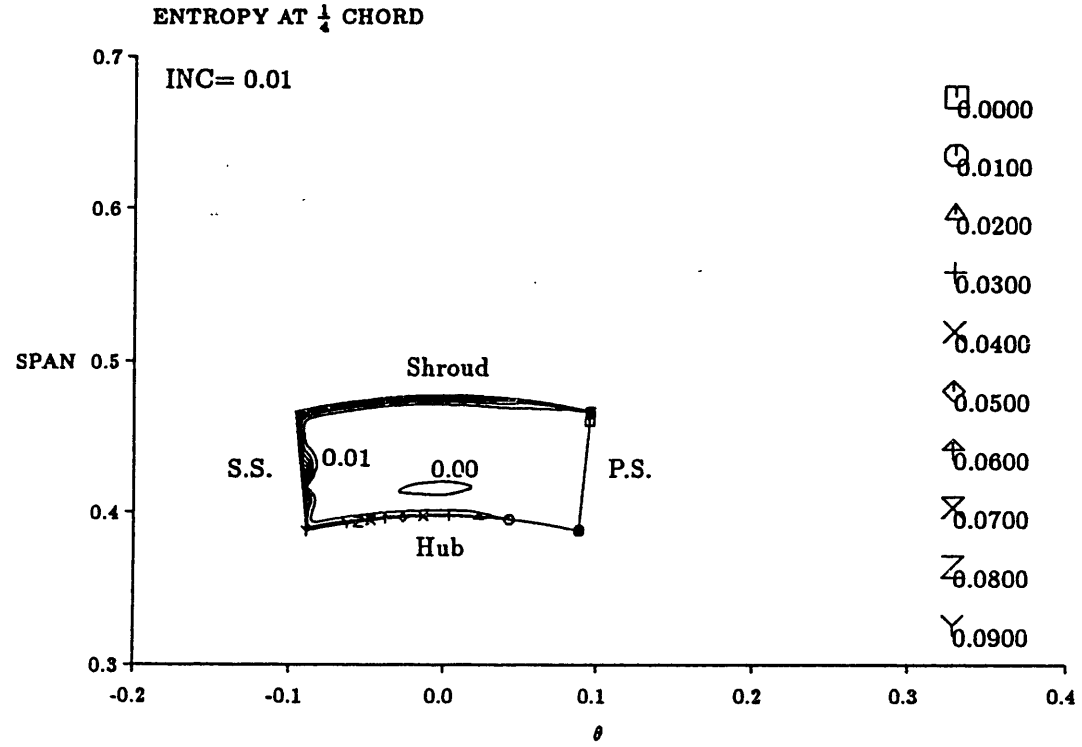


Fig. 7.10b The distribution of entropy S at the $\frac{1}{4}$ chord

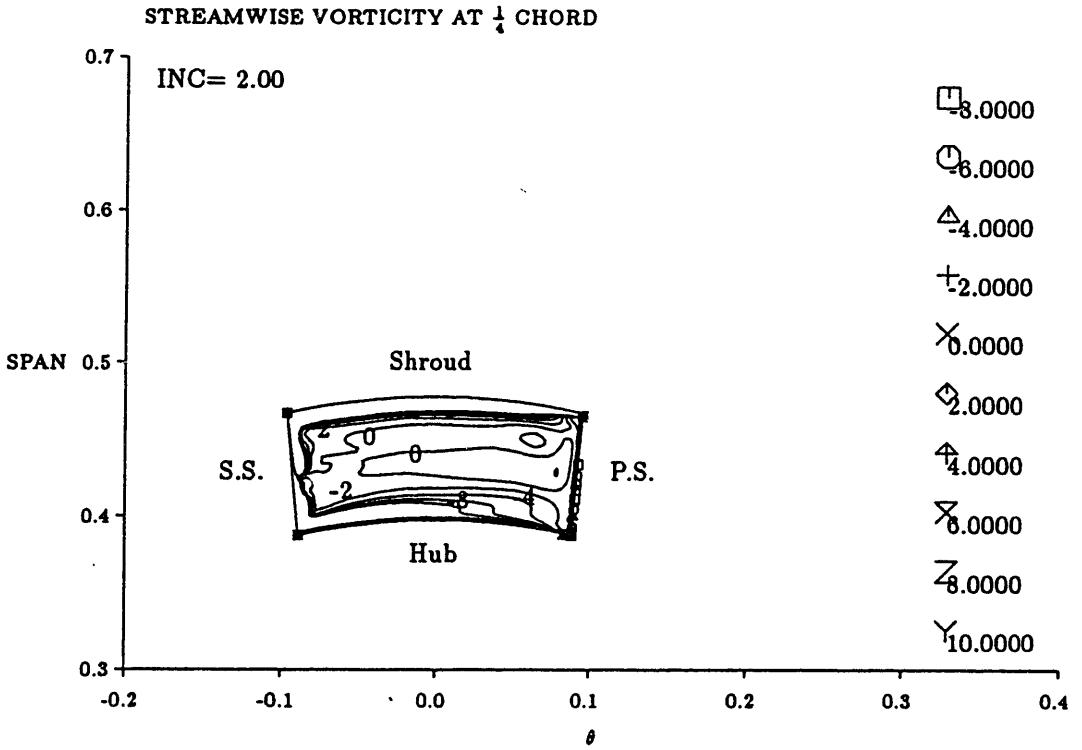


Fig. 7.11b The distribution of streamwise vorticity Ω at the $\frac{1}{4}$ chord

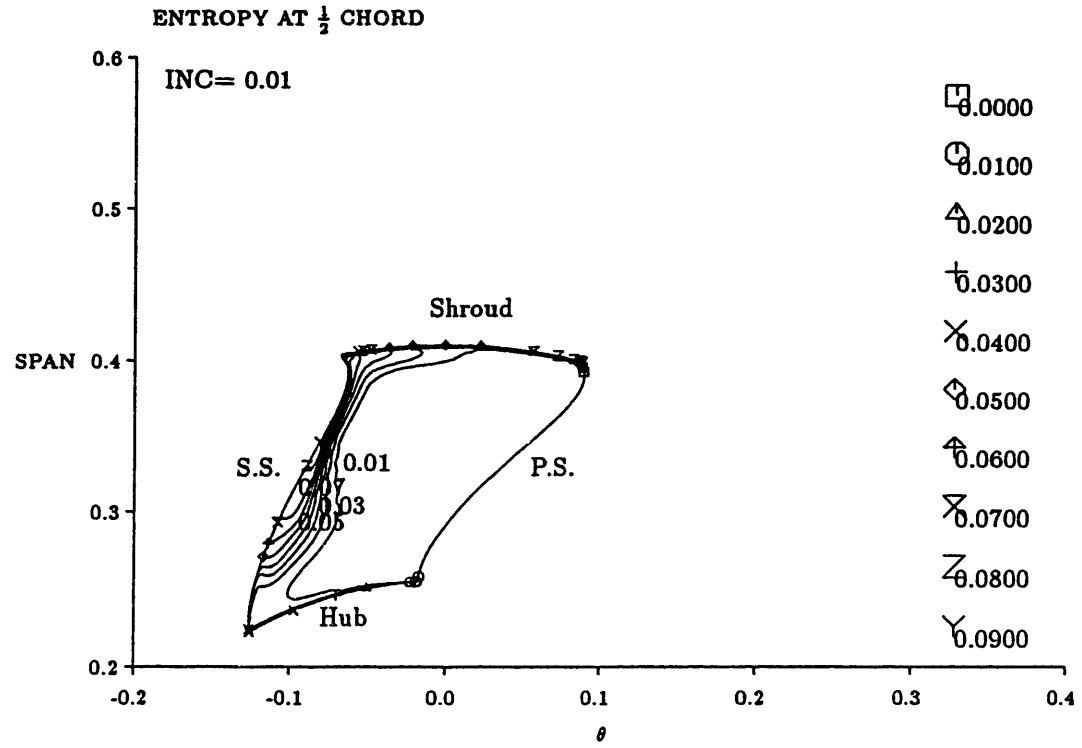


Fig. 7.10c The distribution of entropy S at the $\frac{1}{2}$ chord

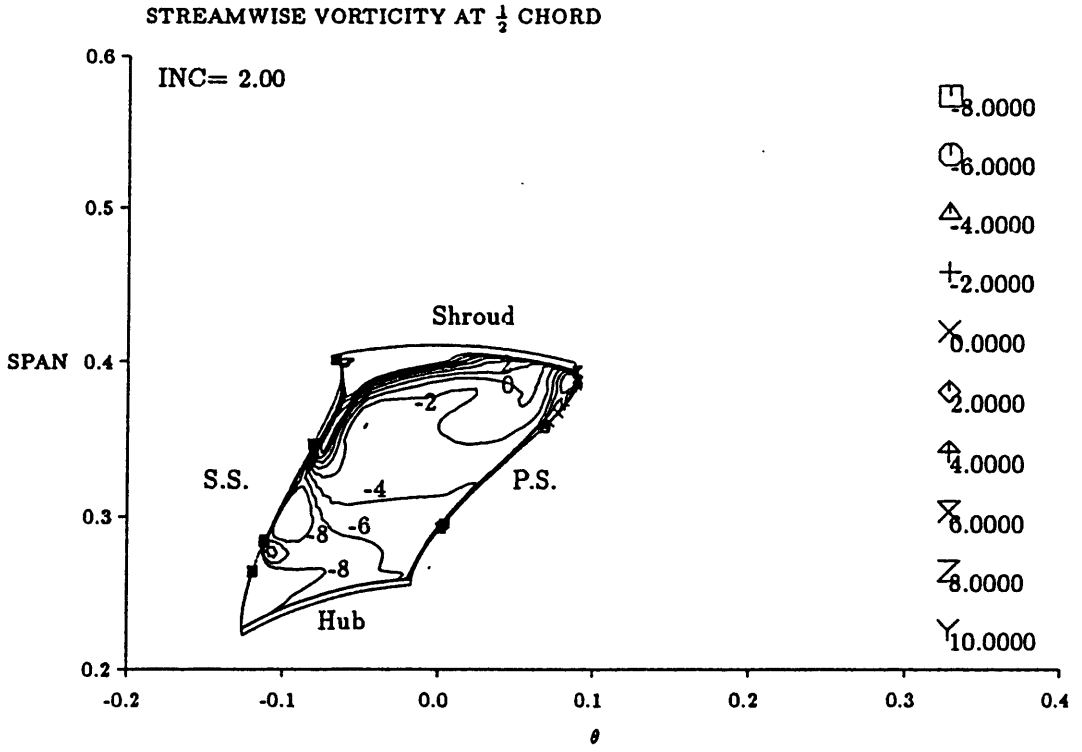


Fig. 7.11c The distribution of streamwise vorticity Ω at the $\frac{1}{2}$ chord

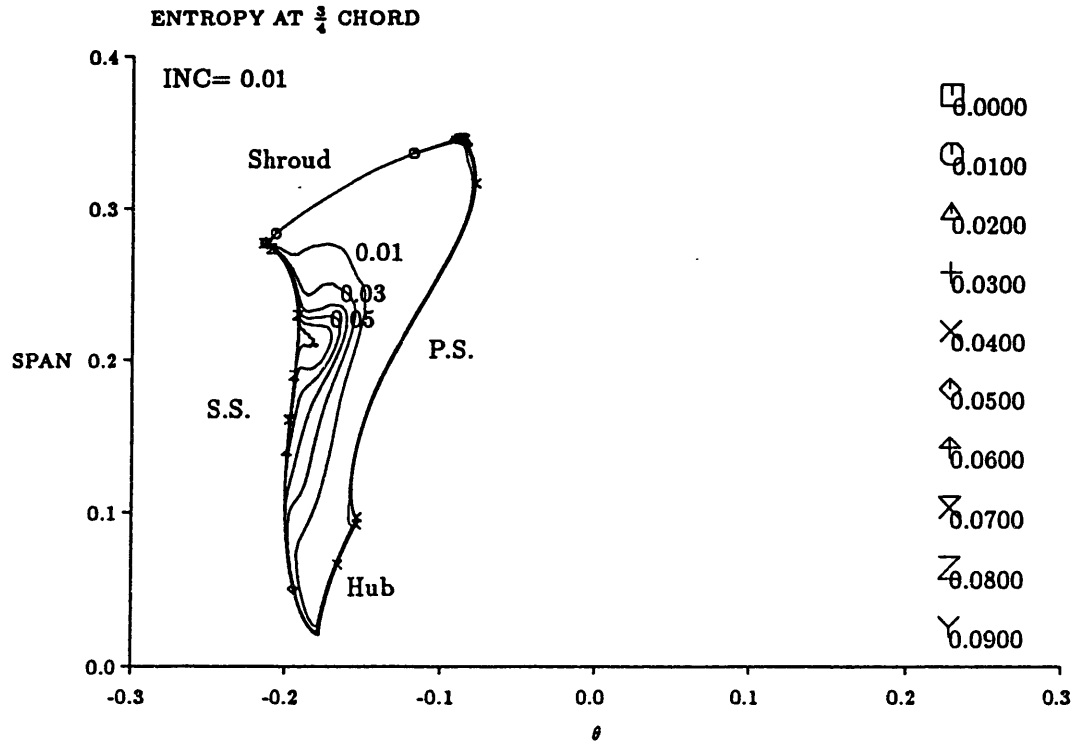


Fig. 7.10d The distribution of entropy S at the $\frac{3}{4}$ chord

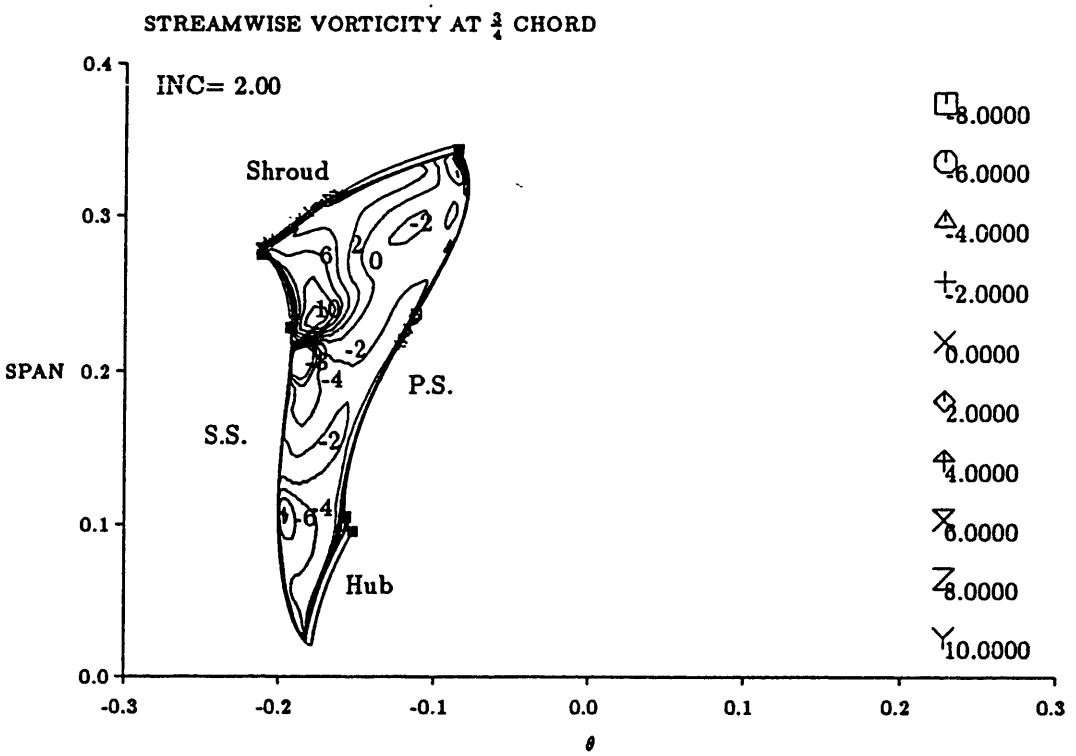


Fig. 7.11d The distribution of streamwise vorticity Ω at the $\frac{3}{4}$ chord

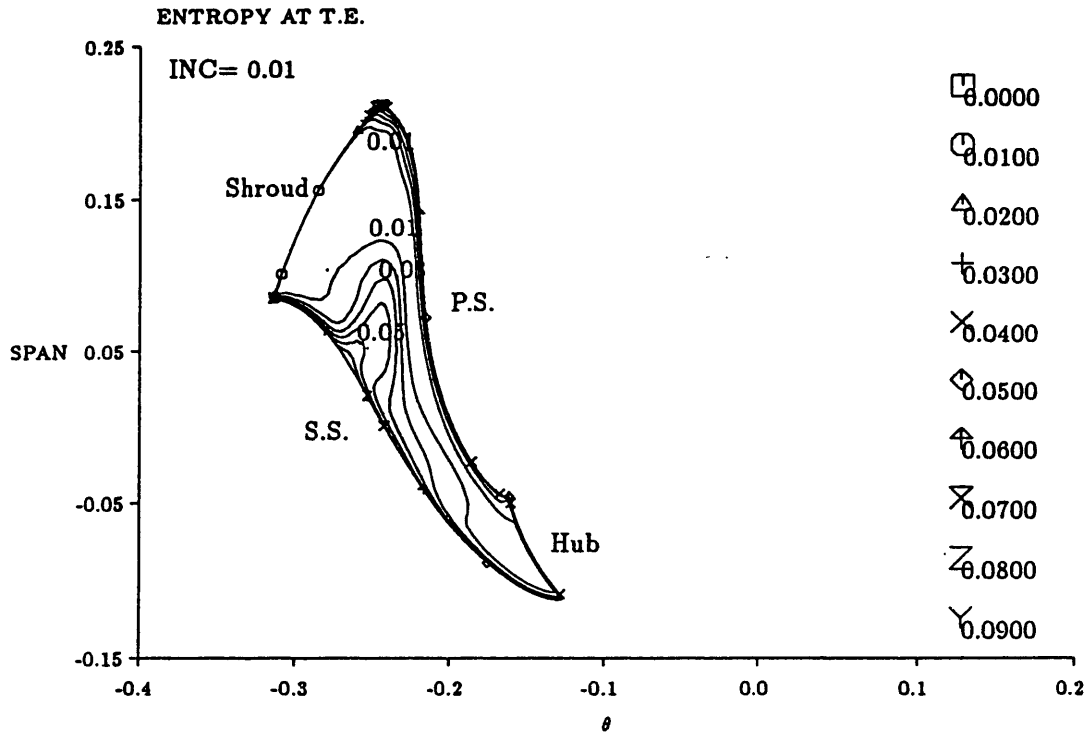


Fig. 7.10e The distribution of entropy S at the trailing edge

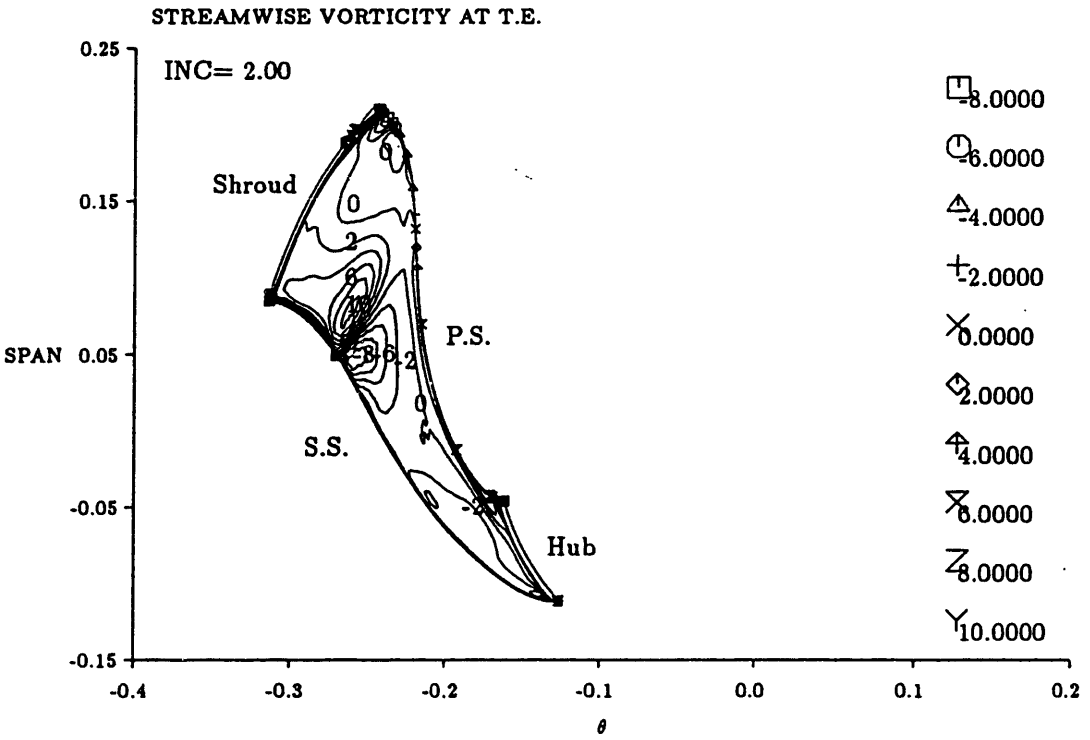


Fig. 7.11e The distribution of streamwise vorticity Ω_z at the trailing edge

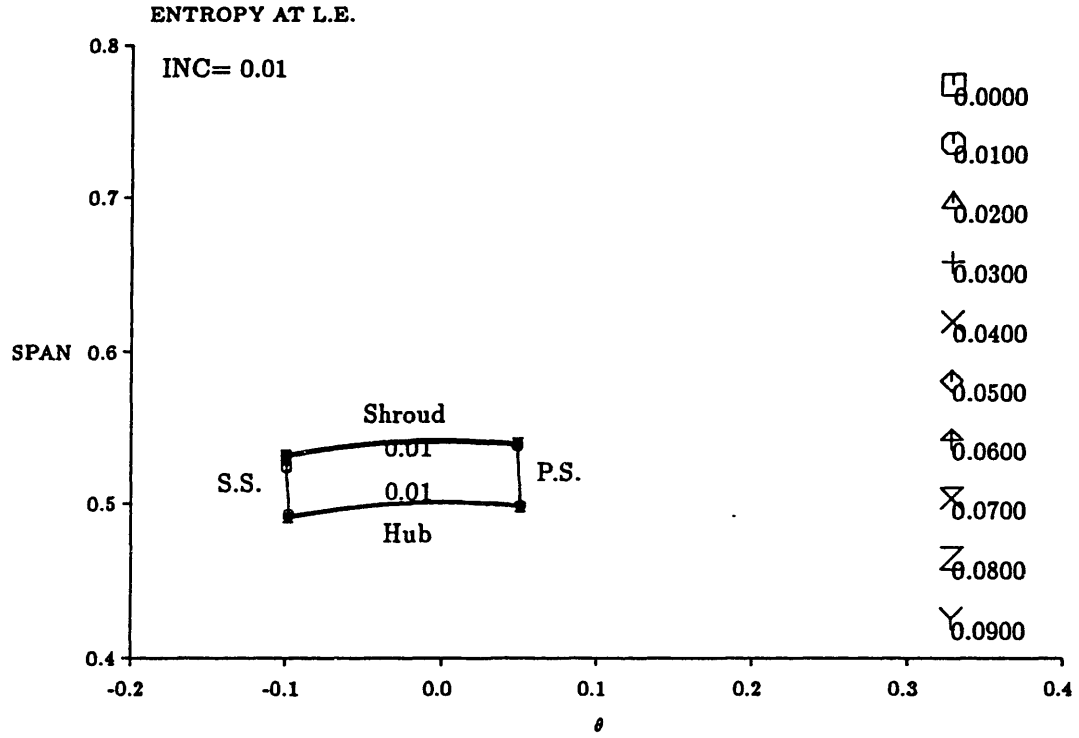


Fig. 7.12a The distribution of entropy S at the leading edge, number of blades $B = 21$

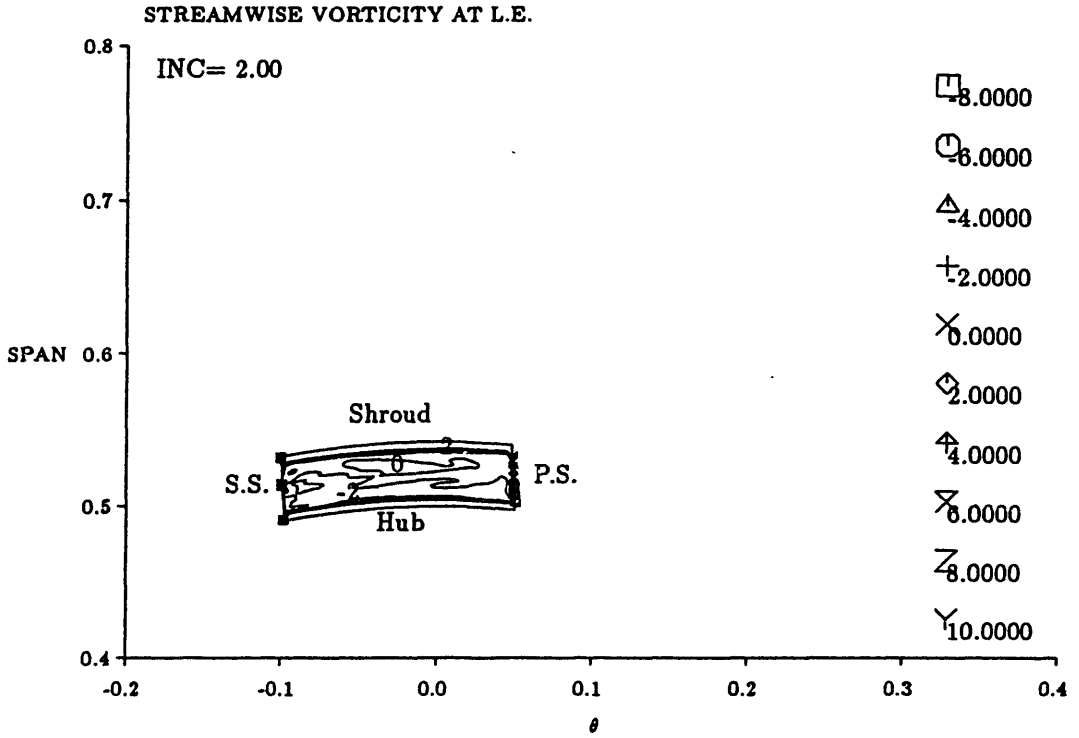


Fig. 7.13a The distribution of streamwise vorticity Ω_r at the leading edge, number of blades $B = 21$

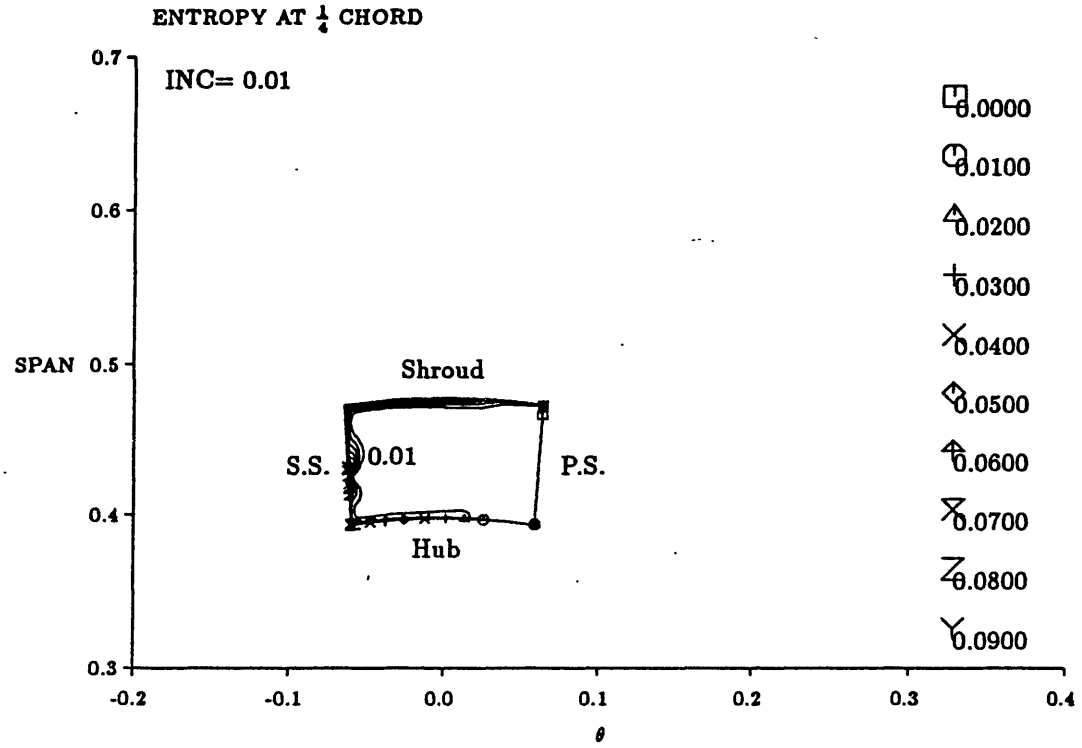


Fig. 7.12b The distribution of entropy S at the $\frac{1}{4}$ chord, number of blades $B = 21$

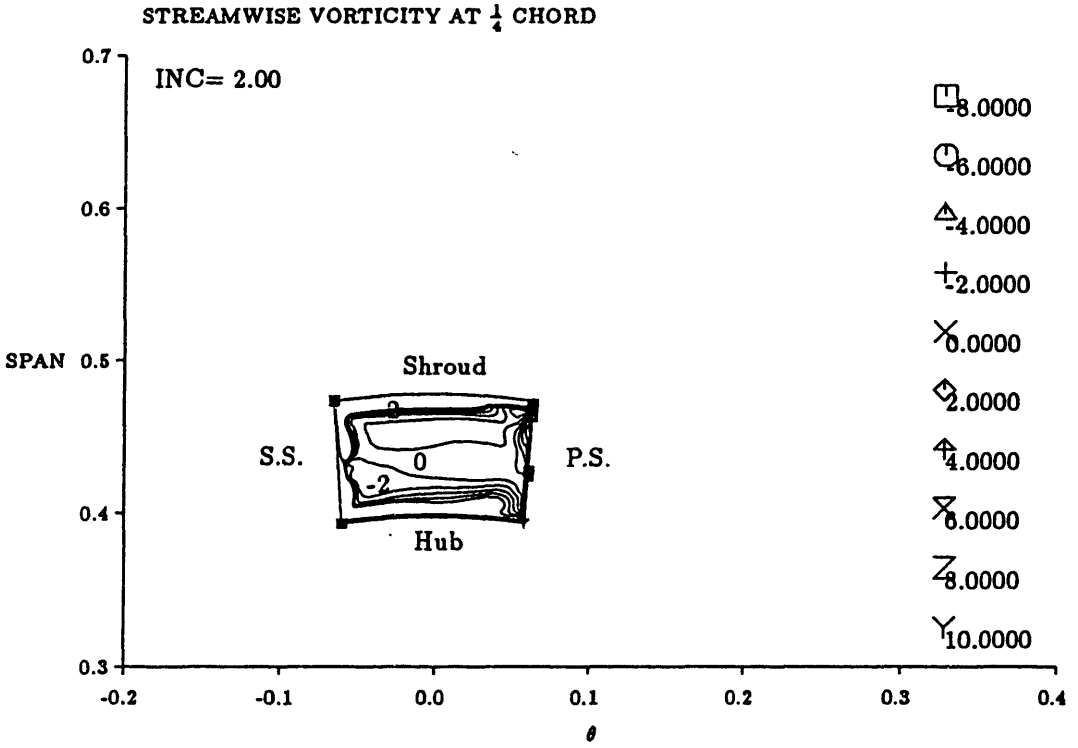


Fig. 7.13b The distribution of streamwise vorticity Ω at the $\frac{1}{4}$ chord, number of blades $B = 21$

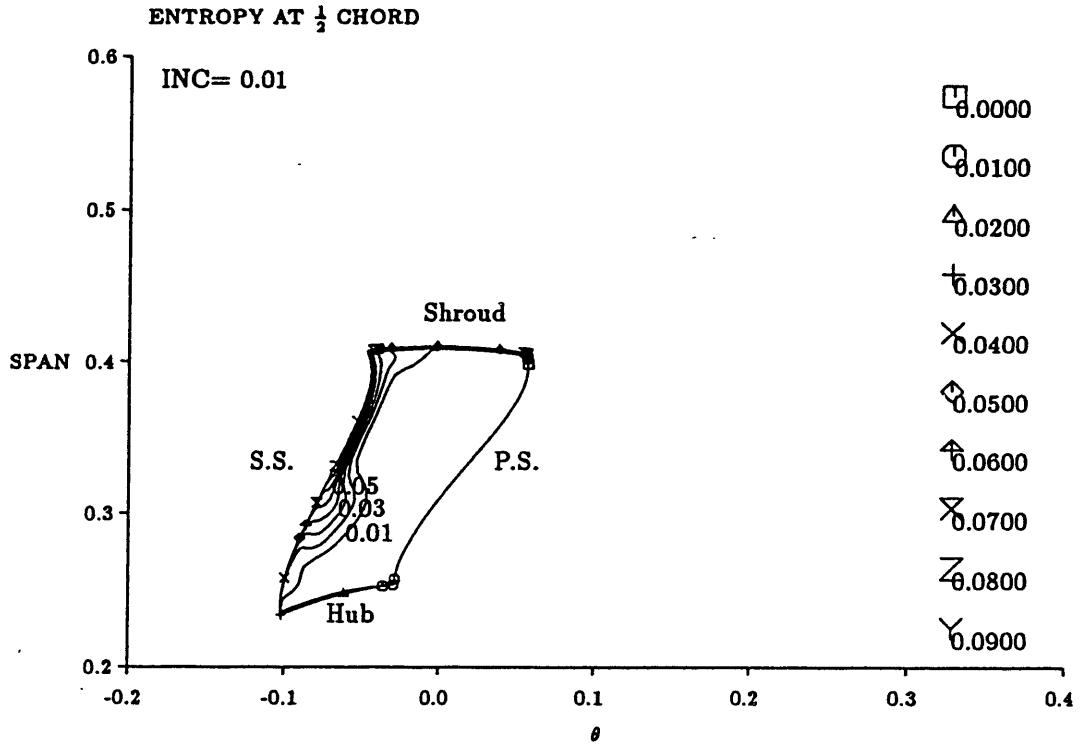


Fig. 7.12c The distribution of entropy S at the $\frac{1}{2}$ chord, number of blades $B = 21$

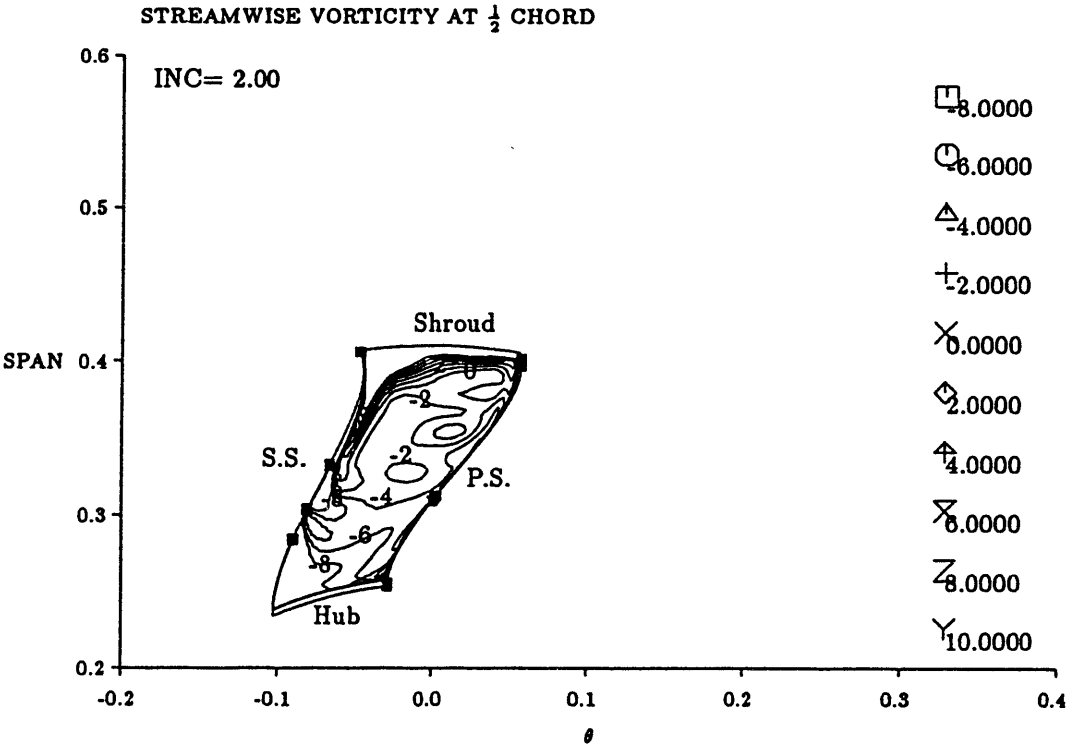


Fig. 7.13c The distribution of streamwise vorticity Ω at the $\frac{1}{2}$ chord, number of blades $B = 21$

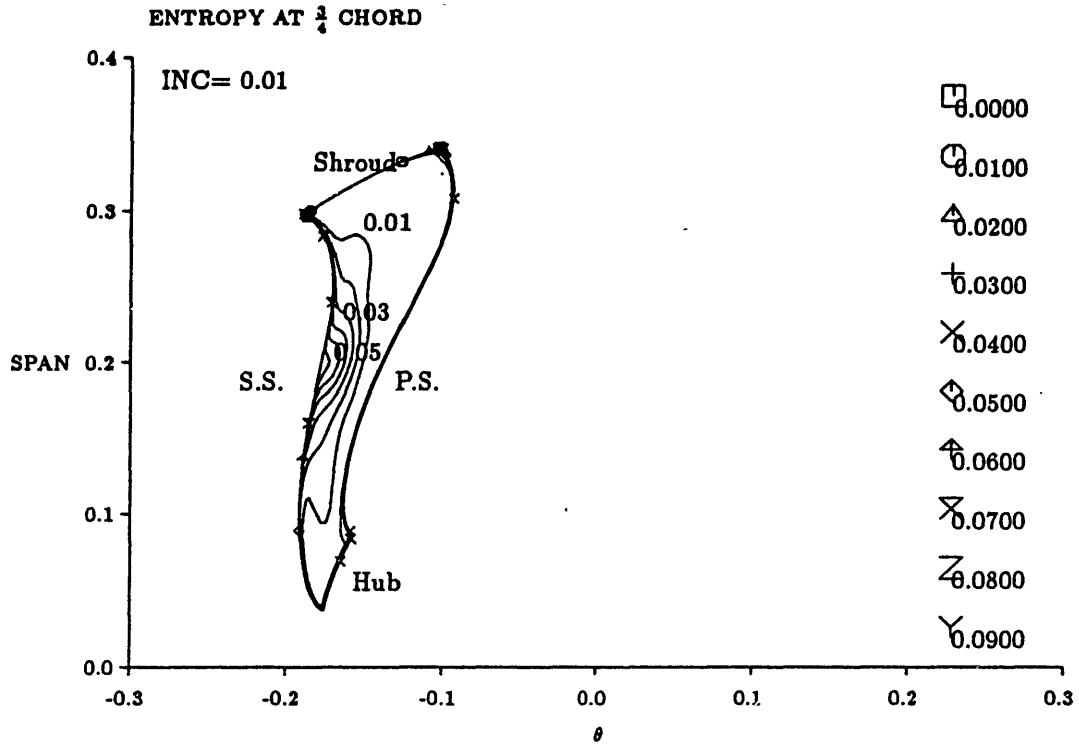


Fig. 7.12d The distribution of entropy S at the $\frac{3}{4}$ chord, number of blades $B = 21$

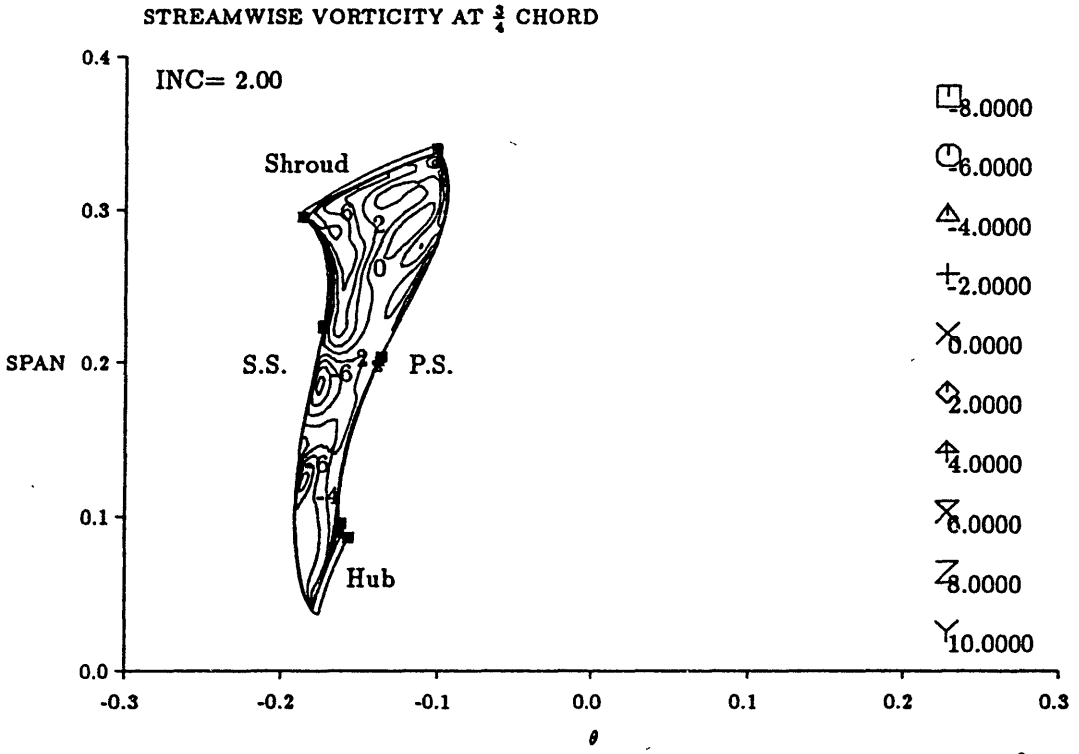


Fig. 7.13d The distribution of streamwise vorticity Ω at the $\frac{3}{4}$ chord, number of blades $B = 21$

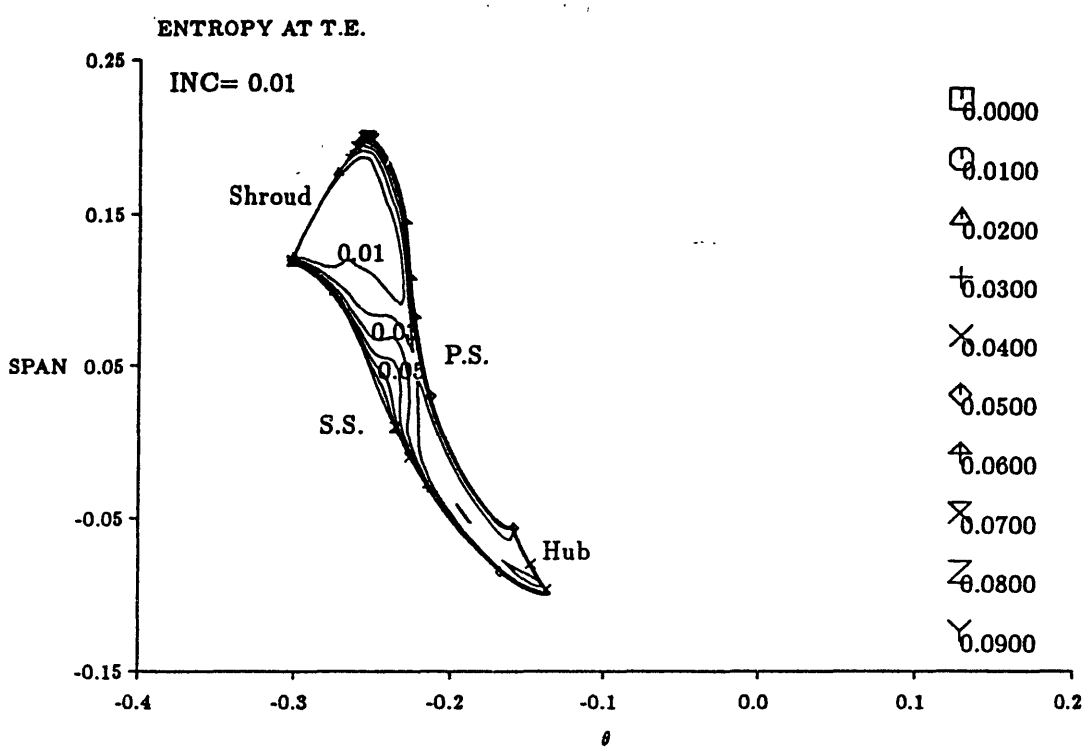


Fig. 7.12e The distribution of entropy S at the trailing edge, number of blades $B = 21$

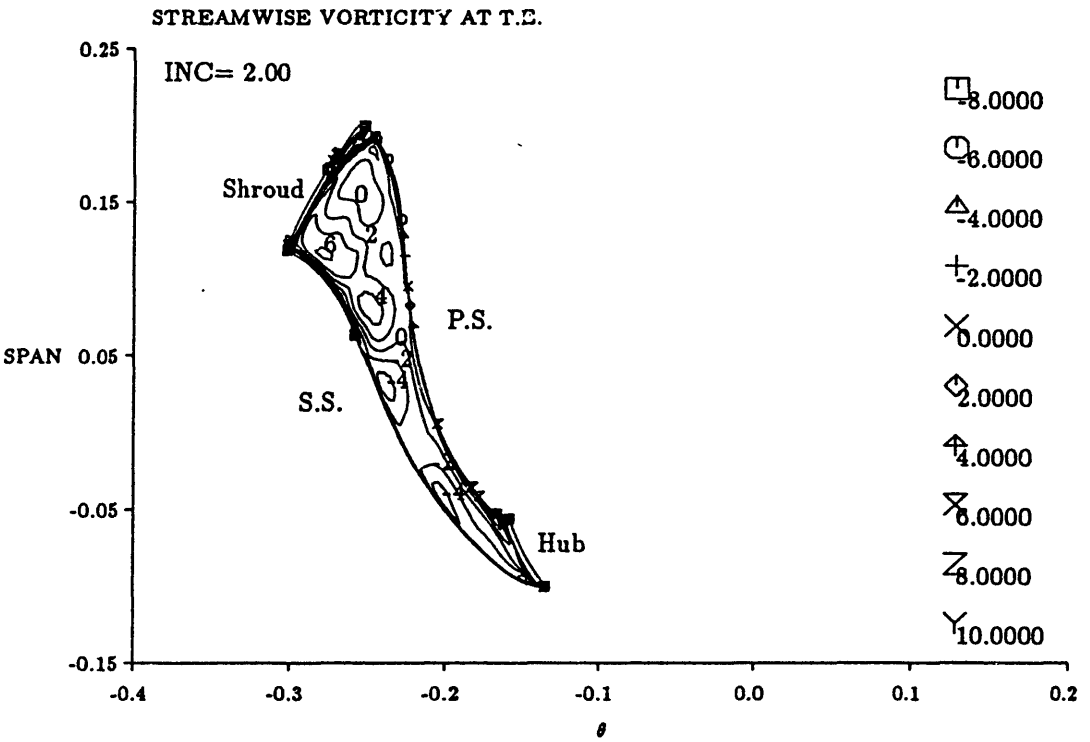


Fig. 7.13e The distribution of streamwise vorticity Ω_r at the trailing edge, number of blades $B = 21$

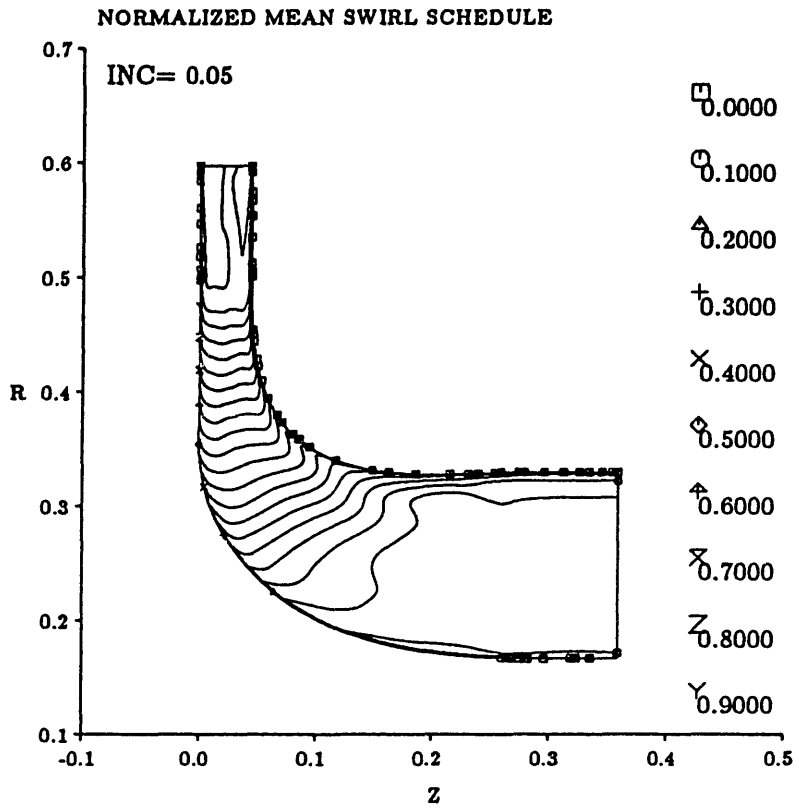


Fig. 7.14a The distribution of $r\overline{V}_\theta$ from the viscous calculation with 3% of tip clearance

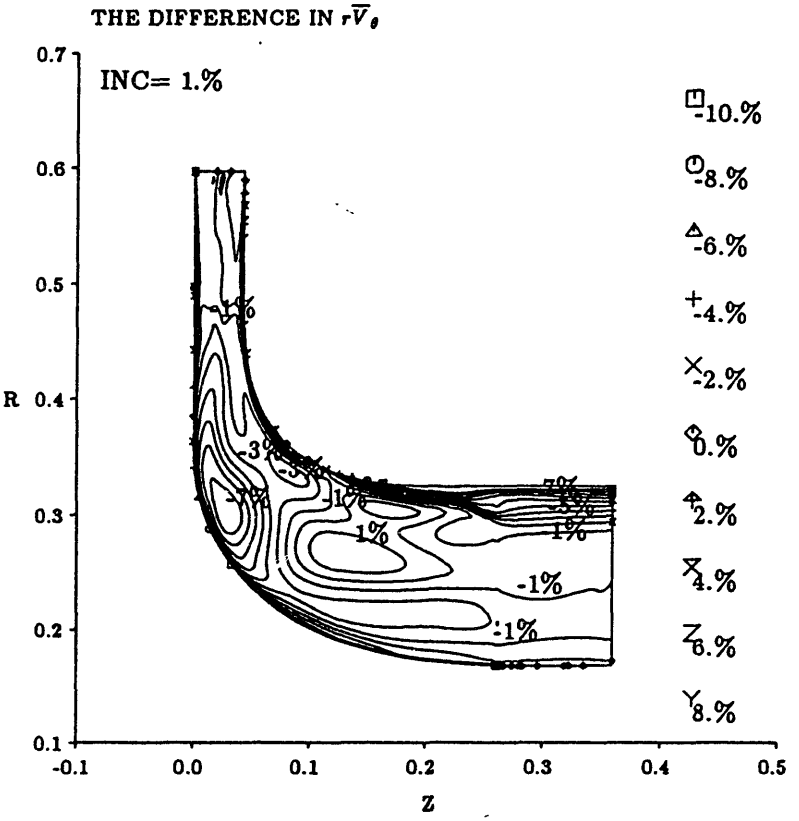


Fig. 7.14b The difference in $r\overline{V}_\theta$ between design specification and viscous calculation with 3% of tip clearance (only the blade region)

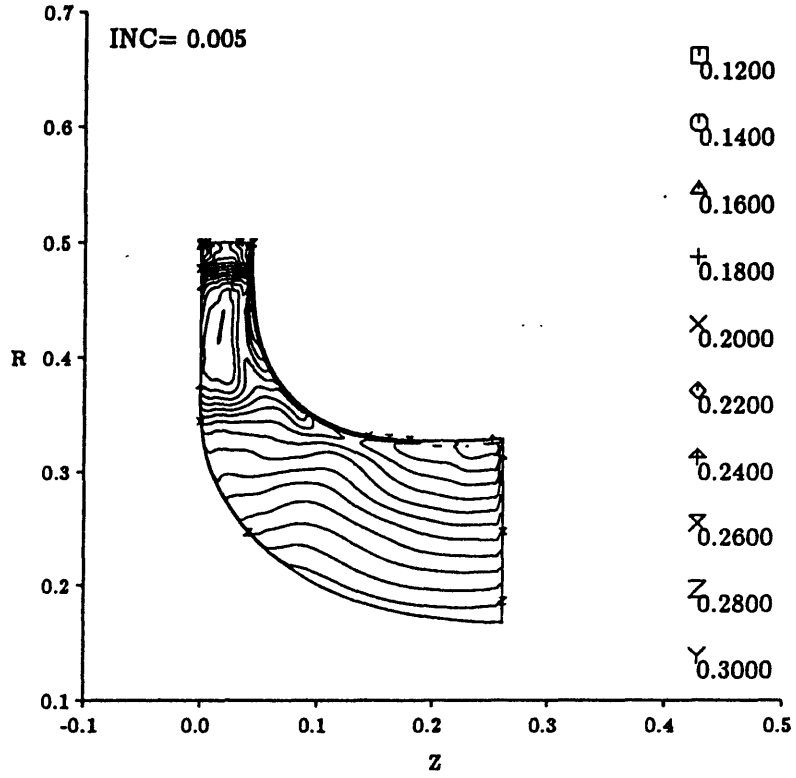


Fig. 7.15a The distribution of $p_{red.}$ on the suction surface from the viscous calculation with 3% of tip clearance

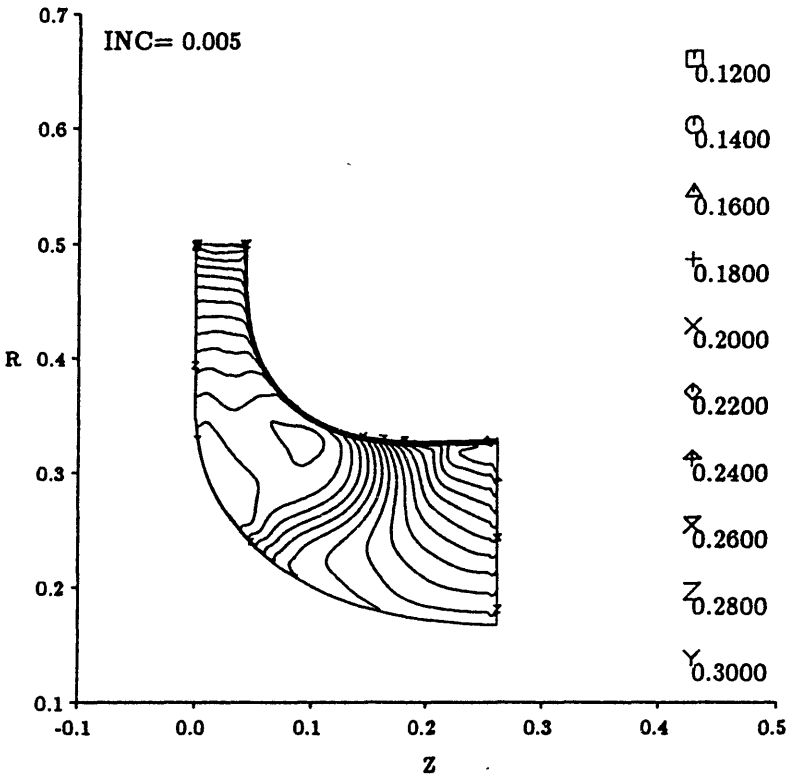


Fig. 7.15b The distribution of $p_{red.}$ on the pressure surface from the viscous calculation with 3% of tip clearance

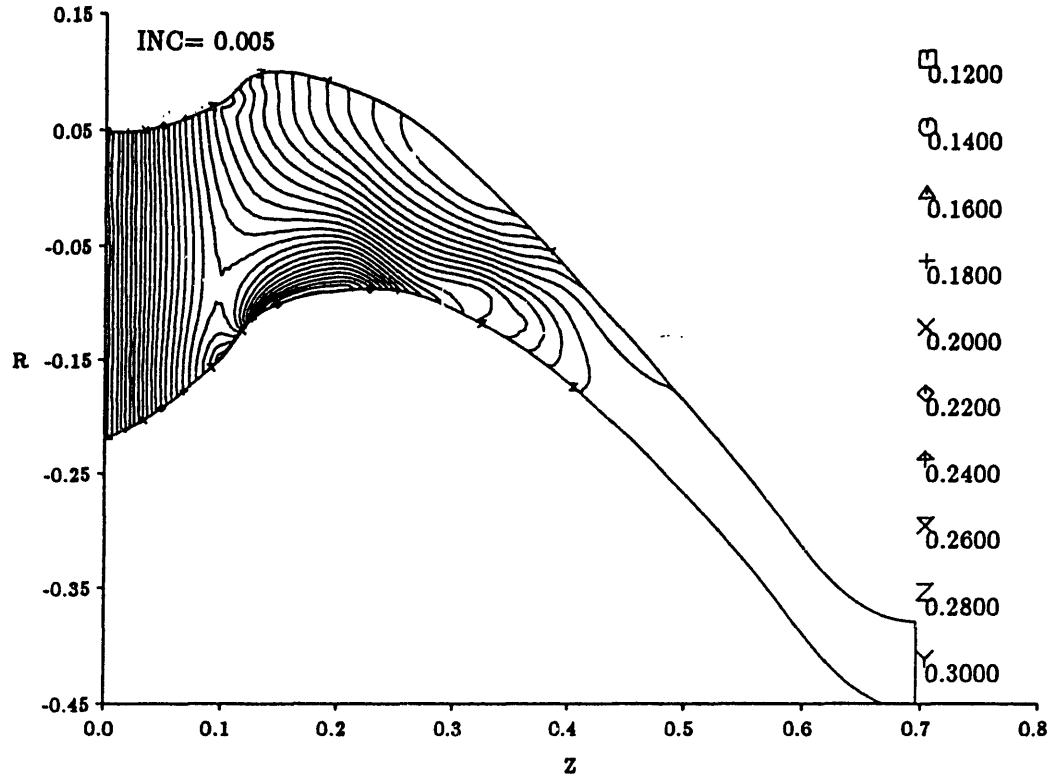


Fig. 7.15c The distribution of $p_{red.}$ on the hub surface from the viscous calculation with 3% of tip clearance

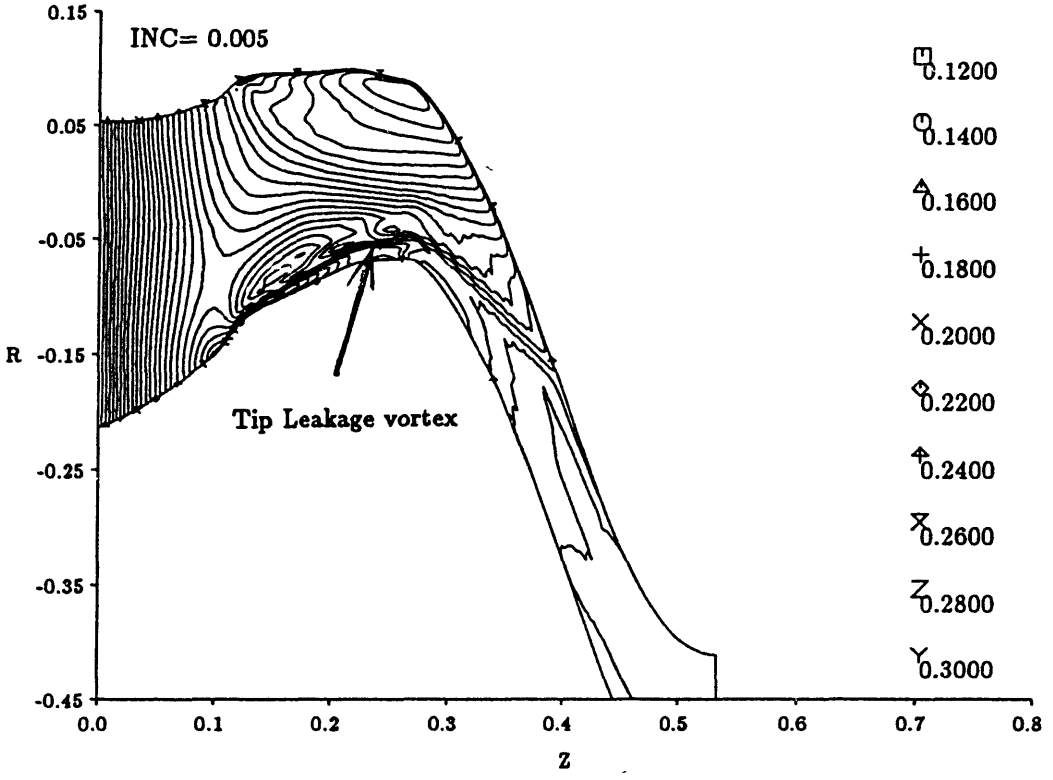


Fig. 7.15d The distribution of $p_{red.}$ on the shroud surface from the viscous calculation with 3% of tip clearance

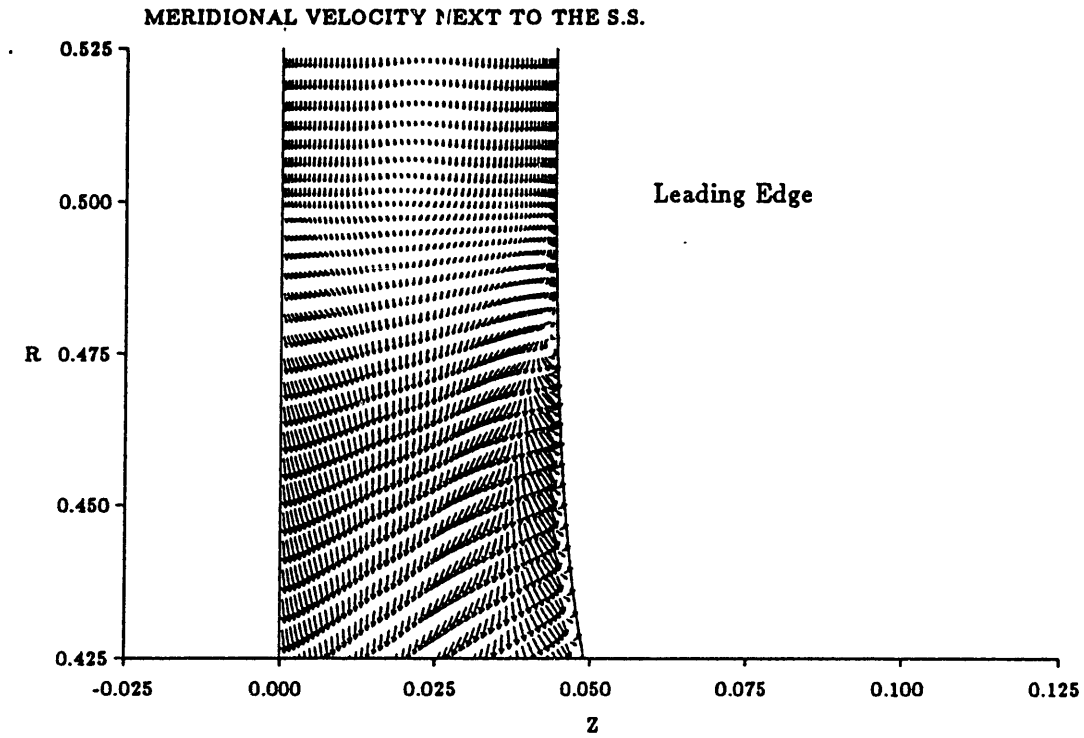


Fig. 7.16a The meridional velocity on the surface 1-point above the S.S. with 3% of tip clearance

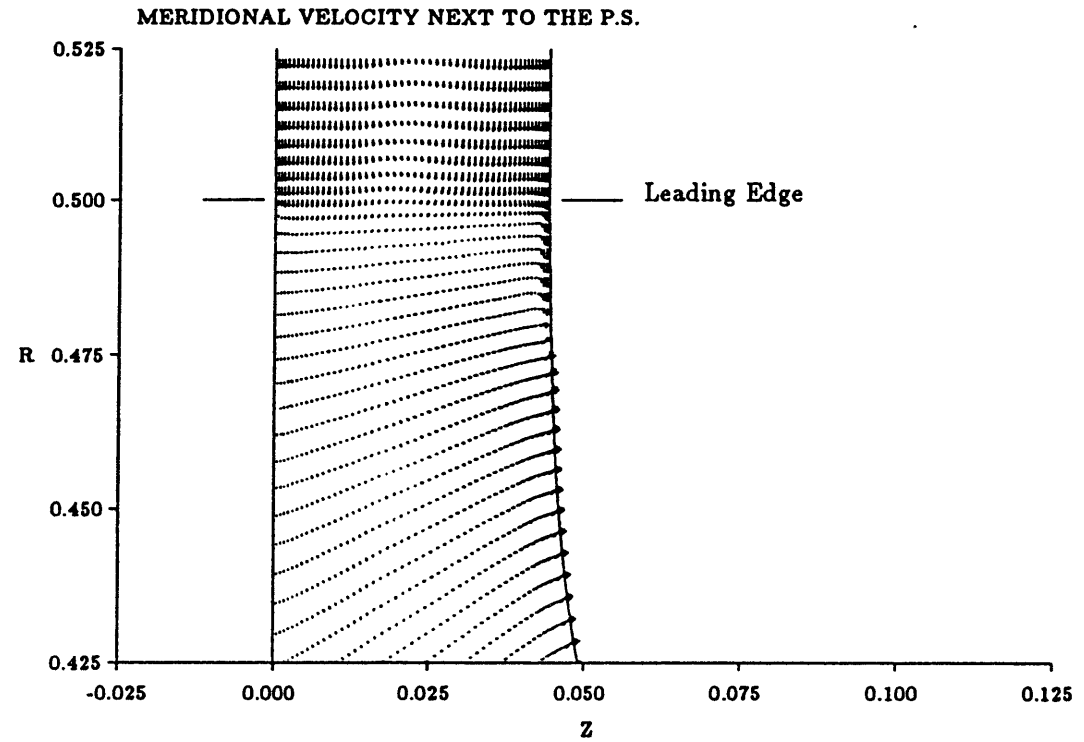


Fig. 7.16b The meridional velocity on the surface 1-point below the P.S. with 3% of tip clearance

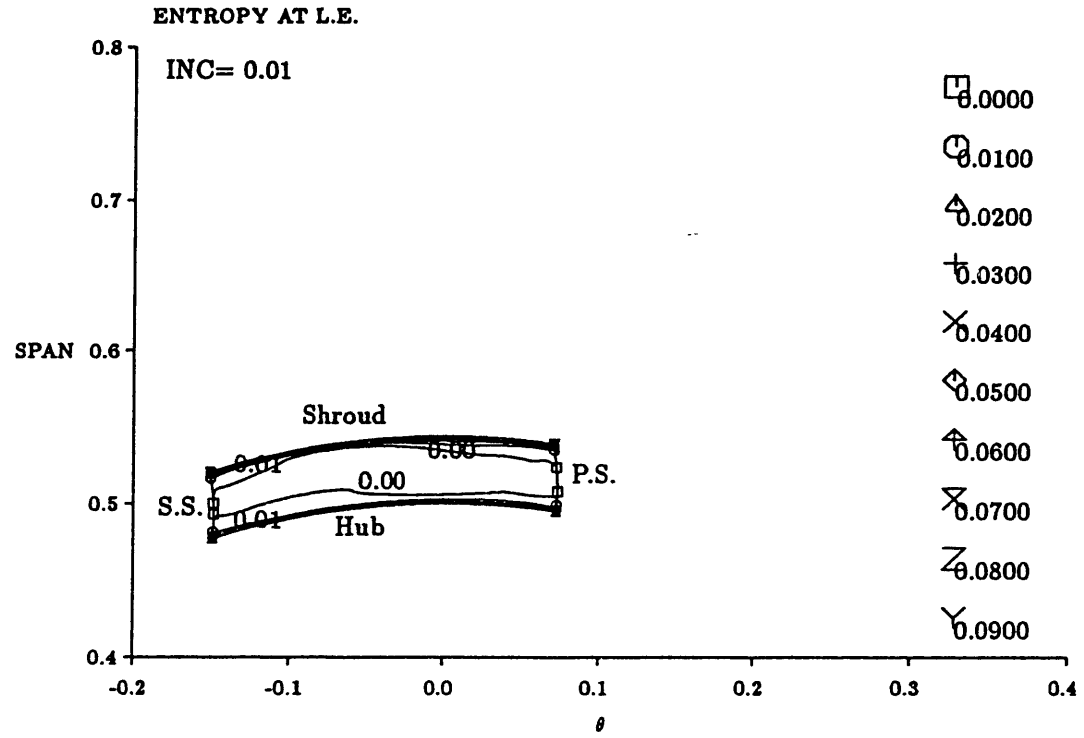


Fig. 7.17a The distribution of entropy S at the leading edge with 3% of tip clearance

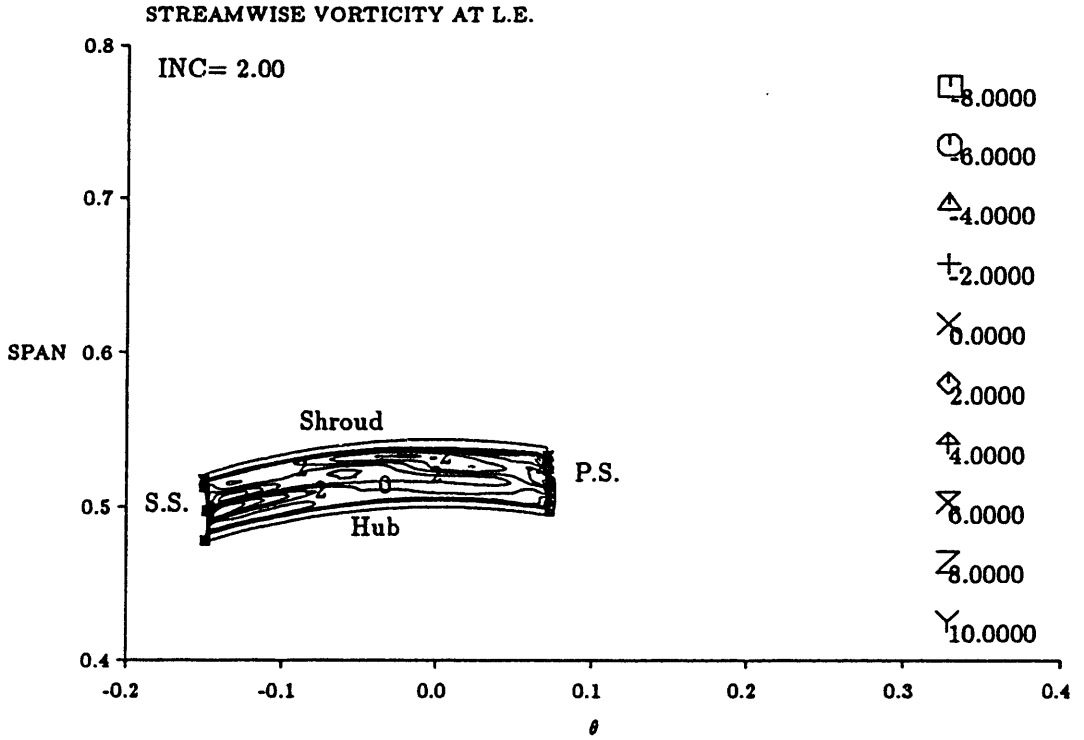


Fig. 7.18a The distribution of streamwise vorticity Ω_r at the leading edge with 3% of tip clearance

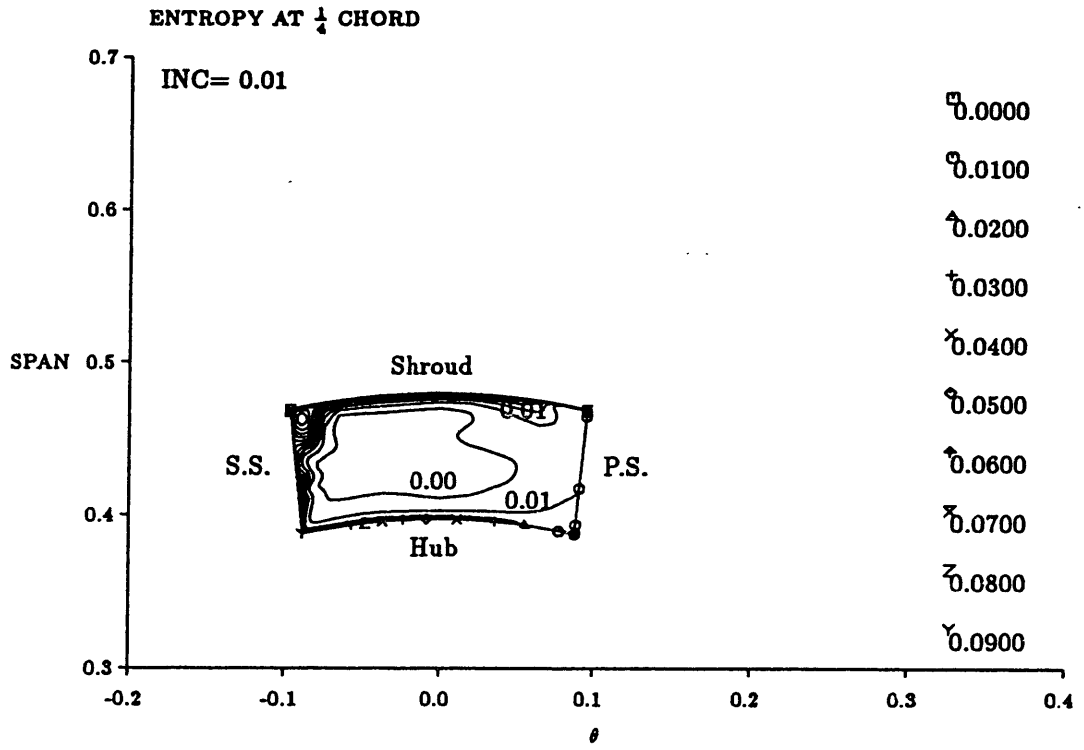


Fig. 7.17b The distribution of entropy S at the $\frac{1}{4}$ chord with 3% of tip clearance

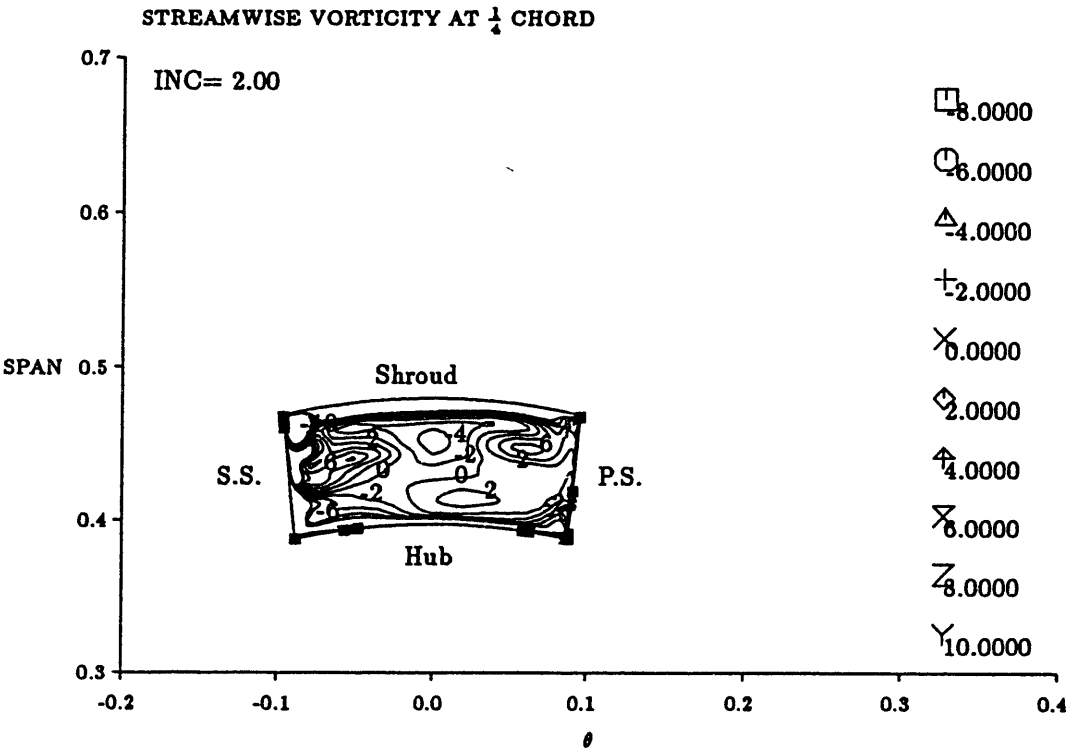


Fig. 7.18b The distribution of streamwise vorticity Ω at the $\frac{1}{4}$ chord with 3% of tip clearance

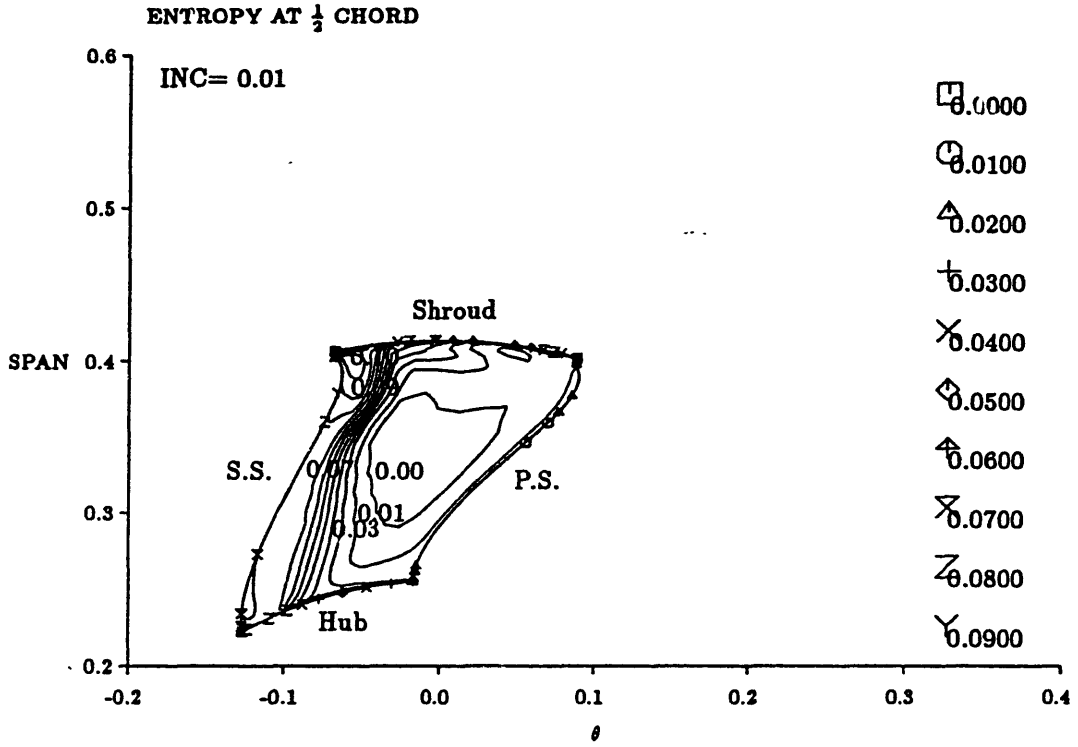


Fig. 7.17c The distribution of entropy S at the $\frac{1}{2}$ chord with 3% of tip clearance

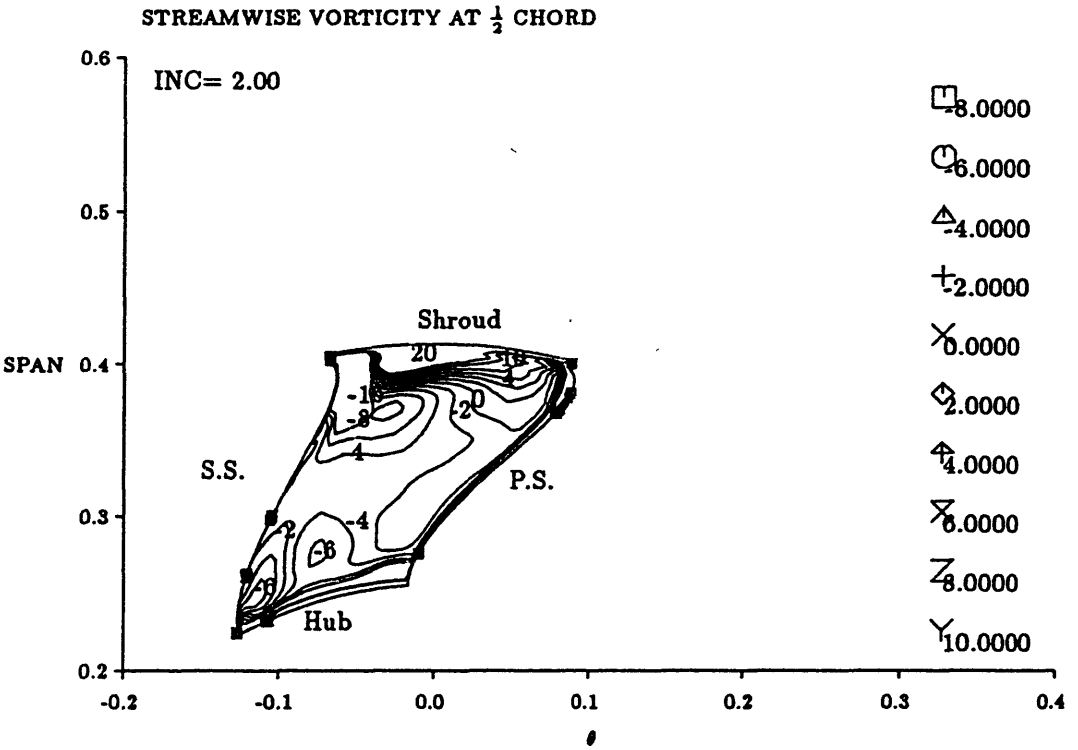


Fig. 7.18c The distribution of streamwise vorticity Ω at the $\frac{1}{2}$ chord with 3% of tip clearance

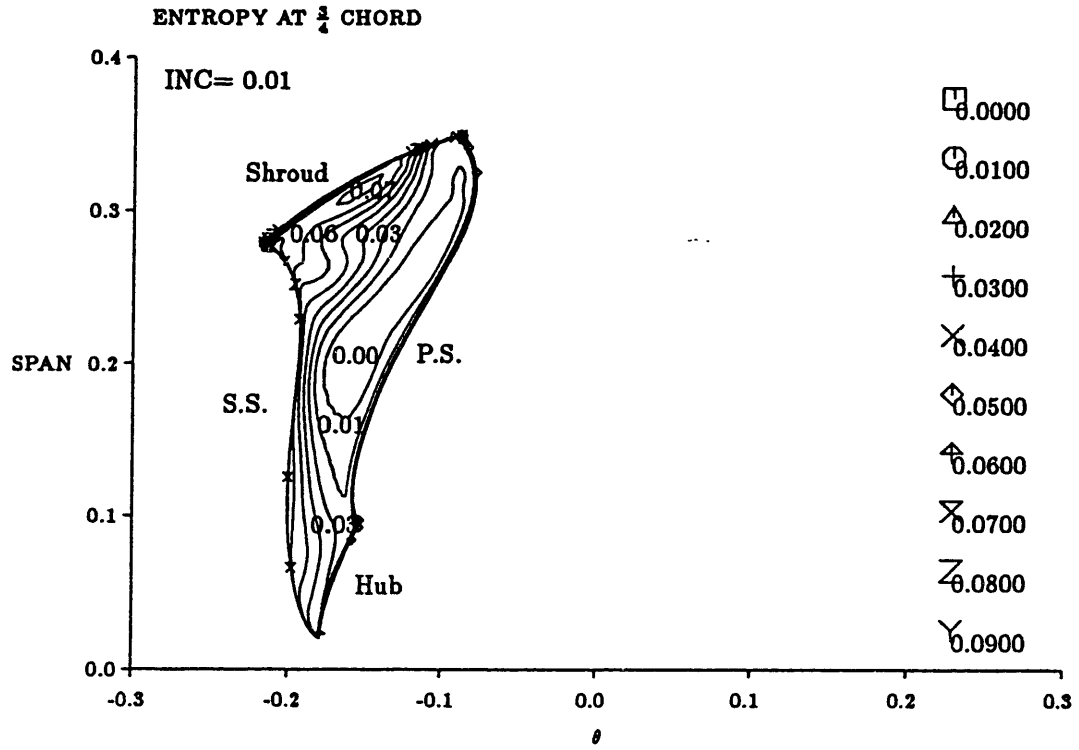


Fig. 7.17d The distribution of entropy S at the $\frac{3}{4}$ chord with 3% of tip clearance

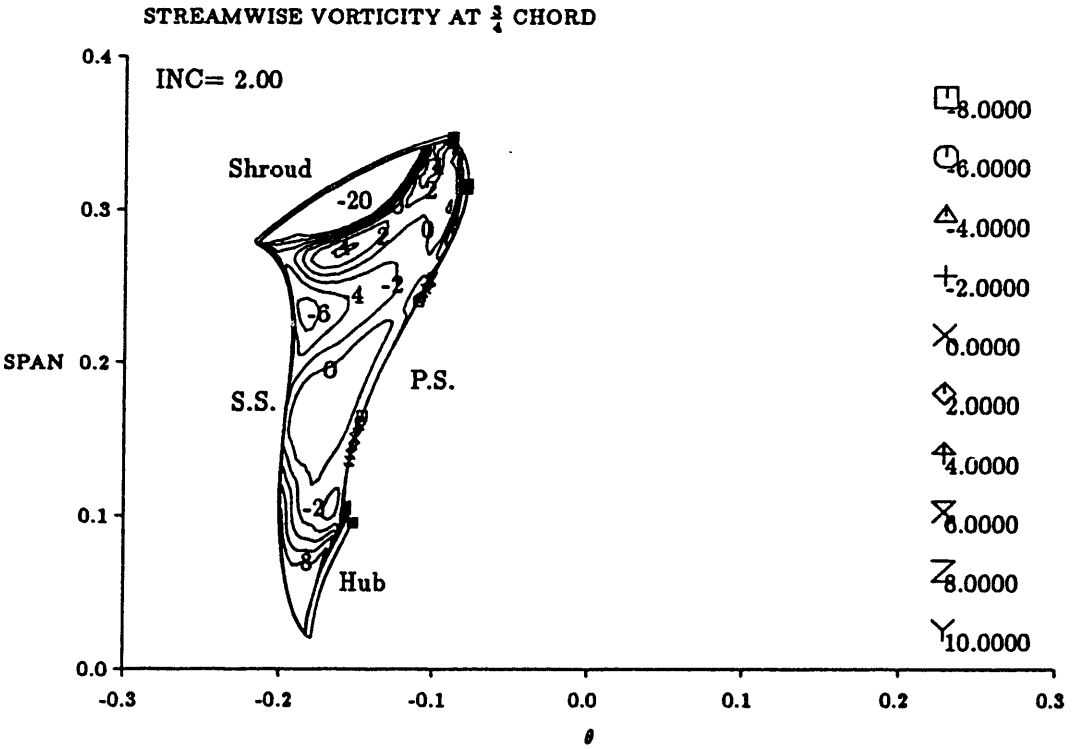


Fig. 7.18d The distribution of streamwise vorticity Ω at the $\frac{3}{4}$ chord with 3% of tip clearance

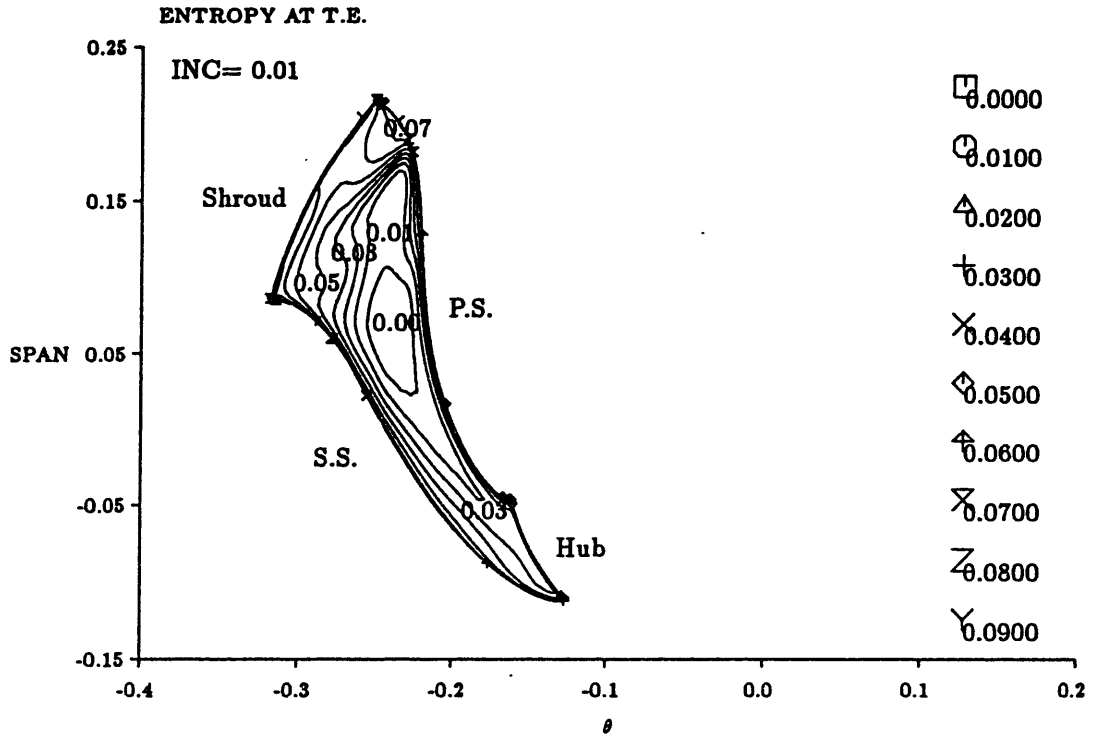


Fig. 7.17e The distribution of entropy S at the trailing edge with 3% of tip clearance

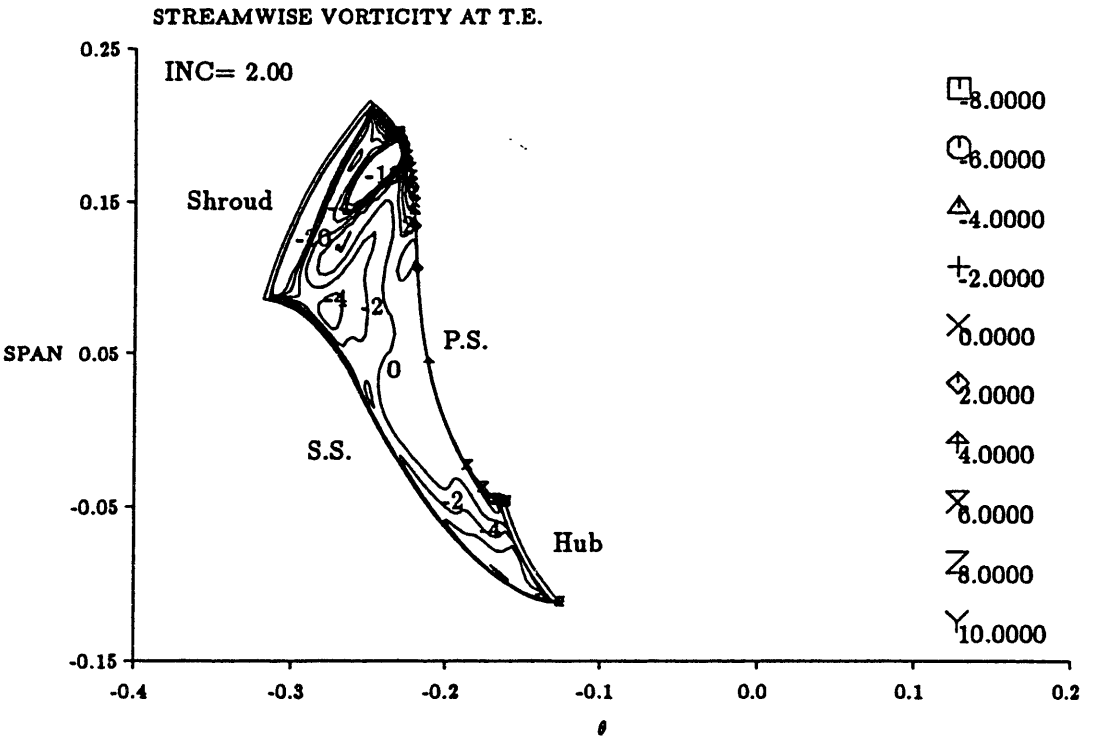


Fig. 7.18e The distribution of streamwise vorticity Ω at the trailing edge with 3% of tip clearance

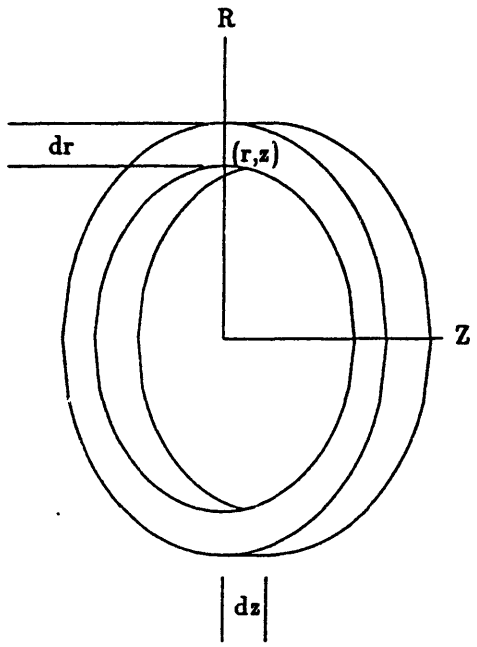


Fig. B.1 Control volume for an axisymmetric flow

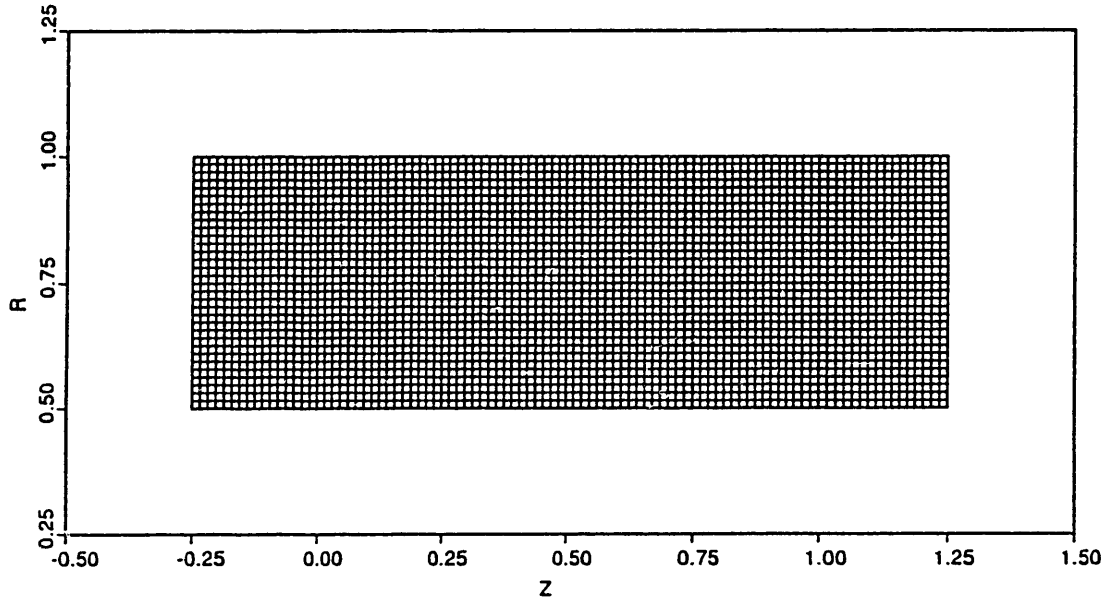


Fig. C.1a Test grid for multigrid study, uniform mesh

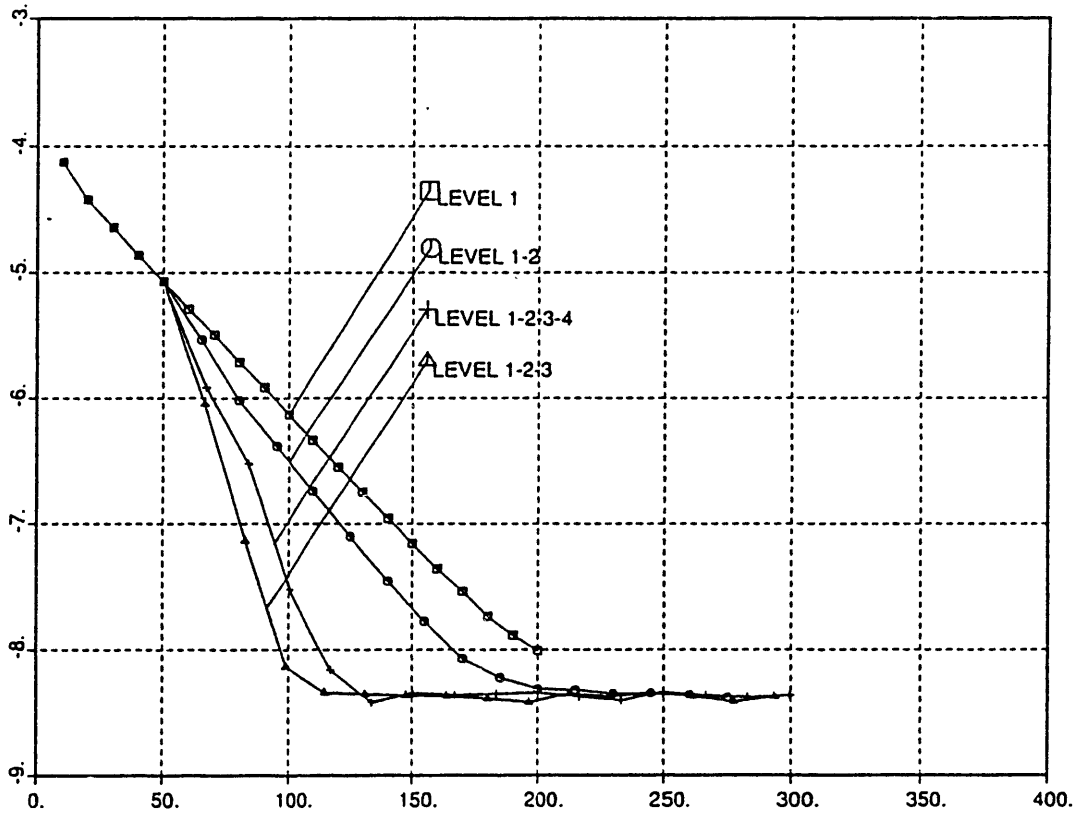


Fig. C.1b Log(residue) verse unit of work for mesh-a

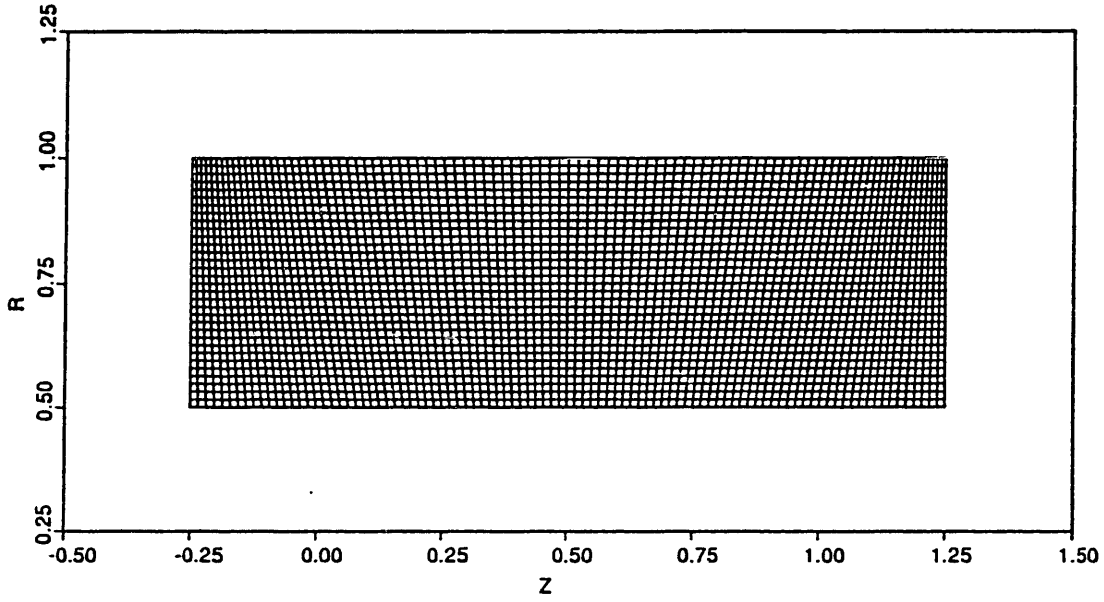


Fig. C.2a Test grid for multigrid study, with distortion in Z direction

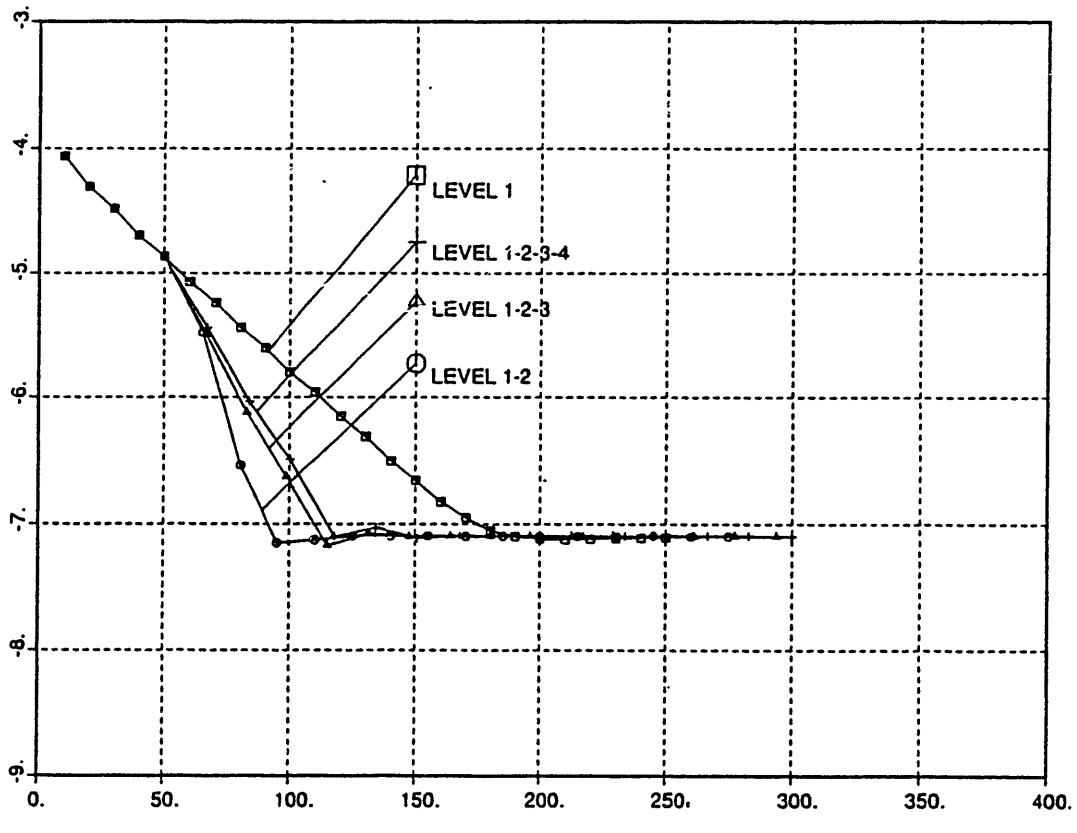


Fig. C.2b Log(residue) verse unit of work for mesh-b

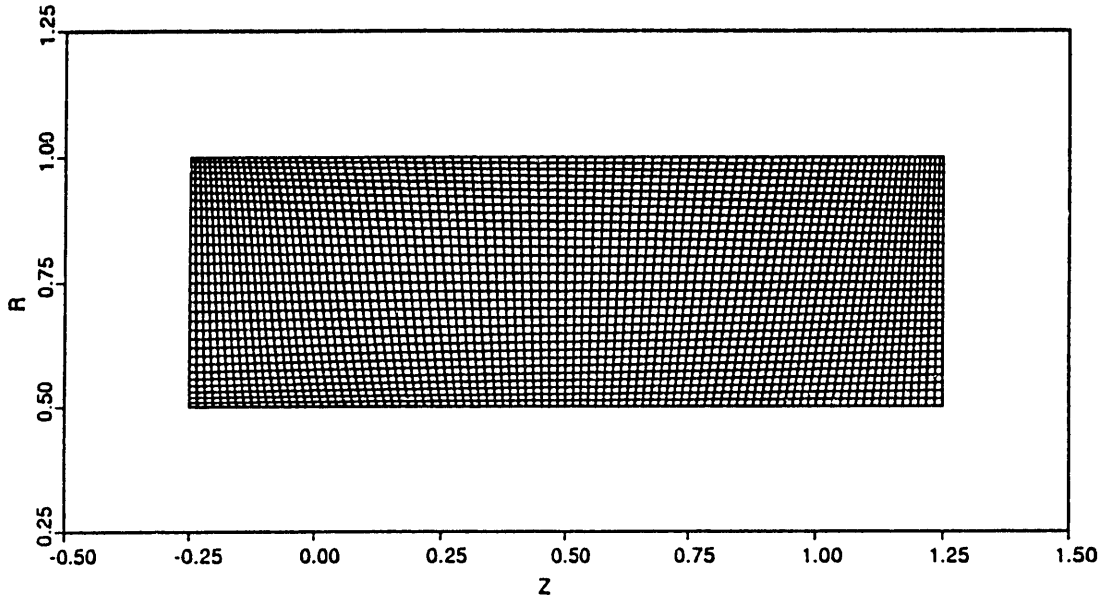


Fig. C.3a Test grid for multigrid study, with distortion in both R and Z direction

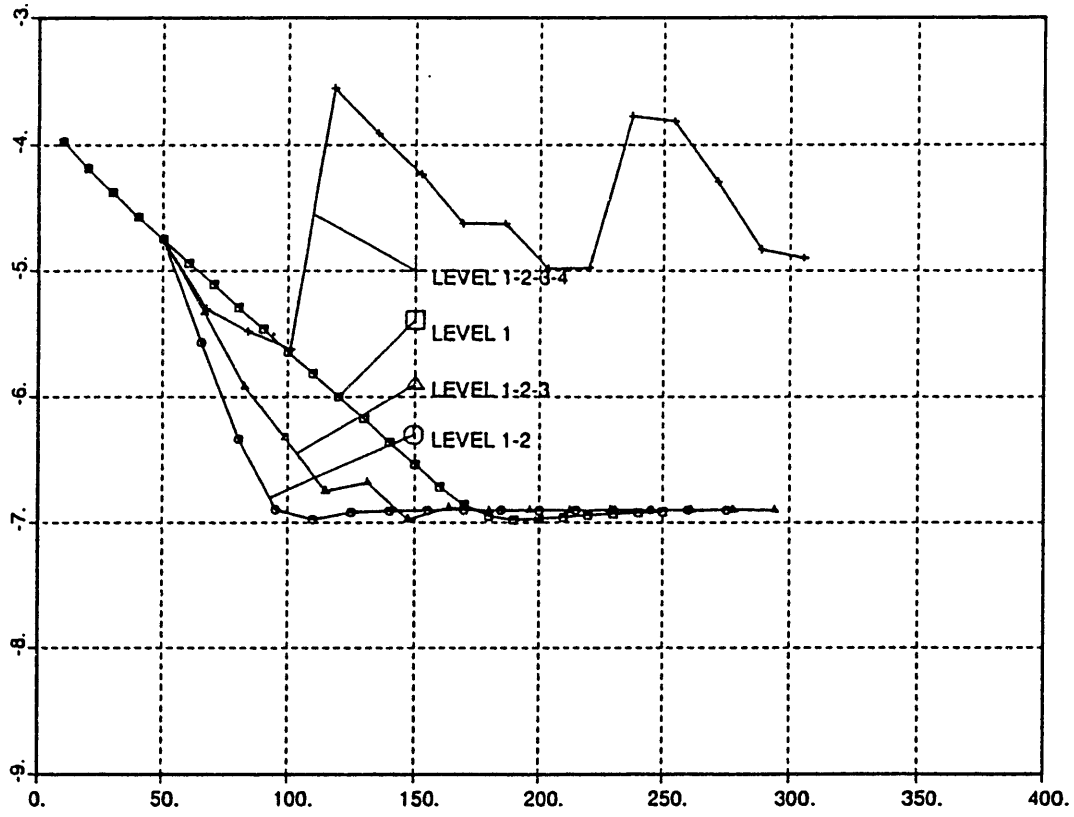


Fig. C.3b Log(residue) verse unit of work for mesh-c

Appendix A

An Expression for Velocity Jump Across the Blade

Let $\vec{\gamma}$ represents the strength of the sheet of vortices lying in the blade surface and assume the blade surface has an infinitesimally small thickness, δ_n, thus

$$\vec{\gamma} = \vec{\Omega}\delta_n \tag{A.1}$$

where

$$\begin{aligned} \vec{\Omega} = & (\nabla r\bar{V}_\theta \times \nabla\alpha)\delta_p(\alpha) \\ = & (\nabla r\bar{V}_\theta \times \nabla\alpha)\frac{2\pi}{B}\sum_{n=-\infty}^{+\infty}\delta(\alpha - n\frac{2\pi}{B}) \end{aligned} \tag{A.2}$$

To obtain $\vec{\gamma}$, we integrate (A.1) and (A.2) with respect to $\vec{n}$ (the unit vector normal to the blade surface) across the singularity, i.e.,

$$\begin{aligned} \vec{\gamma} = & (\nabla r\bar{V}_\theta \times \nabla\alpha)\frac{2\pi}{B}\int_{n=0}\delta(\alpha - n\frac{2\pi}{B})\delta_n \\ = & (\nabla r\bar{V}_\theta \times \nabla\alpha)\frac{2\pi}{B}\int_{n=0}\delta(\alpha - n\frac{2\pi}{B})\frac{dn}{d\alpha}d\alpha \\ = & \frac{2\pi}{B}(\nabla r\bar{V}_\theta \times \nabla\alpha)\frac{dn}{d\alpha} \\ = & \frac{2\pi}{B}\frac{(\nabla r\bar{V}_\theta \times \nabla\alpha)}{|\nabla\alpha|} \end{aligned} \tag{A.3}$$

Now the velocity jump in velocity across the blades : $\Delta\vec{V} = \vec{V}^+ - \vec{V}^- = \vec{W}^+ - \vec{W}^-$ associated with $\vec{\gamma}$ is proportional to $|\vec{\gamma}|$. It is also orthogonal to $\vec{\gamma}$ and $\vec{n}$. Hence,

$$\begin{aligned} \Delta\vec{W} = & \vec{\gamma} \times \frac{\nabla\alpha}{|\nabla\alpha|} \\ = & \frac{2\pi}{B}\frac{(\nabla r\bar{V}_\theta \times \nabla\alpha)\times\nabla\alpha}{|\nabla\alpha|^2} \\ = & \frac{2\pi}{B}[\frac{\nabla\alpha\cdot\nabla r\bar{V}_\theta}{|\nabla\alpha|^2}\nabla\alpha - \nabla r\bar{V}_\theta] \end{aligned} \tag{A.4}$$

Appendix B

Mass-Average of the Continuity Equation with the Effect of Tangential Blockage, b

The introduction of the blockage distribution $b(r,z)$ has been used to account for blade thickness in axisymmetric flow (Ref. 64, 65). In this appendix, we will derive the governing equation for the artifial density $\rho_a(r,z)$ (see chapter 3) with the effect of blockage. If we take a control volume as shown in Fig B.1 and do a mass balance, then we have

$$b\overline{\rho W_r}(2\pi r dz) - (b + \tfrac{\partial b}{\partial} dr)(\overline{\rho W_r} + \tfrac{\partial \overline{\rho W_r}}{\partial r} dr)[2\pi(r+dr)dz]$$
$$+b\overline{\rho W_r}[\pi(r+dr)^2 - \pi r^2] - (b + \tfrac{\partial b}{\partial z} dz)(\overline{\rho W_z} + \tfrac{\partial \overline{\rho W_z}}{\partial z} dz)[\pi(r+dr)^2 - \pi r^2] = 0$$

i.e.,

$$\Longrightarrow \nabla \bullet b\overline{\rho \vec{W}} = 0 \tag{B.1}$$

since $\rho\vec{W} = \overline{\rho}\overline{\vec{W}} + \hat{\rho}\overline{\vec{W}} + \overline{\rho}\widetilde{\vec{W}} + \hat{\rho}\widetilde{\vec{W}}$, Eq. (B.1) can be rewritten as

$$\nabla \bullet b\overline{\rho}\overline{\vec{W}} = -\nabla \bullet b\overline{\hat{\rho}\widetilde{\vec{W}}}$$

or

$$\nabla \bullet \overline{\vec{W}} = -\overline{\vec{W}} \bullet \nabla \ln b\overline{\rho} - \frac{\nabla \bullet b\overline{\hat{\rho}\widetilde{\vec{W}}}}{b\overline{\rho}} \tag{B.2}$$

define the artificial density ρ_a as

$$\nabla \bullet b\rho_a\overline{\vec{W}} = 0$$

or

$$\nabla \bullet \overline{\vec{W}} = -\overline{\vec{W}} \bullet \nabla \ln b\rho_a \tag{B.3}$$

introducing the Stokes stream function ψ to satisfy Eq.(B.3), i.e.,

$$\overline{W}_r = -\frac{1}{b\rho_a}\frac{1}{r}\frac{\partial \psi}{\partial z}$$

$$\overline{W}_z = \frac{1}{b\rho_a}\frac{1}{r}\frac{\partial \psi}{\partial r}$$

Now combine Eq. (B.2) and Eq.(B.3), we have

$$\overline{\vec{W}} \bullet \nabla \ln \rho_a = \overline{\vec{W}} \bullet \nabla \ln \overline{\rho} + \frac{\nabla \bullet b\overline{\tilde{\rho}\tilde{W}}}{b\overline{\rho}} \tag{B.4}$$

which is the Eq.(3.37) with blockage effect. It is interesting to check the consistency for the equation $(B.4)$ when there is no blockage. i.e., $b = 1$.

$$\begin{aligned}
\overline{\vec{W} \bullet \nabla ln\rho} &= \overline{\vec{W}} \bullet \nabla ln\overline{\rho} + \overline{\vec{W} \bullet \nabla ln(1+\tfrac{\tilde{\rho}}{\overline{\rho}})} \\
&= \overline{\vec{W}} \bullet \nabla ln\overline{\rho} + \overline{\vec{W} \bullet [1 - (\tfrac{\tilde{\rho}}{\overline{\rho}}) + (\tfrac{\tilde{\rho}}{\overline{\rho}})^2 - (\tfrac{\tilde{\rho}}{\overline{\rho}})^3 + \cdots] \nabla (\tfrac{\tilde{\rho}}{\overline{\rho}})} \\
&= \overline{\vec{W}} \bullet \nabla ln\overline{\rho} + \overline{\vec{W} \bullet \tfrac{1}{1+(\frac{\tilde{\rho}}{\overline{\rho}})} \nabla (\tfrac{\tilde{\rho}}{\overline{\rho}})} \\
&= \overline{\vec{W}} \bullet \nabla ln\overline{\rho} + \overline{\tfrac{1}{\rho}(\vec{W} \bullet \nabla\tilde{\rho} - \tfrac{\tilde{\rho}}{\overline{\rho}}\vec{W} \bullet \nabla\overline{\rho})} \\
&= \overline{\vec{W}} \bullet \nabla ln\overline{\rho} + \overline{\tfrac{1}{\rho}(\nabla \bullet \tilde{\rho}\vec{W} - \tfrac{\tilde{\rho}}{\overline{\rho}} \nabla \bullet \overline{\rho}\vec{W})} \\
&= \overline{\vec{W}} \bullet \nabla ln\overline{\rho} + \overline{\tfrac{1}{\rho}(\nabla \bullet \tilde{\rho}\vec{W} + \tfrac{\tilde{\rho}}{\overline{\rho}} \nabla \bullet \tilde{\rho}\vec{W} - \tfrac{\tilde{\rho}}{\overline{\rho}} \nabla \bullet \rho\vec{W})} \\
&= \overline{\vec{W}} \bullet \nabla ln\overline{\rho} + \overline{\tfrac{1}{\rho}(\tfrac{\rho}{\overline{\rho}} \nabla \bullet \tilde{\rho}\vec{W})} \\
&= \overline{\vec{W}} \bullet \nabla ln\overline{\rho} + \tfrac{\nabla \bullet \overline{\tilde{\rho}\tilde{W}}}{\overline{\rho}}
\end{aligned}$$

We see the expression of Eq. (B.4) is identical to the area-average form in Eq. (3.21) when $b = 1$.

Appendix C

A Multigrid Method for the Poisson Equation

The multigrid version of a finite element method is presented. The basic multigrid algorithm considers

$$\begin{aligned} \nabla^2 \phi &= S \qquad in \quad G \\ \phi &= \phi^* \qquad on \quad \partial G_1 \\ \tfrac{\partial \phi}{\partial n} &= g \qquad on \quad \partial G_2 \end{aligned} \tag{C.1}$$

where G is the domain and ∂G is the boundary of the domain.

We approximate (C.1) on the finest grid by

$$\begin{aligned} L^m \phi^m &= F^m \qquad in \quad G^m \\ B^m \phi^m &= G^m \qquad on \quad \partial G^m \end{aligned} \tag{C.2}$$

The superscript m denotes an approximation on a grid with mesh h_m. We also use auxiliary grids G^1, G^2,...., G^{m-1}, with $\frac{h_{i+1}}{h_i} = \frac{1}{2}$.

The multigrid cycle begins with a "fine-to-coarse" process which starts with one relaxation sweep on the finest grid. We then have an approximate solution. We then transfer the residual

$$R^m = F^m - L^m \phi^m \tag{C.3}$$

to the next coarser grid using

$$R^{m-1} = T_m^{m-1} R^m \tag{C.4}$$

on the grid G^{m-1}, we solve

$$L^{m-1} \Delta \phi^{m-1} = R^{m-1} \tag{C.5}$$

where $\Delta \phi^{m-1}$ is an approximation to the fine grid error

$$\Delta \phi^m = \phi - \phi^m \tag{C.6}$$

This process is repeated to grid G^k until we get to the coarsest grid. On the coarsest grid we use l relaxation sweeps rather than one relaxation sweep used on the finer grids. To return to the finer grid we begin by using l relaxation sweeps on the coarsest grid. The " coarse-to-fine " process starts by calculating ϕ^2_{new} which is a new approximation to ϕ^2 by

$$\phi^2_{new} = \phi^2_{old} + I^2_1 \, \Delta\phi^1 \tag{C.7}$$

This improved approximation is the correction to the next finer grid. This process is continued until we reach the finest grid G^m. This process consists of one cycle of multigrid. When used as an iteration process, this cycle is repeated until convergence is reached.

As distinct from finite difference approaches the interpolation operators, I^m_{m-1} and T^{m-1}_m, are not arbitrary but based on the finite element interpolation spaces (G^m and G^{m-1}). They are considered in some detail next.

Let us first consider the coarse to fine grid interpolation operator I^m_{m-1}. The only natural choice for the interpolation of a coarse mesh function ϕ^{m-1} to a fine mesh location (x^m_{ij}, y^m_{ij}) is to use the value of ϕ^{m-1} in the location (x^m_{ij}, y^m_{ij}) given by the finite element approximation in space G^{m-1}.

$$[I^m_{m-1} \, \phi^{m-1}]_{ij} = \phi^{m-1}(x^m_{ij}, y^m_{ij}) = \sum_{k,l} I^{ij}_{kl} \, \phi^{m-1}_{kl} \tag{C.8}$$

where the matrix I^{ij}_{kl} is given by

$$I^{ij}_{kl} = N^{m-1}_{kl}(x^m_{ij}, y^m_{ij}) \tag{C.9}$$

On an arbitrary mesh, this results in non-uniform interpolation coefficients I^{ij}_{kl} and for an uniform mesh bilinear elements. This can be written in a simple formula :

$$\begin{aligned}
[I^m_{m-1} \, \phi^{m-1}]_c &= \frac{1}{4}(\phi^{m-1}_1 + \phi^{m-1}_2 + \phi^{m-1}_3 + \phi^{m-1}_4) \qquad \textit{for the center node} \\
[I^m_{m-1} \, \phi^{m-1}]_m &= \frac{1}{2}(\phi^{m-1}_i + \phi^{m-1}_j) \qquad \textit{for the mid side nodes} \\
[I^m_{m-1} \, \phi^{m-1}]_i &= \phi^{m-1}_i \qquad \textit{for the corner nodes (identity)}
\end{aligned} \tag{C.10}$$

Next we consider the fine to coarse grid interpolation operator T_m^{m-1}. As distinct from the finite difference case the residual is an integral quantity which is scaled differently on different grids. A consistent representation of R^{m-1} by means of fine grid quantities is found by approximating the coarse mesh functions in the integral form with fine mesh interpolations in the space G^m, namely.

$$[T_m^{m-1} R^m]_{ij} = \sum_{k,l} I_{ij}^{kl} \int_{S_{ij}^{m-1}} N_{kl}^m(x,y)\, R^m ds \tag{C.11}$$

on an uniformly subdivided coarse mesh, Eq. (C.11) can be reduced to

$$\begin{aligned} [T_m^{m-1} R^m]_{ij} = & \sum_{k,l} I_{ij}^{kl} R_{kl}^m \\ = & R_{i\ j}^m + \tfrac{1}{2}(R_{i\ j+1}^m + R_{i\ j-1}^m + R_{i-1\ j}^m + R_{i+1\ j}^m) + \\ & \tfrac{1}{4}(R_{i+1\ j+1}^m + R_{i-1\ j+1}^m + R_{i+1\ j-1}^m + R_{i-1\ j-1}^m) \end{aligned} \tag{C.12}$$

The convergence of the computation is measured by the evaluation of the L2-norm residual on the finest grid in terms of the work count which is defined in units representing the work needed for one conjugate gradient on the finest mesh. For instance, the work count for one complete multigrid cycle with four-level grids and for the present strategy is given by

$$10 + \tfrac{20}{4} + \tfrac{20}{16} + \tfrac{100}{64} = 17.8125 \text{ units.}$$

The additional work for the residual weighting and other intepolations are not included. All computations are carried out using a fine mesh with 97×33 mesh points and successive coarser meshes of 49×17, 25×9, 13×5 mesh points.

The test case that we choose to assess the algrith is to apply it to the solution of $\nabla^2 \phi = 2r^3 + 6rz^2$ with the Dirichelet boundary condition on four sides. The multigrid grid scheme will turn on after 50 units of work on the finest grid. Three different grids are used (Fig. C.1a, C.2a, C.3a). For mesh in Fig. C.1a which is an uniform grid, the three-level of multigrid scheme results in maximum saving in computational time (Fig. C.1b). It

shows that only 4 cycles of multigrid scheme are needed for the solutions to reach machine accuracy. For the distorted mesh, in Fig. C.2a and Fig. C.3a, the two-level of multigrid scheme results in maximum saving in computational time (Fig. C.2b and Fig. C.3b). For mesh in Fig.C.3a, using four-level of multigrid scheme leads to solution divergence (Fig. C.3b). This may be due to the interpolation errors on the distorted mesh. Thus, the use of a low level of multigrid scheme is more suitable than a high level of multigrid scheme for a distorted mesh.

Appendix D

The Relationship between Number of Grid Points and Number of Harmonic Modes

The periodic potential equations is a Poisson equation with a high frequency in the RHS, i.e., $\nabla^2\phi = S(r,z)e^{inBf(r,z)}$ (see Eq.(3.26)). In order to resolve the information due to the high frequency, a suitable mesh size is needed. A one-dimensional model problem is used to examine the requirement of the mesh size.

$$\frac{\partial^2 \phi}{\partial x^2} = \cos \frac{jx}{2\pi} \tag{D.1}$$

The study shows that regardless the boundary condition and using two-node or three-node elements, the minimum number of elements, M, in order to avoid the solution divergence is given by the relation

$$M = j \tag{D.2}$$

This is the so-called "Nyquist criteria". Thus, the minimum number of elements in the streamwise or spanwise direction for the design code depends on the change in blade wrap, number of harmonic modes, and number of blades. It can be written as

$$M = \frac{n B \Delta f}{2\pi} \tag{D.3}$$

Appendix E

Nondimensional Form of Variables

There are two different ways of nondimensionalization of the variables. One is normalized by the quantities in the relative frame, such as the data used in the design program. The other is normalized by the quantities in the absolute frame, such as the data presented in the thesis. We will state the reference quantities for each case separately.

I. Normalized Form of Variables in the Design Code.

Since the flow is steady in the relative frame, it is convenient to normalize the variables in terms of the quantities in the relative frame. In the design calculation, the tip radius is used to normalize the length. The radial velocity at the leading edge is used as the reference velocity. The thermodynamic quantities are normalized by the rotary total quantities at the leading edge. These normalized variables are shown below:

$$L_{ref} = r_{tip}$$
$$V_{ref} = W_r$$
$$T_{ref} = T_T^*$$
$$\rho_{ref} = \rho_T^*$$
$$P_{ref} = P_T^*$$

II. Normalized Form of Variables in the Output

In general, the far upstream quantities are specified as inputs for a design. It would be suitable to present the variables which are normalized by these upstream quantities. Here, the upstream total pressure, total temperature, diameter are used to normalize the variables. These variables are shown below:

$$L_{ref} = Diameter$$

$$V_{ref} = \sqrt{\frac{P_T}{\rho_T}}$$

$$T_{ref} = T_T$$

$$\rho_{ref} = \rho T$$

$$P_{ref} = P_T$$

For example, from the above normalization, the reduced static prssure is nondimensionalized by P_{ref}, i.e.,

$$\overline{P_{red}} = \frac{P_{red}}{P_{ref}} = \frac{P - \frac{1}{2}\rho\omega^2 r^2}{P_T} = \frac{P}{P_T} - \frac{1}{2}\frac{\rho\omega^2 r^2}{\rho_T(\sqrt{\frac{P_T}{\rho_T}})^2} = \overline{P} - \frac{1}{2}\overline{\rho}(\overline{\omega r})^2$$

Appendix F

The Derivation of the Wake Number

As we have mentioned in chapter 6, the secondary motion of a fluid paritcle can be measured in terms of the Wake number. Here, the derivation of the Wake number developed by W. R. Hawthorne is given in the following.

The Wake number is the ratio of The distance (d_n) that a fluid particle travels in the spanwise direction from the leading edge to the trailing edge along the mid-span over the blade height (D) at the trailing edge, i.e.,

$$Wake\ No. = \frac{d_n}{D} \tag{F.1}$$

As d_n may be calculated by the $\int_0^{t_{T.E.}} w dt$, where w is the velocity in the spanwise direction and $t_{T.E.}$ is the time that a fluid particle travels through the blade passage, the Wake number can be written as

$$Wake\ No. = \frac{1}{D}\int_0^{t_{T.E.}} w dt \tag{F.2}$$

or

$$Wake\ No. = \frac{1}{D}\int_{L.E.}^{T.E.} \frac{w}{W_s} ds \tag{F.3}$$

where W_s is the relative velocity along the mid-span on the suction surface and ds is the distance along the mid-span on the suction surface. If $W \gg w$ and $W \approx W_s$, then

$$Wake\ No. \approx \frac{1}{D}\int_{L.E.}^{T.E.} \frac{w}{W} ds \tag{F.4}$$

For an incompressible flow, the spanwise velocity w is driven by the pressure jump in the spanwise direction, i.e.,

$$\Delta p_{red} = \frac{1}{2}\rho w^2 \tag{F.5}$$

or

$$w = \sqrt{\frac{2\Delta p_{red}}{\rho}} = \sqrt{W_{Shroud}^2 - W_{Hub}^2} \tag{F.6}$$

Thus, the Wake number can be expressed as

$$Wake\ No. \approx \frac{1}{D}\int_{L.E.}^{T.E.} \frac{\sqrt{W_{Shroud}^2 - W_{Hub}^2}}{W} ds \tag{F.7}$$

For a compressible flow, the W in the above expression is replaced by the relative Mach number, i.e.,

$$Wake\ No. \approx \frac{1}{D}\int_{L.E.}^{T.E.} \frac{\sqrt{M_{Shroud}^2 - M_{Hub}^2}}{M} ds \tag{F.8}$$

Even though the expression of the Wake number used in chapter 6 is different from the one derived here. However, both Wake numbers do give the same trend summarized in chapter 6.